MOUNTAIN-PLAINS CONSORTIUM

MPC 24-539 | A. Jones and E. Lawton

FIELD EVALUATION OF GEOGRID-REINFORCED PAVEMENT SYSTEMS OVER SOFT SUBGRADES

MOUNTAIN-PLAINS CONSORTIUM REGION 8

A University Transportation Center sponsored by the U.S. Department of Transportation serving the Mountain-Plains Region. Consortium members:

Colorado State University
North Dakota State University
South Dakota State University
University of Colorado Denver
University of Denver
University of Utah
Utah State University
University of Wyoming

Technical Report Documentation Page

1. Report No.	2. Government Accession No.	3. Recipient's Catalog No.
MPC-635		

4. Title and Subtitle	5. Report Date
Field Evaluation of Geogrid-Reinforced Pavement Systems on Soft Subgrades	August 2024
	6. Performing Organization Code

7. Author(s)	8. Performing Organization Report No.
Evert Lawton, Professor Emeritus Adam C. Jones, Graduate Research Assistant	MPC 24-539

9. Performing Organization Name and Address	10. Work Unit No. (TRAIS)
University of Utah Civil & Environmental Engineering 110 Central Campus Dr., Room 2000 Salt Lake City, Utah 84112	11. Contract or Grant No.

12. Sponsoring Agency Name and Address	13. Type of Report and Period Covered
Mountain-Plains Consortium North Dakota State University PO Box 6050, Fargo, ND 58108	Final Report
	14. Sponsoring Agency Code

15. Supplementary Notes

Supported by a grant from the US DOT, University Transportation Centers Program

16. Abstract

A research section was built within a major highway to compare the performance of different geosynthetic-reinforced pavement systems. The first test section contained no geosynthetic reinforcement. The second section was reinforced with a layer of geogrid. In the third test section, geotextile was placed on the subgrade. In the fourth test, section a second layer of geogrid was placed on top of the geotextile at the subgrade. Each section was instrumented in two locations with moisture sensors, temperature sensors, and strain gages installed on the geosynthetics. Automated cyclic plate load tests were performed using two loading procedures. Static loads were applied using a loaded dump truck. The results of the study were mixed due to variability of the base and subbase thicknesses and densities within the test sections. Permanent deflections and strains in geosynthetics recorded during the plate load tests were small. Due to the inconsistencies in the test sections, analysis of the benefit of the geosynthetics was inconclusive. Significant correlations between predicted CBR values and measured strain in the geosynthetics were discovered. Significant correlations between geosynthetic tensile properties, their depth in the pavement system, and total strain in the geosynthetics were also found.

17. Key Word	18. Distribution Statement
alternatives analysis, field studies, filtration, geogrids, geotextiles, pavement performance, pavements, reinforcing materials, soft soils, subbase (pavements), subgrade materials, test sections	Public distribution

19. Security Classif. (of this report)	20. Security Classif. (of this page)	21. No. of Pages	22. Price
Unclassified	Unclassified	171	n/a

Form DOT F 1700.7 (8-72) Reproduction of completed page authorized

FIELD EVALUATION OF GEOGRID-REINFORCED PAVEMENT SYSTEMS OVER SOFT SUBGRADES

Adam C. Jones
Graduate Student

Evert Lawton
Professor Emeritus

Department of Civil and Environmental Engineering
The University of Utah

August 2024

Acknowledgments

The authors sincerely appreciate and acknowledge the financial support for this research project provided by the Mountain Plains Consortium (MPC) under Contract No. MPC-635, the Utah Department of Transportation (UDOT) under Contract No. 218406 (Research PIC No. UT 20.109), Tensar International Corporation, and Hanes Geo Components. Sincere thanks are also due Tensar International Corporation and Hanes Geo Components for the geosynthetic materials they donated to the project. Special thanks are due Dan Winkle from Tensar International Corporation and Clay Cashatt of Hanes Geo Components for their efforts in securing funding and donations from their companies.

Graduate students Yaqi Huang and Tatiana Gontscharow deserve our sincere gratitude for the substantial amount of time they donated to this project. Their help performing field and laboratory tests and installing strain gages on the geosynthetics was instrumental to the success of this project.

The authors also acknowledge the help and guidance provided by the following individuals from UDOT who served on the Technical Advisory Committee for this research: Jason Simmons, Jeffery Saddler, Lonnie Marchant, and David Holmgren. Sincere thanks are also due to David Stevens and Vincent Liu of UDOT Research and Innovation for managing this project.

Special thanks go to Applied Geotech (AGEC) of Sandy, Utah. Through the generous support of Jim Nordquist, this project was also able to acquire and utilize CPT data. The efforts of Jason Staker, Nathan Salazar, Ty Williams, and Bridger Lambson in operating the Geoprobe and obtaining the necessary information for this project, and Derek Wolfe for synthesizing the CPT data are also sincerely appreciated.

Mark Bryant, the Laboratory Technician for the Structural and Geotechnical laboratories at the University of Utah, provided substantial support and guidance to the students working on this project. His efforts are gratefully appreciated and acknowledged. He has put the students and professors first for many years and truly deserves our gratitude.

Disclaimer

ABSTRACT

A research section was built within a major highway to compare the performance of different geosynthetic-reinforced pavement systems. The first test section contained no geosynthetic reinforcement. The second section was reinforced with a layer of geogrid. In the third test section, geotextile was placed on the subgrade. In the fourth test, section a second layer of geogrid was placed on top of the geotextile at the subgrade. Each section was instrumented in two locations with moisture sensors, temperature sensors, and strain gages installed on the geosynthetics. Automated cyclic plate load tests were performed using two loading procedures. Static loads were applied using a loaded dump truck. The results of the study were mixed due to variability of the base and subbase thicknesses and densities within the test sections. Permanent deflections and strains in geosynthetics recorded during the plate load tests were small. Due to the inconsistencies in the test sections, analysis of the benefit of the geosynthetics was inconclusive. Significant correlations between predicted CBR values and measured strain in the geosynthetics were discovered. Significant correlations between geosynthetic tensile properties, their depth in the pavement system, and total strain in the geosynthetics were also found.

TABLE OF CONTENTS

LIST OF TABLES

LIST OF FIGURES

UNIT CONVERSION FACTORS

SI* (MODERN METRIC) CONVERSION FACTORS

APPROXIMATE CONVERSIONS TO SI UNITS

Symbol	When You Know	Multiply By	To Find	Symbol
		LENGTH		
in	inches	25.4	millimeters	mm
ft	feet	0.305	meters	m
yd	yards	0.914	meters	m
mi	miles	1.61	kilometers	km
		AREA		
in^2	square inches	645.2	square millimeters	mm^2
ft^2	square feet	0.093	square meters	m^2
yd^2	square yard	0.836	square meters	m^2
ac	acres	0.405	hectares	ha
mi^2	square miles	2.59	square kilometers	km^2
		VOLUME		
fl oz	fluid ounces	29.57	milliliters	mL
gal	gallons	3.785	liters	L
ft^3	cubic feet	0.028	cubic meters	m^3
yd^3	cubic yards	0.765	cubic meters	m^3
	NOTE: volumes greater than 1000 L shall be shown in m^3			
		MASS		
oz	ounces	28.35	grams	g
lb	pounds	0.454	kilograms	kg
T	short tons (2000 lb)	0.907	megagrams (or "metric ton")	Mg (or "t")
		TEMPERATURE (exact degrees)		
°F	Fahrenheit	5 (F-32)/9 or (F-32)/1.8	Celsius	°C
		ILLUMINATION		
fc	foot-candles	10.76	lux	lx
fl	foot-Lamberts	3.426	$candela/m^2$	cd/m^2
		FORCE and PRESSURE or STRESS		
lbf	poundforce	4.45	newtons	N
lbf/in^2	poundforce per square inch	6.89	kilopascals	kPa

APPROXIMATE CONVERSIONS FROM SI UNITS

Symbol	When You Know	Multiply By	To Find	Symbol
		LENGTH		
mm	millimeters	0.039	inches	in
m	meters	3.28	feet	ft
m	meters	1.09	yards	yd
km	kilometers	0.621	miles	mi
		AREA		
mm^2	square millimeters	0.0016	square inches	in^2
m^2	square meters	10.764	square feet	ft^2
m^2	square meters	1.195	square yards	yd^2
ha	hectares	2.47	acres	ac
km^2	square kilometers	0.386	square miles	mi^2
		VOLUME		
mL	milliliters	0.034	fluid ounces	fl oz
L	liters	0.264	gallons	gal
m^3	cubic meters	35.314	cubic feet	ft^3
m^3	cubic meters	1.307	cubic yards	yd^3
		MASS		
g	grams	0.035	ounces	oz
kg	kilograms	2.202	pounds	lb
Mg (or "t")	megagrams (or "metric ton")	1.103	short tons (2000 lb)	T
		TEMPERATURE (exact degrees)		
°C	Celsius	1.8C+32	Fahrenheit	°F
		ILLUMINATION		
lx	lux	0.0929	foot-candles	fc
cd/m^2	$candela/m^2$	0.2919	foot-Lamberts	fl
		FORCE and PRESSURE or STRESS		
N	newtons	0.225	poundforce	lbf
kPa	kilopascals	0.145	poundforce per square inch	lbf/in^2

*SI is the symbol for the International System of Units. (Adapted from FHWA report template, Revised March 2003)

EXECUTIVE SUMMARY

A research section was built during construction of a major highway to compare the performance of different geosynthetic-reinforced pavement systems. Test Section 1 was a control section with no geosynthetic reinforcement with 12 inches of Granular Borrow (GB, subbase course) and six inches of Untreated Base Course (UTBC). Test Section 2 was reinforced with a layer of biaxial geogrid placed on top of six inches of GB, with six inches of UTBC on top of the geogrid. Test Section 3 was the same as Test Section 2, except a lightweight, nonwoven geotextile was placed on top of the subgrade as a separator/filter prior to placement of the GB. The fourth test section was the same as the third, except a second layer of biaxial geogrid was placed on top of the geotextile at the subgrade prior to placement of the GB.

Each test section was instrumented in two locations with three moisture sensors, three temperature sensors, and either 10 or 15 strain gauges installed on geosynthetics at each location. At each location, the moisture and temperature sensors were placed at shallow depths below the surface of the subgrade, the top of the GB, and the top of the UTBC. Five strain gages were placed on each geosynthetic at each instrumentation location, with three gages oriented perpendicular to the direction of traffic (transverse) and two oriented in the direction of traffic (longitudinal). For instrumentation location where there was no continuous layer of geosynthetic at one or more interfaces, strain gages were installed on small pieces of geotextile, and the pieces of geotextile were placed on the lower course prior to placement of the next course. For example, in Test Section 1, at each of the two instrumentation locations, a small piece of geotextile, containing five attached strain gages, was placed on top of the subgrade prior to construction of the GB, and a small piece of geotextile with five strain gages was placed on top of the GB prior to placement of the UTBC. A portable data acquisition system was used to record readings of all instruments during the tests that were subsequently performed.

Dynamic Cone Penetrometer (DCP) tests were conducted at selected locations along the test sections to provide data to estimate stiffness of the subgrade, GB, and UTBC at those locations. Automated plate load tests were performed on the surface of the UTBC using a 12-inch diameter plate with two different cyclic-loading procedures. One cyclic-loading procedure consisted of a total of 1,550 cycles with maximum applied stresses increasing from 5 to 40 psi. These tests were used to determine stress-dependent values of resilient modulus (M_r) separately for the UTBC and GB layers at each value of maximum cyclic stress. The other cyclic-loading procedure consisted of 5,000 cycles with 10 different maximum stress levels varying from 5 to 50 psi in a random fashion that simulates real traffic. These tests were used to determine stress-dependent values of resilient modulus (M_r) for the composite system at each value of maximum cyclic stress. Two sets of tests were performed using a loaded dump truck to apply a static load to the pavement system.

The study results were mixed. Due to variability in the test sections arising during construction (for example, substantial variations in thicknesses of the GB and UTBC), significant differences in CBR occurred for the different test sections. The permanent deflection recorded during the automated plate load tests was small, as was the strain in the geosynthetics. Due to inconsistencies in the test sections and data acquisition, the analysis of the benefit of the geosynthetics was inconclusive. Significant correlations between CBR values predicted from the DCP tests and measured strain in the geosynthetic were discovered. Significant correlations between geosynthetic tensile properties, their depth in the pavement system, and total strain within the geosynthetics were also found.

1. INTRODUCTION

One of the main uses of geosynthetics is for the reinforcement of pavement systems. Geogrid can improve the performance of a pavement system through lateral confinement, re-orientation of the shear failure plane, and through the tensioned membrane effect. Geotextiles can offer similar benefits to a pavement system, but their major contribution is to act as separators between soil layers. This separation helps maintain the integrity of reinforcing layers by decreasing the migration of fines into engineered soils in the pavement system (Holtz et al., 2008).

When pavement systems are constructed over soft subgrades, problems can arise in the performance of the roadway. Differential settlement and movement in the base course and subbase layers can damage the pavement system. This can lead to a shortened serviceability life span and consequentially negative impacts to the society that relies on the roadway.

The inclusion of geosynthetics into a pavement system over soft subgrades can increase their performance by impacting the way stress is transferred through the pavement system to the soft subgrade below. The addition of geosynthetics can decrease the amount of sub-excavation that is required to construct the roadway. It can also decrease the amount of subbase and base course that is required for the pavement system. Understanding how geosynthetics impact the performance of pavement systems is important for building sustainable and efficient roadway systems, especially in areas with soft subgrade materials.

2. LITERATURE REVIEW

2.1 Abstract

Geosynthetics are a variety of materials used to improve the properties of soils used in engineered systems. They are widely used in roadway construction to increase bearing capacity and decrease the thickness of the total pavement system. Several studies have been performed analyzing performance capabilities of two geosynthetics: geogrid and geotextile. This literature review analyzes the function of these two materials in roadway construction, their instrumentation for research purposes, the results of current research regarding the properties of these two materials, and possibilities for further research.

2.1.1 Introduction

Geosynthetics are man-made materials typically constituted by polymers formed into a planar material. They are typically used in conjunction with soil and aggregate (Materials 2020) and may be used in roadways or in wall construction (Holtz et al. 1998). Geosynthetics have been a component in roadway construction in the United States as early as 1935 (Beckham 1935). Geosynthetics is an overarching term for an array of synthetic materials. Two of the main groups in this consortium are geogrid and geotextile. Geogrid is typically formed in a grid pattern, either from a solid sheet or from welded cross-members. Its primary function is to act as a reinforcement. Geotextiles are made from fibers arranged in a variety of ways. Their main function is to act as a separator and/or in a filtration capacity. Geogrids and geotextiles can be combined to form geocomposites, which can combine the benefits of both materials (Holtz et al. 1998). Geogrid and geotextile can decrease the cost of roadway construction by reducing the amount of soft subgrade that must be excavated, decreasing the amount of base course that must be used to construct a stable pavement system, by reducing asphalt thickness, and by decreasing the life-cycle cost of the roadway (Al-Qadi et al. 1994; Aran 2006; Cuelho and Perkins 2009; Cuelho and Perkins 2017; Holtz et al. 1998; Perkins and Lapeyre 1997).

This literature review lays out a solid understanding of geotextile and geogrid. This includes the manufacturing of geogrid and geotextile, how the application of geosynthetics in roadway construction have been studied over time, the function of these two materials, how they are installed, and their instrumentation for research purposes. In the reviewed studies, field investigations focused on determining the most beneficial depth of placement of geosynthetics in a pavement system. This included whether depth of placement was dictated solely by an optimum depth below the pavement surface or by placement between specific layers of the pavement system. Laboratory tests focused on a range of experiments, from determining material properties that can be compared between types of geosynthetics to simulating real-life applications of geosynthetics.

Progress has been made in determining geosynthetic's function and how to accurately measure the mechanical properties of geosynthetics (Perkins and Lapeyre 1997). How these properties translate to improvement in a real roadway has not been as robustly studied. Real roadway conditions deal with variable subgrades and introduce an element of error during installation. The extent of the impact of these and other factors is not well known. Another area where further research is needed is in how several layers of geosynthetics interact in a pavement system. The long-term benefits and performance of geosynthetics are also not well-understood.

2.1.1.1 Manufacturing

Geogrid's name comes from the grid-pattern in which it is formed. This can be a square or rectangular pattern, or a triangular pattern (Chen et al. 2021). The grid openings are called apertures. They are a minimum of a ¼ inch in width and allow soil and aggregate from either side of the material to interlock

with the geogrid and the material on its opposite side (Materials 2020). The sides of the apertures are called ribs (E. Cuelho, personal communication, 2022).

Geogrid is manufactured in two main ways. It is either made from a solid sheet of polypropylene, polyester or polyethylene, or it can be made from woven polymer ribs coated in plastic (Holtz et al. 1998).

In the case of geogrid made from a solid extruded sheet of polymer, holes are punched out of the sheet while the polymer is still hot in the manufacturing process (Figure 2.1). In the case of biaxial geogrid, the sheet is then stretched in the direction parallel to manufacturing (machine-direction or MD) and in the direction perpendicular to manufacturing (cross-machine-direction or XMD). The holes punched in the sheet stretch into square or rectangular apertures in the cooled sheet (E. Cuelho, personal communication, 2022). As the hot sheet of polymer is stretched, the polymer strands are aligned in the ribs in between the apertures. This alignment increases the strength of the finished product (Holtz et al. 1998). These apertures can be quite elongated, as in the case of uniaxial geogrid, or they can be triangular, as in the case of multi-axial geogrid (Chen et al. 2021). The sheet is then rolled up for transportation to the jobsite.

Geogrid made from woven material, also known as flexible geogrid, is made by taking individual strands of woven polymer, and then forming them into a grid pattern. The joints between the individual strands are either welded or glued. These grid-oriented strands can then be coated in plastic (Holtz et al. 1998).

Geotextiles are made from the same array of polymers as geogrids, but instead of being extruded in a sheet or formed in gridded strands, they are formed into a textile. The textile can be made from polymer yarn or individual fibers of polymer. Long fibers are called filaments, and short fibers are called staple fibers.

Geotextiles typically fall into the categories of woven or nonwoven geotextiles. Woven geotextiles are made by weaving fibers into a cloth that is either monofilament, multifilament, fibrillated yarn, or from slit films and tapes (Holtz et al. 1998). The strands of polymer oriented parallel to the length of the woven geotextile are called warps, and the strands running perpendicular to the warp are called filling or weft. The edge of the woven material is called the selvage (Materials 2020). Nonwoven geotextiles are made from fibers either welded together by heat or needle punched together (Figure 2.2). Needle punching uses mechanical teeth to tangle the strands of polymer together into a cohesive material. Stress is then transferred from fiber to fiber through this mechanical connection (E. Cuelho, personal communication, 2022).

To characterize geosynthetics for their application in design and comparison purposes, certain properties of these materials are often reported by the manufacturer and can be tested in the laboratory. Several "index" or general properties commonly used are mass per unit area, thickness, aperture size, and tensile strength (Cuelho and Perkins 2017).

Other important properties of geosynthetics can also be determined. One of these is cyclic tensile modulus (ASTM D7556), which is a measurement of the tensile strength of a geosynthetic under cyclic loading, which simulates loading from highway use. Another property is resilient interface shear stiffness (ASTM D7499). This property quantifies the stiffness of the interface between the geosynthetic and aggregate while experiencing small cyclic loads with varying amounts of confinement. Junction strength is another property that can also be measured using ASTM D7737. It is a measure of the average shear strength of junctions in a geosynthetic, like a geogrid per unit width. It is tested by pulling a junction by the ribs attached to it. Junction stiffness is related to junction strength in that it is the secant stiffness of the junction strength at 1.3 mm of displacement. There is not currently an ASTM designated for this property. Aperture stability modulus (ASTM D7864) is also related to the stiffness of a geosynthetic. This property

is applicable for geogrids. It is a measure of the geogrid's dimensional stability under a torque and reported as force-per-unit length per degree of rotation. Secant modulus comes from the wide-width tensile test (ASTM D4595 for geotextile and D6637 for geogrids), which also determines the tensile strength of geosynthetics. Secant modulus is the modulus secant to the point in the stress-strain curve at which the response is no longer linear (Cuelho and Perkins 2017). ASTM D4632 outlines the last property in this list. It is the "grab tensile test," which is used with geotextiles. To strain a specimen measuring four inches in width until tensile failure is reached, one-inch wide clamps are used. This test can be hard to use in design, as it is not clear how the stress is dissipated through different types of geotextiles, which makes comparison between different tests difficult (Holtz et al. 2008).

2.1.2 Function

There are several proposed mechanisms by which geogrid improves the pavement system. The three main ways are through lateral confinement of the soil, increasing bearing capacity by reorienting the shear failure plane of the soil, and by membrane reinforcement (Figure 3).

Lateral confinement can also be described as a "shear-resisting interface" (Perkins 1999). As the road surface is loaded by wheels of vehicles, the aggregate in the soil is pushed downward and out away from the loaded area. This aggregate then interlocks with the apertures of the geogrid, which resists the lateral spread of the soil. The geogrid acts as a tensile reinforcement, confining the aggregate. This, in turn reduces the amount of permanent vertical deformation in the pavement system. This mechanism also increases the mean effective stress within the soil layer, typically the base course layer of the pavement system, which usually leads to an increase in elastic modulus in granular soils (Perkins 1999).

Evidence of this mechanism was shown in research performed by Perkins in 1999. In a laboratory experiment, strain in the geosynthetic, base course, and subgrade were all monitored under cyclic loading. Compared to the control, the radial strain in the base course 50 mm above the geosynthetic was reduced considerably. At the same time, tensile strain was recorded in the geosynthetics. These two measurements showed evidence that the strain in the geosynthetic correlated to a decrease in strain in the base course and subgrade material (Perkins 1999).

The second mechanism is increasing bearing capacity by reorienting the shear failure plane of the soil. As the normal stress in pavement system increases, shear stress develops in the soil. Soils fail when shear loads surpass the shear capacity of the soil matrix. The geogrid forces the shear plane to follow its surface, which can keep the shear plane from reaching weaker subgrade materials where the soil shears more easily (Holtz et al. 1998) The base course is also stiffened by its interaction with the geogrid. By stiffening the base course, normal stresses from wheel loads are dissipated farther through the base course, thereby decreasing the stress applied to the subgrade. This, then, increases the bearing capacity of the pavement system. From the same experiment mentioned previously, Perkins noted the reduction in measured radial strain in the subgrade due to the inclusion of geosynthetic reinforcement was understood to be connected to a decrease in shear strain in the subgrade, which, in turn, meant a reduction in shear stress had taken place (Perkins 1999).

The third improvement mechanism is membrane reinforcement. When a road surface is rutted in excess of 100 mm, the geogrid can be mobilized to the point that it begins to support the wheel load as it is tensioned (Holtz et al. 1998). Rutting is the result of compaction of the base course and/or the subgrade in the pavement system to the point of reaching a bearing capacity failure state. This rutting begins to create a punching failure in the subgrade. As the material is forced down, the geogrid interlocked with the base course beside the rutted material places the geogrid in tension as it strains (Giroud and Han 2004). Due to the stiffness of the geogrid, further rutting can be prevented as the geogrid takes the wheel load in tension. In current research, it is not entirely clear when each of these reinforcement mechanisms come into play.

Further research is needed to determine at which point each of these reinforcement mechanisms becomes active in a pavement system.

Geotextile's main mechanism of pavement system improvement is through separation. Geotextile placed at the interface of two soil layers in the pavement system (i.e., the base course and subgrade) can keep the two layers from mixing. A localized bearing failure occurs when aggregate from the base course penetrates the subgrade layer. This can happen in areas where there is a soft subgrade, typically with a California Bearing Ratio (CBR) of less than three. Long-term dynamic loading, which induces pumping of the subgrade and migration of fines, can also be added to the mixture of the two layers. As the two layers mix, the beneficial properties of the base course layer are altered, weakening the pavement system. The migration of fines impacts the performance of the base course, making it more susceptible to freeze-thaw, drainage issues, and a decrease in resilient modulus. Without being able to properly drain, excess pore pressure will not be allowed to dissipate (Holtz et al. 2008). By placing a geotextile at the interface of the two layers, the aggregate and fines can be separated, thus maintaining the integrity and dimensions of the base course layer (Holtz et al. 1998).

2.1.2.1 Installation

Due to improper installation, many of the benefits afforded by geosynthetics can be negated (Holtz et al. 2008). Proper installation is key to geosynthetic functioning properly in a pavement system design. Geosynthetics used for roadway construction are installed by first preparing the roadway area. If the geosynthetic is being placed on top of the subgrade, the area should be cleared and graded before installation. Proof rolling of the subgrade, if it is not too weak, can help identify weak zones that must be evaluated before placing the geosynthetic (Holtz et al. 2008). Geosynthetics are rolled out on the surface where they are installed. The geosynthetic should never be dragged across the underlying material. If a geogrid is installed on a geotextile to form a geocomposite, it should be rolled out directly on top of the geotextile. They can be installed in between the subgrade and the base course, inside of the base course, directly under the pavement surface, and even between the pavement and an overlay (Aran 2006). It is important to make sure there are no wrinkles in the installed geosynthetic, which can be difficult to accomplish in real roadway construction (Cuelho and Perkins 2009). Geosynthetics are usually rolled out in the direction of traffic, longitudinally down the roadway. In some instances, due to differences in strength in the MD and XMD, they may be placed transversely across the roadway (Webster 1993). Depending on the geosynthetic material, site conditions, and application, the amount of overlap between adjacent rolls can change. Perkins and Cuelho implemented an overlap of 1 m in their research (Cuelho and Perkins 2009), and Webster only overlapped woven geotextiles in his research by 1 ft (Webster 1993). According to the Geosynthetic Design and Construction Guidelines published by the Federal Highway Administration, a minimum overlap of 0.3 m (1 ft) should be used. Depending on the CBR of the subgrade, a geosynthetic placed on the subgrade should have an increased overlap. If the CBR is greater than 2, the minimum overlap of one foot is acceptable. For a CBR of one to two, an overlap of two to three feet should be utilized. If the CBR is less than one, the geosynthetic should be sewn. Most geogrid cannot be sewn, and should instead be connected with wire cables, hog rings, or some other connector that will meet the strength requirements of the design (Holtz et al. 2008). In the case of an overlap-only connection, the only mechanism of stress transfer from roll-to-roll is through friction between the two geosynthetics, and in the case of geogrid, through aggregate strike-through. Without significant overburden stress, the stress transferred through overlap is low (Holtz et al. 1998). Improper installation can impact the performance of a pavement system, but the exact long-term effects are not well known.

2.2 Instrumentation and Testing

There are a variety of ways to measure the performance of a geosynthetic in a pavement system. The first is to look for physical indications of failure in the pavement system, such as asphalt issues, including cracking, rutting, and deflections (Aran 2006). Another way to use physical data to measure performance is to inspect the geosynthetic after loading (Figure 2.4), (Bathurst and Raymond 1987; Cuelho and Perkins 2009).

Data can also be obtained during an experiment by measuring displacement at the surface of the pavement system. Displacement measured at the surface can be performed in between load or traffic cycles and during loading. Cuelho and Perkins measured rutting using a robotic total station to compare the performance of different test sections (Cuelho and Perkins 2017). Webster in 1993 simply used a metal straight edge to measure upheaval and rutting at the pavement surface (Webster 1993). In the case of the 2019 study by Feng et al., settlement in a test section was simply measured in relation to the side of the test container (Feng et al. 2019).

Linear variable differential transformers (LVDTs) can provide real-time data acquisition during an experiment, as implemented by Bathurst and Raymond. They can be used to measure strain in the soil layers of a pavement system or in the geosynthetic. A single LVDT measured displacement of a footing loading a test section to specified stress levels (Bathurst and Raymond 1987). A more elaborate measurement of surface displacement in a lab setting is the implementation of LVDTs in an array across the pavement section (Bathurst and Raymond 1987). Also using an array setup, Dash and Majee utilized eight dial gages over the surface of their laboratory section to measure displacement at the surface (Dash and Majee 2021). Qian et al. used an array of five displacement transducers to measure surface displacement in their 2010 test (Qian et al. 2010). In another experiment, Perkins used eight LVDTs at the test pavement section surface, with two of the LVDTs measuring displacement through holes in the loading plate (Perkins 1999).

For measuring strain in the soil layers, a variety of sensors are implemented. Perkins in 1997 implemented vibrating wire sensors that measured strain and displacement. The vibrating wire (VW) sensors were ideal for long-term measurements, but due to the low sampling rate of these sensors, they are not ideal for dynamic loading. LVDTs were also used. The sensors were placed in the base course and asphalt layers. The sensors placed in the base course and asphalt layers had two circular aluminum plates attached to either end to interlock with the soil. The sensors were aligned with the expected wheel path of the traffic going over the test section, so vehicles would drive directly over the sensors. Sensors were also placed near the bottom of each layer of material they were monitoring (Perkins and Lapeyre 1997).

To protect the sensors during compaction, a combination of rigid and flexible containers was used. The container was placed around the sensor during compaction, and then removed after the base course layer was above the level of the sensor. With the containers removed, soil was packed around the sensors by hand (Perkins and Lapeyre 1997). In 1999, Perkins performed another experiment in which LVDTs with metal plates were placed in the subgrade and base course layers of a pavement test section. They were oriented in the vertical, radial, and circumferential directions and measured strain. The instruments were placed near the base-subgrade interface. Stress cells were also used to monitor the dynamic stress in the base course and subgrade. To determine how accurate the strain gages were in the experiment, a control test section was constructed with two gages spaced equally and on opposite sides from the center of the loading point. When the vertical strain of the two gages was plotted, the LVDT strain gages performed similarly to each other, with their strain being within .04% or less of each other (Perkins 1999). Another sensor used to measure displacement and strain in the base and subgrade is the multi-depth deflectometer (MDD). The MDD is a set of LVDTs arrayed in a borehole and anchored at different depths to measure displacement at that point relative to the surface of the pavement section. A diagram of an MDD module

is shown in Figure 2.5. Four sets of MDDs were used in Webster's experimental test sections (Webster 1993). The utilization of instrumentation in the field can be complicated by factors, such as the stresses on instrumentation incumbent with transportation of materials and construction practices and the environmental strains placed upon instrumentation in a field scenario.

Other instruments can be used in situ to obtain strength values for subgrade and base course layers. In the reviewed studies, the vane shear test and the DCP were the most prominent. These two devices were used to determine the in situ CBR of the subgrade and base course materials through empirical correlations (Cuelho and Perkins 2009; Feng et al. 2019; Qian et al. 2010). A common correlation from the Army Corps of Engineers between DCP data and CBR values is given in ASTM D6951 as follows:

$$CBR = 292/DCP^{1.12} \quad (1)$$

where CBR = California Bearing Ratio value for all soils, except CH soils and CL soils with CBR<10 (%), and DCP = Dynamic Cone Penetrometer Index (mm/blow). This correlation is for all soils besides CL soils with a CBR less than 10, and CH soils. For CL soils with a CBR less than 10 the following equation applies:

$$CBR = 1/(0.017019 * DCP)^2 \quad (2)$$

where CBR = California Bearing Ratio value for CL soils with CBR<10 (%) and DCP = Dynamic Cone Penetrometer Index (mm/blow) For CH soils the following equation should be used:

$$CBR = 1/(0.002871 * DCP) \quad (3)$$

where CBR = California Bearing Ratio value for CH soils (%) and DCP = Dynamic Cone Penetrometer Index (mm/blow).

CBR values can also be correlated to tip resistance data from cone penetration testing (CPT). One such correlation was developed by Hardiyatmo:

$$CBR\ (\%) = 0.454\ qc \quad (4)$$

where qc= tip resistance (kg/cm^2) and CBR = California Bearing Ratio (%).

This correlation was then modified by Arbianto et. al. (2021) to better match the CBR values determined by the DCP correlations:

$$CBR_{DCP}\% = 0.617\ CBR_{CPT} \quad (5)$$

where CBR_{DCP}= California Bearing Ratio per dynamic cone penetration correlation (%) and CBR_{CPT} = California Bearing Ratio per cone penetration test (%).

Maximum dry density of the base course was also determined using a nuclear density gage (Cuelho and Perkins 2009). Webster utilized a falling weight deflectometer (FWD), a device thta uses an impact force to determine the impulse stiffness modulus (ISM) of a pavement system. This modulus is a combination of deflection in the test section correlated with the load applied (Webster 1993). A plate load test was used by White in 2017 to determine modulus of subgrade reaction (k_u) and the strain moduli of the pavement system (E_{v1} and E_{v2}). This test defines a modulus based on elastic deflections in the pavement section and does not include plastic deflections like the FWD (David 2017).

A new testing method has also been implemented by White and is called an Automated Plate Load Test (APLT). It utilizes an electronically controlled hydraulic ram with a loading plate to apply cyclic loading to the soil in the field. During the test, the force applied to the loading plate is controlled using a computerized system and the hydraulic ram. Deflections at the plate and at two and three radii from the center of the loading plate are also measured using rigid curved disks that are in firm contact with the soil. The purpose of the test is to determine the resilient modulus (M_r) of the pavement system. It can also be used to determine the resilient modulus of individual layers of a pavement system. The M_r of the entire pavement system can be calculated using Boussinesq's half-space equation:

$$M_r = \frac{(1-\nu^2)*\Delta\sigma_p*r}{\delta_r} * f \quad (6)$$

where M_r = in situ composite resilient modulus, δ_r = resilient deflection of plate during unloading cycle, ν = Poisson's ratio (typical assumed value = 0.40), $\Delta\sigma_p$ = cycle stress, r = loading plate radius, and f = shape factor (8/3 for rigid plate on granular material).

This equation operates on several assumptions. The first is that a typical Poisson's ratio is assumed and used in the formula. The second is that the pavement system behaves like an infinite half-space that is also linearly-elastic. Both of these assumptions are not always applicable. Poisson's ratio for the pavement system can, in actuality, vary significantly, and pavement systems do not always behave in a linearly-elastic fashion (David 2017).

A method for determining the M_r of individual layers of the pavement system using APLTs has also been developed. The following equation is used to determine the M_r of the subgrade:

$$M_{r(sg)} = \frac{(1-\nu^2)*P}{\pi*r'*\delta_{r,r'}} \quad (7)$$

where $M_{r(sg)}$ = in situ subgrade resilient modulus, $\delta_{r,r'}$ = resilient deflection of plate during unloading cycle at r' = 2r or 3r from plate center, ν = Poisson's ratio (typical assumed value = 0.40), $\Delta\sigma_p$ = cycle stress, and P = cyclic load. For a two-layer system, equations 8 and 9 can also be used to determine the M_r of the base layer:

$$h_e = h * \sqrt[3]{\frac{M_{r1}(1-\nu_1^2)}{M_{r2}(1-\nu_2^2)}} \quad (8)$$

where ν_1 = Poisson's ratio for the base layer (typical assumed value = 0.40), ν_2 = Poisson's ratio for the subgrade (typical assumed value = 0.40), and h = thickness of base layer:

$$\delta_r = (1-\nu^2)\sigma_0 rf\left[\frac{1}{M_{r(sg)}\sqrt{1+\left(\frac{h}{r}*\sqrt[3]{\frac{M_{r(base)}(1-\nu_1^2)}{M_{r(sg)}(1-\nu_2^2)}}\right)^2}} + \frac{\left(1-\frac{1}{\sqrt{1+\left(\frac{h}{r}\right)^2}}\right)}{M_{r(base)}}\right] \quad (9)$$

where ν_1 = Poisson's ratio for the base layer (typical assumed value = 0.40), ν_2 = Poisson's ratio for the subgrade (typical assumed value = 0.40), h = thickness of base layer, δ_r = resilient deflection of plate

during unloading cycle, $M_{r(sg)}$ = in situ subgrade resilient modulus, $M_{r(base)}$ = in situ base layer resilient modulus, σ_0 = stress corresponding to δr, r = radius of plate, and f = shape factor. To determine the resilient modulus of the base layer, Odemark's method of equivalent thickness is used. This method transforms the top layer of the system into a layer of equivalent thickness (h_e) that has the same properties as the bottom layer. Equation 9 can be solved for the resilient modulus of the base layer through an iterative process (David 2017).

For these equations to apply, certain assumptions must be made. First, the same assumptions are made as for the original Boussinesq's equation (Equation 6). Also, the measurements of deflection must be made at a certain radius from the center of the plate. The correct radius for this measurement can be estimated using an assumption of effective moduli for all layers of the pavement system and a graphical solution provided by AASHTO. This radius must be large enough that the deflection measured reflects the subgrade modulus and is not impacted significantly by the moduli of the layers above it and small enough that the magnitude of the deflection is great enough to measure accurately. In the case of the APLTs, whichever measured value of deflection at either 2 radii or 3 radii from the center of the loading plate that gave the lowest modulus was utilized in these equations and was checked against the graphical solution to ensure it was greater than the specified minimum radius (David 2017).

Beyond instrumenting and testing the properties of the soil in a pavement system, instrumentation of the geosynthetic itself can also be accomplished in a variety of ways. In 1997 Perkins and Lapeyre mounted VW strain and displacement sensors to geosynthetics using mounting plates that bolted onto the geosynthetics being tested. The mounting plates had collars through which the VW gages were inserted. Mounting the VW gages in this way meant they were raised above the surface of the geosynthetic. In the case of the VW strain gages, the axis of the gage was 14 mm above the geosynthetic and 25 mm above the geosynthetic in the case of the VW displacement gages. The VW gages also had thermistors to record temperature at their location. LVDT displacement gages were also mounted in a similar fashion on the geosynthetics. The LVDT gage axis was 14 mm above the surface of the geosynthetic. Foil strain gages were also used in the experiment. These foil strain gages were attached to the flat side of ribs on the geogrid being tested. Another foil strain gage was installed on a small piece of geogrid in the vicinity of each of these gages, so it could act as a control to account for temperature fluctuations affecting the readings from the gage. These gages were protected from being damaged while in the pavement section by encasing them in sheets of rubber and neoprene. They were then enclosed with plastic and silicone. All these sensors were installed to measure strain and displacement perpendicular to the direction of trafficking (Perkins and Lapeyre 1997).

In the experiment, the VW strain and displacement gages showed 0.3-0.4% strain in the geosynthetics during compaction of the base course. The base course was leveled and compacted again, adding 0.05-0.15% additional strain. Throughout the long-term monitoring of strain, the VW gages showed an increase in strain of 0.05% over approximately 1200 hours. When comparisons were drawn between this data and the data from the LVDTs, there were complications due to the LVDTs not having a control sensor for temperature compensation. It was also noted that the mounts for the LVDTs were high enough that the strain they recorded was affected by their interaction with the base course material surrounding them. The foil gages were utilized for dynamic load monitoring. For this type of monitoring, they performed quite well. LVDT data for dynamic monitoring was not as easy to analyze. The researchers noted that the foil gages needed further investigation, as there was potential for their use with geotextiles and not just geogrid (Perkins and Lapeyre 1997).

Another way to attach LVDTs to the geosynthetic is to attach them to the ribs of geogrid with zip ties, and then to use brass pipes and schedule 80 PVC pipe to protect the lead wires. In the case of the geotextile, a small drill bit was used to drill holes for the LVDT to be threaded through to attach it. This allowed for a low-profile mount of the LVDT, which decreased the interaction of the LVDT and the base course

material. The PVC pipe went from the control box used to collect data over to the edge of the geosynthetic. The brass pipes ran from inside the PVC pipe to where the LVDTs were connected to the geogrid using zip ties. The LVDT lead wires ran through the brass tubing and the PVC pipe. Cuelho and Perkins used LVDTs attached to the geosynthetics to measure displacement near the rut bowl created by trafficking a pavement section. A series of three LVDTs was used: one centered under the tread path of the truck being used to traffic the test sections, and one on either side of the tread path. Each of the sensors was oriented in the transverse direction, perpendicular to the direction of trafficking (Cuelho and Perkins 2009).

The general behavior recorded by the LVDTs was that under initial trafficking, the geosynthetic would displace away from the traffic line on either side of the tread path. After a certain number of traffic passes, the geosynthetic would begin to displace toward the location of the tread path. Cuelho's analysis of this information was that initially the outward displacement correlated to the lateral spread of the aggregate and the geosynthetic restraining that lateral movement. After several passes of the loaded truck being used to traffic the sections, the surface of the pavement section would begin to fail, and rutting would become more apparent. As rutting increased, the stresses in the area being trafficked increased, and the stress started to cause failure in the subgrade in the form of permanent vertical strain. This strain would mobilize the geosynthetic inward as it began to take stress in the form of membrane reinforcement. The majority of the strain seen in the geosynthetic was static (Cuelho and Perkins 2009).

In a laboratory test in 1999, Perkins and Cuelho used five extensometers to measure displacement in geosynthetic samples. The geosynthetics were contained in a pullout box apparatus with cables attached to the geogrid with metal clips and with a bolt assembly tying through the weave of the geotextile. The extensometers were attached to the pullout box apparatus outside of the box itself (Perkins and Cuelho 1999).

Also in the 1999 laboratory experiment, Perkins used foil strain gages to measure strain in geosynthetics. The foil strain gages were bonded to the ribs of geogrid and bonded to geotextile using a robust epoxy. They were oriented to measure radial and circumferential strain, positioned at different distances from the center of a test pavement section. The output from these gages was measured and recorded during the entire experiment. Cyclic loading was used in the experiment, and the foil strain gages performed well (Perkins 1999).

Gages used to monitor strain in geosynthetics must be calibrated to determine the actual strain in the material. This calibration can be performed in the laboratory. One way that this can be accomplished is by using a wide-width tension frame. Global strain can be measured as a specimen is elongated, and this global strain can then be compared to the strain recorded by the attached strain gage. In Perkin's 1997 study, the VW and LVDT gages all recorded lower strain than the global strain when calibration testing was performed in the laboratory. The foil strain gages reported similar strain to the global strain. From these calibration tests, a correction factor was developed to be used on the results from the field experiments (Perkins and Lapeyre 1997).

Beyond measuring strain in the geosynthetic, data concerning temperature, traffic patterns, and moisture all can contribute to determining the performance of geosynthetics. In a long-term analysis of a geosynthetic reinforced pavement system, Al-Qadi and Appea utilized moisture sensors, temperature sensors, and piezoelectric traffic sensors to gather other important data for their analyses (Ai-Qadi and Appea 2003).

2.3 Research

Many studies have been conducted on geosynthetics. Several studies were analyzed in this Literature Review. These can be divided into lab-based studies and field-based studies. Lab studies typically involve creating a representative cross-section of the pavement system with the geosynthetic installed. The system is then loaded either with a static or cyclic load. Measurements of displacement can be taken at the surface and/or through instrumentation in the pavement system, either free-floating in the soil layers or attached to the geosynthetic.

The drawback of lab testing is it only approximates the actual conditions of an application in a roadway. There are boundary conditions in a laboratory experiment that do not exist in a roadway, and it is difficult to run a laboratory experiment at the same scale as an actual road section. Due to these and other factors, it remains challenging to use laboratory tests to replicate the results seen in the field. It is also important to note field experiments add a layer of difficulty in that it becomes harder to control all the independent variables in the experiment, whether it be subgrade and base course strength and uniformity, proper construction practices at a larger scale, and/or environmental extremes in temperature and moisture (Cuelho and Perkins 2017).

Testing in the field falls into two categories of test sections: those fabricated only for research, and test sections that are part of an actual roadway. Test sections fabricated for research, such as in the 2017 research done by Perkins and Cuelho, have the benefit of being able to control the subgrade composition, base course material, and construction practices. This helps to eliminate differences in results due to the inherent property transience found in a natural subgrade (Cuelho and Perkins 2017). The level and frequency of traffic can also be controlled in such an experiment. Test sections that instrument geosynthetics and the pavement system in an actual roadway do have their own benefits. Instead of simulating a pavement system and the traffic on that pavement system, measurements of the actual application of the geosynthetic can be made. With proper characterization of the subgrade and soil layers in the pavement system, accurate data can still be obtained and analyzed. The effects of real construction installation and actual trafficking can also be measured when testing is performed on an actual roadway. Long-term performance can also be monitored.

2.4 Properties of Geosynthetics That Impact Performance

When designing with a geosynthetic, knowing which of its properties make the biggest impact on its effectiveness is important. Several studies have been performed to try to identify a property that can be used to accurately predict the benefit of the geosynthetic on the performance of the pavement system. Properties shown to correlate to performance are tensile strength, junction strength and stiffness, separation capacity, and shear interface strength.

In 1993, Webster performed a series of field tests using six different geogrids. Part of the experiment involved comparing their performance in the same application. The geogrids were placed in a pavement system with two-foot-thick artificial subgrade with a CBR of 3. The geogrid was placed at the subgrade-base course interface. The base course of crushed limestone was 14 inches thick. A two-inch layer of asphalt concrete was placed on top of the base course. The test sections were trafficked using a 30,000-pound loaded C-130 tire with a pavement contact stress of 68 psi. The tire was driven back and forth over the test sections in a two-foot width of the pavement until one-inch of surface rutting was achieved.

Using the material properties of aperture size, cell area, aperture opening, rib width, rib thickness, junction thickness, secant modulus at 2%, 5%, ultimate strain, and aperture stability modulus, a correlation between properties and the increase in performance over the control section was attempted. With the given properties and performance, a clear correlation was not apparent. In general, it appeared

that the thicker, stiffer geogrids performed better, with the two best-performing geogrids being the sheet-type geogrids. One of the other geogrids was a sheet-type geogrid, but it did not perform well. General statements about quality and performance were made according to the engineer's judgment. It was determined that angular ribs were better than rounded ribs, round or square apertures were better, a minimum junction strength was necessary, a minimum secant modulus was needed, and the newly developed aperture stability modulus was a possible candidate for correlating performance (Webster 1993).

Two triaxial geogrids were compared by Qian et. al. at the University of Kansas in 2010. The two geogrids had the same aperture dimensions, but one had thicker ribs and nodes. The study used a 100 mm thick subgrade made of sand and kaolinite with a CBR of 2. A relatively weak base course was also used, being placed and compacted 15 cm deep to a CBR of 5. The test sections were built in a loading apparatus that was 2 meters by 2.2 meters by 2 meters high. It was loaded with a steel plate with a 0.3-meter diameter. Cyclic loading was used, with a minimum force of 0.5 kN and a peak cyclic force of 40 kN at a frequency of 0.77 Hz (Qian et al. 2010).

During the first four to five cycles, the control section and the two reinforced sections performed similarly. With increasing load cycles beyond that, the unreinforced section began to displace much more. The two geogrids improved the number of load cycles to reach 70 mm of permanent settlement by 153% and 215% respectively (Figure 2.6). The geogrid with the thicker ribs and nodes performed better than the geogrid with thinner ribs and nodes (Qian et al. 2010).

Another project conducted by Al-Qadi et. al. compared the performance of two geotextiles and a geogrid. Four laboratory test sections were created, each with a subgrade CBR close to 4.5. The geosynthetics were placed at the subgrade-base course interface. A base course of crushed granite with an average thickness of 14.3 cm was used. A pavement of hot-mix asphalt was placed with an average of 7.3 cm over each test section. The test sections were loaded using a loading plate with a diameter of 30 cm controlled by an electronic loading system. A cyclic loading with a 0.5 Hz frequency was used and a peak load of 40 kN was used. The sections were each loaded 200 cycles at a time until 25 mm of permanent surface deformation was achieved. After the test was completed, each section was excavated, so the geosynthetics could be inspected (Al-Qadi et al. 1994).

The results of the experiment showed that much of the displacement in the pavement system occurred in the first 25 loading cycles. It was determined that this was a load seating period. During the load seating period, the geogrid increased the number of cycles needed to reach the same settlement as the control by 247%. The geotextiles outperformed the geogrid, improving the pavement system performance by 539% and 614%. After the seating period, the geogrid performed better than the control by 2%, while the geotextiles performed better by 100% and 117% (Al-Qadi et al. 1994). A graph of the data adjusted for the seating load is shown in Figure 2.7.

Two reasons for the better performance of the geotextiles were considered. The first was that upon excavation, it was observed that the granite base course had mixed with the subgrade material in the control and the geogrid sections. The geotextiles had prevented this mixing — they acted as separators. Their increased performance was attributed in part to this separation function (Al-Qadi et al. 1994).

The second reason for their better performance could have been in part due to their ultimate tensile strength being 149.7% and 201% greater than that of the geogrid. The geotextile with the greatest ultimate tensile strength performed the best out of the three. It should be noted though that at 2% and 5% strain, the tensile strength of the geogrid was greater and/or the same as the strongest geotextile. If tensile strength were the only factor controlling which geosynthetic performed the best, it could be inferred that

the geogrid would initially outperform the geotextiles at low strain, but this was not observed in the project results.

Another laboratory test compared the performance of two geogrids and one woven geotextile. Perkins set up an experiment using a 2 m square load frame with a steel plate having a 305 mm diameter to simulate a pavement system being loaded cyclically by traffic. The subgrade was clay with a CBR of 1.5 and a thickness of 1000 mm. Two base course thicknesses were used, one being 300 mm thick and the other 375 mm thick. Two control sections were constructed without reinforcement with these two thicknesses of base course. The base course in all the test sections was compacted to at least 21 kN/m^3 at an optimum water content. The geosynthetics used for direct comparisons of performance were placed at the interface of the subgrade and the base course materials. A 75 mm layer of asphalt concrete was used as the pavement surface in each test section. The test sections were loaded at a frequency of 0.67 Hz up to a force of 40 kN, or a pressure of 550 kPa. The test was terminated when the permanent deformation, or rutting, at the surface reached a depth of 25 mm (Perkins 1999).

From the results of the experiment, it was concluded that the two geogrids performed better than the geotextile (Figure 2.8). The ratio of load cycles in a reinforced section divided by the number of load cycles in the control to reach the same settlement was termed the traffic benefit ratio (TBR). Though all the geosynthetics resulted in a TBR greater than one, both geogrids outperformed the geotextile (Figure 2.9). The geotextile had a higher wide-width tensile strength at 5% strain and at failure strain, but it did not perform as well as the two geogrids with lower tensile strength. Other material properties had to have accounted for its lower performance.

In the experiment, Perkins used LDVTs embedded in the base course 50 mm above the geosynthetics to measure radial strain in the base course at 100, 200, and 300 mm from the center of the loading axis. Foil strain gages were also adhered with epoxy to the geosynthetics to measure their in-plane strain. In the first load cycle, the strain in the base course for the geotextile was greater than that for the geogrids. The surface deformation of the geotextile-reinforced section was also similar to the two control sections during the early load cycles. The measured strain in the geotextile was significantly lower than the strain measured in the geogrids (Figure 2.10). Excavation of the geotextile section also showed dimpling in the geotextile, most likely from the large aggregate during loading. It was hypothesized that the geotextile failed to interlock with the base course aggregate during the early load cycles. It could not laterally constrain the base course and the geogrids, and it took longer for it to mobilize and spread out the stress from the loading (Perkins 1999).

In 2009, the Western Transportation Institute set up a research experiment to compare the performance of 10 geosynthetics. This consisted of seven geogrids and three geotextiles. The test section was located at the Transcend research facility in Lewiston, Montana. To control as many independent variables as possible, the test section was set up with an artificial subgrade, a base course of even thickness, and each test section was in line with the next. The complete test area was 195 meters long with a control section at each end. The width of all the test sections was four meters, and the length of each of the test sections was 15 meters, except for the control sections and one of the test sections, which were all 20 meters long. The artificial subgrade was an AASHTO A-2-6 or USCS clayey sand with gravel. It was placed 1 meter deep on top of a plastic liner in a trench to maintain moisture content. It was compacted to a CBR of 1.7%. A DCP and a vane shear device were both used to confirm the CBR in each of the test sections. The geosynthetics were then carefully installed on top of the prepared subgrade. Next, instrumentation was installed. This included three LVDTs measuring transverse strain in the geosynthetics and a pore pressure sensor in the subgrade underneath the outside wheel path. A 200 mm thick AASHTO A-1-a or USCS GW-GM base course was then placed and compacted to 90% of its maximum dry density on top of the geosynthetics (Cuelho and Perkins 2009).

The research area was trafficked using a three-axle fully loaded dump truck. The loaded truck proceeded to traverse the test sections at 15 kph, going in a straight line from one end of the test section to the other. The test sections were trafficked until each had rutted a minimum of 100 mm deep. After the trafficking, a vacuum truck was used to excavate sections of the geosynthetic for physical inspection and to observe the condition of the base course and subgrade (Cuelho and Perkins 2009).

In assessing performance of each geosynthetic in the research, the properties of tensile strength and aperture stability modulus were considered. When the depth of rutting in the test sections reached 75 and 100 mm, a correlation was observed between the tensile strength of the geosynthetics at 2% and 5% strain, and the number of passes needed to reach that depth of rutting. The correlation was made by subtracting the number of passes needed to reach a certain depth of rutting in each test section from the number of passes needed to reach that same level of rutting in the control. The extra passes needed were considered the improvement in performance for each test section (N_{add}). Figure 2.11 shows a graph of the mean rut depth for each of the geosynthetics versus the N_{add}. The correlation between N_{add} and tensile strength at 2% and 5% at a rut depth of 75 mm had R2 values of 0.4502 and 0.3586, respectively. At a rut depth of 100 mm, the R2 values for 2% and 5% strain were 0.4890 and 0.3795 respectively, which were considered significant in the study (Figure 2.12 and Figure 2.13). At rut depths less than this value, the correlation was not as strong (Cuelho and Perkins 2009).

The research also performed an analysis of a design methodology developed by Giroud and Han. The design method used aperture stability to determine the benefit of geogrid in a pavement system design. The design used this property, among several others, to determine the necessary thickness of base course needed to handle the design traffic loads. The predicted design base course thickness was compared to the needed base course thickness determined in the field experiment. In every case, the needed base course thickness was underpredicted — the larger the aperture stability modulus, the greater the error in prediction. Based on this research, it was determined that tensile strength of the geosynthetics at 2% and 5% was a better property than aperture stability for predicting the performance of geosynthetics in a pavement system (Cuelho and Perkins 2009).

A similar experiment to the one just analyzed was performed in 2017. The tests were performed at the same research site, this time with an additional control section and 12 geosynthetics (10 geogrids and two geotextiles). The research sections were 4.9 meters wide, and each section was 15 meters long. The research area was 255 meters long. The artificial subgrade was 0.9 meters thick, with an average CBR of 1.79. The base course in all of the geosynthetic-reinforced test sections was 27.7 cm thick, on average, with a CBR of 20. One of the control sections had the same thickness as the base course, with the other two control sections having a base course thickness of 41.1 cm and 63.2 respectively. The test sections were trafficked similarly to the previous research. A three-axle loaded dump truck weighing 20.6 metric tons was driven over the test sections at 8 kph in one direction until ruts 75 mm deep developed (Cuelho and Perkins 2017).

Several material properties were determined through laboratory testing for each of the geosynthetics tested. These included cyclic tensile strength at 0.5%, 1.0%, 1.5%, 2.0%, 3.0%, and 4.0% strain, resilient interface shear stiffness, junction strength, junction stiffness, and aperture stability modulus (ASM). Linear regression analysis was utilized to determine which of these properties best predicted the rutting response in each of the test sections. This analysis was performed at varying rut depths to determine if different characteristics better predicted the rutting response at different levels of rutting. The measure of performance was the same used in the previous experiment (N_{add}). An R^2 value of 0.5 or greater was considered significant in the analysis (Cuelho and Perkins 2017).

The properties that demonstrated the greatest correlation when predicting the performance of the geosynthetics were in the cross-machine direction. Properties in the machine direction resulted in

correlations with negative R^2 values except for the ultimate wide-width tensile strength. Of the cross-machine properties, junction strength and junction stiffness in the cross-machine direction showed the best correlation (Figure 2.14). As rutting increased, the strength of the correlation also increased. After identifying this relationship, a second linear regression was performed, excluding two geosynthetics that had low junction stiffness and strength. These two materials did not perform well in the experiment. With the elimination of these two materials, significant correlation was shown in the properties of wide-width tensile strength, with the strongest correlation being made by the wide-width tensile strength at 5% strain (Figure 2.15). Significant correlation was also shown by the cyclic tensile strength properties (Cuelho and Perkins 2017).

This research also used six of the same geosynthetics used in the previous research project. This same analysis was made on the rut data from that research. The subgrade strength in the previous research project was slightly weaker, and utilized 75 mm less base course material, which resulted in an increased rutting rate, when compared to the current research project. The results of the analysis showed that at levels of rut greater than 76.2 mm, wide-width tensile strength in both the machine and cross-machine direction showed the most significant correlation to performance (Figure 2.16). At lower rutting levels, junction strength and stiffness correlated better. Due to the limited number of geotextiles used in the experiment and limited material properties applicable to the geotextiles, it was harder to make any significant correlations using their properties (Cuelho and Perkins 2017).

2.5 Location of Geosynthetic in Pavement System

In the body research, there are two schools of thought on the location of the geosynthetic in the pavement system. The first is that the most benefit from the geosynthetic comes from placing it at the interface of the subgrade and base course. Locating the geosynthetic at this point in the pavement system allows it to act as a separator between the subgrade and base course. It can laterally restrain the material above it, and if enough deformation occurs, it can act as a tensioned membrane to decrease further settlement (Das and Shin 1994). The second school of thought is that there is an optimum depth for the placement of the geosynthetic based on the magnitude of the load and the width over which the load is applied.

Perkins studied a research pavement system in which 300 mm of base course was placed over a subgrade with a CBR of 1.5. In one scenario, geogrid was placed at the subgrade-base course interface (C5), in another, it was placed at a depth of 200 mm, or 100 mm above the above the interface (C7) and, in another, the geogrid was placed at the subgrade-base course interface, but 375 mm of base course was used, putting the geogrid at a depth of 375 mm. Cyclic loading of the systems with a loading plate measuring 305 mm in diameter showed that for the same number of load cycles, the section with the elevated geogrid (C7) performed at least 1.5 times better than the system with the geogrid at the interface (C5), and at least 1.2 times better than the section with 75 more mm of base (C6). This configuration also outperformed another test section with a stiffer geogrid placed at the subgrade-base course interface (C8), as can be seen in Figure 2.8. Other depths of embedment in the base course were not tested, but moving the geogrid from a depth of one loading plate diameter to a depth of 1/3 of the loading plate diameter increased the effectiveness of the geogrid reinforcement (Perkins 1999).

Part of the 1993 experiment by Webster, previously mentioned, tested the effect of embedment depth and the performance of geosynthetic reinforcement. Four lanes of the test section were constructed to be trafficked. The layout of the traffic lanes can be seen in Figure 2.17, Figure 2.18, Figure 2.19, and Figure 2.20. Each section was trafficked with a test cart using a single tire for a C-130 airplane. The contact pressure was 68 psi, and the applied load was 30,000 lbs. The apparatus was driven forward and back over the test sections until 1 inch of rutting was achieved at the surface of each test section or until 10,000 passes had been made (Webster 1993).

The results of the experiment showed that the amount of improvement in decreasing rutting was maximized with a geogrid depth of 8 inches (see Figure 2.21, Figure 2.22, and Figure 2.23). As the geogrid was placed deeper in the pavement section, the amount of improvement over the control section decreased (Webster 1993). It should be noted that the rate of rutting decreased in both the control and the reinforced section with a greater thickness of base course, but the most benefit from the reinforcement was in the test section with 6 inches of base course, covered with 2 inches of asphalt concrete. It was also noted in the experiment that the reinforced section with 6 inches of base course performed as well as the control section with 10 inches of base course. It was concluded that placing the geogrid at a depth of 8 inches, under 2 inches of asphalt and 6 inches of base course, was the optimum depth of placement for maximum reinforcement under the given conditions and loading (Webster 1993).

Webster also used an additional two sections to see if placing the geogrid in the middle of the base course layer would perform better than placing the geogrid at the subgrade-base course layer. Lane 3 item 2 placed the geogrid (SS-2 Geogrid) in the middle of a base course layer, which was 14 inches thick, with 2 inches of asphalt concrete and a subgrade with a CBR of 2.9. This was compared to Lane 3 item 3 with a pavement section with the same layer thicknesses, but the geogrid was placed at the interface of the base course and the subgrade. The result of this comparison was that the geogrid performed more than twice as well at the bottom of the base course layer at the interface of the base course and subgrade than in the middle of the base course layer. (Webster 1993). The fact that the geogrid placed in the base course was at a depth of 9 inches performed so poorly, just an inch lower than the optimum depth determined from the previous test, is notable. It shows the complexity of the mechanisms at play.

In contrast to the findings by Webster, a research project performed by Dash and Majee showed that improvement in deformation under a cyclic load could be achieved by placing a geogrid in the base course layer instead of at the interface between the subgrade and base course. In their research, a laboratory experiment was performed simulating sub soil, subgrade, and subballast under a railway load. For comparison, the subballast performs a similar function to base course in roadways, being placed over the subgrade with the load placed on top of it. The loading apparatus used in the study was 2 meters by two meters by 2.1 meters tall. A 300 mm diameter loading plate was used to transmit a preloading of 0.01 MN/m2 for 30 seconds, and then the specimen was loaded in steps up to 0.5 MN/m2 or until 5 mm of settlement occurred. At this point, the test section was unloaded in steps of 0.5 MN/m2 and then reloaded with dwell times of two minutes (Dash and Majee 2021).

The subgrade in all the test sections was 1000 mm thick. A weak subgrade with a CBR of 5.5 was used for some of the tests, and a strong subgrade with a CBR of 10.7 was used for some of the tests. With both the weak and strong subgrade, tests were performed with a subballast thickness of 400 mm. The subballast had a CBR of 36. To compare the performance of the geogrid at different depths of embedment, the geogrid was placed at the interface of both the weak and strong subgrade and the subballast, as well as at depths of 300, 200, 100, and 50 mm below the loading plate within the 400 mm of subballast. This meant the independent variables were confined to the CBR of the subgrade and the depth of reinforcement below the load (Dash and Majee 2021).

Placing the geogrid at all depths increased the bearing capacity of the test section when compared to the control (see Figure 2.24, Figure 2.25, and Figure 2.26). The bearing capacity of the test section with a hard subgrade at 1 mm of settlement was increased by as much as 2.3 times. This was achieved by the geogrid placed 200 mm below the loading plate, or at a depth of 0.67 loading plate diameters (0.67D). The least benefit from the geogrid was seen when it was placed at the subgrade-subballast interface. This was also true for the test sections with weak subgrade, except the greatest benefit seen from the geogrid was when it was placed at a depth of 300 mm, or 1D. It improved bearing capacity by more than three times (Dash and Majee 2021).

From comparisons of the settlement data and vertical strain moduli for the soil, it was shown that there was an optimum depth for the embedment of the geogrid. If it was placed shallower than this point or deeper than this point, the increase in bearing capacity from its reinforcement would decrease. The analysis in the research discussed a model proposed for failure under a rigid foundation. It described an upper failure zone and a lower failure zone. In the upper failure zone, shearing planes in the soil diverge from the loading plate. In the lower failure zone, shearing planes converge under the loading plate. If a geosynthetic reinforcement is placed at the bottom of the upper failure zone, it can influence more soil that is diverging, and increase the amount of support it can provide through lateral constraint and reorientation of the shearing planes. If it is placed in the lower failure zone, it is no longer confining the soil, but, instead, is offering support through the tensioned membrane effect (Dash and Majee 2021).

Bathurst and Raymond also performed an experiment modeling the use of a geosynthetic in a ballasted track system for railway usage. A large-scale model of a tie and ballast system over subgrade was constructed in the laboratory. The model simulated half of a rail tie and the loading from one rail onto the ballast and subgrade. In the experiment, a geogrid reinforcement (Tensar® GM1 geogrid) was placed at different depths in the ballast layer. Three different subgrade conditions were simulated, with a rigid subgrade being represented by the concrete floor of the laboratory, a weaker subgrade simulated by a closed-cell gum rubber mat with a CBR of 39, and a very weak subgrade simulated by a layer of closed-cell gum rubber mat combined with a layer of open-sheet neoprene rubber with a CBR of 1. Control sections were also tested, with no geogrid in the test section. Crushed limestone aggregate was used for the ballast. It was placed 300 mm deep. The experiment's loading procedure loaded the simulated railway tie up to 370 kPa with loading frequencies from 0.5 to 3 Hz (Bathurst and Raymond 1987).

In the case of a rigid subgrade, little settlement was recorded in any of the test configurations. In the case of the subgrade with a CBR of 39, permanent vertical strain was reduced when the geogrid reinforcement was 50, 100, and 150 mm below the railway tie. Improvement in the permanent vertical strain was not seen with the geogrid being placed at a depth of 200 mm (Figure 2.27). It was concluded that in this laboratory test the geogrid at this point was below the depth at which the reinforcement could be mobilized. With a subgrade with a CBR of 1, the decrease in permanent vertical strain when compared to the control was even greater with the reinforcement at a depth of 100 mm and 200 mm (Figure 2.28). At 100 mm, permanent vertical strain was decreased 20% more and 50% more at 200 mm when compared to the test with a subgrade having a CBR of 39 (Bathurst and Raymond 1987). Even with equivalent amounts of base, it was demonstrated that an optimum depth of reinforcement embedment existed.

The research concluded that the optimum depth of reinforcement is 50-100 mm below the railway tie, or a ratio of depth of embedment to width of load of 0.2-0.4. For a CBR of 1, an even greater depth may be optimum. The results of the experiment also showed that the compressibility of the subgrade impacted the amount of vertical strain more than the depth of embedment for the reinforcement (Bathurst and Raymond 1987).

In the case of geogrid reinforcement being placed in the base course in the Webster experiment, it is possible that at a depth of nine inches the geogrid was in the lower failure zone and did not offer as much reinforcement as it would have if it was placed at the determined optimum depth of eight inches. This comparison is hard to make due to the fact that the optimum depth determined in the study was with a subgrade CBR of 8, and the geogrid placed in the base course had a subgrade with a CBR of 3. Whatever the case may be, evidence supports the concept that a geotextile can increase the performance of a pavement system when used as a separator to stop the migration of fines from the subgrade into the base course. This was demonstrated by Al-Qadi's previously mentioned research in which two geotextiles outperformed a geogrid when all three were compared when placed at the subgrade-base course interface (Al-Qadi et al. 1994). The studies listed also provide evidence supporting there being an optimum depth of placement for geogrid reinforcement. The optimum depth is impacted by the thickness of base course

and the CBR of the subgrade, but several of the studies found that a depth of placement from 0.33D to 1D being effective, with D being the width or diameter of the load at the surface (Bathurst and Raymond 1987; Dash and Majee 2021).

2.6 Geosynthetic Reinforcement Equivalent Thickness of Base Course

Several of the studies drew conclusions about how much base course could be replaced by using a geosynthetic. In Webster's 1993 study, a geogrid reinforced section with six inches of base over a subgrade with a CBR of 8 performed as well as a comparable unreinforced section with 10 inches of base course (see rut depth measurements from Items 1 and 3 in Lane 1, Figure 2.21). It showed that in the application, 4 inches of base course could be replaced by the geogrid reinforcement. This equated to a 40% decrease in base course thickness (Webster 1993).

A geogrid-reinforced section also performed very similarly to a control test section with two more inches of AC, and test sections with four inches more base course, which can be seen in the comparison of the SR-C section (control) and the SR-T section (reinforced). This conclusion is drawn from the fact that the reinforced section (SR-T) showed less rutting and deflection than the control section (SR-C) when deflection testing was performed, as shown in Table 2.1 (Aran, 2006). SR-T also outperformed SR-C when long-term falling weight deflectometer testing was performed (Table 2.2). This improvement in performance was equivalent to a 40% reduction in base course thickness, which is similar to the findings from Webster. Another comparison was made in the same study showing that adding one more inch of base and reinforcing the base with geogrid performed better than a control section having one inch less base course and six inches of lime stabilized subgrade (Aran 2006).

The results from Dash and Majee's research showed that geogrid reinforcement at an optimum depth of one third the diameter of the loading plate improved the pavement system's performance equivalent to an additional 200 mm of subballast (base course). The reinforced test section had 400 mm of base course with geogrid reinforcement at a depth of 100 mm. It performed as well as a control section without reinforcement and 600 mm of base course, equating to a reduction in base course thickness of 33%. These results are shown in Figure 2.24 and Figure 2.26 (Dash and Majee 2021).

Perkins' research in 1999 showed that each of the two geogrids and one geotextile tested in his research provided a greater traffic benefit ratio than an unreinforced section with an additional 75 mm of base course material (C3 versus C4, C5, C7, and C8 in Figure 2.8). The reinforced sections were constructed with 300 mm of base course over a subgrade with a CBR of 1.5. The control had the same subgrade CBR, but 375 mm of base course. This shows that at least a reduction in base course thickness of 20% was possible due to geosynthetic reinforcement (Perkins 1999). The research shows that in a variety of applications, geosynthetics can provide the same structural capabilities as pavement systems with 20%-60% more base course thickness.

2.7 Effect of Subgrade CBR on Geosynthetic Reinforcement Effectiveness

The performance benefit a geosynthetic can provide in a pavement system is impacted by a variety of factors, one of which is the CBR of the subgrade. Several studies used research sections with varying subgrade CBR values to analyze this factor.

Dash and Majee's research on "Geogrid Reinforcement for Stiffness Improvement of Railway Track Formation over Clay Subgrade" was performed using a strong and weak subgrade. The strong subgrade

had a CBR of 10.7 and a weak subgrade with a CBR of 5.5. For these comparisons, the improvement in performance is measured by the amount of settlement at the surface of the system that is decreased when compared to the control. The control sections without reinforcement showed that the strong subgrade system performed 1.77 times better than the weak subgrade system when 400 mm of subballast (base course) was used (Figure 2.24 and Figure 2.25). As shown in the same two figures, when 600 mm of base course was used, the performance increase dropped to approximately 1.17 times better (Dash and Majee 2021).

When geogrid was introduced as a reinforcement into the system and at the optimum placement depth, the performance increase in the system with 400 mm of base course over the weak subgrade was approximately 3.33 times greater (Figure 2.26). In contrast, the increase in performance in the system with a strong subgrade was 2.22 times that of the control (Figure 2.25). The researchers concluded greater yielding in the subgrade led to more deformation in the base course. This, in turn, meant more reinforcement was given by the geogrid, as it mobilized a greater amount. When the vertical strain moduli of the strong and weak subgrade sections were compared, the inclusion of reinforcement in the weak subgrade system made the vertical strain modulus almost the same as the vertical strain modulus in the stronger subgrade system without reinforcement. These findings clearly show a decrease in benefit from geogrid reinforcement as the subgrade CBR increases (Dash and Majee 2021).

The research performed by Bathurst and Raymond showed that with a simulated subgrade of infinite CBR, little settlement was experienced no matter how the geosynthetic was applied Figure 2.29. With a subgrade CBR of 39, geogrid reinforcement decreased settlement when placed at depths of 50, 100, and 150 mm. At greater depths, no improvement was seen (Figure 2.27). With a subgrade CBR of 1, geogrid reinforcement at depths of 100 mm and 200 mm decreased settlement much more than the tests with a subgrade CBR of 39 (Figure 2.28). With a subgrade CBR of 39, settlement was decreased by 20% compared to the 50% reduction in settlement with a subgrade CBR of 1 (Bathurst and Raymond 1987).

Every study showed that as the CBR of the subgrade decreased, settlement increased. It also showed that as subgrade CBR decreased, the benefit of including geosynthetics in the pavement system increased. The highest subgrade CBR tested in the research analyzed was by Bathurst and Raymond with an infinite CBR value. No improvement was shown at this strength of subgrade. The second highest subgrade CBR was also tested by Bathurst and Raymond — it was a subgrade CBR of 39. Even at this level of CBR, geogrid reinforcement still showed a 29.4% decrease in settlement (Bathurst and Raymond 1987). The lowest subgrade CBR was tested by Perkins. The subgrade CBR was 1.5. The test he performed with a geogrid embedded in the base course showed an estimated traffic benefit ratio of 70.2, or 6,920% better performance than the control (Perkins 1999). Dash and Majee tested a subgrade with a CBR of 10.7 and were able to demonstrate a decrease in settlement with reinforcement of 121%. It is evident that as the subgrade CBR decreases, the benefit provided by geosynthetic reinforcement increases.

2.8 Displacement Necessary for Geosynthetic Mobilization

The amount of displacement needed for geosynthetics to mobilize in a pavement system is important to quantify. If the surface displacement or rutting is greater than the service requirements of a roadway, then that roadway will not benefit from a design utilizing geosynthetics. Several of the studies in this literature review drew conclusions on what this value would be.

Al-Qadi's laboratory research using two geotextiles and a geogrid showed that even after only a few loading cycles, the surface deformation in the reinforced test sections showed less settlement than the control. At a displacement of 2.5 mm, the weakest reinforced section took 60% more cycles than the control to reach that amount of settlement. This was using 150 mm of base course over a subgrade with a CBR of 4 (Al-Qadi et al. 1994). The laboratory experiment performed by Dash and Majee showed similar

results, with the reinforced sections seeing performance benefits at settlements as low as 2 mm when placed in a base course 400 mm thick and with a subgrade with a CBR of 1.5 (Dash and Majee 2021). A slightly higher amount of settlement was required to mobilize the geotextile reinforcement in Perkin's laboratory experiment. It took 6–7 mm of settlement at the surface before the geotextile began to improve the performance of the test sections when a base course thickness of 300 mm was utilized with a subgrade having a CBR of 1.5. In the same research project, the geogrids began to mobilize at as low as 3 mm of settlement when used with a base course of 375 mm. The traffic benefit ratio showed that the effect of the reinforcement was nearly immediate, as shown in Figure 2.9 (Perkins 1999).

In contrast to these findings, several researchers demonstrated that much greater deformation was required before geosynthetic reinforcement would occur. In the laboratory research performed by Qian et. al., the difference in permanent displacement due to reinforcement from a triaxial geogrid was not readily apparent until 30 mm of displacement had occurred, although some benefit was seen at permanent displacements as low as 20 mm (Figure 2.30). This experiment was conducted using 150 mm of base course over a subgrade with a CBR of 2. It should be noted that the base course used in this study had a CBR of 5, which is lower than is typical for base course material. Settlement in the base course could have contributed to the greater amount of settlement measured before the effect of the reinforcement became apparent (Qian et al. 2010). Cuelho also showed in his field experiment that when correlating the reduction in surface rutting to the geosynthetic properties of tensile strength at 2% and 5%, it wasn't until 75 mm to 100 mm of rutting occurred that a strong correlation could be made (Figure 2.16). Using the data from 25 mm of rutting, there was not a strong correlation between the tensile strength properties of the geosynthetics and their effect on test section performance (Cuelho and Perkins 2009). This may just show that at lower levels of deformation, other properties of geosynthetics are in play to offer reinforcement.

Though not entirely clear, it appears that geosynthetic reinforcement can begin to increase the performance of a pavement system almost immediately under the ideal circumstances that exist in scientific research. Increased performance was observed to take place at surface deformation as low as 2 mm (Dash and Majee 2021).

2.9 Long-Term Benefits of Geosynthetics

Few studies have investigated the long-term performance of geosynthetic reinforced pavement systems utilized in actual roadways over several years. However, two studies that did look at the long-term benefits of geosynthetics were performed that were analyzed in this literature review.

Al-Qadi performed a laboratory study analyzing the performance benefits of two geotextiles and a geogrid that was published in 1994 (Al-Qadi et al. 1994). Following this experiment, he and a research team began a field study in an actual secondary roadway in June 1994. It had nine test sections with each test section being 15 meters long. There were three groups with base course thicknesses of 100, 200, and 300 mm. The base course material was made of crushed limestone. Each of the three groups had a control, a geotextile reinforced section, and a geogrid reinforced section. The subgrade CBR in the test sections varied from 6-10. The hot-mix asphalt (HMA) thickness in the test sections was on average 95 mm. The HMA and soil were instrumented with strain gages, earth pressure cells, temperature sensors, moisture sensors, and piezoelectric traffic sensors (Al-Qadi and Appea 2003).

Further performance data was acquired by measuring rutting in the pavement surface at the end of construction in accordance with ASTM 1703. Five years later, rut measurements were again taken at the pavement surface in just one of the test lanes. In October 2001, a more complete measurement of rutting was carried out. Analysis of the rutting data showed that in the test sections with 100 mm of base course, the amount of rutting in the control and the geogrid and geotextile reinforced sections were similar.

Slightly more rutting was observed in the control sections in the second and third years. After the third year, the rutting in the control section became much greater than in the reinforced sections, as seen in Figure 2.31 (Al-Qadi and Appea 2003).

Falling weight deflectometer testing (FWD) was also utilized throughout the duration of the study to obtain data about the condition of the test sections. The falling weight deflectometer uses a 300 mm diameter plate to apply 40 kN pulses to the pavement surface for pulse durations of about 0.4 milliseconds. This loading simulates the loading due to a half-axle load travelling at highway speeds. FWD tests were performed on the test sections in October 1994, March 1995, August 1995, three separate times in 1996, three separate times in 1997, and then again in 1999, 2000, and 2001 (Al-Qadi and Appea 2003).

FWD tests are used to calculate several different pieces of data. Through back calculation, the elastic modulus of each layer in the pavement system can be estimated through an iterative process. Each of the nine test sections was tested using five drops of the FWD. The software MODULUS Version 5.0 was used to analyze the FWD data. Three metrics based on the data from the FWD are used to characterize the structural integrity of the pavement system. The first is the base damage index (BDI). As the BDI increases, the base course in the pavement system deteriorates. An increase in BDI can also indicate that fines from the subgrade are migrating into the base course. The second metric is the SCI, which is the surface curvature index. The SCI is indicative of the stiffness of the pavement system. The spreadability metric (SP) correlates to how well the pavement can distribute loads (Al-Qadi and Appea 2003).

The results of the FWD tests over the eight years of monitoring show that, in general, the test sections with thicker base courses (150 mm and 200 mm) had lower BDI values. In the 150 mm base course section, the BDI values between the control, geogrid, and geotextile reinforced sections had similar values. The results from the 200 mm test section had peculiar results that did not appear to correlate with the data from the other two sections. The analysis in the research, therefore, focused on the 100 mm base course section. In this section, the BDI in the geogrid and geotextile reinforced sections were less than half the BDI of the control. In the measurements taken in 1995, the BDI of the geotextile section was 80, while the BDI of the geogrid section was close to 98. The control's BDI was approximately 107. The BDI of the control, geotextile, and geogrid sections in 2001 were 150, 80, and 90 respectively (Figure 2.32). The results of the SCI parameters were similar when comparing the performance between the three sections (Al-Qadi and Appea 2003).

One of the factors attributed to the increase in performance in the two reinforced sections was their function as separators between the subgrade and the base course. Part of the test sections were excavated to analyze the pavement system and geosynthetics. In the control section with 100 mm of base course, the fines content in the 50 mm above the subgrade was greater than 14%. This change in gradation was thought to have impacted the performance of the base course in the pavement system (Al-Qadi and Appea 2003).

The data from the study was used to predict the service life of the test sections. This prediction tooki nto account the rutting rate observed over the duration of the study, the measured traffic, and a terminal rut depth that indicated termination of service life (20 mm). This analysis determined that the addition of the geotextile reinforcement increased the service life of the test section with a base course thickness of 100 mm by 3.5 years, and the geogrid reinforcement increased the service life of the section by 2.8 years (Al-Qadi and Appea 2003).

The second study that analyzed the long-term benefits of geosynthetic reinforcement was performed by Shirwan Aran. The study analyzed the long-term results of an experiment performed by the Georgia Department of Transportation in 1986. Biaxial geogrid was used as a reinforcement in two different actual

roadways, one being SR-155 and one being the East Rome Bypass (ER). The SR-155 test site had a 1,400-foot-long control section and a 1,200-foot-long geogrid reinforced section. The control section (SR-C) had 6.25 inches of AC and the geogrid section (SR-T) had 4.25 inches of AC. Both had 10 inches of graded aggregate base course. The geogrid was placed at the subgrade-base course interface. The control section's subgrade CBR was 7.7 and the geogrid reinforced section had a subgrade CBR of 8.5 (Aran 2006).

The ER test location had a 1,220-foot-long geogrid reinforced section (Section 1, ER-T1) next to a bridge. On the other side of the bridge a 690-foot-long control section (ER-C) was built, with another geogrid reinforced section beside the control (Section 2b, ER-T2b). Another bridge was located between Section 2b and Section 2a (ER-T2a), which were 420 feet and 1,970 feet long, respectively. ER-T1 had 6.5 inches of AC, 6 inches of base course, the geogrid reinforcement, and then 6 inches of lime stabilized subgrade. ER-C had 6.5 inches of AC, 10 inches of base course, and 6 inches of lime stabilized subgrade. ER-T2a and ER-T2b both had 6.5 inches of AC, 6 inches of base course, geogrid reinforcement, and an additional five inches of base course in between the geogrid and the subgrade, which was not lime stabilized. The CBR of the unstabilized subgrade was 8.0.

To analyze the performance of the different sections, pavement performance was evaluated every year from the end of construction for five years until 1991. Deflection and rut measurements were taken, and crack surveys would have been performed, except none of the test sections developed any cracks over the five years. FWD tests were also performed on the test sections. The 1991 five-year analysis of the test sections showed that no significant difference in performance could be seen between the control sections and the reinforced sections. This finding was attributed to the fact that the test sections had been overdesigned for the traffic load they had received. Due to the sections being overbuilt, none of the sections had been damaged to a point where the benefit of the geogrid reinforcement could be detected (Aran 2006).

The research sections were revisited in 2005 by Aran. Crack surveys, pavement condition surveys, and FWD tests were performed. Surface Condition ratings were given to each of the test sections based on Pavement Condition Evaluation System (PACES) found in the GDOT Road Surface Management manual. The SR-155 site was overlaid in 2004, which prohibited visual surveying of the pavement surface from yielding useful data. Meaningful data was obtained at the ER site through visual inspection and asphalt coring. Based on the PACES scoring rubric, ER-T2a had a rating of 72% while the control section had a rating of 65%. ER-T1 scored 66%. The FWD data also showed that ER-T2a outperformed all the other sections with an average SCI of 1.455 (0.49 less than the control) and an average BCI of 1.15 (0.27 less than the control). ER-T2b performed poorly, but this was attributed to its location near the bridge and the disturbance to the subgrade that occurred during its construction. It was noted that possible reasons for the increase in performance in ER-T2a over the other sections were that it had one more inch of base course than the other sections, it had a subgrade with a slightly higher CBR (8.5% comparted to 8.0%), and the geogrid reinforcement combined with the extra inch of base course allowed it to perform better than the control with one inch less base course and six inches of lime stabilized subgrade. (Aran 2006).

The FWD tests showed that in the SR-155 test sections, the control section and the geogrid reinforced section performed almost identically. When deflection was measured in the FWD test, the reinforced section deflected 0.08 mm more than the control, which is insignificant. The SCI of the control was 2.5 compared to the SCI of 2.48 for the reinforced section, which would be expected since the control had two more inches of AC. The BDI value for the reinforced section was slightly better than the BDI of the control at 1.55 and 1.63 respectively. In the long-term analysis, it appeared that the geogrid reinforcement performed just as well as the control, which had two inches more AC (Aran 2006).

Both long-term studies showed that geosynthetic reinforcement could provide performance enhancement in actual roadway applications. The geosynthetics held up well over the eight years studied by Al-Qadi, and over the 19 years studied by Aran. It should also be noted that the improvement displayed by the reinforcement became more noticeable over longer periods of time as the control sections began to degrade while the reinforced sections showed greater endurance (Al-Qadi and Appea 2003).

2.10 Conclusions

Geosynthetics can be used in a variety of geotechnical applications. Their use in roadway reinforcement has been explored since the 1930's in the United States (Beckham 1935). Geosynthetics are typically made from polymers (Holtz et al. 1998). Two main materials make up the majority of geosynthetics. These two groups are geogrids and geotextiles. Geogrids tend to be more rigid than geotextile and are formed in a grid pattern with individual ribs and apertures. Geotextiles are a fabric material formed in a variety of ways, including woven and nonwoven textiles. The mechanisms by which they reinforce pavement systems have been studied over the last several decades. Geogrid acts as reinforcement in the pavement section through lateral confinement or by acting as a shear resisting interface. It also can strengthen the pavement section by changing the path through which shear stress travels through the cross section. The third mechanism by which it can reinforce the pavement section is through membrane reinforcement (Perkins 1999). Geotextiles primarily improve pavement sections through separation of soil layers and filtration of fines (Holtz et al. 1998).

Instrumentation of geosynthetics in experimentation is essential to collecting data and drawing accurate conclusions. This instrumentation can be achieved using vibrating wire gages, linear variable differential transducer displacement and strain gages, foil strain gages, extensometers, and multi-depth deflectometers (Perkins and Cuelho 1999; Perkins and Lapeyre 1997; Webster 1993). Research suggests there is an optimum depth at which a geosynthetic can add the most reinforcement to a pavement system. This depth is, in part, controlled by factors, such as the strength of the subgrade and the width and magnitude of the load being applied. (Bathurst and Raymond 1987; Perkins 1999; Webster 1993). Research also shows that geotextiles can contribute to the strength and longevity of a pavement system when used as reinforcement but especially as separators at the subgrade-base course interface (Al-Qadi and Appea 2003; Al-Qadi et al. 1994). In the body of current research, there is a gap in knowledge pertaining to geosynthetics' performance in actual roadways and its long-term performance. There is also an opportunity to learn more about the interactions between several layers of geosynthetics, and in determining how and when the reinforcement mechanisms of geosynthetics come into play in a pavement system. Further research into new technologies for measuring the performance of geosynthetics in roadways (such as APLTs) is also needed.

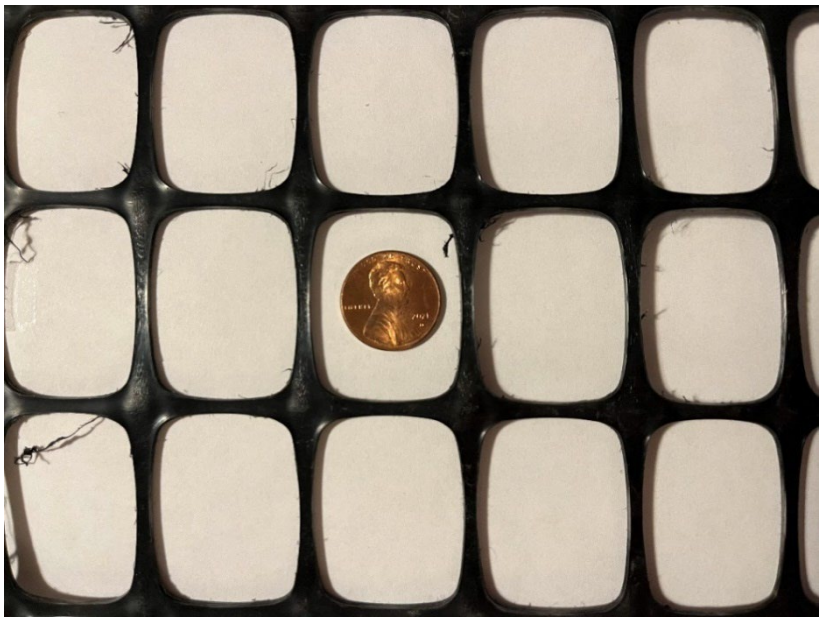

Figure 2.1 Up-close photograph of punched and drawn biaxial geogrid

Figure 2.2 Up-close photograph of nonwoven geotextile

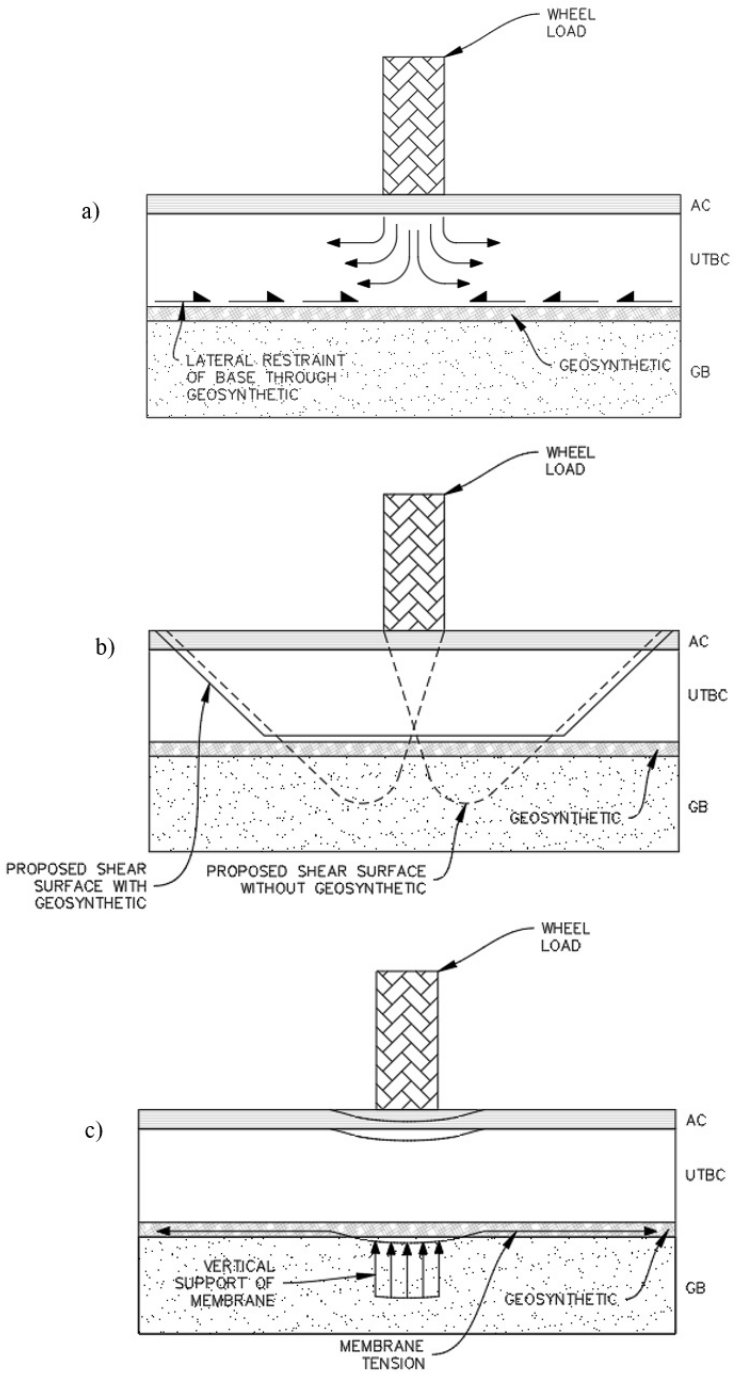

Figure 2.3 Three proposed functions of geosynthetic reinforcement in pavement systems: a) lateral confinement; b) re-orientation of the shear failure plane; c) tensioned membrane effect

Figure 2.4 Inspection of geogrid after experimentation in the field (Cuelho & Perkins, 2009), courtesy of Western Transportation Institute and Montana State University - Bozeman

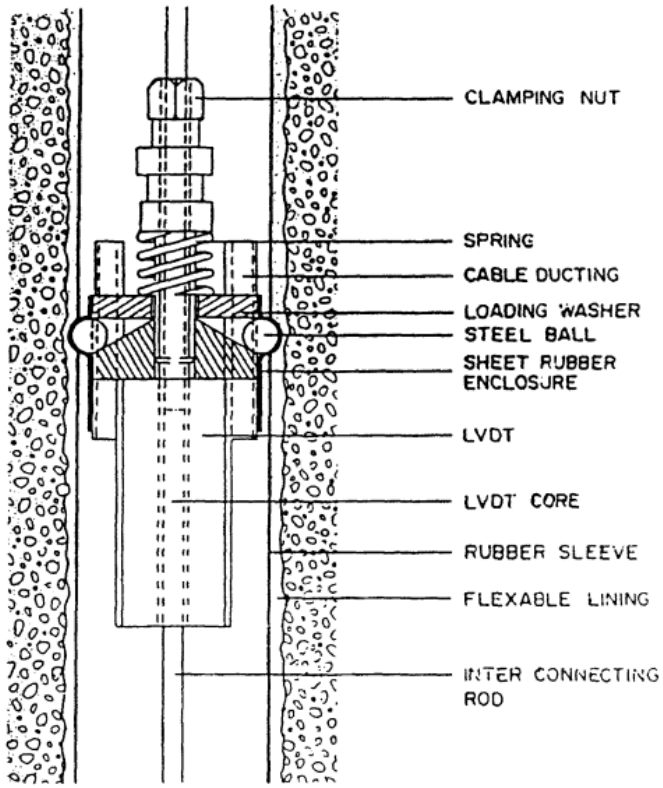

Figure 2.5 Diagram of MDD module (Webster, 1993), courtesy of US Army Corps of Engineers, Federal Aviation Administration

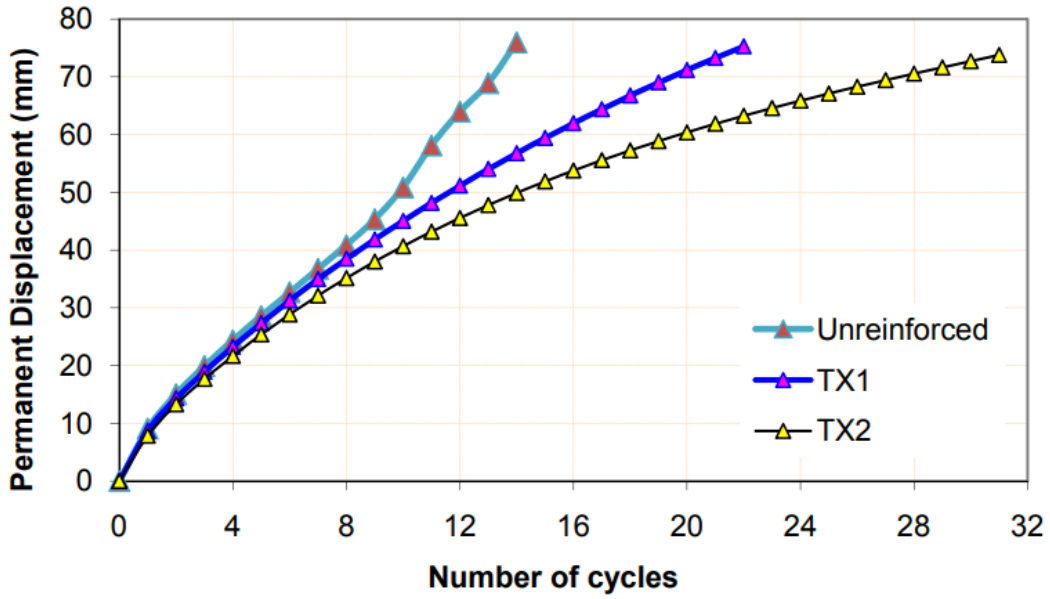

Figure 2.6 Graph of permanent displacement versus number of load cycles (Qian et al., 2010), courtesy of American Society of Civil Engineers. © 2010 American Society of Civil Engineers

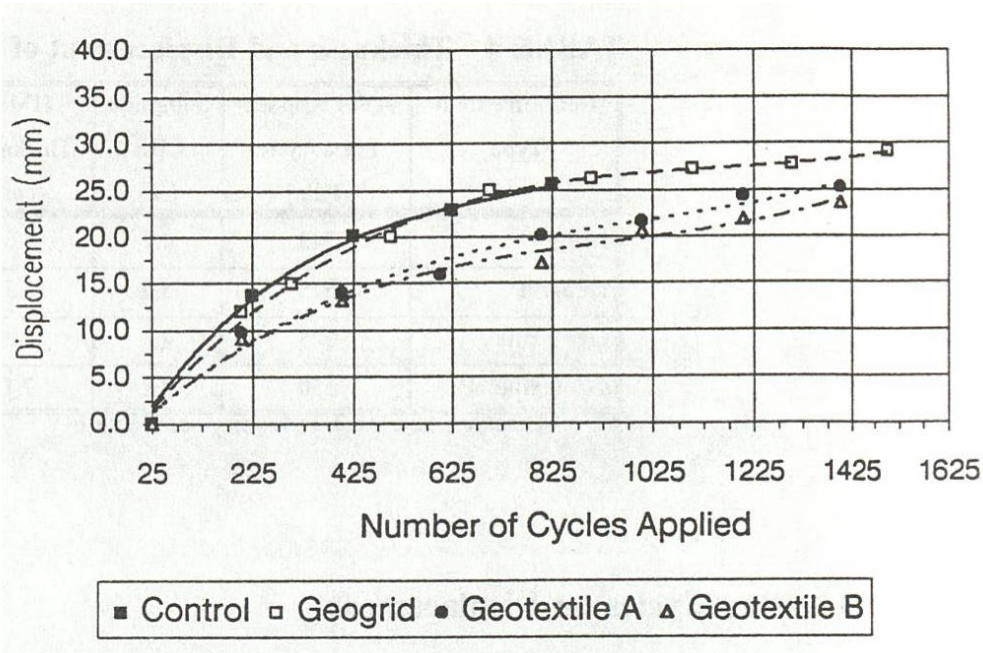

Figure 2.7 *Displacement versus number of cycles applied, adjusted for load seating (Al-Qadi et al., 1994), courtesy of Sage Publications. Al-Qadi, I. L., and Appea, A. K. 2003. "Eight-year field performance of secondary road incorporating geosynthetics at subgrade-base interface." Transportation Research Record, 1849, (1), 212–220*

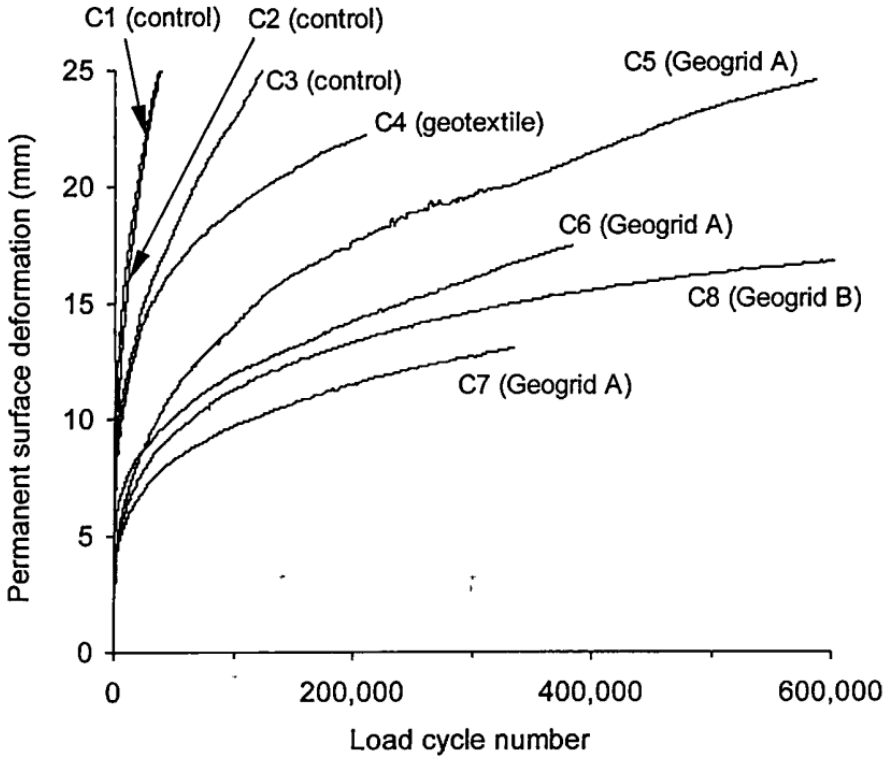

Figure 2.8 Graph showing load cycle versus permanent surface deformation (Perkins, 1999), courtesy of Emerald Publishing

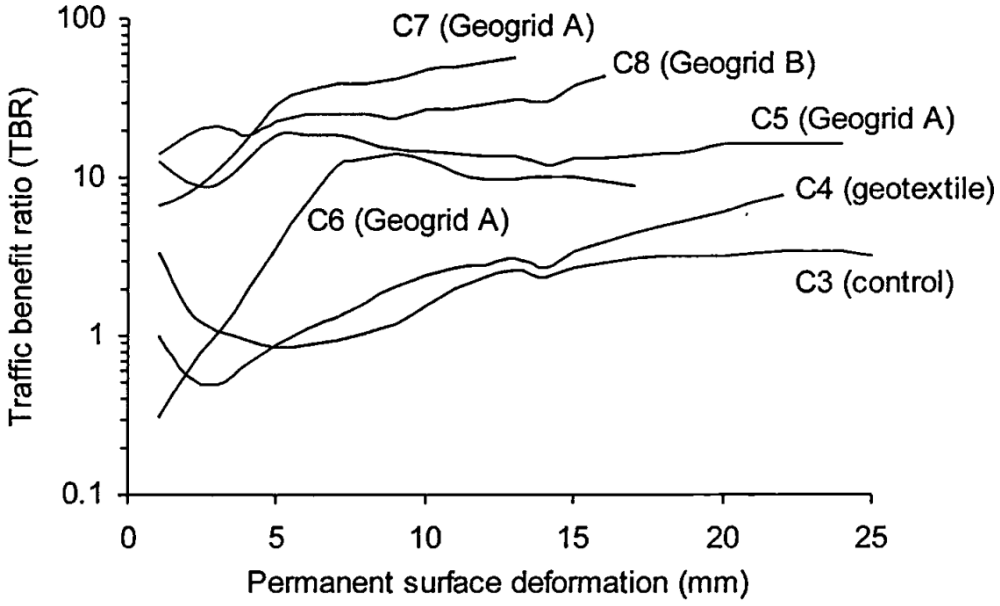

Figure 2.9 Traffic benefit ratio (TBR) versus permanent surface deformation (Perkins, 1999), courtesy of Emerald Publishing

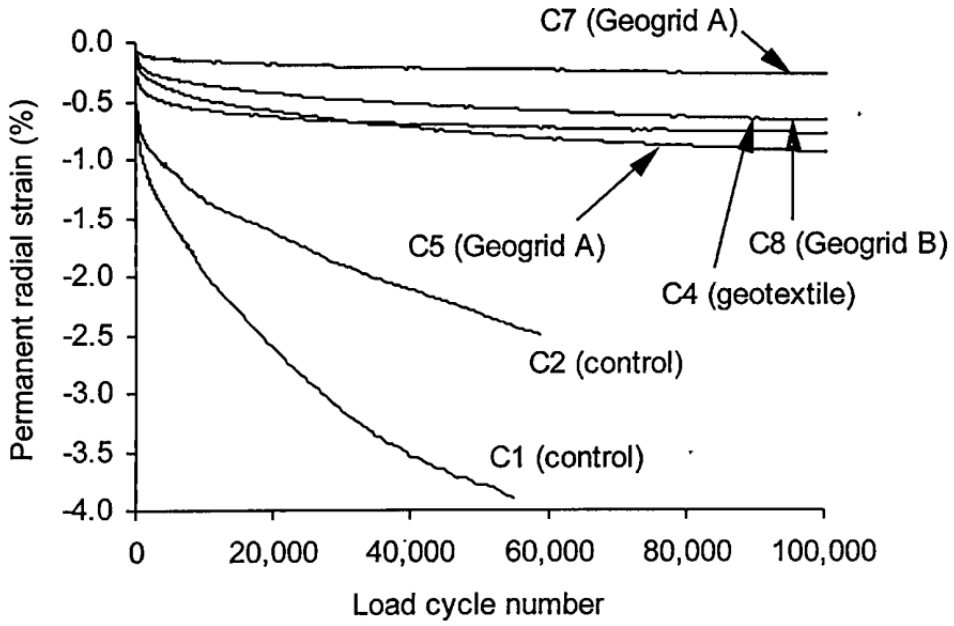

Figure 2.10 Graph of permanent radial strain versus load cycle number at a radial distance of 100 mm and 325 mm below the surface of pavement, (Perkins, 1999), courtesy of Emerald Publishing

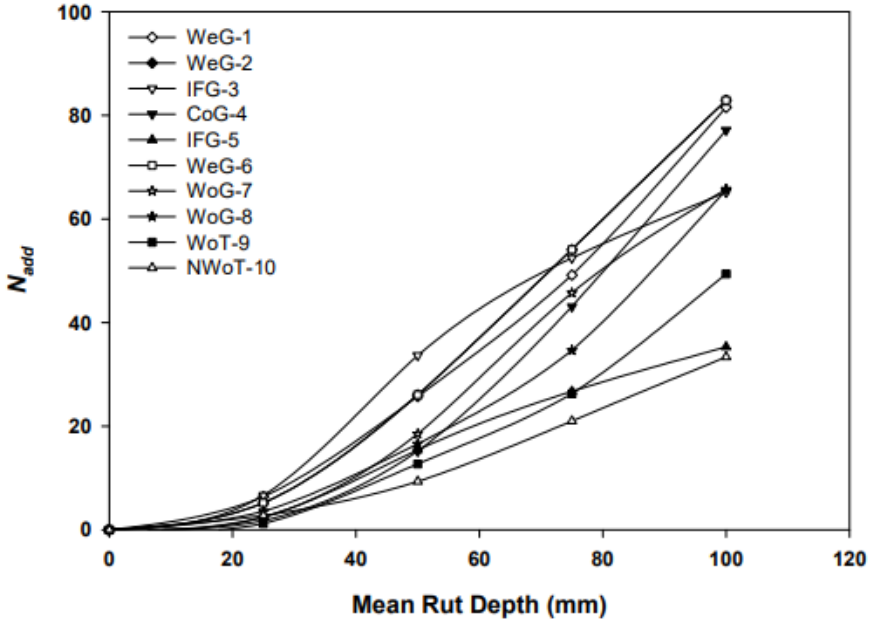

Figure 2.11 Graph of mean rut depth versus N_{add} (Cuelho & Perkins, 2009), courtesy of Western Transportation Institute and Montana State University - Bozeman

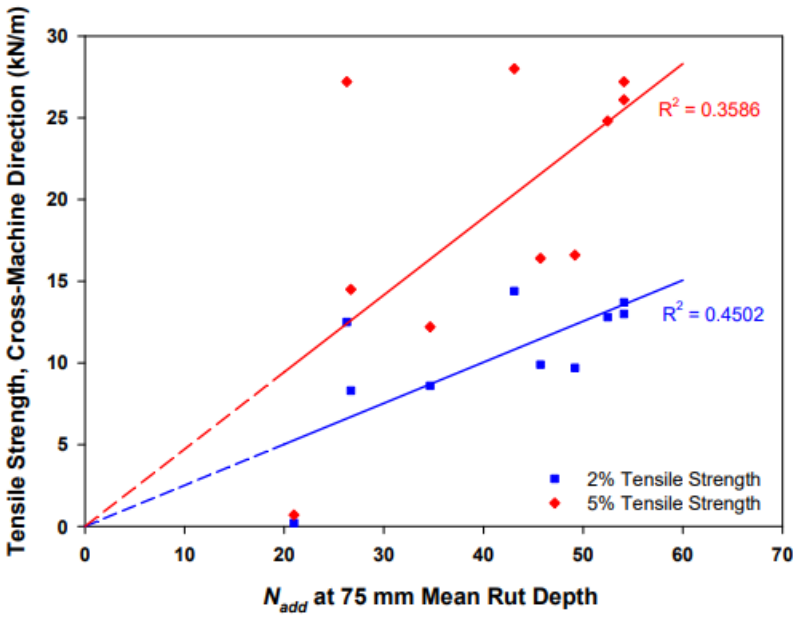

Figure 2.12 Graph showing N_{add} at 75 mm mean rut depth versus tensile strength, cross-machine direction and data trends with R squared values (Cuelho & Perkins, 2009), courtesy of Western Transportation Institute and Montana State University - Bozeman

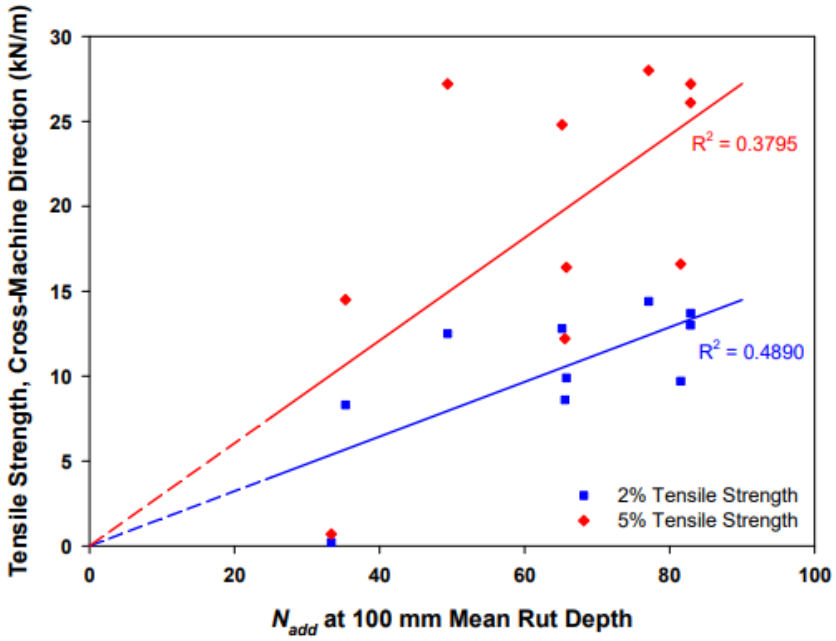

Figure 2.13 Graph showing N_{add} at 100 mm mean rut depth versus tensile strength, cross-machine direction and data trends with R squared values (Cuelho & Perkins, 2009), courtesy of Western Transportation Institute and Montana State University - Bozeman

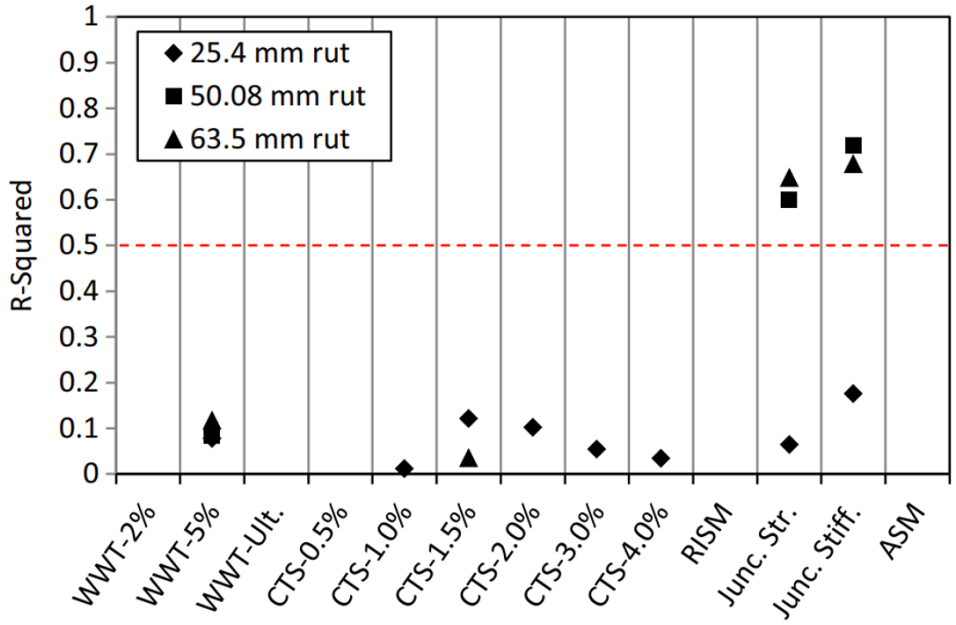

Figure 2.14 Results of regression analysis utilizing cross-machine direction properties (Cuelho & Perkins, 2017), courtesy of Transportation Geotechnics. © 2016 Elsevier Ltd. All rights reserved

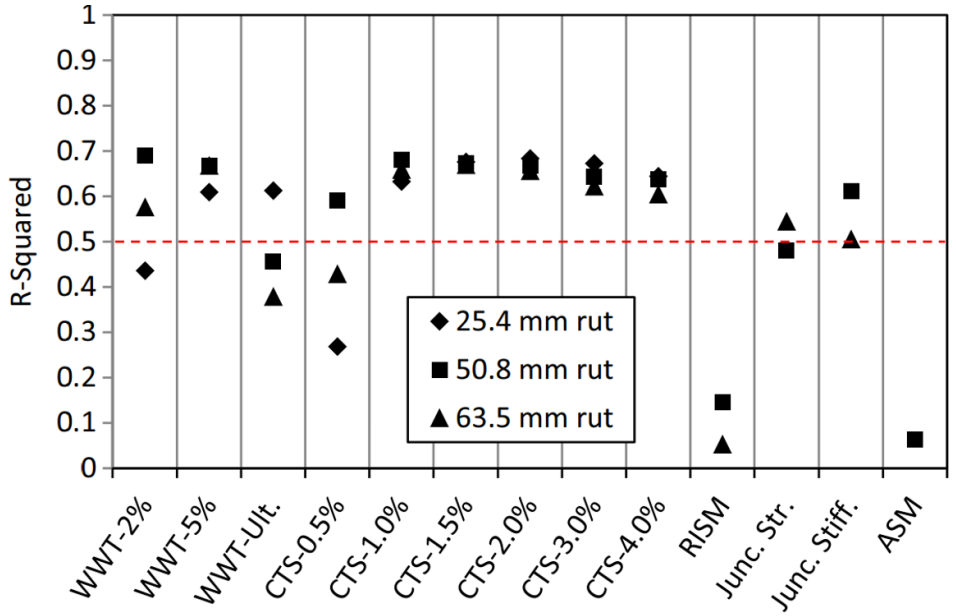

Figure 2.15 Results of regression analysis utilizing cross-machine direction properties and select data set (Cuelho & Perkins, 2017), courtesy of Transportation Geotechnics. © 2016 Elsevier Ltd. All rights reserved

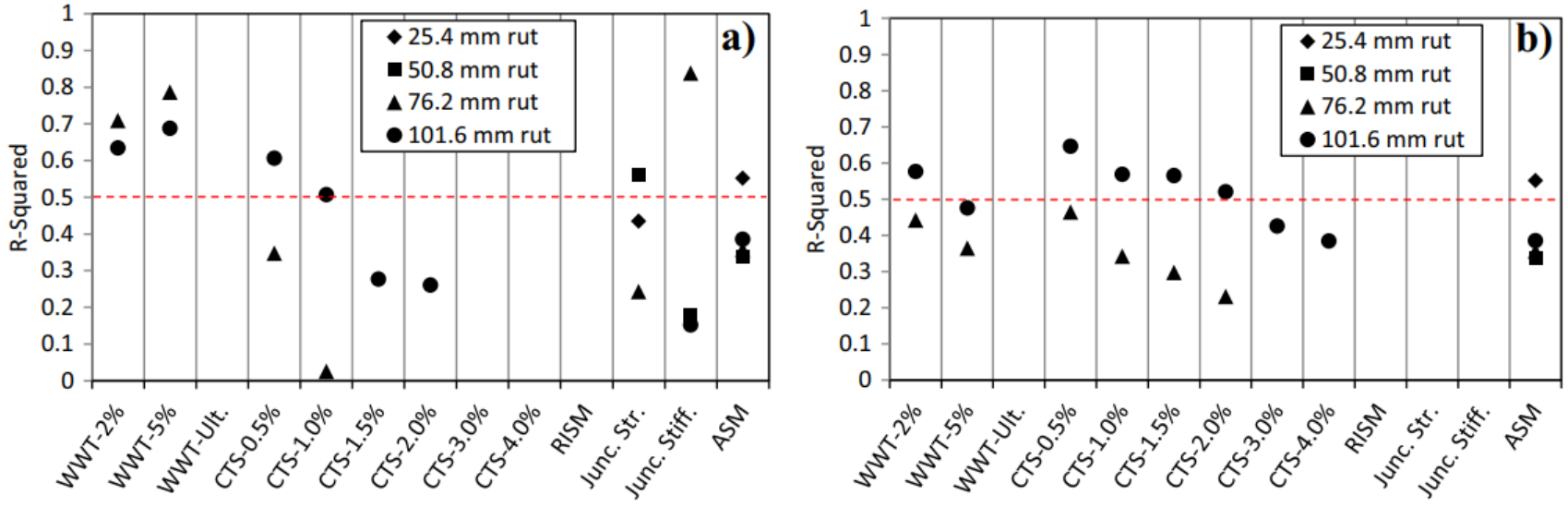

Figure 2.16 Results of regression analysis utilizing geosynthetic properties from the previous research project (Cuelho & Perkins, 2017), courtesy of Transportation Geotechnics. © 2016 Elsevier Ltd. All rights reserved

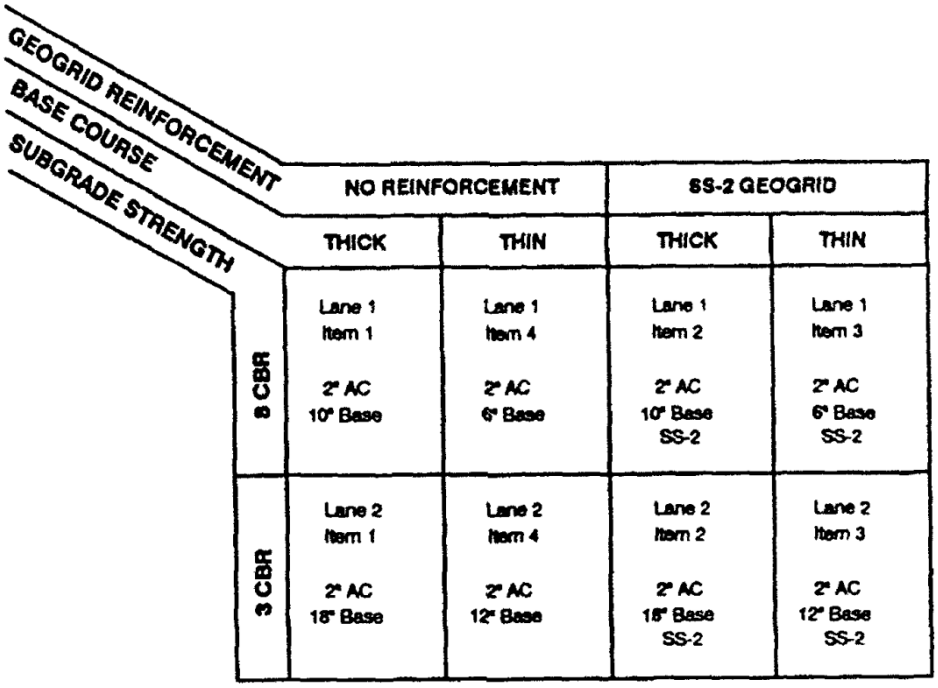

Figure 2.17 Layout for test lanes and items (Webster, 1993), courtesy of US Army Corps of Engineers, Federal Aviation Administration

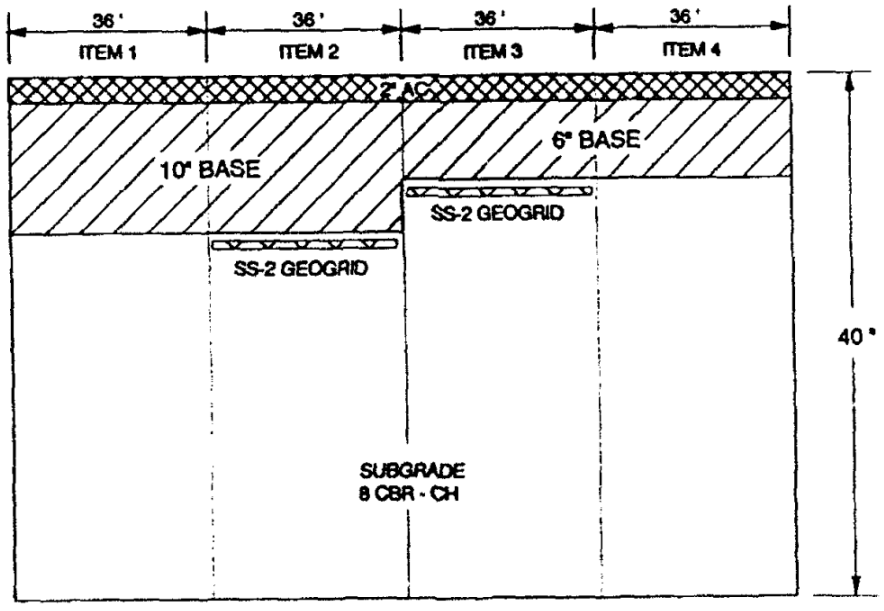

Figure 2.18 Test section layouts for Lane 1 (Webster, 1993), courtesy of US Army Corps of Engineers, Federal Aviation Administration

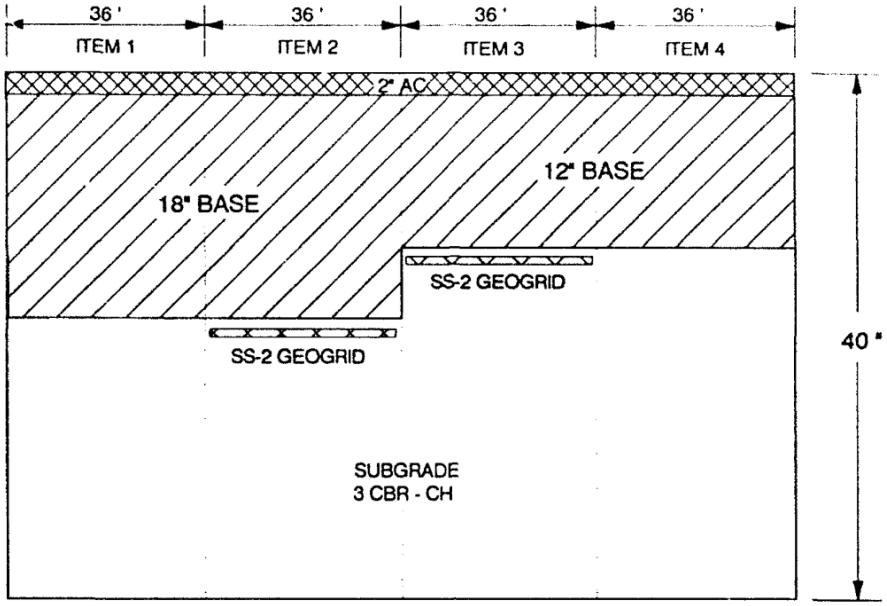

Figure 2.19 Test section layouts for Lane 2 (Webster, 1993), courtesy of US Army Corps of Engineers, Federal Aviation Administration

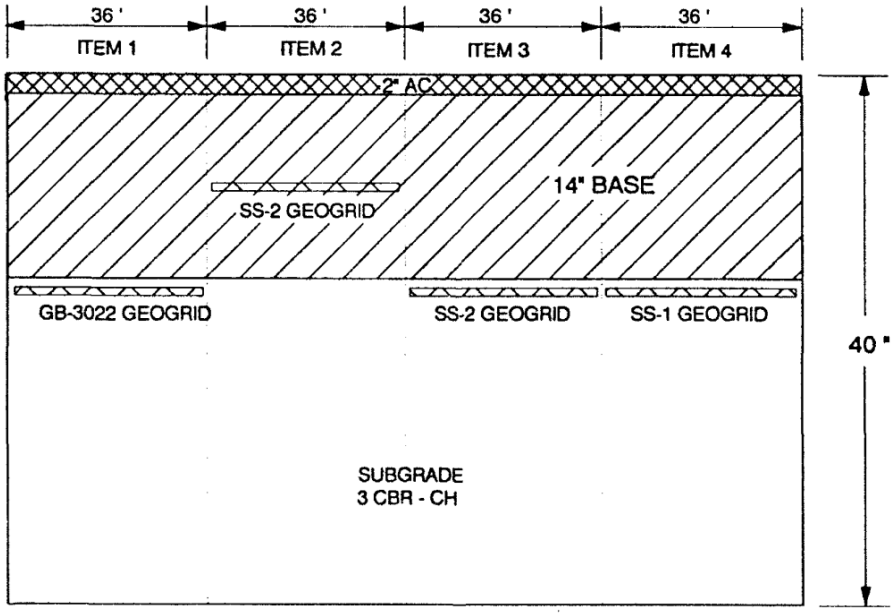

Figure 2.20 Test section layouts for Lane 3 (Webster, 1993), courtesy of US Army Corps of Engineers, Federal Aviation Administration

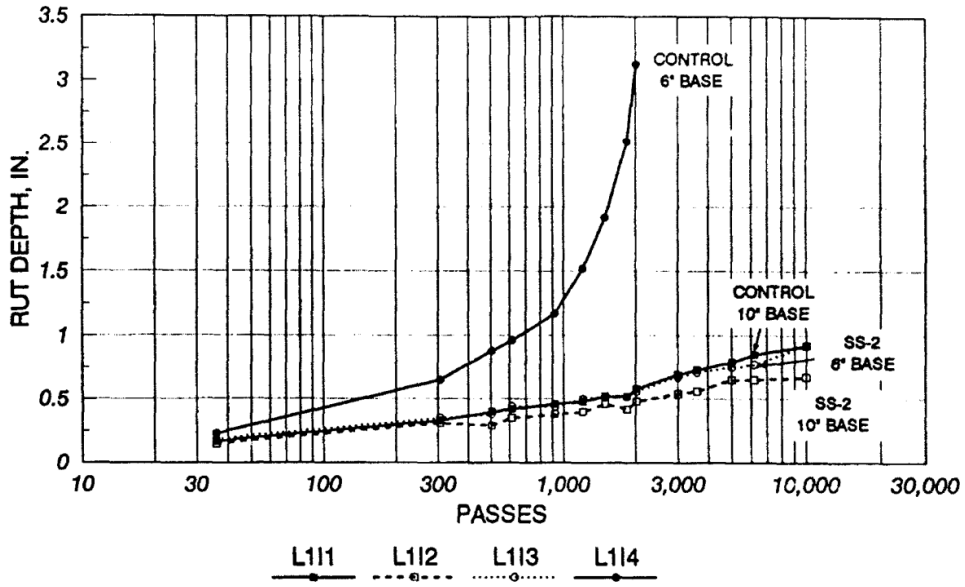

Figure 2.21 Graph showing rut depth measurements for Lane (Webster, 1993), courtesy of US Army Corps of Engineers, Federal Aviation Administration

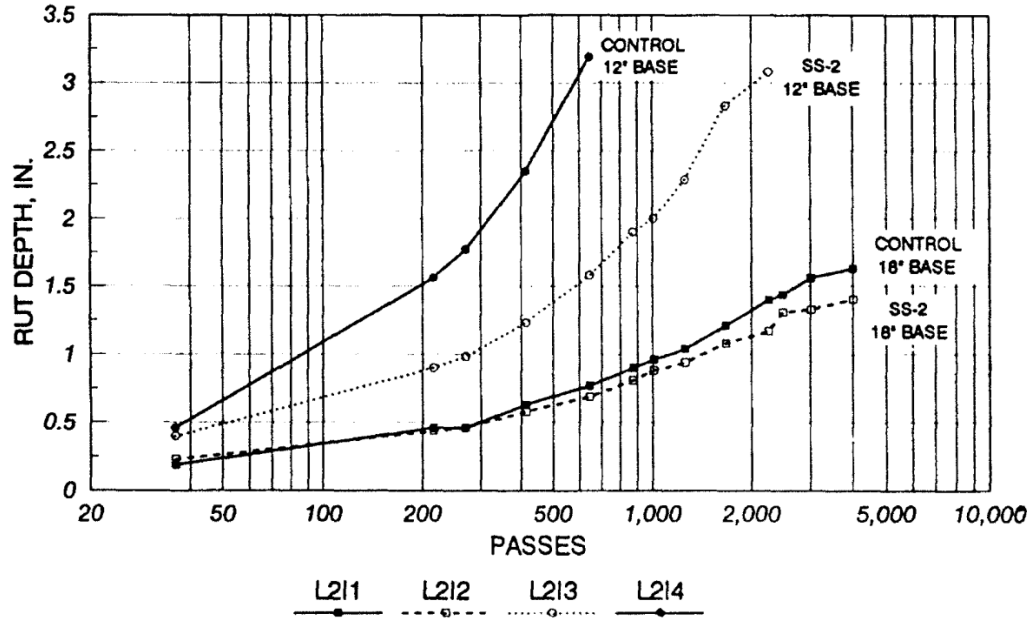

Figure 2.22 Graph showing rut depth measurements for Lane 2 (Webster, 1993), courtesy of US Army Corps of Engineers, Federal Aviation Administration

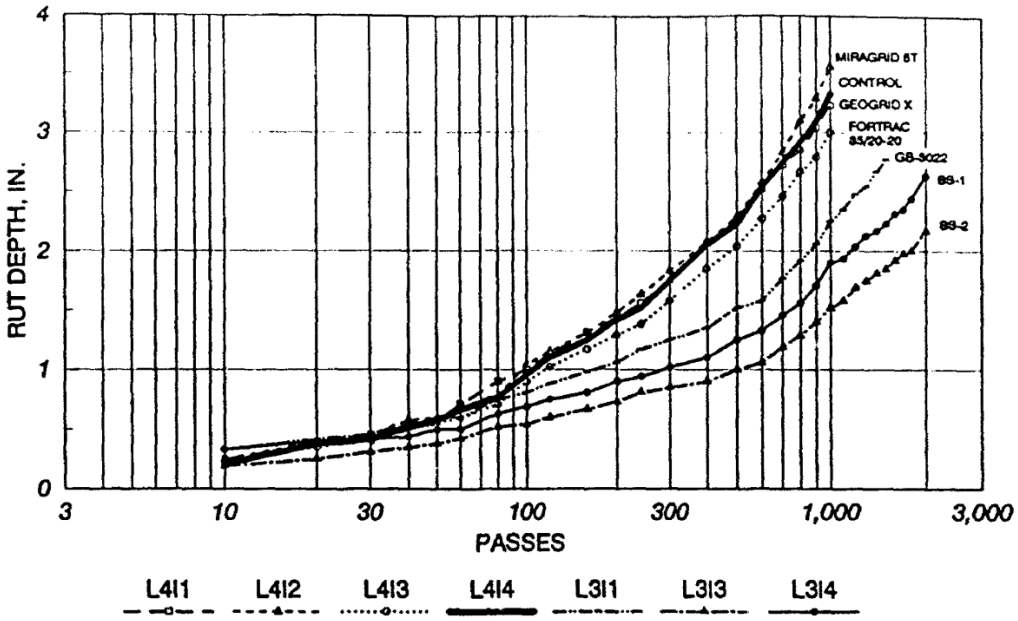

Figure 2.23 Graph showing rut depth measurements for Lanes 3 and 4 (Webster, 1993), courtesy of US Army Corps of Engineers, Federal Aviation Administration

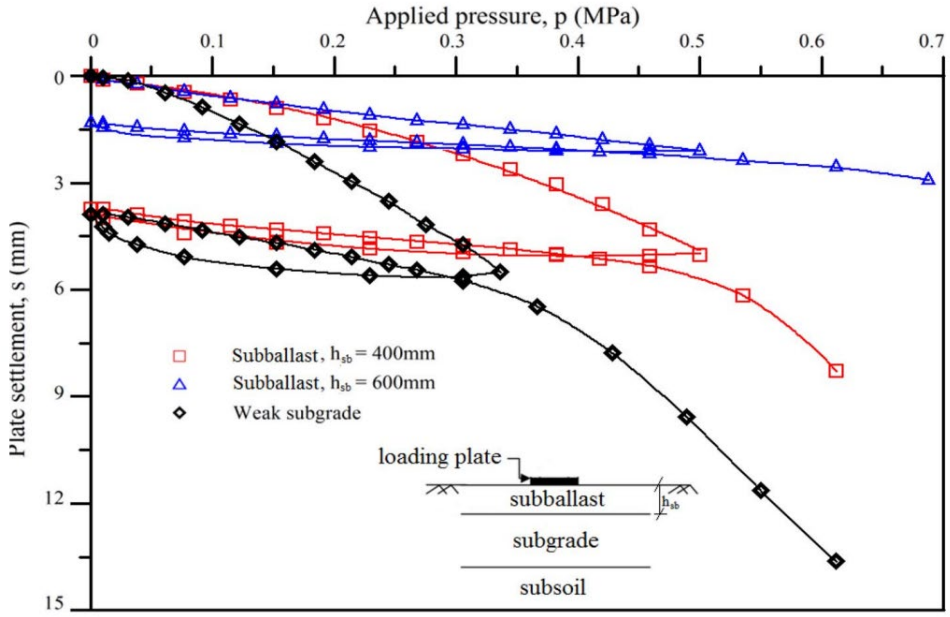

Figure 2.24 Graph of settlement response of unreinforced subballast over weak subgrade (Dash & Majee, 2021), courtesy of American Society of Civil Engineers. © 2021 American Society of Civil Engineers

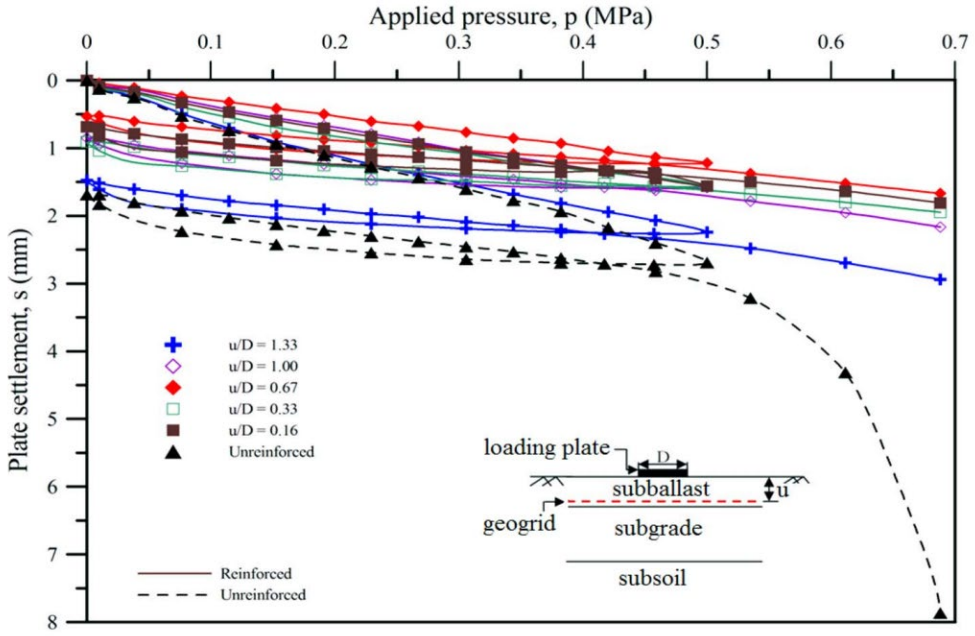

Figure 2.25 Graph of settlement response of subballast over strong subgrade, reinforced and unreinforced (Dash & Majee, 2021), courtesy of American Society of Civil Engineers. © 2021 American Society of Civil Engineers

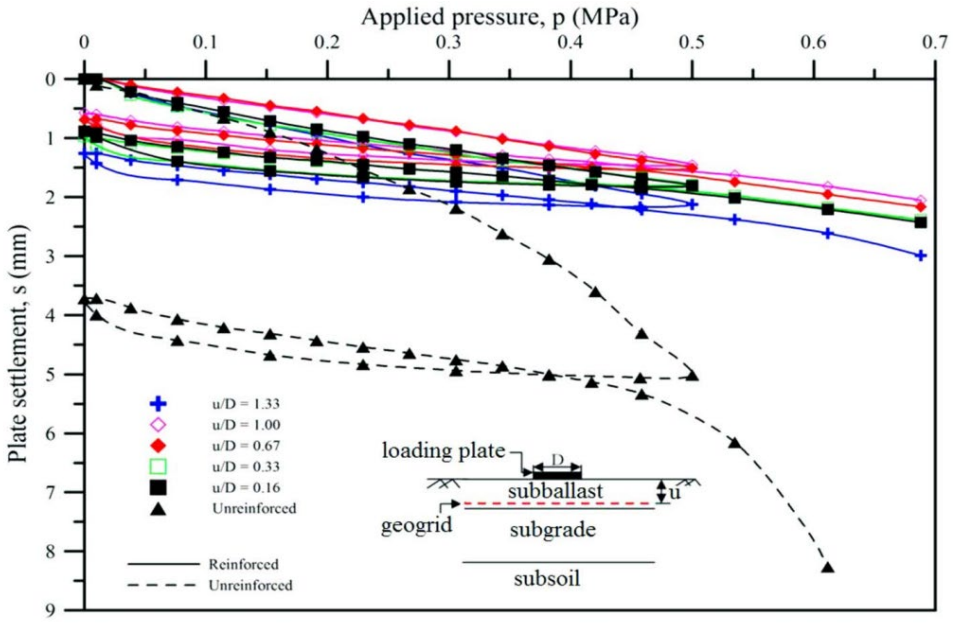

Figure 2.26 Graph of settlement response of subballast over weak subgrade, reinforced and unreinforced (Dash & Majee, 2021), courtesy of American Society of Civil Engineers. © 2021 American Society of Civil Engineers

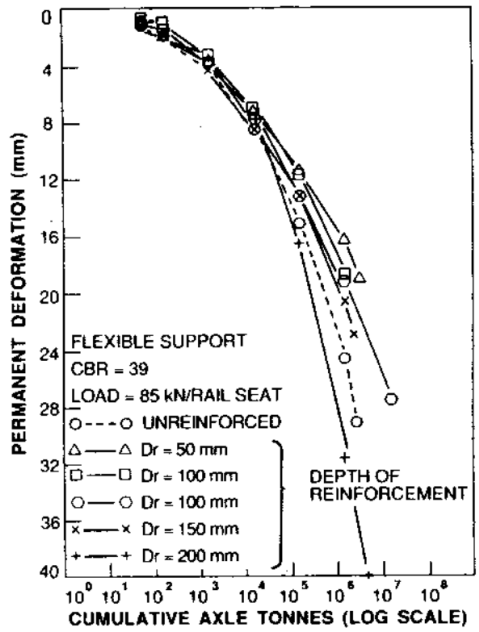

Figure 2.27 Graph of permanent deformation with a support with a CBR of 39 (Bathurst & Raymond, 1987), courtesy of Transportation Research Record. © National Academy of Sciences. All rights reserved

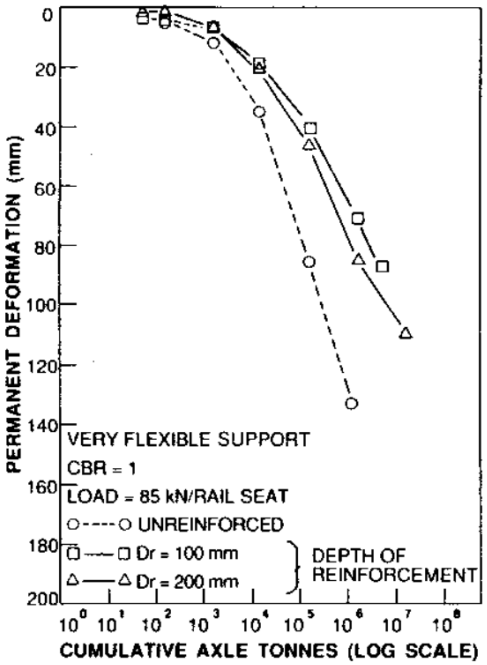

Figure 2.28 Graph of permanent deformation with a support with a CBR of 1 ((Bathurst & Raymond, 1987), courtesy of Transportation Research Record. © National Academy of Sciences. All rights reserved

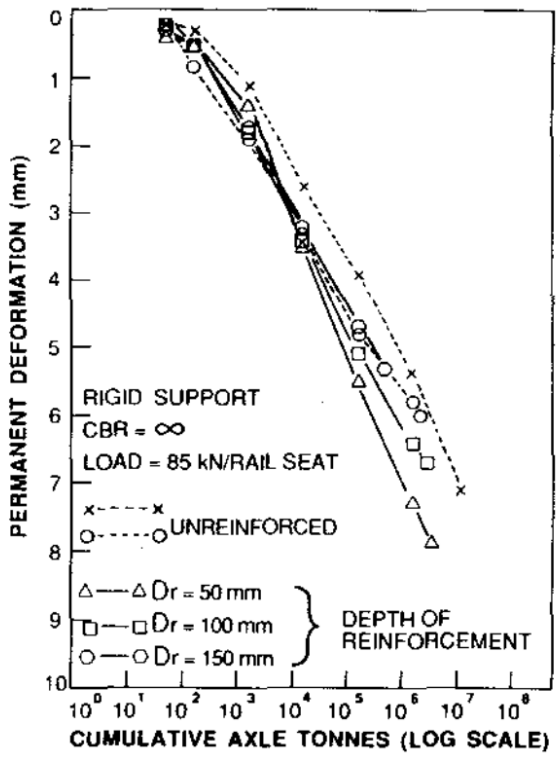

Figure 2.29 Graph of permanent deformation with a support with a theoretically infinite CBR (Bathurst & Raymond, 1987), courtesy of Transportation Research Record. © National Academy of Sciences. All rights reserved

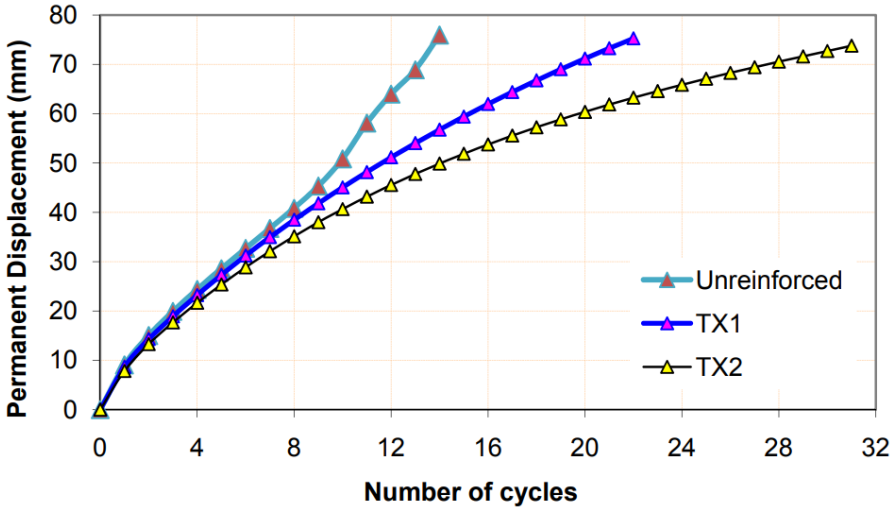

Figure 2.30 Graph of permanent displacement versus number of loading cycles (Qian et al., 2010), courtesy of American Society of Civil Engineers. © 2010 American Society of Civil Engineers

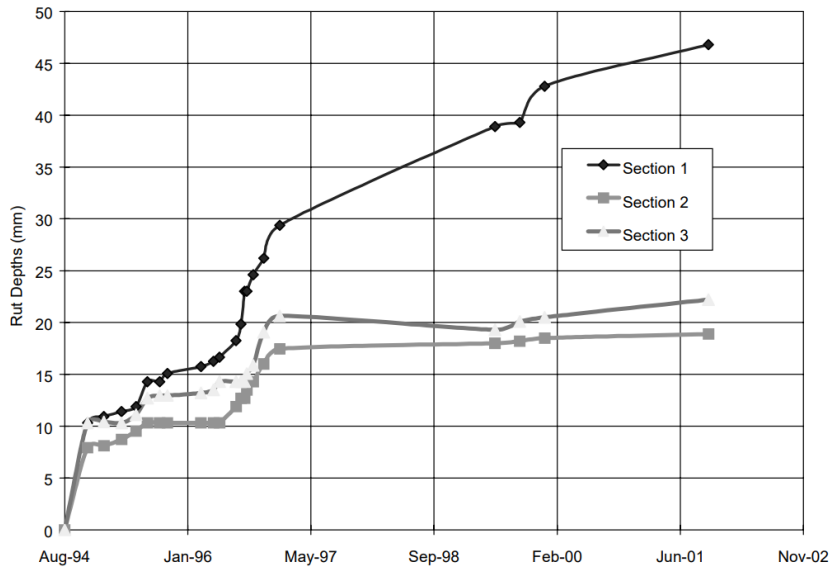

Figure 2.31 Graph of measured rutting in 100-mm base course section (Al-Qadi et al., 1994), courtesy of Sage Publications. Al-Qadi, I. L., and Appea, A. K. 2003. "Eight-year field performance of secondary road incorporating geosynthetics at subgrade-base interface." *Transportation Research Record*, 1849 (1), 212–220

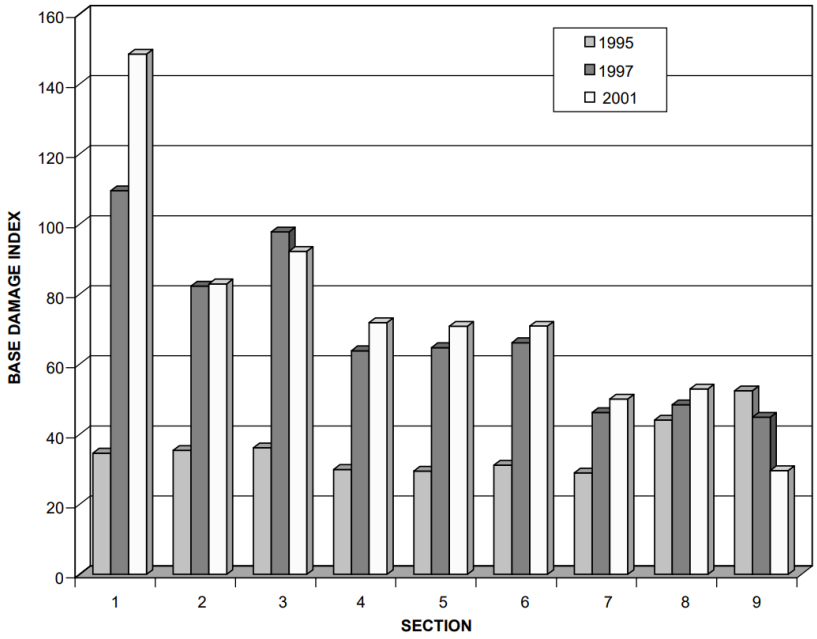

Figure 2.32 BDI of pavements from 1995 to 2001 (Al-Qadi et al., 1994), courtesy of Sage Publications. Al-Qadi, I. L., and Appea, A. K. 2003. "Eight-year field performance of secondary road incorporating geosynthetics at subgrade-base interface." *Transp. Res. Rec.*, 1849 (1), 212–220

Table 2.1 Measurement of ruts and deflection data from 1991 (Aran, 2006), courtesy of Transportation Research Record

	Average Rut Depth (in.)	W1 Maximum Deflection (Sensor 1)[a]	W5 Minimum Deflection (Sensor 5)[b]	SCI[c]	BCI[d]	SPR%[e]
SR-155						
Control Section SR-C (plan typical design)	0.0792	1.11	0.31	0.22	0.14	65
Geogrid Section SR-T (alternate design)	0.0525	1.17	0.17	0.35	0.11	52
East Rome Bypass						
Control Section ER-C	0.0375	0.43	0.10	0.08	0.05	60
Geogrid Test Section 1 (ER-T_1)	0.0580	0.52	0.11	0.09	0.07	59
Geogrid Test Section 2 (ER-T_2)	0.0257	0.42	0.07	0.08	0.06	58

[a] W1: indication of relative strength of the total road. Lower values indicate greater strength.
[b] W5: indication of relative strength of the subgrade. Lower values indicate greater strength.
[c] SCI (surface curvature index) = W1 − W2 indication of relative strength of the upper bound layers of the road section. Lower values indicate greater strength.
[d] BCI (base curvature index) = W4 − W5 indication of relative strength of the unbound base and subgrade. Lower values indicate greater strength.
[e] SPR% (spreadability) = [sum of all deflections/5W1] * 100 represents the ability of the pavement to spread the load throughout the pavement structure. Higher values indicate greater strength.

Table 2.2 Long-term deflection data (Aran, 2006), courtesy of Transportation Research Record

	D_1 (mils)	D_7 (mils)	$SCI = D_0 - D_{12''}$	$BCI = D_{12''} - D_{24''}$	SPR%
SR test site					
Geogrid section (SR-T)	10.32	1.17	3.50	1.55	58.01
Control section (SR-C)	10.24	2.10	2.48	1.63	68.70
ER test site					
Outside lane					
Geogrid Section 2a (ER-T_{2a})	4.15	0.54	1.13	0.76	61
Geogrid Section 2b (ER-T_{2b})	8.06	0.60	2.57	1.47	59
Control section (ER-C)	6.44	0.84	1.83	1.07	60
Geogrid Section 1 (ER-T_1)	6.45	0.70	2.00	1.04	62
Inside lane					
Geogrid Section 2a (ER-T_{2a})	4.96	0.47	1.78	1.54	57
Geogrid Section 2b (ER-T_{2b})	7.84	0.85	2.45	2.33	59
Control section (ER-C)	6.92	0.97	2.06	1.77	59
Geogrid Section 1 (ER-T_1)	6.04	0.69	2.32	2.24	61

SPR = spreadability, the ability of the pavement to spread the load throughout the pavement structure. Higher values indicate greater strength.

3. EXPERIMENTAL METHODS

3.1 Research Section Design and Layout

3.1.1 Research Section Layout

The research area was located east of the Legacy Parkway and south of Farmington, Utah. It was part of the West Davis Corridor, being constructed by the Utah Department of Transportation to connect the Legacy Parkway and I-15 to towns in western Davis County, Utah, via State Road 177. The coordinates of the project locations are 40°57'40.82" N, 111°53'51.78" W. An area 970 feet long near the west end of the bridge approach for the connection of the West Davis Corridor to the Legacy Parkway was designated as the research area (Figure 3.1). Four test sections were utilized in the experimental design. Information for each individual test section is shown in Table 3.1. Figure 3.2 through Figure 3.5 show the cross section of each of the test locations. A photo taken from Section 3 is shown in Figure 3.6.

Each section was 242.5 feet long, except for the control section. Due to construction on the bridge located on the west end of the study area, part of the control section subgrade was heavily disturbed and could not be used as a comparison to the other sections. The control section (S1) was shortened to 156 feet in length. Each test section spanned the width of the southbound lanes and inner and outer shoulder. In the research area this included three 12-foot-wide travel lanes, an inner shoulder that was ten feet wide, and an outer shoulder that was 8 feet wide.

3.1.2 Geosynthetics

Two types of geosynthetic were utilized in the research. The first was SKAPS GT-180 geotextile (GT-180). It is a needle-punched nonwoven geotextile made of polypropylene fibers. The second geosynthetic was Tensar® BX1200 biaxial geogrid and Hanes® TerraGrid RX1200 (BX1200/RX1200). The two geogrids have matching properties and were used interchangeably. The geogrid is an integrally formed geogrid made from polypropylene that has been punched and drawn. Figure 3.7 shows a roll of both the GT-180 geotextile and the BX1200 geogrid.

The GT-180 geotextile was used in sections 3 and 4 as a separator between the subgrade and the subbase, termed granular borrow (GB). It was also used at any of the interfaces between soil layers where geogrid and/or geotextile was not used as a reinforcement or as a separator. At these locations, a 2-foot by 3-foot piece of GT-180 was used to install the array of five strain gages (Figure 3.8). The purpose of this piece of GT-180 was to have a material on which to attach the strain gage array while trying to minimize the reinforcement potential of the geosynthetic. These locations were the interface layers in S1 and the Subgrade-GB interface in S2. The two interfaces specified were unreinforced with geosynthetics and, therefore, the only purpose of the GT-180 was to allow the strain gages to measure the strain in the soil by having enough interface with the soil to mobilize strain. In the other locations where the GT-180 was used as a separator for the entire test section at an interface, the strain gages were installed on a 37-foot-long strip of GT-180.

The BX1200 was used as tensile reinforcement in sections 2, 3, and 4 (S2, S3, and S4). In S2 and S3 it was placed at the interface between the untreated base course (UTBC) and the GB. In S4 it was placed at the UTBC-GB interface as well as at the subgrade-GB interface. The BX1200 at the subgrade-GB interface was laid directly on top of the GT-180. The two materials used together operated as a composite geosynthetic, performing as a separator and as tensile reinforcement. The strain gages were attached to a 37-foot-long piece of BX1200 geogrid.

3.1.3 Instrumentation

Each test section had instrumentation installed at two locations, 18.5 feet from each end longitudinally. The two sets of instruments in each section were designated as “A” and “B”. “A” was located up station of location “B”. The set of instruments included an array of five strain gages installed at the UTBC-GB interface and at the Subgrade-GB interface. A temperature sensor and a moisture sensor were also installed with each array of strain gages, and 2 inches below the surface of the UTBC.

The strain gages were foil-type micro-strain gages. The purpose of the foil strain gages was to measure the in-plane strain in the geosynthetics used in each test section. The foil strain gages were installed following the procedures given in “Documentation of Strain Gage Installation Procedures” published by TRI Environmental and prepared by Eli Cuelho. Two types of strain gages were installed. L50-350-PPY-L strain gages were installed on the geotextile and L6E-350-PC23-L strain gages were installed on the geogrid. Both types of strain gages were purchased from Micro-Flexitronics, Ltd.

In the strain gage array, three strain gages were installed on the geosynthetic in a straight line transversely across the road, and two strain gages were installed longitudinally going down the road. This array of strain gages was centered on the wheel path of the outside travel lane of the road.

The arrangement and spacing of the strain gages were determined based on several parameters. The first was the necessity of redundancy in instrumentation. In every experiment, there is the possibility of instrument failure. According to Dr. Eli Cuelho, it is not uncommon for up to 20% of foil strain gages to fail when installed in the field (Cuelho, 2022). To increase the likelihood of obtaining data that would allow comparisons to be drawn between the different test sections, it was determined that redundant strain gages should be installed at each test location. The first redundancy was to have two instrumented locations in each test section (A and B). The second redundancy was that three strain gages would be placed transversely across the road, and two strain gages would be oriented longitudinally down the road at each test location. Three strain gages were installed transversely across the road.

Roadways are often modeled using a plane strain model, with the assumption that the majority of stress and strain occurs transversely across the road and not longitudinally along the length of the road. Another purpose for having three strain gages oriented transversely at each location was to increase the likelihood that a vehicle traveling down the roadway would drive over at least one of the three strain gages oriented this direction.

Care was taken during installation to ensure the strain gages oriented longitudinally were as close to parallel to the machine direction on the geotextile as possible and the strain gages oriented transversely were as close to perpendicular to the machine direction of the geotextile material as possible. The strain gages installed on the geogrid were attached to the longitudinal and transverse ribs. They were installed parallel to the longest dimension of the rib to which they were attached. Care was also taken to center them on the ribs in each direction.

The spacing of the individual gages in an array was based on several factors. The first factor was each gage needed to be far enough from the other gages to minimize its effect on the strain experienced in the geosynthetic being measured by the other gages in the array. Each gage has a layer of flexible material covering it to protect it from environmental conditions, such as moisture and contact with sharp aggregate in the roadway. For the GT-180 geotextile and L6E-350-PC23-L strain gages, the environmental protection layer was made from RTV-3145 manufactured by Dow Corning. For the BX1200 geogrid and the L50-350-PPY-L strain gages, the environmental protection layer was made from M-Coat JA. Another factor in the spacing of the strain gages was the lead wires for the strain gages had to be securely fastened to the geosynthetic. This was accomplished by using zip ties to connect the wire to the ribs of the geogrid

and to the fabric of the geosynthetic in a serpentine pattern. The reason for this connection was that if tension was ever applied to the lead wire, it would not be pulled apart at its soldered connection to the strain gage. Therefore, it was necessary to space strain gages in the array far enough apart to keep them from interfering in the strain developed in the geosynthetic at each of their locations, and to keep the environmental protection and lead wires for each gage from overlapping. The geogrid apertures dictated the exact spacing of the strain gages, as the L6E-350-PC23-L strain gages had to be installed on the ribs of the geogrid. The final spacing of the strain gages for both the geogrid and geotextile is shown in Figure 3.9 and Figure 3.10. Figure 3.11 and Figure 3.12 show the strain gages attached to the geosynthetics in the field.

For continuity, the strain gages on the geogrid and geotextile had the same spacing. This meant the centers of the L50-350-PPY-L strain gages attached to the geotextile aligned directly over the centers of the L6E-350-PC23-L strain gages installed on the geogrid when the two materials were overlain. This repetition in spacing was chosen to help reduce the variability that would have been introduced by changing the gage spacing between the two materials.

When the strain gages were installed on the geosynthetic, it was decided the geosynthetic would end at the outside lane of travel. Each travel lane in the roadway is 12 feet wide. Vehicles tend to travel down the center of the travel lane, with the rut lines from the tires being three feet in from the edge of each side of the travel lane. For this reason, the center of the center gage in the strain gage array was placed three feet in from the outside edge of the geosynthetic. This methodology was used for the locations where the geotextile was used as a separator and the geogrid was used for tensile reinforcement. In the locations where the strain gage arrays were attached to a 2-foot by 3-foot piece of GT-180, the center strain gage was centered on the rectangle.

The strain gage array was also centered on the long direction of the geosynthetic, 18.5 feet from either end. The GT-180 geotextile came in a roll that was 15 feet long in the cross-machine direction. The BX1200 geogrid is manufactured in a roll that is 13 feet long in the cross-machine direction. In locations where the geotextile was used as a separator, 37 feet by 15 feet strips of the GT-180 were utilized, and in the locations reinforced by the geogrid, 37 feet by 13 feet strips of the BX1200 were used.

The moisture sensors used in the experiment were TEROS 10 Simple Soil Water Content Sensors manufactured by METER Group. These sensors have two long prongs that are pushed into the soil. They were connected to a METER Group ZL6 Data Logger.

Temperature sensors were manufactured in-house using 24 AWG K-Type Thermocouple wire with PVC insulation from MN Measurement Instruments, and Twidec K-Type Thermocouple Plug Adapter Cable Wire Connectors. For each temperature sensor, 13.75 feet of the thermocouple wire was utilized. On one end, the exterior and interior PVC insulation was stripped back far enough that the plug adapter could be connected to the two wires. On the other end of the wire, the exterior PVC insulation was stripped back 1.25 inches. The interior insulation was stripped back 1 inch. The two exposed ends of the wire were tightly twisted together and soldered. Each of the thermocouples was calibrated by measuring the temperature of boiling water, room-temperature water, and ice water using a DANOPLUS High Accuracy Digital K-Type Thermocouple Thermometer Meter Tester. These measurements were compared against two laboratory glass thermometers to calibrate the readings of each of the temperature sensors.

3.2 Field Installation of Instrumentation

3.2.1 Subgrade

Before any field work was performed by the research team, the contractor cut the research area subgrade down to approximately the design subgrade elevation. Surveying performed by the research team showed these elevations were below the design subgrade elevation by as much as nine inches. In sections 2-4 the average elevation below the design elevation was measured to be 5.9 inches. 75 Dynamic Cone Penetration (DCP) testing was performed on the originally prepared subgrade in accordance with ASTM D6918 (Figure 3.13). These tests were then correlated to CBR values. Tests were performed 10 feet right of the SB control line, two feet left, 14 feet left, and 21 feet left of the SB control line. The contractor then regraded and compacted the subgrade to align it with the design elevations. 38 DCP tests were then performed, this time on the final subgrade.

Instrumentation was then installed in the subgrade. The location for the strain gage arrays was surveyed by the contractor. Moisture sensors were installed three feet down station from the center of the strain gage arrays, and temperature sensors were installed four feet down station of the strain gage arrays. A trench was dug in the subgrade using a hoe and a pickax so that the moisture sensor and temperature sensors could be installed below the surface of the subgrade (Figure 3.14). The moisture sensor was installed with the center of the moisture prongs three inches below the surface of the final subgrade. The temperature sensor was also installed three inches below the surface of the final subgrade. A 1.5-inch-long landscaping staple was used to secure the temperature sensor in place in the bottom of the trench. The trench extended to the location on the side of the road where all measurements would be taken. The two sensors were then covered with subgrade soil and compacted using an eight-inch square hand tamper.

The strain gage array was then installed. In all installation instances, the geosynthetics were installed with the machine direction oriented longitudinally to the flow of traffic, and the cross-machine direction oriented transversely to the flow of traffic. To properly orient the strain gage arrays, survey points were used. The point corresponding to the location of the strain gage array on the SB control line was marked. A chalk line was taken from this point to the survey point for the strain gage array. The ground was marked with a chalk line. Two points surveyed on either side of the strain gage location up station and down station were also utilized with the chalk line. Using these points, the four 2 feet by 3 feet pieces of geotextile holding the strain gage arrays for sections 1 and 2 were easily oriented.

To keep the strain gages safe during transportation, pieces of ¾ inch OSB and/or plywood were used as backing boards for the strain gage arrays. Four smaller squares of OSB and/or plywood were screwed onto the backing board with the geotextile sandwiched between them. This kept the strain gages from being flexed during transportation and installation. The backer boards were removed right before final installation was completed. With the backer board removed, the piece of geotextile was oriented on the subgrade surface using the marks from the chalk line. The geotextile had also been marked to line up its edges with the lines on the subgrade. Once oriented flat on the subgrade, the four corners of the geotextile were stapled to the subgrade using two-inch landscaping staples.

A trench was dug approximately two inches deep by pickax and by a skid steer for the lead wires. The trench for the lead wires from the temperature and moisture sensors intersected this trench six feet closer to the edge of the roadway than the strain gage array location. A landscaping staple was used to hold the strain gage lead wires in the bottom of the trench at the edge of the piece of geotextile. The wires were buried in the subgrade material removed to make the trench then, the trench was compacted using the eight-inch square hand tamper. The strain gages were then covered with a thin layer of sand to help protect them from sharp aggregate in the GB.

In S3 and S4, the moisture and temperature sensors were installed the same as they were in S1 and S2. The strain gage arrays in S3 and S4 were attached to 37 feet by 15 feet geotextile strips. These strain gage arrays were also protected during transport using backer boards. The geotextile was rolled onto a two-inch PVC pipe. To install the geotextile and strain gages, the same process as was used for the smaller pieces of geotextile was also used with a few additional steps. Another line was made with the chalk line three feet closer to the outside edge of the road running parallel to the length of the road. The geotextile was aligned parallel and tangent to this line. To aid in aligning the geotextile transversely across the road, a stake was driven into the ground at the surveyed point on the SB control line and the same station as the strain gages, and 25 feet left of the control line. A string line was strung between the stakes slightly above the strain gages and geotextile. Using this string line and the line marked on the subgrade, the geotextile was properly aligned.

Once aligned, the backer board was removed from the geotextile. A wire was attached to the edge of the backer board, so the board could be removed without lifting up the geotextile. Using the wire, the backer board was pulled out from under the geotextile to the outside edge of the road. The alignment of the strain gages was then rechecked. Four staples were used to hold the strain gages in place, spaced similarly to their spacing with the 2 feet by 3 feet pieces of geotextile in sections 1 and 2. Once the strain gages were held in place by the landscaping staples, any folds in the geotextile were straightened, so the geotextile was flat and smooth against the subgrade. The edges of the geotextile were also stapled down with the landscaping staples. The strain gage lead wires were then buried in the same manner as in S1 and S2 (Figure 3.15). Sand was also used to thinly cover the strain gages.

In S4, geogrid was installed on top of the geotextile. The geogrid was rolled up and zip-tied for transportation. Backer boards were also used to keep the strain gages safe during transport. Once the geogrid was rolled out at the test location, it was aligned with the strain gages on the geotextile beneath it (Figure 3.16). The geogrid was stapled down with the landscaping staples and with 60 penny nails, similarly to the geotextile. Due to the memory of the geogrid due to being rolled during manufacturing and transport, it was difficult to make the geogrid lay perfectly flat with complete contact with the geotextile beneath it. Staples were used to minimize this.

Once instrumentation was installed, the contractor installed the rest of the geotextile in sections 3 and 4. The geotextile was rolled out starting at the up-station side of section 3; however, the installation was not as precise as was expected. There were folds in the geotextile, in part, due to curvature of the roadway in the test sections. To correctly install the geotextile, it was required that any edge of the geotextile should overlap any adjoining edge by at least 12 inches. This was not always the case. Due to wind during installation, some of the geotextile was blown out of place and had to be replaced and stapled down with landscaping staples, and the contractor supplied large staples (Figure 3.17). The researchers made sure that the geotextile overlapped the geotextile strips with the strain gages installed by the specified 12 inches and that the geotextile directly around the strain gage area was installed correctly.

Similar problems were encountered when the geogrid was installed by the contractor in section 4. In some areas, the geogrid was folded entirely over in the road section, and large folds were left in the geogrid (Figure 3.18 and Figure 3.19). In one area the geogrid was not overlapped properly, so a strip of geogrid was cut and overlapped into this area, oriented in the opposite direction than the rest of the geogrid. The researchers made every effort to ensure the geogrid overlapped the section with the strain gages by 12 inches and that any folds were minimized in this location. Due to the nature of an actual construction site, the research team was not able to control all the activities of the contractor in the research section. As a result, the geotextile and geogrid were installed the same way they would normally be installed in the field by a contractor.

3.2.2 Granular Borrow

Once the geosynthetics were installed, the contractor began to place the GB. Where the GB was placed over the strain gage arrays, a loader or a skid steer was used to carefully place the material. The GB was placed first on the strain gages, and then worked out to the edges of the geosynthetic. The GB in the rest of the project area was placed using a loader and a grader with GPS control of the blade. It was placed in one lift. The GB was compacted using a vibratory smooth drum compactor. The compaction and depth of placement was not uniform. By comparing survey data from the top of the final subgrade and the top of the GB, it was determined the measured thickness of the GB varied from 6.6 inches to 10 inches thick with an average thickness of 8.2 inches in sections 2-4. The GB was 11.2 to 16.7 inches thick with an average thickness of 14.7 inches in section 1.

Water content was not carefully controlled or monitored during compaction. Once the GB was placed and compacted, DCP testing was again performed. The DCP testing went through the entire layer of the GB, and, depending on the thickness of the GB, six inches into the subgrade. The DCP results were correlated with CBR values for the GB and subgrade. The calculated average CBR for the GB layer varied from 13.77% to 84.3% with a standard deviation of 16.51.

After the DCP testing and surveying was completed, the instrumentation was installed. The temperature and moisture sensors were installed in the same manner as they were in the subgrade. The strain gages were also installed as they were in the subgrade (Figure 3.20). Similar problems were experienced when the contractor installed the geogrid in sections 2-4. The geogrid was folded and did not overlap properly in all cases. The researchers again ensured the proper installation of the geosynthetics near the strain gages but could not control the variability in the installation of much of the rest of the research area.

3.2.3 Untreated Base Course

Similar variability in the placement and compaction of the UTBC was also experienced. The measured thickness of the UTBC varied from 2.9 inches to 6.7 inches thick with an average thickness of 4.8 inches. The correlated CBR values from the DCP data varied from 13.57% to 52.27% with a standard deviation of 9.16. After the DCP tests and surveying were performed on the final grade of the UTBC, temperature and moisture sensors were installed at the instrument locations two inches below the surface of the UTBC. The lead wires were buried approximately an inch below the surface of the UTBC. All the lead wires for the instruments came together at the edge of the road.

To further characterize the GB and UTBC used in the project, 10 five-gallon buckets of each of the materials were collected. Sieve analyses were completed on each material following ASTM D6913.

3.2.4 CPT and NDT Testing

Data at each instrument array location was also collected by nuclear density testing and Cone Penetration Test (CPT) soundings. A nuclear density gage was used to measure the density of the soil five feet down station from the center of each instrument array and five feet down station of four additional automated plate load tests that were performed near the midpoint of each test section. The nuclear density tests were performed at depths of 12, 8, 6, 4, and 2 inches (Figure 3.21).

The CPT tests were performed five feet up station of the instrument array locations. They were also performed at the location of the four additional automated plate load tests. The CPT tests were performed by AGEC using a Geoprobe 3230DT and a 10 cm^2 nova cone. The cone was pushed into the ground to a minimum depth of six feet. At location 1B the cone was pushed down to 22.5 feet and a pore pressure dissipation test was performed. A pore pressure dissipation test was also performed at location 3B at a

depth of 70.5 feet. The purpose of the pore pressure dissipation test was to determine the equilibrium pore pressure at depth. This value can then be used to determine the height of the water table or if there is artesian pressure present. The CPT data included the tip resistance of the cone (tsf), the sleeve friction (tsf), the pore pressure (psi), the friction ratio (%), and the Robertson Soil Behavior Type with depth.

3.3 Test Procedures

Two main tests were performed in the project areas instrumented with strain gages, moisture sensors, and temperature sensors. Each of these tests were performed on top of the UTBC. The first test was an automated plate load test (APLT) performed by Ingios Geotechnics. The second test was the truck load test (TLT), performed by using a loaded triple-axle dump truck to load the test location with a large static load.

3.3.1 Automated Plate Load Tests

The purpose of the APLT tests were to determine the resilient modulus (M_r) of each of the layers in the pavement system and a composite resilient modulus (M_r) for the entire pavement system. The APLT test also measured deflection of the pavement system under the plate being loaded and deflection at two, three, and four radii from the center of the loading plate.

The APLT testing utilized a trailer-mounted electronically controlled hydraulic ram to perform cyclic plate load testing at each instrumented location (Figure 3.22). A 12-inch diameter loading plate was used on Ingios' APLT field system setup. The loading plate was aligned over the center of the middle strain gage in the array being tested (Figure 3.23). Sand was used to ensure even and complete contact between the loading plate and the UTBC. Sand was also used underneath the array of instruments being used to measure deflection at three radii greater than the loading plate (Figure 3.24). The specific APLT test performed at the locations of the instrument arrays was an Incremental Cyclic M_r Test. 1,550 stress cycles were used. The minimum applied stress was 2 psi, and six stress levels were used: 5, 10, 20, 30, and 40 psi. At each stress level, a specific number of load/unload cycles were applied to the pavement system. Load was increased to the predetermined stress level for 0.1 seconds, and then unloaded for 0.1 seconds. A dwell period of 0.8 seconds was used between each load/unload cycle. During the APLT test, a CR9000x data acquisition unit was used to record the strain registered by the strain gage array. Data was then transferred to a laptop running RTDAQ software. The strain gages were sampled every 100^{th} of a second to accurately record the strain from the APLT testing. The strain gages were excited with a five-volt current. The output from RTDAQ was the millivolt output from each of the strain gages. Each APLT test lasted approximately 20 minutes. At the beginning of each APLT test, the temperature at the depth of each strain gage array was measured. Throughout the duration of the test, soil moisture content was measured via a METER Group ZL6 Data Logger. The water content measurements were sampled at a rate of every half a second.

Four additional APLT tests were performed near the midpoint of each of the test sections. This test (Test B) was a Random Loading Sequence Extended Cycle Test. It was also performed with a 12-inch diameter loading plate and involved loading the pavement system with 5,000 cycles with a minimum 2 psi contact stress and from 5 to 50 psi in 5 psi increments. This test was specifically developed to mimic the random loading that occurs during trafficking of an actual roadway.

3.3.2 Truck Load Tests

The second test performed was the truck load test (TLT). A three-axle dump truck was fully loaded with soil, and an 11.23-inch diameter half-inch steel plate was placed centered over each strain gage array. The dump truck was then driven over the plate and the outside wheel of the passenger middle axle was

centered on the plate. The same measurements of temperature, moisture, and strain taken in the APLTs were taken in the TLTs. One set of the dual wheels on the truck's center axle was allowed to dwell centered on the plate for approximately 10 minutes while measurements of strain and water content were taken. The purpose of these tests was to measure the strain in the geosynthetics at different depths under a static heavy load.

After reviewing data from the first TLTs, it was determined that better results might be obtained by using a large loading plate. The purpose of this change in loading is discussed further in the Results section. The TLTs were performed again using a one-inch-thick steel plate with a diameter of 34 inches. The test procedure was the same as for the first TLTs, except the dwell period was increased to 15 minutes.

3.3.3 Strain Data Collection

Strain gages were connected to circuitry boxes designed by TRI Environmental and built by the research team. (The naming pattern and layout for each strain gage array is shown in Figure 3.25). A circuitry box was built for each A and B test location, and each box contained a wheat stone bridge for each strain gage and a header that connected to the data acquisition equipment with a data cable. The strain data during the tests was collected using a CR9000x with three CR9052DC filter modules (Figure 3.26). These modules gave the data collection greater precision due to their digital signal-filtering capabilities. The strain registered by the strain gages was recorded every 100th of a second during the testing. The data was uploaded to a computer running RTDAQ software, and the measure-range parameter of the program was set at a 50-mV threshold to maximize accuracy of the recorded data. Data recorded by the RTDAQ program was the output voltage of each strain gage in mV.

To convert mV to strain, two conversion factors were used. The first was a gage factor calculated specifically for the strain gages used in the project. The gage factor was determined by the method of shunt calibration. TRI Environmental performed preliminary shunt calibrations on the lab specimens were used to determine the global strain factors for the geosynthetics. The average gage factor determined by TRI Environmental was 1.4. The TRI Environmental "Global Strain Calibration Report" can be found in the supplement material.

Shunt calibration was also performed in the field to account for resistance in the lead wires going to each of the strain gages. To perform this shunt calibration, one leg of the wheat stone bridge linking the strain gage to the data collector was shunted by putting a precision resistor in parallel with the resistor in the leg of the wheat stone bridge. This was done at the wheat stone bridge for each strain gage in each of the control boxes used to connect the strain gages to the data acquisition equipment (Figure 3.27 and Figure 3.28). In most cases, the calculated gage factors for the operational gages in the field were within one or two hundredths of 1.4.

A 2 kΩ resistor with an accuracy of plus or minus 0.01% was used in the shunt calibrating. Due to the relatively high microstrain (με) simulated by the 2 kΩ resistor (106,382.979 με), a 75 kΩ precision resistor was also used to perform several shunt calibrations in the field. The calculated gage factor using the 75 kΩ resistor was within one or two thousandths of the factor calculated using the 2 kΩ resistor. This showed the gage factors calculated using the 2 kΩ resistor were accurate.

Using Equation 10, the strain gage output in mV could be converted to strain:

$$\epsilon = \frac{4V_r}{GF(1+2V_r)} \quad (10)$$

where ε = strain (multiply ε by 106 to convert to units of microstrain), $V_r = V_{out} / V_{in}$, V_{out} = voltage output from the strain gage and wheat stone bridge, V_{in} = voltage input into wheat stone bridge and strain gage, and GF = gage factor. The units of strain the data was converted into was με. The reason the strain was reported in units of με was due to the strain levels experienced in the geosynthetics being quite small. Reporting the strain in με made the results easier to work with.

The initial mV output of each strain gage varied widely. To normalize all of the data, the change in mV's from the original steady state of each strain gage at the beginning of the test was used to determine the strain being generated by the loading cycles during the APLTs and during the TLTs. All comparisons, unless otherwise noted, are made using the change in strain from the original steady state.

The change in mV readings converted to με showed only the strain being experienced directly by the strain gage. This strain did not necessarily represent the strain being experienced globally by the geosynthetic, in part, due to the stiffening effect of bonding the strain gage to the geosynthetic, and the stiffening effect of the environmental protection covering the individual strain gages. To correlate the strain experienced by the strain gage to the global strain in the geosynthetic, strain recorded by the strain gage was multiplied by a global strain factor. This factor was determined through laboratory testing performed by TRI Environmental (see supplemental material "Global Strain Calibration Report"). A global strain factor was determined in the machine direction and cross-machine direction for the BX1200 and the GT-180. Using both the gage factor and the global strain factor, the mV output of the strain gages was converted into actual strain experienced by the geosynthetics in units of micro strain.

To make comparison between sections easier, the strain gages at each location were given a designation. Starting with the strain gages in the array located at the UTBC-GB interface, the strain gages were labeled SG1-SG10 in S1-3, and SG1-SG15 in S4. SG1 was the first transverse gage farthest from the edge of pavement (EOP). SG2 was the center transverse gage, SG3 was the transverse gage closest to the EOP, SG4 was the longitudinal gage farthest up station, and SG5 was the strain gage farthest down station (Figure 3.25).

The numbering scheme continued at the GB-subgrade interface, with strain gages SG6-10 in the same ascending order and orientation. In S4, where both BX1200 and GT-180 were placed at the subgrade-GB interface, SG6-10 were located on the geogrid above the geotextile, and then SG11-15 was located on the geotextile.

The second test performed was the truck load test (TLT). A three-axle dump truck was fully loaded with soil, and an 11.23-inch diameter half-inch steel plate was placed centered over each strain gage array. The dump truck was then driven over the plate, and the outside wheel of the passenger middle axle was centered on the plate. The same measurements of temperature, moisture, and strain taken in the APLTs were taken in the TLTs. One set of the dual wheels on the truck's center axle was allowed to dwell centered on the plate for approximately 10 minutes while measurements of strain and water content were taken. The purpose of these tests was to measure train in the geosynthetics at different depths under a static heavy load.

After reviewing the data from the first TLTs, it was determined that better results might be obtained by using a large loading plate. The purpose of this change in loading is discussed further in the results section. The TLTs were performed again using a one-inch-thick steel plate with a diameter of 34 inches. The test procedure was the same as for the first TLTs, except the dwell period was increased to 15 minutes.

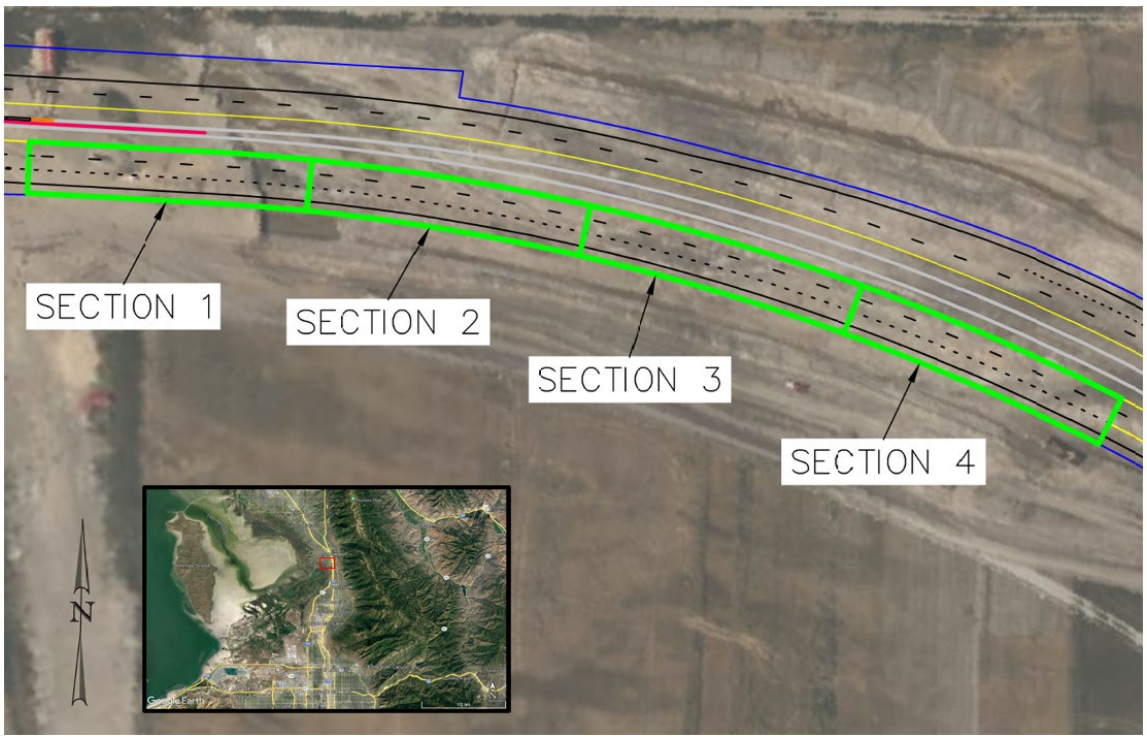

Figure 3.1 A map of the location of the test sections

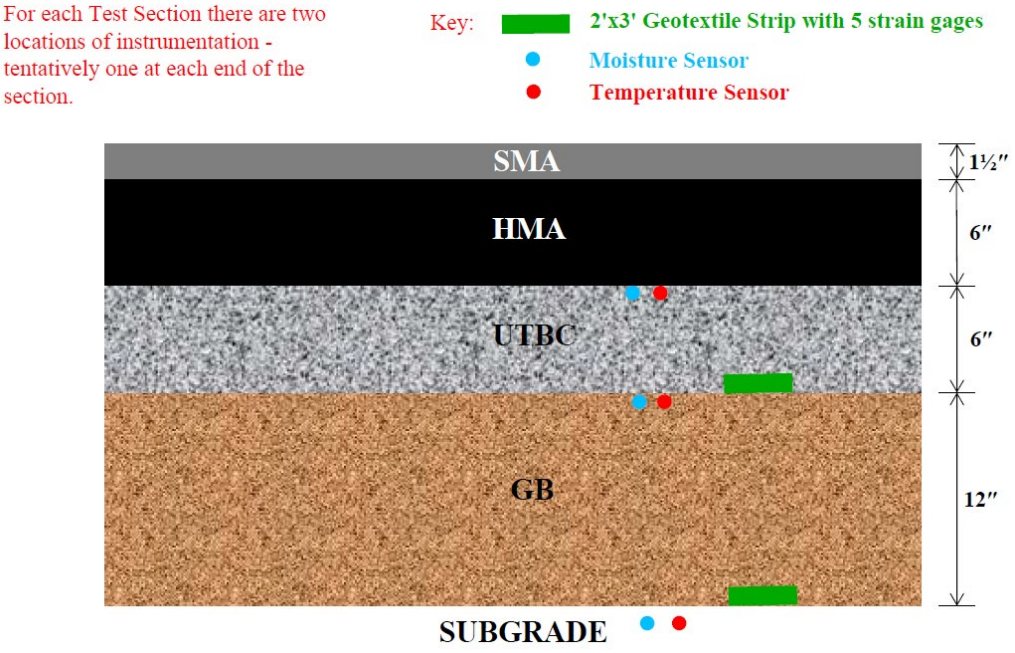

Figure 3.2 Cross section of pavement system for test section #1 (control)

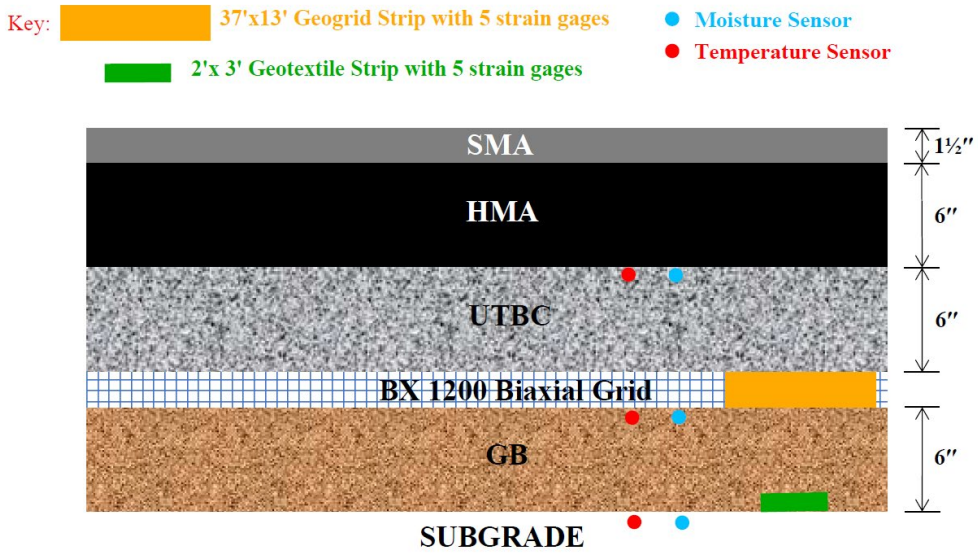

Test Section #2
(Biaxial Geogrid with No Separator)

Figure 3.3 Cross section of pavement system for test section #2

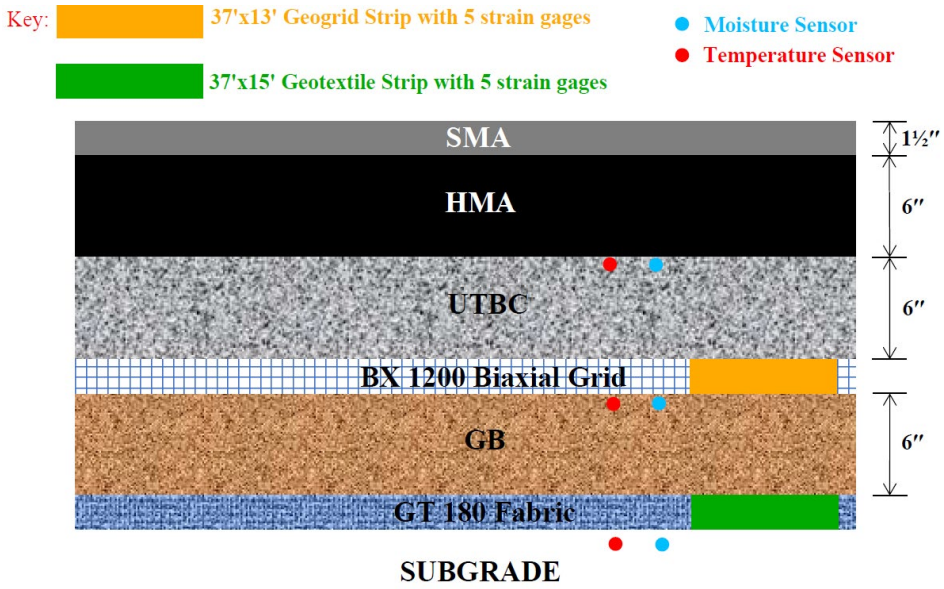

Test Section #3
(Biaxial Geogrid with Geotextile Separator)

Figure 3.4 Cross section of pavement system for test section #3

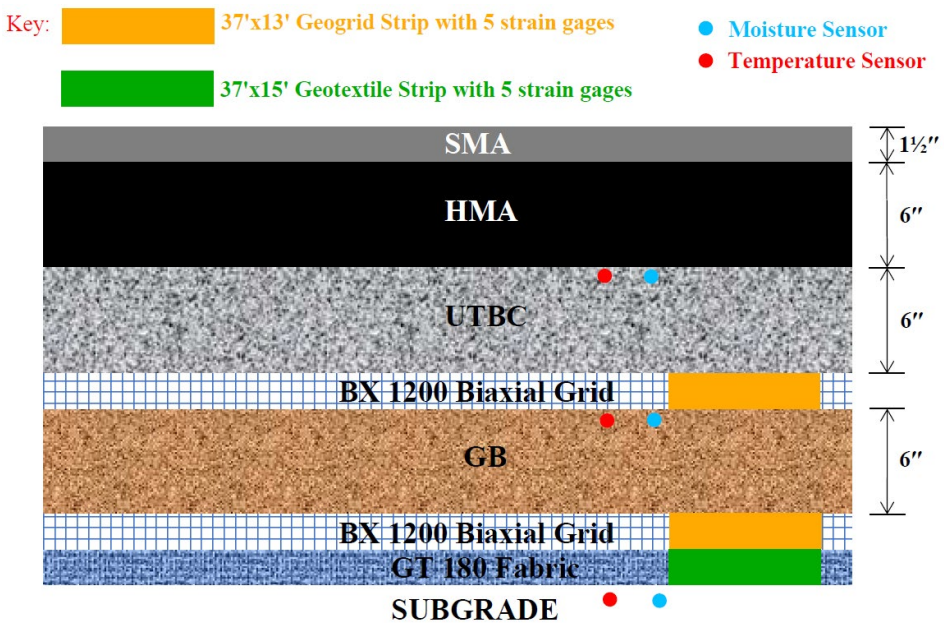

Figure 3.5 Cross section of pavement system for test section #4

Figure 3.6 Research section facing west from approximately test section 3

Figure 3.7 GT-180 and BX1200 geotextile and geogrid

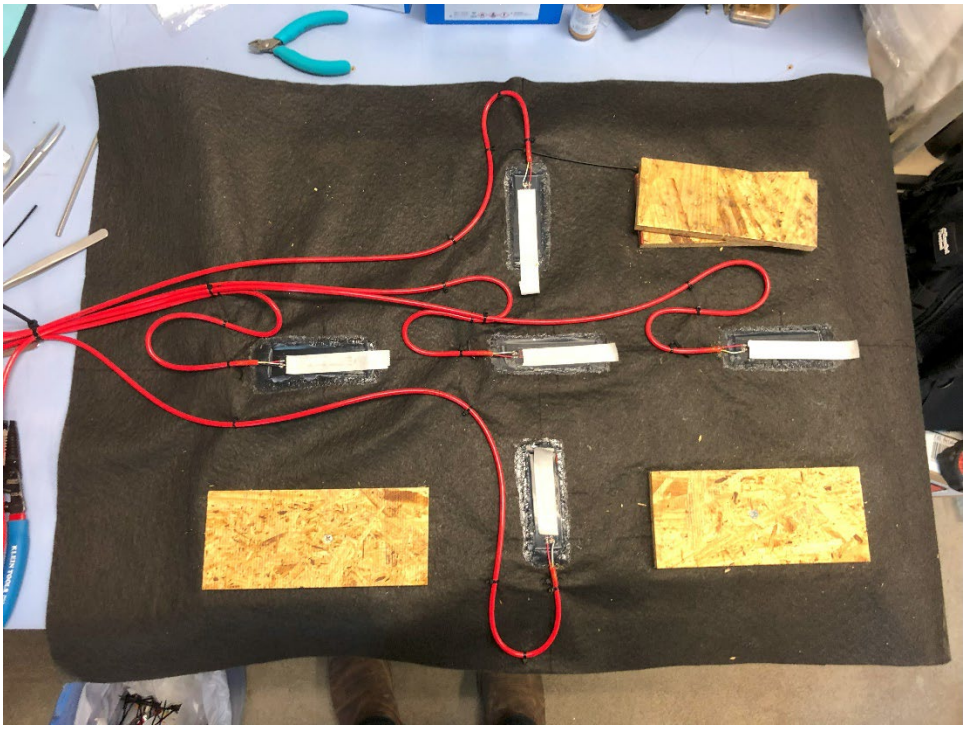

Figure 3.8 Two-foot by three-foot coupon of GT-180 with strain gages attached

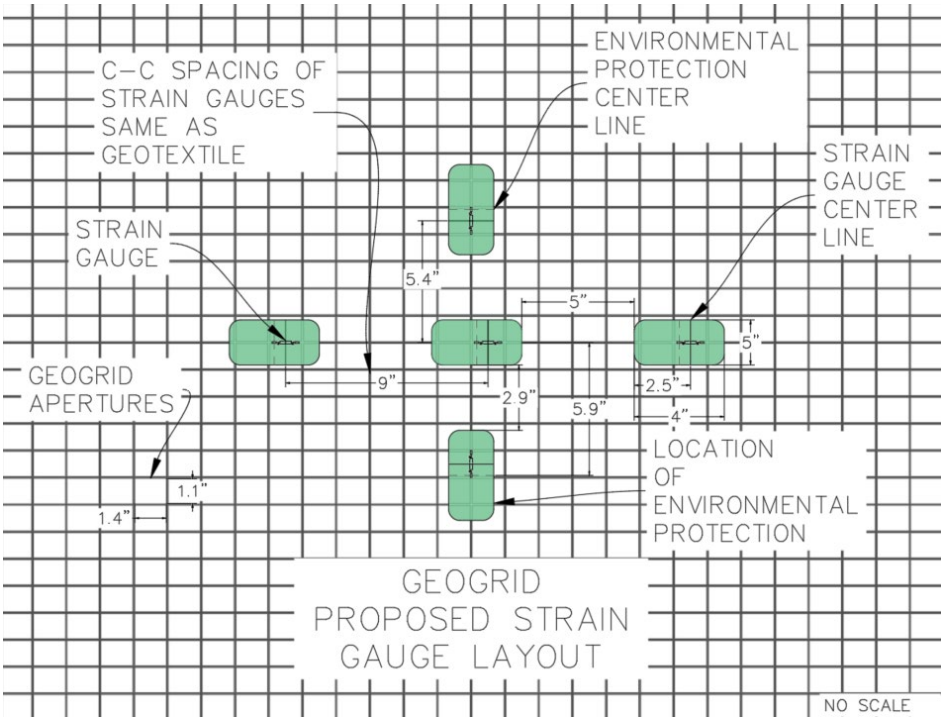

Figure 3.9 A schematic of the layout of strain gages on the BX1200 geogrid

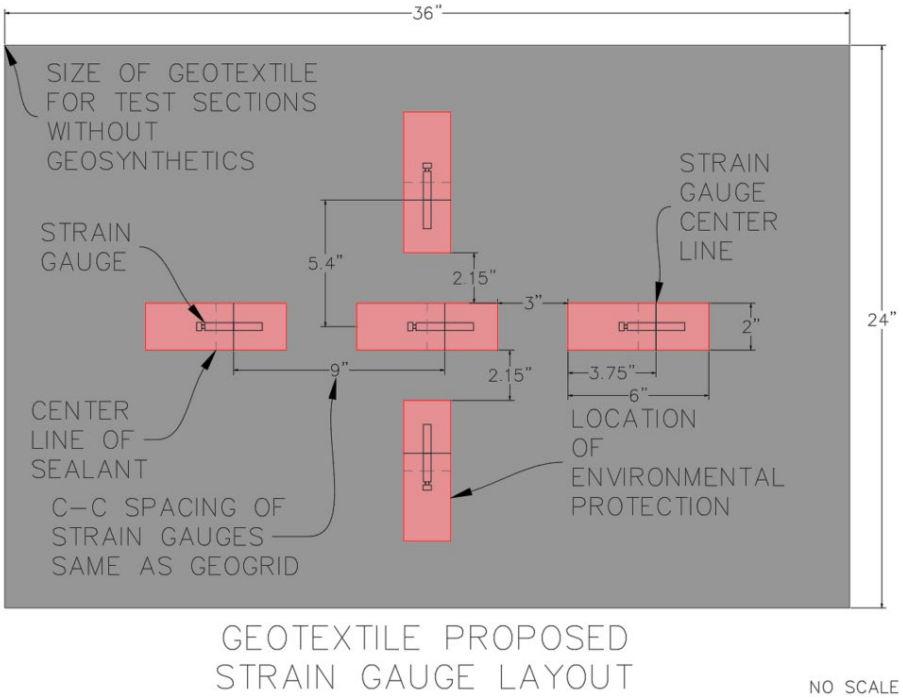

Figure 3.10 A schematic of the layout of strain gages on the GT-180 geotextile

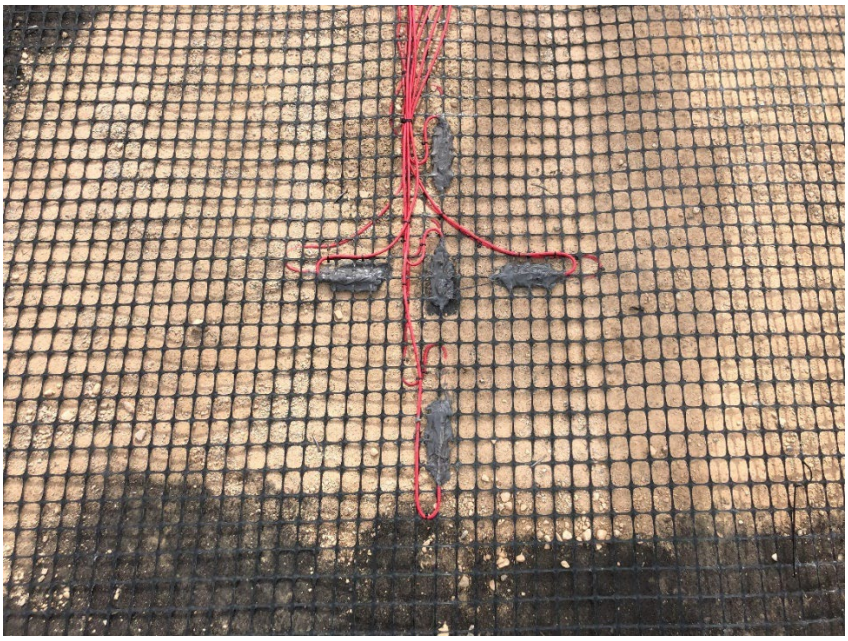

Figure 3.11 Strain gage array installed on geogrid in the field

Figure 3.12 Geotextile with strain gages installed in the field

Figure 3.13 Photo of DCP testing being performed on the original subgrade

Figure 3.14 Photo of moisture and temperature sensor installed in the subgrade

Figure 3.15 One of the 37-foot instrumented sections of geotextile installed on the subgrade

Figure 3.16 Photo of geogrid with strain gages installed on top of the geotextile in S4 as part of the geocomposite

Figure 3.17 Photo of geotextile installed on the subgrade with folds and uneven overlap

Figure 3.18 Photo showing geogrid being folded during installation

Figure 3.19 Photo showing folds in geogrid during installation

Figure 3.20 Trenches dug for the installation of the moisture and temperature sensor two feet and three feet down station from the strain gage array at location 2A

Figure 3.21 Nuclear density testing being performed and Geoprobe 3230DT onsite to perform CPT soundings

Figure 3.22 Ingios trailer mounted mobile APLT system

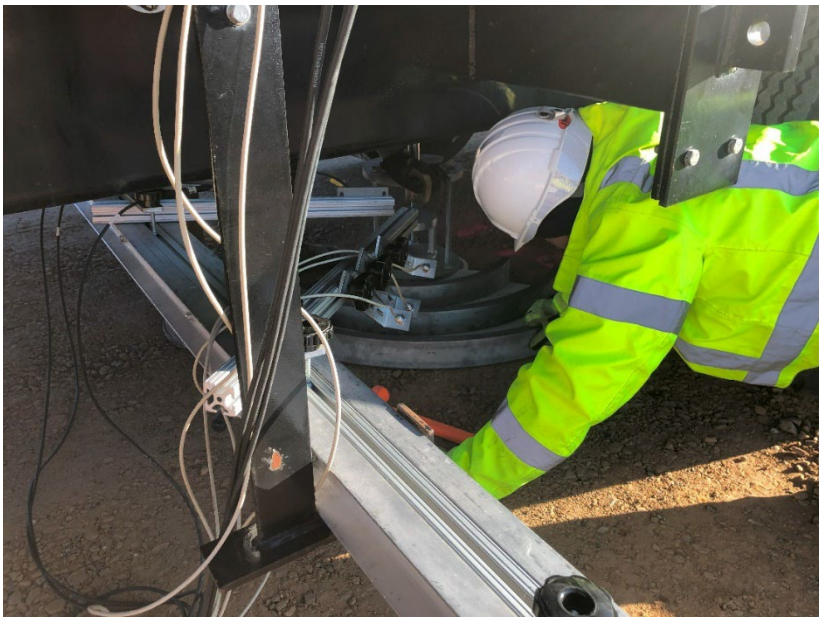

Figure 3.23 The loading plate for APLT being aligned with three radial bands used to measure deflection beside the loading plate

Figure 3.24 Sand used to ensure contact with the UTBC at the location of APLT after completion

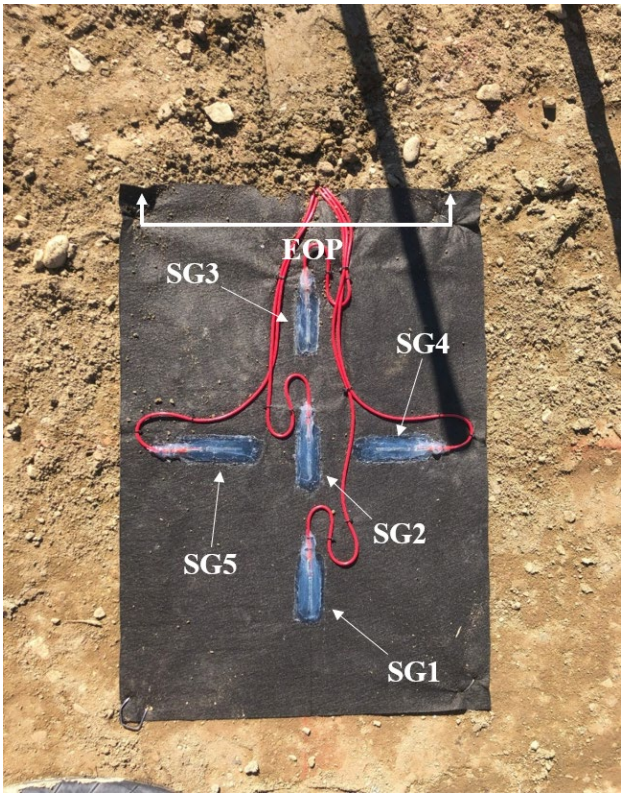

Figure 3.25 Diagram showing the pattern of naming for strain gages at the UTBC-GB interface

Figure 3.26 Photograph showing the CR9000x connected to a control box to collect strain gage data during an APLT test

Figure 3.27 A precision resistor used for shunt calibrations

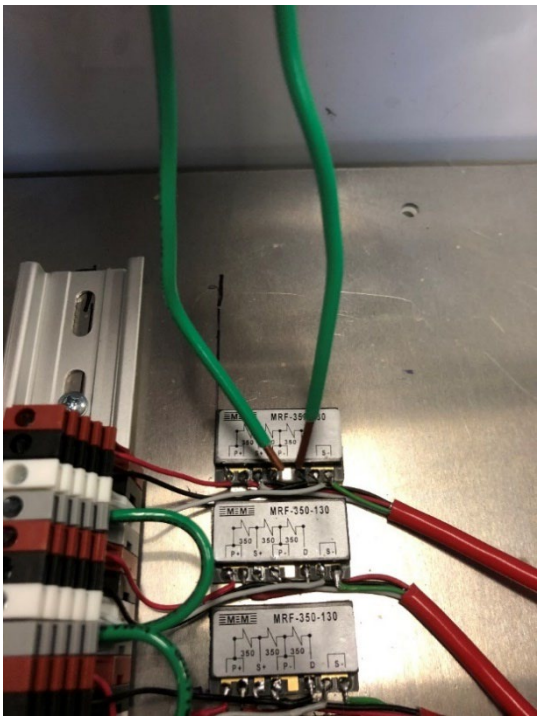

Figure 3.28 Shunt calibration being performed on wheat stone bridge in strain gage control box

Table 3.1 Test section information

A table showing test section stationing, instrumentation, pavement system layers' thicknesses, and geosynthetics.

Test Section	Stationing	Instrument Array A Stationing	Instrument Array B Stationing	GB Thickness (in)	UTBC Thickness (in)	Geosynthetic Reinforcement at Subgrade-GB Interface	Geosynthetic Reinforcement at GB-UTBC Interface
1	11015+68.5 to 11014+12.5	11015+00	11014+31	12	6	-	-
2	11014+12.5 to 11011+70	11013+94	11011+88.4	6	6	-	BX1200 geogrid
3	11011+70 to 11009+27.5	11011+51.5	11009+46	6	6	GT-180 geotextile	BX1200 geogrid
4	11009+27.5 to 11006+85	11009+09	11007+03.51	6	6	GT-180 geotextile and BX1200 geogrid	BX1200 geogrid

4. RESULTS AND ANALYSIS

4.1 Subgrade Properties

The subgrade was characterized using several different sets of data. First, a geological map of the area was consulted. According to the Farmington Quadrangle published by the Utah Geological Survey in 2018, the test location is located within an "Older liquefaction-induced landslide deposit." The deposit is from the lower Holocene to upper Pleistocene eras, and the soil is a composition of silt, fine sand, and some gravel. From the map data, it is less than 70 feet deep (Jensen and Hill 2018).

The second data set used to characterize the subgrade was from the DCP testing. The DCP data was correlated to CBR using the correlation developed by Webster, Brown and Porter (Webster et al. 1994). This correlation can also be found referenced in ASTM D6951/D6951M-18. An attempt was made to determine soil layers based on the CBR values of the soil based off their elevation. 75 CBR tests were performed on the original subgrade. These tests went to a minimum depth of three feet, with some of the tests being performed to a depth of four feet. The original subgrade CBR data is shown in Figure 4.1. The CBR data for the original subgrade calculated from the DCP data shows the subgrade strength trends downward from the surface (CBR average of 16.75) to a depth of about 2.7 feet (CBR average of 6.96). At that point, the CBR average increases to 27.44 at a depth of about 5.5 feet. The average CBR again trends downward for the next three feet to a minimum recorded value of 11 at a depth of about 8.6 feet.

Before the first installation of geosynthetics at the subgrade-GB interface, DCP testing was performed again because the contractor had reworked some of the original subgrade. The CBR values from the final subgrade are shown in Figure 4.2. A comparison of the two datasets is shown in Figure 4.3. The comparison of CBR values from the original and final subgrade at comparable elevations shows the final subgrade had an average CBR value greater than the original subgrade by 8.4 at an elevation of about 4223.4. The average difference trends lower down to a depth of about 2.5 feet (difference in average CBR of 1.0). At this point, the average CBR of the final subgrade trends higher than the original subgrade to a maximum difference of 24.9 in average CBR values at a depth of about 3 feet. The average CBR for the final subgrade then trends down below the average CBR of the original subgrade by a maximum of 16.7 at a depth of about 5.7 feet. Table 4.1 shows the final subgrade average CBR values by section and for each location.

It is unlikely the contractor reworked the subgrade down to a depth of 5.7 feet. Due to the relatively small difference in average CBR values in the top 2.5 feet of the two datasets compared to the difference in CBR values at a depth of over five feet, the average CBR value of the subgrade before and after being reworked by the contractor is close to the CBR value of the original subgrade. One notable difference is that in the top 2.5 feet of the final subgrade, the average CBR values have a greater spread than those of the original subgrade. This could be due to the disturbance caused by the contractor. It may also be because more data points were available for the final subgrade than the original subgrade, and this spread in average values may not be considerably different than those for the original subgrade.

DCP tests were also performed by Ingios within three feet of the instrumented locations immediately after the APLTs were completed. These DCP tests were completed again the following spring by the research team. Table 4.1 shows the average CBR values for the subgrade at each of these locations. Besides an outlier in the data at location 1B in the Ingios data, the average CBR values for the original subgrade and the final subgrade are within five CBR percentage points of each other. Given the variability of DCP testing, these values are similar.

Utilizing Equation 5, tip resistance data from the CPT soundings performed by AGEC were correlated to CBR values. The correlation between the CPT CBR values and the DCP CBR values was reasonable, as

shown in Figure 4.4. Comparing the CBR values from the CPT and DCP data shows another interesting trend. The values for the DCP correlated CBR percentages tend to increase with depth in the subgrade when compared to the CPT correlated CBR percentages. One reason for this could be that as the DCP penetrates deeper into the ground, it is more easily pushed off course by aggregate and hard layers of soil than the CPT. This was experienced by the researchers, especially when the extension was attached to the DCP to reach depths of 4.5 feet. In many cases, the DCP would become more difficult to keep at a vertical orientation as the rod went deeper into the soil. Because of the horizontal travel of the DCP at depth, the DCP rod would bend, and greater horizontal forces would exist between the rod and the soil on the walls of the hole. It is possible that an increase in friction between the DCP rod and the soil caused an artificial increase in the calculated CBR of the subgrade. An example of this difference in CBR with depth between the DCP-CBR and CPT-CBR can be seen in the data from location 2A (Figure 4.5). When comparing the DCP correlated CBR of the subgrade to the CPT correlated CBR of the subgrade, the CPT predicts a subgrade average CBR at the location of instrumentation of 8.4, 8.3 percentage points below the DCP correlated subgrade average CBR at the location of instrumentation (Table 4.1). The CPT CBR values also have the lowest standard deviation of any of the values in Table 4.1 (standard deviation of 2.5). This suggests the CPT CBR correlation may give more accurate results than the DCP CBR correlation. Plots showing the results of the CBR correlations between the CPT data and the DCP data are found the appendix.

Based on the Normalized Soil Behavior Type (Roberston, 1990), CPT data from the site showed the subgrade was composed of interbedded layers of soil that behaved like silty sand and sandy silt, clay and silty clay, and clay to silty clay. The upper layer directly underneath the GB behaved like silty sand and sandy silt in every sounding. Full CPT data can be found in the supplemental material entitled “CPT Data All Cones by Absolute Elevation” from Applied Geotech in Sandy Utah. Comparisons of the CPT logs were made for each section, and between CPT logs for instrument locations that were adjacent to each other (1B and 2A, 2B and 3A, and 3B and 4A).

A simplified comparison of the soil behavioral type from the CPT data for the control section (S1) shows the top layer of the subgrade behaved like a silty sand and sandy silt layer from an elevation of approximately 4,220 to 4,218.5 feet. The layer below it behaved like a clayey silt to silty clay from an elevation of approximately 4,218.5 feet to the bottom of the CPT soundings at A and C, with small layers behaving like silty sand and sandy silt.

Instrument locations for 1B and 2A showed similar subgrade characteristics. Both had a layer that behaved like silty sand and sandy silt from approximately 4,220 to 4,218.5 feet. At this point, the subgrade at 2A differed from the subgrade at 1B in that it behaved like a clay to silty clay instead of like a clayey silt to silty clay.

S2’s subgrade behavior differed from location to location, but, in general, the subgrade behaved like a silty sand to sandy silt from 4,220.5 feet to 4,219.4 feet. The 2C location behaved like a clayey silt to silty clay below this elevation while the 2B location behaved like a clayey silt to silty clay to a depth of 4,218.5 feet. It then behaved like a clayey silt to silty clay for the duration of the sounding.

Sounding 2B and 3A differed in that 3A behaved like a clayey silt to silty clay from 4,220.5 feet to the bottom of the sounding at 4,218 feet. Sounding 2B as described before had a layer from 4,219.8 feet to 4,218.5 feet.

Soundings at 3A and 3C showed the most similar soil behavior of all the test locations, with the subgrade behaving like clayey silt to silty clay from an elevation of 4,220.5 feet to the end of each sounding (4,218 feet and 4,218.8 feet). The subgrade soil behavior at 3B behaved differently than the other two locations in S3 in that it showed more variance in the soil behavior. 3B’s soil behaved like silty sand to sandy silt

from 4,221.5 feet to 4,219.4 feet, with a thin layer of soil behaving like clean sand to silty sand from 4,220.1 feet to 4,220 feet. From 4219.4 feet to 4218.1 feet, it behaved like clayey silt to silty clay, and then like clay to silty clay from 4218.1 feet to 4,217.2 feet.

The subgrade soil behavior at locations 3B and 4A both behaved like clayey silt to silty clay and silty sand to sandy silt, but the elevations of these soil behaviors did not correlate to a high degree. S4's two soundings show a soil behavior type of predominantly clayey silty to silty clay, with the sounding at 4A showing layers of soil behaving like silty sand to sandy silt from 4,219.7 feet to 4,219.3 feet and then again from 4,218.9 feet to 4,218.6 feet.

Most soundings showed the subgrade soil behaves like clayey silt to silty clay with thinner layers of soil behaving like silty sand to sandy silt. The boundaries of most of these layers do not perfectly coincide with each other. The average CBR value for the subgrade at the location of instrumentation was 8.4, based on the CPT CBR correlation. This CBR value would mean the research section is in a location with a soft subgrade.

4.2 Granular Borrow Properties

Five five-gallon buckets of GB were taken during the construction of the test sections. Two gradations were performed on the GB material according to ASTM D6913/D6913M-7. The two gradations were similar, and the average of the two is shown in Figure 4.6. DCP testing was performed on the GB after it was placed and compacted. The calculated average CBR values for the instrument locations is shown in Table 4.1. The average CBR value for the GB layer at the instrument locations was 23.1 with a standard deviation of 5.2. The maximum CBR value at the instrument locations was at 1A with a CBR of 32.1, and the lowest was at 4B (CBR of 16.6). The thickness of the GB layer determined from the survey data in sections 2-4 was 8.2 inches with a standard deviation of 0.5 inches. The thickness of the GB layer in the control section at 1A and 1B was 14.0 inches and 13.9 inches. The thickness of the GB in the control section at the instrument locations was within two inches of the design value of 12 inches. In S2-S4, the average GB thickness at the instrument locations was 2.2 inches greater than the design value of six inches. The maximum difference was at location 4A with a thickness of nine inches.

The GB CBR was calculated again from the DCPs performed by Ingios and by the research team in April of 2023, as well as from the CPT soundings. These DCP tests were performed after the UTBC had been placed and compacted on top of the GB. The average CBR values at the instrument locations from the CPT and DCP were within one standard deviation from each other, being 43.7 and 54.8 respectively (Table 4.1). On average, the CBR values for the GB from before the placement of the UTBC to after increased by 31.7 percentage points to an average of 54.8. This increase in CBR could possibly be attributed to the compactive effort used on the UTBC transferring to the GB, and to the increased confining stress from the UTBC placed and compacted on top of it.

It is interesting to note that when compared to the GB layer, the CBR values of the subgrade did not change as much when soil was placed and compacted on top of it. The CBR at the instrument locations increased on average by a maximum of 1.1 percentage points when the data from Ingios and the Spring 2023 data were compared to the final subgrade data when outliers from the Ingios data at locations 1B and 2B were replaced with data points from the Spring 2023 data (Table 4.1).

4.3 UTBC Properties

Three gradations were performed on three different samples of the UTBC material according to ASTM D6913/D6913M-17. The results of each gradation were not as uniform as those from the gradations for the GB. The average of the three tests is shown in Figure 4.7.

The DCP-correlated CBR values for the UTBC layer at the locations of instrumentation are also shown in Table 4.1. The average value for the CBR of the UTBC at these locations was 27.2 with a standard deviation of 11.2. The maximum CBR value from this data was 47.9, and the minimum was 14.1. The CPT correlated average CBR values at the instrument locations was 21.6 with a standard deviation of 6.6 (Table 4.1). In most cases, the CPT-correlated CBR values were lower than the DCP-correlated CBR values and with a smaller standard deviation. The average thickness of the UTBC at the location of the instrumentation was 4.9 inches with a standard deviation of 1.04 inches. The UTBC thickness at every instrument location is shown in Table 4.1.

4.4 APLT Results

4.4.1 M_r, Permanent Deformation, and CBR Comparisons

4.4.1.1 Resilient Modulus Comparisons

The Ingios results from the APLTs performed at the locations of instrumentation can be found in Table 4.2. These are the results for the 1,550 cycle test at step 6 of the test at a surface stress of approximately 40 psi. The location with the greatest $M_{r\text{-}comp}$ value at this step was 3B, followed by 2B, then 1B, and then 1A, 3A, 4A, 4B, and 2A in descending order magnitude (Table 4.3). S3 was reinforced with a layer of BX1200 geogrid at the UTBC-GB interface and had a separator of GT180 geotextile at the subgrade-GB interface. It had less reinforcement than S4, which performed second to last, with only 2B performing worse. A and B in S2 performed differently when considering $M_{r\text{-}comp}$. 2B had the second highest $M_{r\text{-}comp}$ value, while 2A had the lowest $M_{r\text{-}comp}$ value. All the sections had different values for $M_{r\text{-}comp}$, when comparing their A and B locations. The smallest difference in $M_{r\text{-}comp}$ between A and B was in S1, with a difference of 526 psi. The greatest difference was in S2 (6,691 psi). The average difference between A and B was 3,213 psi.

The results for $M_{r\text{-}UTBC}$ were similar to the results for $M_{r\text{-}comp}$. The location with the greatest $M_{r\text{-}UTBC}$ was 3B, followed in descending order by 4A, 2B, 1B, 1A, 2A, 4B, and 3A. The section with the least difference between $M_{r\text{-}UTBC}$ values from A to B was S1 (5,037 psi), the same as for $M_{r\text{-}comp}$. The greatest difference between A and B was found in S3 (18,450 psi). The average difference in $M_{r\text{-}UTBC}$ values between locations A and B was 11,676 psi.

The difference in $M_{r\text{-Top of GB}}$ values between locations A and B was 3,152 psi on average. The smallest difference between A and B was in S3 (650 psi), and the greatest was in S2 (6,325 psi). Out of all the test sections, S1 showed the greatest continuity in M_r values between locations A and B.

At the C test locations, Ingios performed a different type of APLT. This test (Test B) used the same size of loading plate (12-inches in diameter), but different loading parameters, than the tests performed at locations A and B. The test loaded the area with 5,000 cycles in a random pattern at 10 different stress levels from 5 psi to 50 psi. This differed from the APLT loading parameters at locations A and B in that the test performed at these two locations in each section had 1,550 cycles that stepped up in stress from 5 to 40 psi cyclic loads (Test A). The $M_{r\text{-}comp}$ values reported in Table 4.4 are predicted values at a 40-psi cyclic stress after 5,000 cycles. This $M_{r\text{-}comp}$ value is different from the $M_{r\text{-}comp}$ value from Test A, but statistically significant comparisons were still able to be made using the predicted $M_{r\text{-}comp}$ values from Test B and the $M_{r\text{-}comp}$ values from Test A. At test location C, the section that performed the best was 1C, followed by 2C, 3C, and 4C in descending order of $M_{r\text{-}comp}$ values. The $M_{r\text{-}comp}$ value for location 1C was the greatest calculated $M_{r\text{-}comp}$ value out of all the tests, including C, A and B. 2C had the second highest $M_{r\text{-}comp}$ value, and 3C was higher than every $M_{r\text{-}comp}$ value from locations A and B, except for 3B. The $M_{r\text{-}comp}$ value for 4C was greater than only the $M_{r\text{-}comp}$ values for test locations 4B and 2A. In general, the $M_{r\text{-}comp}$ values for the tests performed at location C were higher than the values for the tests performed at

locations A and B. Location 1C, which had the highest $M_{r\text{-}comp}$ value, also had the greatest Ingios DCP-CBR value for the GB layer (Table 4.2). Due to the GB layer being more than twice as thick and better compacted, 1C was able to outperform all other sections when it came to $M_{r\text{-}comp}$ (Table 4.1).

When analyzing data at the end of the test, a correlation between permanent deformation and M_r values was seen. Typically, as M_r increased, permanent deformation decreased (Table 4.2). In the case of $M_{r\text{-}comp}$ and $M_{r\text{-Top of GB}}$, the two locations with the lowest M_r values also had the greatest amount of permanent deformation. The location with the highest $M_{r\text{-}comp}$ and $M_{r\text{-UTBC}}$ values (3B) had the second-to-least amount of settlement. Only 0.001 more inches of settlement was recorded at 3B than at the location with the least amount of settlement (2B), so the location with the highest $M_{r\text{-}comp}$ performed almost as well as the location that had the least permanent deformation. A multivariable linear regression was used to determine how well each of the $M_{r\text{-}comp}$ values could be used to predict the amount of permanent deformation experienced at the corresponding location. The regression produced an R squared value of 0.614 (Table 4.5), but none of the P-values corresponding to $M_{r\text{-}comp}$, $M_{r\text{-UTBC}}$, or $M_{r\text{-Top of GB}}$ were too low (0.328, 0.989, and 0.507 respectively). The regression analysis, however, did show some correlation between the M_r values and the permanent settlement measured.

When comparing the $M_{r\text{-}comp}$ values of each instrumented location in regard to the level of geosynthetic reinforcement, the greatest amount of geosynthetic reinforcement did not correspond to higher $M_{r\text{-}comp}$ values. S4 had two layers of BX1200 geogrid and one layer of GT-180 geotextile, but 4A and 4B had the second and third lowest $M_{r\text{-}comp}$. S3, which had the second greatest amount of geosynthetic reinforcement with a layer of BX1200 geogrid and a layer of GT-180 geotextile, had the highest $M_{r\text{-}comp}$ (3B) and the fourth lowest $M_{r\text{-}comp}$ (3A). S2 had the second highest $M_{r\text{-}comp}$ (2B) and the lowest $M_{r\text{-}comp}$ (2A). The control section (S1) had a higher $M_{r\text{-}comp}$ than all but two of the reinforced locations (3B and 2B). There did not appear to be a correlation between the level of geosynthetic reinforcement and the $M_{r\text{-}comp}$ values for the test sections.

4.4.1.2 CBR Comparisons

The parameters that correlated best with the permanent deformation recorded during the APLT testing were the Ingios CBR values for the soil layers in the pavement system. The Ingios DCP testing was performed in conjunction with the APLTs; therefore, making the Ingios DCP-CBR correlation closest in time to the completion of the APLTs. When the Spring 2023 DCP testing and CPT soundings were performed the following spring after the APLTs, it was apparent that some disturbance at the surface of the UTBC had occurred due to traffic from construction activities in the vicinity of the research area. Multi-variable linear regression between both the Spring 2023 DCP-CBR values and the CPT-CBR correlated values to predict permanent deformation yielded no statistically significant relationships. A multi-variable regression was performed using the Ingios DCP-CBR average for the UTBC layer, UTBC thickness at instrument locations, the Ingios DCP-CBR average for the GB layer, GB thickness at instrument locations, and the Ingios DCP-CBR average for the subgrade as independent variables to predict the dependent variable of permanent deformation. The R squared value for the correlation was 0.621 (Table 4.6). The P-values for UTBC and GB Avg. CBR correlated to the Ingios DCPs were 0.030 and 0.068, respectively. Both P-values showed these two parameters either were statistically significant or were close to being so.

Another multi-variable linear regression was performed using only the Ingios DCP-CBR average values for the UTBC and GB to predict permanent deformation. The R squared value was lower than with all the variables used in the previous regression, but the P-value for the UTBC Avg. CBR (Ingios Data) was even lower (0.021). The P-value for the GB Avg. CBR (Ingios Data) was slightly higher than before (0.066). This analysis showed again that the UTBC Avg. CBR (Ingios Data) was statistically significant, and the GB Avg. CBR (Ingios Data) was almost below the significant threshold when an α value of 0.05

was considered. The results of this multi-variable linear regression are found in Table 4.7 and graphically in Figure 4.8.

Multi-variable linear regression was also used to determine the relationship between the Ingios CBR values for the UTBC, GB, subgrade, and the $M_{r\text{-}comp}$ values. When the Ingios DCP-CBR average values from each test location were used to predict $M_{r\text{-}comp}$, the R squared value was 0.605. The lowest P-value for the dependent variables was for the GB Avg. CBR (Ingios Data), which was 0.087 (Table 4.8). A second regression analysis was conducted using just the Ingios UTBC and GB CBR values (Table 4.9). The R squared value for this regression was lower (0.456), but the P-value for the Ingios GB CBR value was higher (0.052). This relationship was weaker than the relationship between UTBC Avg. CBR (Ingios Data) and permanent deformation, but there is possibly statistical evidence for this relationship as well. Statistical analysis did not yield any strong correlations between the soil layer CBR values and $M_{r\text{-}UTBC}$ or $M_{r\text{-}Top\ of\ GB}$.

4.4.2 M_r, Permanent Deformation, and Geosynthetic Strain Analysis

4.4.2.1 Strain Gage Results

Strain data was collected throughout the duration of each of the M_r tests performed at A and B locations. In the control section, strain data was collected using two 2 feet by 3 feet coupons of GT-180 geotextile with an array of five strain gages attached. One of these arrays was located at the UTBC-GB interface, and one was located at the GB-subgrade interface. A coupon of GT-180 with an array of strain gages was also used to collect strain data at the GB-subgrade interface in S2. Strain gages were attached to the geogrid or geotextile reinforcement at the UTBC-GB and GB-subgrade interfaces in all other instances in S2-S4.

Several factors complicated making direct comparisons of strain gage information between sections and A and B locations. The first was that some of the strain gages failed due to the rigors of construction. 22 of the 90 strain gages were damaged to the point that they would not report mV readings. Of the remaining strain gages, seven began to give erratic readings during the performance of the APLTs.

Another complicating factor was that 25 of the 61 functioning strain gages recorded negative changes in strain (compression). With the strain gages oriented in a cross, it was anticipated that the three transverse gages would read similar strain to each other, and the two longitudinal gages would also read similar strain to each other. The actual result was that in every APLT test, the operating center strain gages would read positive changes in strain (tension), and the surrounding strain gages would typically read less strain. Much of the time, they would record a negative change in strain (compression). Of the readings given by the outside strain gages, 34.7% were negative. The greatest frequency of negative readings came from SG1, SG3 and SG4. These were the outside strain gages located at the UTBC-GB interface. these strain gages reported compression. The next strain gage with the highest frequency of negative readings was SG8 (38%).

Due to these factors, 36 of the 90 original strain gages were working and showing a tensile change in strain. It was anticipated that the best comparisons of tensile strain in the geosynthetics between test sections would be drawn between SG2, SG7, and SG12. Overall, 25% of SG2 gages failed, and 38% of SG7 gages failed. It was anticipated that the best comparisons of strain in between test sections would be between locations A and B of adjacent test sections, since the subgrade conditions and CBR of two locations 37 feet away from each other were more likely to be similar than two locations 242.5 feet apart. SG2 failed at locations 3A and 4B and had high enough readings at location 1A that it was considered an outlier. This eliminated the comparison between SG2 at locations 3A and 2B. SG7 failed at locations 2A, 2B, and 4A. This eliminated all comparisons of adjacent test locations from different test sections for

SG7. In the end, the effect of the difference in CBR values in the UTBC and GB would have made these anticipated comparisons difficult.

An attempt was made to determine why compression was being recorded in the outside strain gages during the APLTs. A multi-variable linear regression was performed using the Ingios DCP-CBR average values for the UTBC and GB layers as dependent variables to predict the percentage of strain gage readings that recorded compression in each of the instrumented locations. The R squared value was relatively low (0.431), but not insignificant, considering all the variables that cannot be controlled in geotechnical engineering. The p-values for the CBR of the UTBC and the GB were 0.117 and 0.591 respectively. A second linear regression was performed using only the Ingios DCP-CBR average values for the UTBC. The R squared value was slightly lower (0.393), but the P-value for the UTBC CBR was higher (0.096, as seen in Table 4.10). The regression showed there was possibly a significant correlation between the UTBC CBR values and the percentage of strain gages in a section that recorded compression in the outside strain gages. The relationship suggested was that as UTBC CBR increased, the number of strain gages that read negative decreased.

4.4.2.2 Analysis Using Tensile Change in Strain Data

Despite these setbacks, significant correlations were still found in the data. To make comparisons in the APLT data, several terms were developed to describe the strain experienced in the geosynthetics. During the APLT loading, loading occurred at predetermined stress levels. The load was applied in load/unload cycles which lasted 0.2 seconds, followed by a 0.8 second dwell time in between cycles. During these load/unload cycles, the geosynthetic would strain under the load, and then decrease in strain during and after the unload cycle. For each load cycle, the total change in strain ($\Delta\varepsilon_t$) was determined to be the difference between the maximum strain registered during the load/unload cycle and the last permanent strain from the end of the previous dwell period. The elastic change in strain ($\Delta\varepsilon_e$) was the difference between the maximum change in strain and the permanent change in strain at the end of the unload cycle. The plastic change in strain ($\Delta\varepsilon_p$) was the difference between the last permanent change in strain before the load cycle and the permanent change in strain at the end of the unload cycle. These terms are shown on a graph representing the strain response in the geosynthetic during an APLT (Figure 4.9).

Due to the number of strain gages that did not return data or return tensile change in strain values, the data was analyzed in several ways to make comparisons between the test sections. The first way was to use the outside strain gages that recorded a tensile change in strain for each test section and average their values. This average was used to compare the performance between the test sections. This comparison was performed with the permanent change in strain at the end of the 30 psi loading cycles, since it had a more complete data set than the 40-psi loading cycle due to troubles with data acquisition not recording the end of every APLT. Using this comparison, the location that experienced the greatest tensile change in strain in the outside strain gages was 4B, followed in descending order by 2B, 3A, 4A, 3B, 1A, 2A, and 1B (Table 4.2).

1B could not accurately be ranked because none of the outside strain gages at 1B recorded any data during the 30 psi loading cycles. Location 4B experienced almost seven times as much change in tensile strain as any of the other locations using this comparison. SG1 at location 4B recorded over 2,000 times more strain than the other outside strain gages at 4B and was eliminated from the comparison as an outlier. This did not change the ranking of the locations in terms of change in tensile strain, and 4B still had the greatest change in tensile strain in the outside strain gages (483.2 με). 2A performed the best at a change of 21.0 με, which was 91% lower than the average change in tensile strain in the outside strain gages. Locations 2B and 2A performed differently from one another, with 2B ranked second to worst, and 2A ranked best. 3A and 3B performed the most similarly between locations in the same test section, with 3A performing third worst and 3B performing fifth worst.

When ranking the sections by the amount of strain experienced at the end of the 30 psi loading cycles and only looking at the change in tensile strain in the outside strain gages, it appeared that the amount of tensile reinforcement of the test sections did not control their performance. When the performance of the A and B locations for the test sections was averaged together, S4 experienced the most change in tensile strain in the outside strain gages at the end of the 30 psi loading cycles, followed by S3, then S2, and then S1. If the reinforcement was controlling their performance, it would be expected that this ranking would be inverted (Table 4.2).

In analyzing data from the experiments, a correlation was discovered when the permanent change in strain from the end of the 30-psi load cycles was compared to the Ingios DCP-CBR values for the UTBC. When the Ingios DCP-CBR values for the UTBC were used in a linear regression with the available data for tensile strain recorded by SG2, the R squared value was not very high. One outlier was removed (SG2 from section 1A) and the regression was calculated again. The R squared value using SG2 from locations 3B, 2B, 2A, and 1B was 0.991. The p-value for the Ingios DCP-CBR was 0.005 (Table 4.11 and Figure 4.10).

These results showed a greater correlation than any of the other correlations discussed thus far. The regression was performed again, this time using the average combined Ingios DCP-CBR of the UTBC and GB. Data from SG2 in section 1A was also included. The R squared value of this regression was 0.758, and the p-value for the combined Ingios DCP-CBR value was 0.054878. When this regression was performed without the strain in SG2 from 1A, the R squared value dropped to 0.646, and the p-value for the combined Ingios DCP-CBR value rose to 0.196. This result could indicate that the thicker layer of GB in S1 made more of an impact on the strain in that location than it did in the other test sections where the GB layer was thinner. The design thickness of the GB in S1 and S2-4 was 12 inches and 6 inches, respectively.

Due to the relatively low number of comparisons made in the regression, an effort was made to find a more robust correlation from the APLTs. To increase the number of data points, the absolute value of the strain recorded by each of the outside strain gages (minus the strain gages that behaved erratically) for each individual test location were averaged. This was done for the strain gages at the UTBC-GB interface and for the strain gages at the GB-subgrade interface. The strain values used were the permanent changes in strain recorded at the end of the 30-psi loading cycle. Using this data, the number of data points for making a correlation was seven instead of four. When a linear regression was calculated again using the Ingios DCP-CBR values for the UTBC layer and the absolute value of the average strain recorded at the UTBC-GB interface, the R squared value was 0.470, and the p-value for the Ingios DCP-CBR values was 0.089. This showed a reasonable correlation, but when an outlier was removed from the data set (the strain from location 1A, which was also the outlier removed in the previous correlation), the R squared value rose to 0.814, with a p-value of 0.013 (Table 4.12, and graphically in Figure 4.11). It is notable that the use of the strain gages reporting compression in the geosynthetics correlated well in the linear regression performed. This suggested that the negative readings in the geosynthetic were related to the response of the pavement system and not an anomaly due to improper installation.

An attempt was made to correlate the strain recorded at the UTBC-GB interface and permanent deflection, $M_{r\text{-}comp}$, and $M_{r\text{-}UTBC}$. These correlations were not as strong as the correlation between strain and the Ingios DCP-CBR values. Given the strong correlation between the recorded strain and the Ingios DCP-CBR values, one reason for this weaker correlation could be the lower number of data points for the strain data when compared to the number of data points for the Ingios DCP-CBR values. Attempts were made to find the same correlations between the strain recorded at the GB-subgrade interface and the Ingios DCP-CBR values for the GB layer. Of the comparisons made, none of them were statistically significant.

The data collected suggests that at the UTBC-GB interface, the amount of strain in the geosynthetic is strongly related to the CBR of the UTBC layer. As the CBR of the UTBC layer increases (and thereby the UTBC layer becomes stiffer), the amount of strain in the geosynthetic decreases proportionally. As the CBR of the UTBC decreases, the strain in the geosynthetic increases.

4.4.2.3 Strain Analysis and Geosynthetic Properties

Two analyses of the data were performed focusing on correlating the total change in tensile strain in the geosynthetic to properties of the geosynthetics. The total change in strain is defined as the maximum tensile change in strain recorded during a loading cycle subtracted by the last permanent change in tensile strain recorded before the beginning of the loading cycle. This can be visualized in Figure 4.12, where the permanent change in strain is shown as the lower values in between the peaks in the change in strain data. The peaks show the maximum change in strain during the load and unload phase of the loading protocol.

As shown in the plot, there is a large peak in change in strain that corresponds to the loading phase of the APLTs. In between these load/unload phases, the readings are relatively the same, until the next load cycle begins. From analysis of the data, it was found that in most cases, the average total change in strain (i.e. the difference between the maximum strain and the average permanent strain recorded during load/unload cycles) increased in magnitude as the stress applied during the APLTs increased. It was also observed that at the beginning of an increase in stress, the magnitude of the total change in strain was greater than it was at the end of a step up in the stress applied during the APLTs. This shows that at the beginning of an increase in stress, the test sections generally behaved more elastically. Under repeated load/unload cycles, the test sections began to have a lower elastic response, and more permanent strain was observed, but at a decreasing rate.

In the first analysis, several attempts were made to correlate the tensile strength properties of the geosynthetics and the change in total strain from the beginning to the end of the 30-psi load cycle. The properties of the geogrid utilized were tensile load at 2% and 5% strain, ultimate strength, junction strength, and aperture stability. Where the values were different, both the machine direction and cross machine direction properties were used based on the orientation of the strain gages. For example, strain gages 4, 5, 9, 10, 14, and 15 were all oriented in the machine direction. The machine direction properties of the geogrid were used for these strain gages, while the cross-machine direction properties were used for the other strain gages oriented in that direction. The properties for the SKAPS GT180 that were used were grab tensile strength and trapezoidal tear strength. The geotextile had the same properties in the cross-machine and machine direction.

No correlation with a significant R squared value could be found between the total change in strain and properties of the geosynthetics. A relationship with a statistically significant p-value was found between the difference in total change in strain from the beginning to the end of the 30-psi load cycle and both the Ingios combined UTBC-GB CBR and the $M_{r\text{-}UTBC}$. This regression yielded p-values of 0.047 and 0.030, respectively. The corresponding R squared value was 0.146, but when the data is plotted, it does appear to show that as the two correlated values increase, the change in elastic response decreases (Figure 4.13 and Figure 4.14). This seems to lend some support to the inference that as the number of load cycles increases, the geosynthetic begins to carry more and more of the load applied. If the soil layers were stiffer, they would carry more of the load and the transfer of load to the geosynthetic would decrease, and a greater number of loads and displacement would be needed to begin to mobilize the geosynthetic.

The second analysis also looked at the total change in strain at the end of the 30-psi load cycle. For this analysis, instead of using the average permanent change in strain, the last permanent change in strain was taken before the next load/unload cycle. The maximum change in strain during the load cycle was still

used. The total change in strain was the difference between the maximum change in strain and the last permanent change in strain before the next load cycle began.

Several different correlations were explored. The first correlation discovered was between the Ingios DCP-CBR for the UTBC layer and the average total change in tensile strain at the end of the 30 psi load cycles in the inside strain gages at locations 1B, 2A, 2B, and 3B. The R squared value for the linear regression was 0.574 and the p-value for the Ingios DCP-CBR UTBC was 0.243. While the R squared value was less than 0.5, the p-value was higher than 0.05, suggesting the correlation was not very statically significant (Table 4.13).

The next correlation was found by performing a linear regression between the total change in strain in the center strain gages (strain gages 2, 7, and 12) with the ultimate tensile strength of the geogrid, the 50% strain grab strength the geotextile, and the depth of the strain gage in the pavement system. When this correlation was performed using the elastic tensile change in strain data from the 10 center strain gages that returned viable data, the R squared value and p-values were not statistically significant (Table 4.14). When the same analysis was performed but the data points from location 1A were excluded, one of the most significant correlations of the study was discovered. The linear regression between the data sets had an R squared value of 0.990. The p-values for the data sets of depth of strain gage, geogrid ultimate tensile strength, and geotextile grab strength at 50% strain were each significant or close to being significant with the highest value being 0.006 (Table 4.15). The predicted versus actual values for tensile change in strain for this correlation are shown in Figure 4.15. When the analysis was performed with only the geogrid ultimate strength and the depth of the strain gages, the R squared value dropped to 0.844, and when only the depth of the strain gages was used in the analysis, the R squared value dropped to 0.844 as well (Table 4.16 and Table 4.17). When only the geogrid ultimate tensile strength was used to predict the total tensile change in strain of the same dataset, the R squared value dropped to 0.05 (Table 4.18).

The linear regression data shown in Table 4.15 is the most significant correlation discovered between properties of the geosynthetics and the change in strain recorded. It is reasonable to predict the depth of the geosynthetic would impact the amount of strain experienced during loading. The correlation between the total tensile change in strain in the inside strain gages, excluding location 1A, and the depth of the strain gage was significant. The p-value for the depth of the strain gages was 0.001, meaning, there was a strong correlation between the two data sets. The correlation showed that as a geosynthetic was located deeper in the pavement system, the amount of total tensile change in strain increased (Figure 4.16).

It is interesting that the one strain gage from 1B that was used in the analysis was predicted with a high degree of accuracy using the developed linear regression shown in Table 4.15 (Table 4.19). Though the linear regression predicts the total tensile change in strain in 1B accurately, it does not accurately predict total tensile change in strain at location 1A. This may be due to differences in CBR values and thicknesses of layers in the pavement system at 1A.

The fact that using the tensile properties of the geosynthetic not only increased the accuracy of the regression but also yielded significant p-values shows that in the dataset used, those properties correlate with the amount of strain in the geosynthetics. It is reasonable to use this correlation to infer that the tensile properties of the geosynthetics contribute to the total change in strain results of the reported strain. The geosynthetics total change in strain appears to be represented in the total tensile change in strain in the inside strain gages. As shown in Table 4.14, this correlation does not apply to all the strain gages. Efforts to use data from the outside strain gages did not yield significant correlations in similar analyses.

Though this analysis does show the impact of the geosynthetic properties on the total tensile change in strain in the geosynthetic, efforts to correlate the resilient modulus, permanent deflection, or CBR values of the pavement system did not yield any strong correlations.

Several other observations were made from analyzing strain gage data from the APLTs. The first was that strain was registered in the geosynthetics as soon as a load was applied. The recorded strain data from the strain gages matches well with the time of the APLT loading. Noticeably clear extrema are visible in the strain gage data that correspond to the load pulses from the APLT testing. The frequency of recorded load pulses almost perfectly matched the loading protocol specified by Ingios for the APLTs. The strain is recorded with every load pulse from the beginning of the test. This shows that both the geogrid and geotextile were interlocked with the soil. Vertical recorded deformations at the surface of the pavement system as small as 0.005 inches resulted in recorded strain in the geogrid and geotextile.

Another notable observation made from the strain gage data was that even when the permanent change in strain in the geosynthetics was negative (compressive), load pulses from the APLT testing would be positive (tensile). A strain gage would be reporting a greater and greater magnitude of compressive strain, but, simultaneously, every time a load pulse would be applied, the change in strain would trend upward, and then after the response to the load pulse was complete, the magnitude of the permanent strain would be even more compressive (Figure 4.17). Further analysis from the TLTs provided more information regarding the compressive trend in the strain gages and is discussed later in this chapter.

Also notable is the fact that the recorded strain during the APLTs was small. The greatest average change in strain in the geosynthetics at an interface was in the BX1200 geogrid at the subgrade-GB interface. The greatest average value for strain at the end of the 30-psi loading stage was 1,098,617 με, or 1.10% strain. This value was much greater than the next highest average strain recorded. The next highest average strain was 2,241.529 με (0.002% strain), recorded at the UTBC-GB interface at location 1A at the end of the APLT, which suggests the 1.10% strain is an outlier. Both strains are small, and both were considered to be outliers in the data set. All the strain recorded in the BX1200 at the subgrade-GB interface was quite high in comparison to the strain in the other geosynthetics. This data did not coincide with greater permanent deformation at the pavement system surface, nor with lower CBR values. The reason for the higher strain values is possibly because the geogrid was placed directly on top of the geotextile at the subgrade-GB interface in sections 4A and 4B. This meant that the geogrid did not lie flat against the soil layer beneath it, due to the relief created by the environmental protection covering the strain gages on the geotextile beneath it. When soil was placed and compacted on top of the geogrid, it was strained more than normal as it was formed around the strain gages installed on the geotextile. Several of the readings from the strain gages in section 4A were somewhat erratic. This suggests they may have been damaged during installation or construction, or both.

Disregarding these two outliers, the maximum average strain was 724.71 με. This is equivalent to 0.0007% strain. Though the data from the strain gages indicates clearly that the geosynthetics responded immediately to the load applied to the pavement system, though the corresponding strain was minute. It is possible that the strain in the geosynthetics was not great enough to allow them to give a comparable level of reinforcement under the APLT loads. The correlation between strain and UTBC CBR suggests that if the CBR of the pavement system layers (especially the upper layer) were lower, the geosynthetics would undergo greater strain and presumably offer a greater amount of reinforcement. Due to the low levels of strain experienced during the test combined with the variability in the pavement system in terms of thicknesses and CBR of the soil layers, any attempts to compare the reinforcement benefit of the geosynthetic between test sections was inconclusive.

4.5 TLT Results

4.5.1 TLT #1

4.5.1.1 Introduction

The first set of truck load tests (TLTs) were performed in November 2022. The passenger set of dual wheels on the middle axle of the triple-axle dump truck was centered on the 11.3-inch diameter, half-inch-thick steel loading plate over the center of the strain gage array at locations A and B in each test section (steel loading plate shown in Figure 4.18). The truck used in the test is shown in Figure 4.19. The truck was left to dwell on the plate for approximately 10 minutes before the data collection of strain from the strain gage arrays was paused (Figure 4.20). The exact weight of the dump truck was not measured, but as a basis of comparison, Cuelho and Perkins used a similar triple-axle dump truck in his testing. When it was weighed, the average load from one set of the dual tires on the back two axles of the dump truck was 8,567.7 lbs. (Cuelho & Perkins, 2009). An acceptable estimate for the load on the loading plate during the truck load tests would be 8,500 lbs. Using this estimation, the approximate stress applied to the strain gage array by the truck using the loading plate with a diameter of 11.3 inches would be 85 psi.

From the plots of the strain gage data, a clear response to the loading of the truck can be seen. The strain gages register each load from a wheel in the change in strain recorded. There appear to be spikes in the recorded change in strain that correlate to the crossing of each wheel of the truck over the loading plate. Interpreting the data during this part of the test was difficult because the truck was moved back and forth several times over the loading plate while centering it. Figure 4.21 shows an example of the raw data readout from the beginning of a TLT.

4.5.1.2 Beginning of Truck Load Dwell Time Analysis

The same hindrances to interpreting the APLT data existed with the TLTs. The same number of strain gages had failed, and analysis showed several of the strain gages that reported data behaved erratically. Another complicating factor was that centering the load from the truck directly over the strain gage array was more difficult than with the precise equipment available with the APLTs. Due to these factors, four of the 13 center strain gages reported a negative change in strain (SG2 at locations 3A and 4A, and SG7 at locations 3A and 3B).

Just as in the APLTs, gage factors and global strain factors were used to convert the change in mV recorded by the strain gages into actual strain. The units used to present the data are microstrain (με). To help compare different test sections to one another, the tensile change in strain recorded by the four outside strain gages in the strain gage arrays at both the UTBC-GB interface and the GB-subgrade interface at each instrumented location were averaged together. A similar method of comparison was used in the APLT analysis, but there were more data points to compare in the TLTs, so the compressive data was not needed. It was also found that correlations between the outside strain gages were better when used without the center strain gages. Also, half of the center strain gages in the test sections were not operating or reported a compressive change in strain. For these reasons, the data set used in the first comparisons was the tensile change in strain recorded at the beginning of the dwell time for the truck load using the outside strain gages. The values of average tensile change in strain in the outside strain gages can be found in Table 4.20.

The greatest change in tensile strain recorded by the outside strain gages at the beginning of the dwell time for the truck load was at 4A, and then in descending order 4B, 3A, 1A, 2A, 1B, 3B, and 2B. When analyzing the data, it was observed that Location 2B experienced less strain than any other test section, and 82.4% less change in strain than the average. 2B was reinforced with one layer of geogrid at the

UTBC-GB interface. It had less reinforcement than sections 3 and 4 but had less change in strain than both of those sections. It had the second greatest Ingios DCP-CBR average for the UTBC layer and the third greatest composite Ingios DCP-CBR value for the UTBC and GB layers combined. 3B was the only location with a greater Ingios DCP-CBR value. It also was one of the two locations with a higher composite Ingios DCP-CBR value, but it had a lower Ingios DCP-CBR value for its GB layer than 2B. The difference in CBR of the GB for the two locations was greater than their difference in CBR for the UTBC layer (4.77 versus 1.56). It is possible this contributed to 2B outperforming 3B. The other location with a higher composite Ingios DCP-CBR value for the UTBC and GB was 2A. 2A had a greater Ingios DCP-CBR value for its GB layer (53.54 versus 51.27) but a significantly lower Ingios DCP-CBR value for its UTBC layer (24.01 versus 33.52). It is possible that 2B's higher Ingios DCP-CBR value contributed to it having a lower change in strain than 2A.

Although 2B performed best, when considering the tensile change in strain in the outside strain gages, 2A did not perform as well. 2A experienced less change in tensile strain than sections 4 and locations 3A and 1B but experienced more tensile strain than 1B and 3B.

When the tensile strain at the beginning of the truck load dwell time from the outside strain gages was considered, the only test section to have its locations outperform the same number of test sections was S4. All other test sections A and B locations were spread out with other sections A or B locations outperforming them. The test section with the least difference in change in tensile strain for the outside strain gages was S4, with a difference between A and B of 102.0 με, and then S1 with a difference of 116.8 με, and then S3 an S2 with differences of 552.1 and 681.8 με respectively.

When the combined Ingios DCP-CBR average values for the UTBC and GB layers was correlated to the average change in tensile strain in the outside strain gages at the beginning of the dwell period for each test location, a trend was observed. The linear regression between the two data sets was significant. The R squared value for the regression was 0.612 and the p-value for the Ingios DCP-CBR average value was 0.022 (Table 4.21 and graphically in Figure 4.22). This combined Ingios DCP-CBR average for the UTBC and GB was created by treating the two layers as one layer and weighting the CBR value by the thickness of the layer. The combined Ingios DCP-CBR average value also correlated with the change in tensile strain in the outside strain gages at the UTBC-GB interface with an R squared of 0.550 and a p-value of 0.035 (Table 4.22).

Other correlations were also discovered through linear regression. A correlation was discovered between the change in tensile strain in the outside strain gages at the UTBC-GB interface and the resilient modulus of the UTBC layer that was calculated from the APLT tests (R squared of 0.513 and a p-value of 0.046).

4.5.1.3 End of Truck Load Dwell Time Results and Analysis

The order of the test sections that experienced the greatest change in strain in each test section at the end of the truck load dwell time was the same as at the beginning. At the end of the dwell time, when the strain gages that showed a change in tensile change were analyzed, on average, they recorded a lower change in strain. 30.1% of the strain gages that recorded a tensile change in strain had higher readings by the end of the dwell period. Based on the number of gages that were working, the test location with the greatest frequency of strain gages recording an increase in tensile change in strain by the end of the dwell period was at 4A (75%). Table 4.23 shows the total percentage of each locations' strain gages that recorded a negative change in strain by the end of the dwell period.

The average decrease in change in strain recorded during the test was 52.3 με. The average increase in change in strain recorded during the test was 40.8 με. Several attempts were made to find a correlation between the CBR values for the pavement system, the M_r values for the pavement system, and the tensile

strength properties for geosynthetics at the locations where a large percentage of strain gages recorded a greater change in strain at the end of the dwell time, but no strong correlations were identified. It is possible the decrease in tensile change in strain by the end of the dwell period shows the geosynthetics and the pavement system were relaxing after the initial truck load was applied. The exact mechanics of this response could not be determined from the collected data.

Data for the difference in the change in strain from the beginning of the dwell period to the end was analyzed in several ways. None of the analyses showed any significant correlation. The data was sorted by whether the strain gages recorded a negative or positive change in strain at the beginning of the test, by an increase in strain during the dwell time, decrease in strain during the dwell time, whether the change in strain was in the geogrid or the geosynthetic, and all the data was considered together. The best correlation found was using the data from the strain gages at the UTBC-GB interface that first, recorded a tensile strain during the test, and second, showed a decrease in the difference in change in strain from the beginning to the end of the dwell period. These values were positive (tensile) from the beginning of the test and decreased in magnitude by the end of the test.

In this correlation, only the strain gages that registered tensile change in strain during the test were used. Of those gages, only those that showed a decrease in change in strain by the end of the test were used. The difference between these gages reading at the beginning to the end of the dwell period were correlated with the Ingios DCP-CBR of the UTBC and the GB. When considered together, the R squared value was 0.814 and the p-values for the Ingios DCP-CBR for the UTBC and the GB were 0.036 and 0.086 respectively (Table 4.24 and graphically in Figure 4.23). When each of these factors was considered separately, the R squared values and the p-values decreased. When considered alone, the Ingios DCP-CBR for the UTBC produced a correlation with an R squared of 0.420 and a p-value of 0.164 (Table 4.25). When the Ingios DCP-CBR for the GB was considered on its own, the R squared value was 0.073583, and the p-value was 0.603 (Table 4.26). Both p-values were well above the threshold of statistical significance. To try and determine if the correlation was tied to how the two acted together, the same set of strain gage data was used in another linear regression with the combined Ingios DCP-CBR value for the UTBC and GB. This regression resulted in an R squared value of 0.0005 and a p-value of 0.968 (Table 4.27). Because of the results of performing linear regressions with these two factors alone, it is suggested there is not strong correlation between the difference in the change in strain at the beginning and end of the dwell period and the CBR of the UTBC and GB.

When data from the TLT #1 was analyzed, the strongest correlation for the change in tensile strain experienced in the outside strain gages was with the combined Ingios DCP-CBR value for the UTBC and GB layers. The second strongest correlation was between the change in tensile strain at the UTBC-GB interface recorded by the outside strain gages at the beginning of the truck load dwell time and the combined Ingios DCP-CBR for the UTBC and GB. The change in tensile strain recorded by the strain gages in the test sections did not appear to be controlled by the addition of geosynthetic reinforcement. The most reinforced section, S4, recorded the greatest average change in tensile strain in the outside strain gages for any of the sections. Reinforced S2 and S3 did experience less strain, but they also had higher CBR values for the UTBC and GB layers, which is in line with the correlation between change in strain and CBR. No correlation was discovered between the difference in the change in strain from the beginning to the end of the truck load dwell time and properties of the geosynthetics, their placement in the pavement system, or the CBR of the pavement system.

4.5.2 LT #2

4.5.2.1 Introduction

The second truck load test was performed using a triple-axle truck, too, but this time, a water truck was utilized (Figure 4.24). It was of similar size and weight to the dump truck used in the first TLT, but its exact weight was not known. Based on exact weight measurements taken of a similar truck by Cuelho and Perkins, an appropriate estimation of the load applied by one set of the dual wheels on one side of the center axle of the dump truck would be 8,500 lbs (Cuelho & Perkins, 2009). Instead of the 11.3-inch diameter, half-inch-thick steel loading plate used in TLT #1, a 34-inch diameter, inch-thick steel loading plate was used for TLT #2 (Figure 4.25). The truck load time was also increased to 15 minutes with the driver-side dual wheels of the middle axle of the truck centered on the loading plate. An appropriate estimation of stress applied to the pavement system by the truck on the loading plate would be 9 psi.

The response of the strain gages in TLT #2 was similar to the response in TLT #1. Clear responses could be seen between the crossing of a wheel over the loading plate and the change in strain recorded in the strain gages. The tests were recorded with a video camera, so the video could be correlated with the strain data. Determining the beginning of the truck load dwell period was not difficult, but further analysis of the dynamic loading from the truck being maneuvered into place would be aided by footage of the experiments.

4.5.2.2 Beginning of Truck Load Dwell Time Results and Analysis

The change in strain recorded in TLT #2 at the beginning of the truck load dwell time was different from during TLT #1. Table 4.28 shows the comparison in average tensile change in strain for the outside gages for TLT #1 and TLT #2. From the table, it can be seen that in TLT #2, 1B experienced the greatest change in tensile strain at the beginning of the dwell time. This was followed by 4A, 2A, 4B, 3B, 3A, 1A, and 2B. In both tests, 2B experienced the least amount of change in tensile strain in the outside strain gages. In TLT #2, 2B performed 90.2% better than the average and 82.4% better in TLT #1. 1B performed the third best in TLT #1, but the worst in TLT #2. 4A and 4B still recorded some of the highest changes in strain in the outside strain gages at the beginning of the dwell time, but 2A surpassed 4B (1299.819 με compared to 1124.136 με). 1A also performed better in TLT #2, performing second best as opposed to fifth in TLT #1. 3A outperformed 3B when 3A had previously outperformed it and 1A, 2A, and 1B in TLT #1.

Another difference was magnitude of the change in strain experienced in the two tests. When all the strain gages were averaged, TLT #2 experienced an average compressive change in strain of -419.7 με at the beginning of the dwell time, while TLT #1's average was -337.4 με. When tensile strain in all the strain gages was compared, TLT #2 experienced an average of 1434.6 με compared to TLT #1's average of 1049.8 με. greater change in strain. When comparing just the change in tensile strain in the outside strain gages, TLT #2's average tensile strain was 1594.5 με, 34.4% greater than TLT #1's 982.9 με change in tensile strain in the outside strain gages (Table 4.29).

Just as in TLT #1, correlations between properties of the test locations were correlated with the change in tensile strain in the outside strain gages at the beginning of the truck load dwell time in TLT #2. Correlations between the change in tensile strain at the beginning of the truck load dwell time were not as strong as they were for TLT #1. One statistically significant correlation was found between the combined DCP-CBR UTBC-GB values from spring 2023 and the average tensile change in strain in the outside strain gages at the beginning of the dwell time. These CBR values came from DCP testing that was performed the week before TLT #2. The correlation had an R squared value of 0.62167 and a p-value of 0.03514 (Table 4.30). A plot of the data and the linear regression can be seen in Figure 4.26. The second

strongest correlation was between the difference in change in tensile strain in the outside strain gages from the beginning to the end of the dwell period and the $M_{r\text{-top of GB}}$, with an R squared value of 0.612435 and a p-value of 0.037509 (Table 4.31). It is worth noting that 1B, which recorded 2.82 times the average change in tensile strain, also had the lowest M_r of any of the test sections. 4B, which also experienced one of the higher levels of change in strain also had a low M_r. With the number of variables present in the field experiment, it was difficult to determine which of them impacted the results the most.

4.5.2.3 End of Truck Load Dwell Time Analysis

By the end of the dwell time in TLT #2, the order of the magnitude of tensile change in strain in the outside strain gages was the same as at the beginning of TLT #2. Though all strain gages recorded a different change in strain by the end of the dwell time, none of them had increased or decreased to the point where they performed better or worse than another test location. This is the same result as for TLT #1. Just as in TLT #1, most outside strain gages recorded a decrease in change of tensile strain. Most of the locations had some strain gages that also experienced an increase in tensile strain. Location 1A and section 2 were the only locations to not have any strain gages record an increase in tensile change in strain by the end of the dwell period. Of the locations that did have strain gages record an increase in tensile change by the end of the dwell period, 3A and 3B had the most (75% for each location).

Table 4.32 shows the full list of percentage of operational strain gages in each section that reported an increase in tensile change in strain at the end of the truck load dwell period for both TLT #1 and TLT #2. When comparing the two tests, both tests had the same percentages for 1A and 2B. TLT #2 had a decrease in the percentage of strain gages reporting an increase in tensile strain by the end of the dwell period in locations 1B and 4A, but all other sections had a greater percentage in TLT #2 than TLT #1. In total, TLT #2 had 21.5% of all operating strain gages that recorded a tensile change in strain show an increase in tensile change in strain by the end of the dwell period, as opposed to the 30.3% of TLT #1. The average decrease in tensile change in strain for TLT #2 was 76.4 με and the average increase was 19.8 με. This was a smaller decrease in average tensile change in strain when compared to TLT #1 (52.3 με), and also a smaller increase than TLT #1 (40.8 με). Table 4.33 shows data for the change in tensile strain at the end of the truck load dwell time for each TLT and the difference in change in strain from the start to end of the dwell time for both tests.

It could be possible this correlates to the fact that the change in tensile strain in TLT #2 was greater at the beginning of the dwell period than in TLT #1. With greater strain, on average, the geosynthetics and the pavement system could not recover as much strain by the end of the dwell period. However, this is an inference that needs greater evidence to ascertain its viability.

In TLT #1, the average change in tensile strain in the outside strain gages for each A and B test location was less at the end of the dwell time. This was the same for TLT #2, except for 3A. Its average change in tensile strain in the outside strain gages at the end of the dwell time was greater than at the beginning. The greatest decrease in change in tensile strain was in 4B (116.9 με).

The tensile properties of geosynthetics in the cross-machine and machine-direction were used to try to correlate the difference in change in tensile strain from the beginning of the dwell period to the end of the dwell period in each of the A and B test locations. Correlations were also attempted to be found between the difference in tensile change in strain at the beginning and end of the dwell period and the CBR values for the UTBC, GB, subgrade, combined UTBC and GB layers, $M_{r\text{-comp}}$, $M_{r\text{-UTBC}}$, and $M_{r\text{-Top of GB}}$. None of the attempted regressions had statistically significant correlations. It was noted the only section with an average increase in change in tensile strain by the end of the dwell period also had the lowest CBR values for the GB layer and for the subgrade. Correlations between the CBR of the GB and subgrade beyond this were not statistically significant.

4.6 Results and Analysis of Tension and Comprehension in Strain Gages

It was not expected for so many of the strain gages to report a compressive change in strain during the tests. In TLT #1 and TLT #2, 29.2% and 16.7% of the strain gages reported a negative change in strain when loaded, respectively. In the APLT tests, 40% of the operating strain gages recorded negative values. Several hypotheses were formulated to explain the compression being experienced in the geosynthetics. First, equipment error was ruled out, since when shunt calibrations were performed, all the strain gages returned a positive change in resistance. This lent evidence to the theory that the data acquisition was not giving false negative values.

Another hypothesis was formed by analyzing the deformation data from the Ingios data. During the APLTs, displacement at the surface of the pavement system was measured at the loading plate and at two and three radii from the center of the loading plate. In the plot, the deflection recorded is connected by straight lines. But when the lines are smoothed, which would be a better approximation of the deflection occurring in the pavement system in between the points that were measured, it could be seen that a concavity in deflection is manifest in a range from the edge of the plate (six inches from the center of the strain gage array) until approximately 10 inches from the center of the strain gage array. This assumed zone of concave deflection in the subgrade coincided with the location of the outside strain gages in the transverse and longitudinal direction. It was hypothesized that as the geosynthetics were deflected in this manner, the bottom of the geosynthetic was placed in tension and the top of the geosynthetic was placed in compression. The strain gages were attached to the top of the geosynthetic, and this would presumably place the strain gages in compression, if the compressive forces on the top of the geosynthetic were greater than the tensile forces in-plane in the geosynthetic.

One purpose of using a larger loading plate in TLT #2 was to try to gain greater insight into this phenomenon. The original loading plate used in TLT #1 was 11.3 inches in diameter, and the loading plate in the APLTs was 12 inches in diameter. The loading plate's diameter in TLT #2 was more than double this (34 inches in diameter). When a larger loading plate was used, it was assumed the deflection basin caused by the loading would be spread out farther and the location of concave deflection would go beyond the location of the strain gages.

In TLT #2, there was a decrease in the number of strain gages that measured a compressive change in strain (16.7% versus 40% in the APLTs). However, during TLT #1, there was also a decrease in the number of strain gages that measured a compressive change in strain (29.2% versus 40%). TLT #1 had a slightly smaller loading plate than the APLTs. If the only factor controlling the number of strain gages reading a compressive change in strain, then the smaller plate used in TLT #1 would have had the same or a smaller number of strain gages that recorded a negative change in strain when compared to the APLT results.

The number of strain gages that measured a compressive change in strain was less than half that of the APLTs during TLT #2, but it was not zero. If the curvature of the deflection basin was controlling the number of strain gages that returned a compressive change in strain, it may be expected that there would be no gages recording a compressive change in strain. However, it is a simplification of reality to assume the load was distributed evenly and uniformly over the loading plate. There are other factors not measured that complicate determining the exact reason for the compressive change in strain reported by the strain gages.

Another hypothesis as to why the strain gages were recording a compressive change is strain deals with the movement of the soil in the pavement system and its interaction with the geosynthetics. The

hypothesis is that the compressive change in strain being experienced by the strain gages is due to the lateral spread of the base course under the load.

One of the mechanisms proposed as a benefit of geosynthetic reinforcement in a pavement system is to act as an arrestor for lateral spread. As a wheel load is applied to the surface of a pavement system, the soil is pushed down and out away from the load. Under the center of the load, it could be assumed the greatest tensile forces would be experienced in the geosynthetic, as the soil at this location is under the greatest stress, and the soil all around the point load would be pushed away from the center of the load in all directions. This is the case at least for the loading being applied to the pavement system in the APLTs and TLTs, as the load is not moving down the highway as it does with normal traffic. What the geosynthetic does is interlocks with aggregate in the soil and acts as shear resistance to the lateral spread of the aggregate. This interlock with the aggregate would cause the geosynthetic to be placed in tension as it acts against the spread of the soil under the load.

The greatest change in strain experienced during the APLTs was in the center strain gage in each array. None of these strain gages experienced a compressive change in strain reported by the strain gages. All of them recorded a tensile change in strain. Since centering the APLTs was done accurately, using the APLT mobile apparatus from Ingios, these loads were centered very well on the strain gage arrays. Centering the truck during the TLTs was more difficult. In TLT #1, three of the 14 functioning center gages recorded a compressive change in strain, and in TLT #2, five of the 13 functioning center gages recorded a compressive change in strain. In comparison, in TLT #1 eight of the 51 operating outside strain gages recorded a compressive change in strain, and 14 of the 52 operating outside strain gages recorded a compressive change in strain in TLT #2. In all cases, a greater number of outside strain gages returned a compressive change in strain. The fact that all the APLT tests saw only a tensile change in strain during the test supports the hypothesis that lateral spread is concentrated under the center of the load and in turn led to the greatest change in strain being in the center strain gages, and for that change to always be tensile. The TLTs do not necessarily support this hypothesis, as several of their center strain gages showed compressive changes in strain, though the difficulty in centering the truck may have contributed to this.

The hypothesis of lateral spread also accounts for the fact that the majority of gages that measured a compressive change in strain were located at the UTBC-GB interface and not the GB-subgrade interface. In Perkins' 1999 study, he included a diagram showing the mechanism of lateral confinement (or shear resistance to lateral spread) (Perkins & Cuelho, 1999). This diagram is shown in Figure 4.27. In the diagram, Perkins shows a zone of compressive strain in the geosynthetic outside the tensile strain zone directly under the wheel load. In the diagram, it is shown as being smaller in magnitude than the tensile strain. This zone of compressive strain is not discussed in the study, but it is shown in the diagram.

One theory for this zone of compressive strain in the geosynthetic reinforcement would be that while the soil under the load is trying to spread laterally, the soil around it is static, since it is not experiencing the same increase in stress at the surface as the soil directly under the load. This static soil is interlocked with the geosynthetic and confined by the soil around it. As the soil spreading laterally comes into contact with the surrounding soil, it confines it, causing compression. The tensile strain in the geosynthetic causes elongation under the load, and this elongation does not translate only into vertical deflection, but also lateral deflection. The geosynthetic around the load is interlocked with the soil and remains stationary. This causes a zone of compression to occur in the geosynthetic. An example of a strain gage array possibly exhibiting this behavior is shown in a diagram of the change in strain of a strain gage array during a TLT (Figure 4.28).

The APLTs help support this hypothesis in that only the outside gages measured a compressive change in strain during the tests. They also support this hypothesis in that a greater number of the strain gages that

recorded a compressive change in strain were at the UTBC-GB interface, and not the GB-subgrade interface. It would be reasonable to expect a greater amount of lateral spread to occur near the surface of the UTBC where the soil is not being confined by as much stress as it is deeper in the pavement system.

Further evidence for this theory comes from the existence of a weak correlation between the CBR of the UTBC and the percentage of strain gages that recorded a compressive change in strain. The regression had an R squared value of 0.393 and a p-value of 0.096 and showed that as the CBR in the UTBC decreased, the percentage of outside strain gages that recorded a compressive change in strain increased. This supports the theory as CBR decreases, it reflects the fact that the soil stiffness is decreasing. If the soil is not as stiff, it has a greater chance of experiencing lateral spread.

This theory has some support from the correlation between the percentage of strain gages measuring a compressive change in strain and the UTBC of the CBR, the fact that none of the center strain gages recorded a compressive change in strain during the APLTs, and the diagram shown in the Perkins 1999 study. However, data from the TLTs did have center strain gages that recorded a compressive change in strain, and the correlation discussed is not significant by normal statistical standards (p-value of 0.05). Due to these facts and the small body of evidence, this theory cannot be confirmed.

4.7 Synthesis

The results from the study were mixed. The best correlations were found from the APLT data, although the amount of data for these correlations was less than that for the TLTs. The APLT results showed when the average change in tensile strain in the outside strain gages at the end of the 30 psi loading cycles was considered, S4 had the greatest change in strain, and S1 had the least. When comparing the amount of permanent deflection that occurred during the APLTs, S1 had the greatest deflection, and S3 had the least. When Mr-comp was considered, S3 performed the best and S4 performed the worst.

In TLT #1, S4 experienced the greatest change in tensile strain in the outside strain gages at the start and finish of the truck load dwell time, while S2 experienced the least. In TLT #2, S1 experienced the greatest change in tensile strain in the outside strain gages, and S2 experienced the least. The results of each test did not correlate with each other very well. It was difficult to compare the test sections directly because of the difference in CBR for the UTBC, GB and subgrade layers.

The strongest correlation in predicting performance of the test sections was the CBR of the UTBC. This correlation was the strongest in the APLTs when predicting the change in tensile strain in SG2 at the end of the 30-psi loading cycle at locations 3B, 2B, 2A, and 1B. The R squared for this correlation was 0.991, with a p-value of 0.0046. This correlation was strong but not robust as it did not use many data points.

Another strong correlation was found between the total change in strain in the geosynthetics and both the depth of the geosynthetic in the pavement system and the ultimate tensile strength of the geogrid and the grab strength of the geotextile. The R squared value was 0.990, and the p-values for the two correlated data sets were significant at 0.000049 for the depth of the geosynthetic in the pavement system, 0.006 for the ultimate tensile strength of the geogrid, and 0.0017 for the grab strength of the geotextile. This correlation was significant and more robust than the previous correlation.

In TLT #1, the strongest correlation was found between the combined Ingios DCP-CBR values for the UTBC and GB and the average change in tensile strain in the outside strain gages at the beginning of the truck load dwell time. This correlation had an R squared of 0.612 and a p-value of 0.022. The combined CBR value just mentioned also correlated significantly with the average change in tensile strain at the UTBC-GB interface (R squared of 0.550 and a p-value of 0.035).

In TLT #2, no statistically significant relationships were discovered. The best relationship found was between the Mr-Top of GB and the change in tensile strain in the outside strain gages at the beginning of the truck load test, with an R squared value of 0.415 and a p-value of 0.085.

Due to strain gage failures, differences in CBR in the layers of the pavement system and some data acquisition problems, direct comparisons between the test sections were difficult. In many cases, the geosynthetic reinforced test sections did not perform as well as the control, and the most reinforced sections sometimes performed the worst. The best correlation was found between performance of the test sections and CBR values of the pavement system layers, particularly the UTBC layer.

A possible explanation for the number of strain gages that recorded a change in compression during the testing was proposed. The hypothesis was that a compression zone in the geosynthetic existed due to lateral spread. A correlation between the percentage of strain gages that recorded a negative change in strain at the UTBC-GB layer and the CBR value of the UTBC layer suggest that when the CBR of the UTBC increased, the number of strain gages that recorded a compressive change in strain decreased. This explanation would also correspond with greater tensile forces being experienced in the center strain gages during the APLT tests and the observation that only outside strain gages in the strain gage arrays showed a compressive change in strain during the APLTs. This possible explanation does not have enough data or analysis to support it substantially.

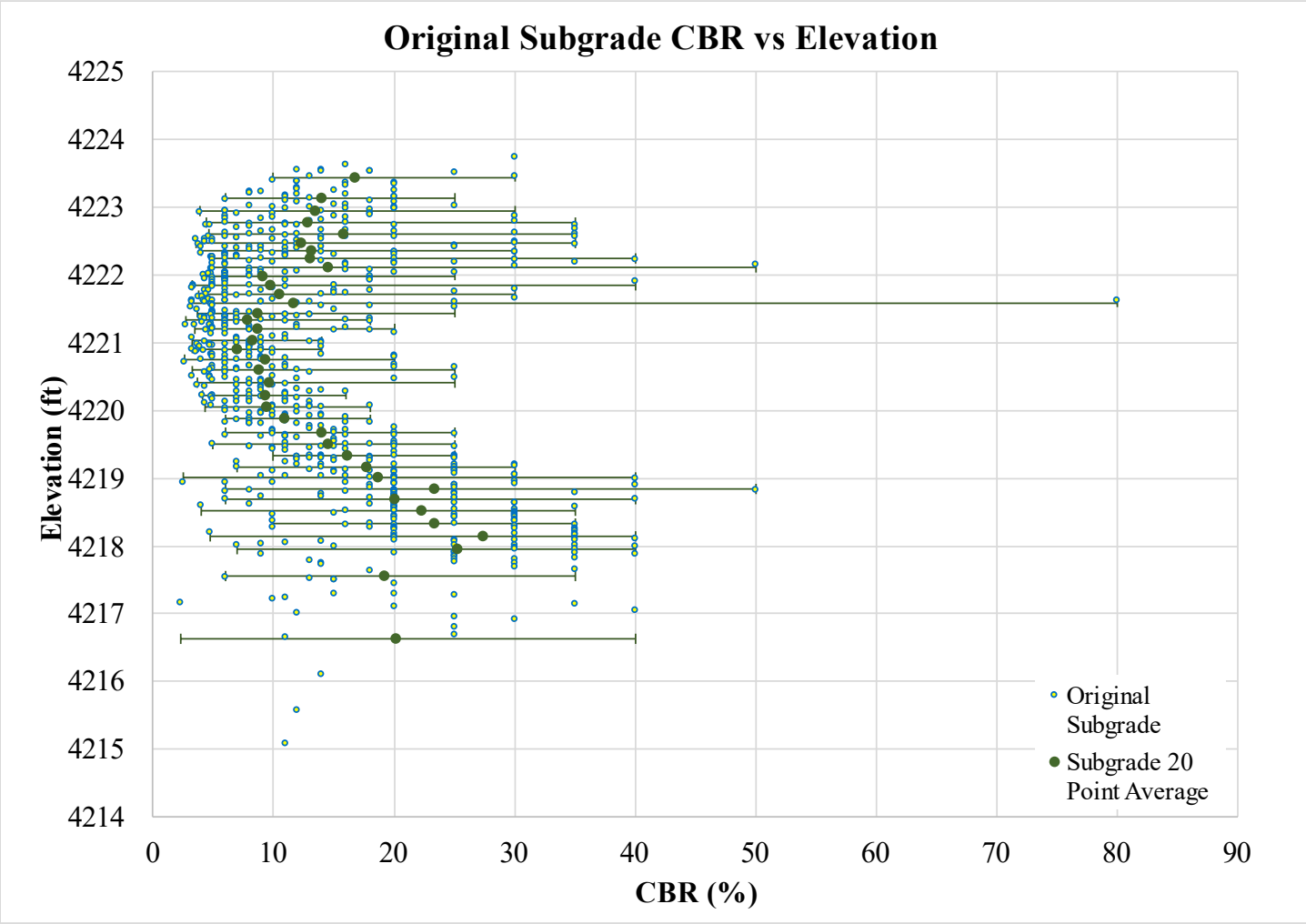

Figure 4.1 Plot of the original subgrade CBR versus elevation

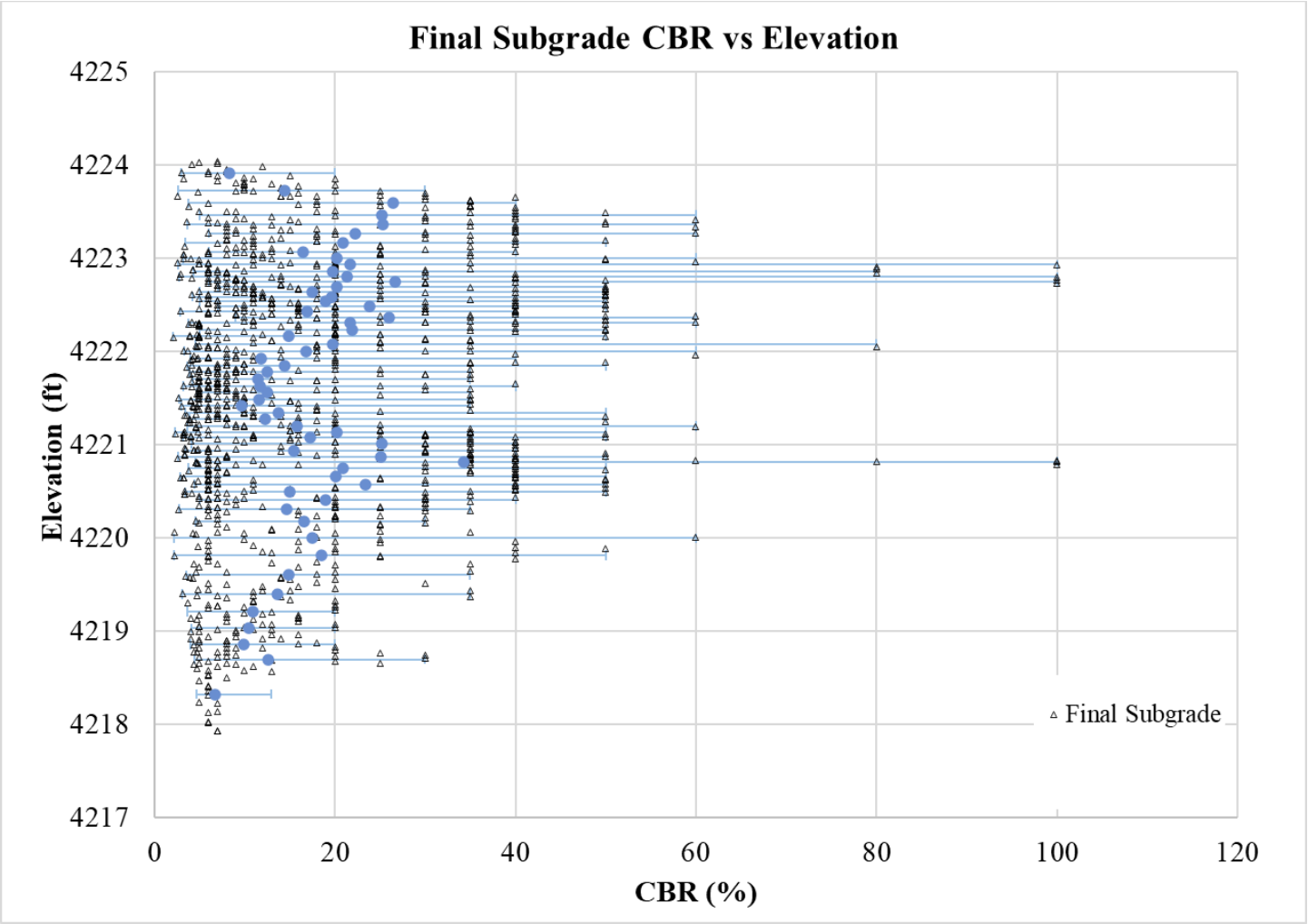

Figure 4.2 Plot showing the final subgrade CBR versus elevation

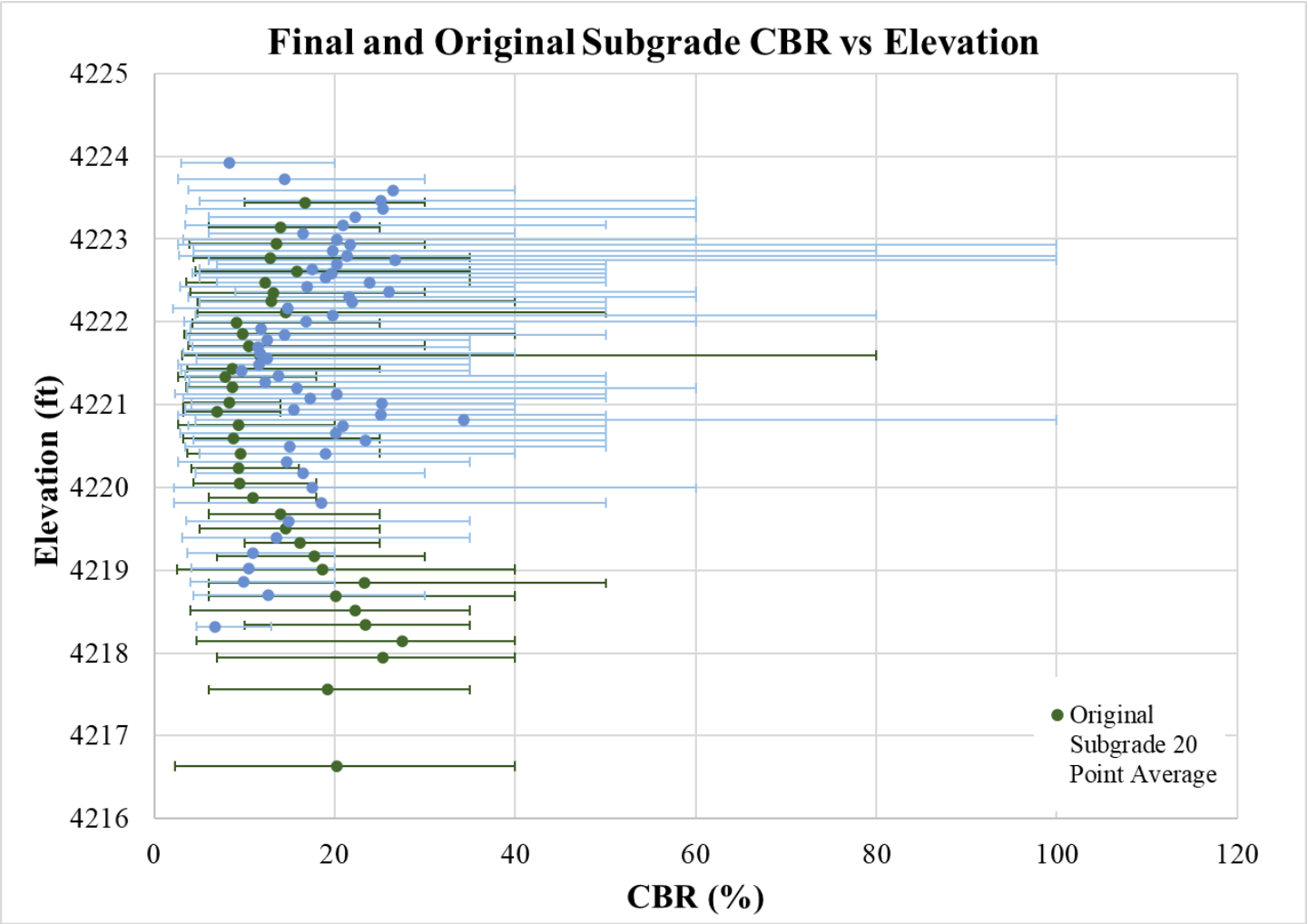

Figure 4.3 Plot showing the final and original subgrade CBR versus elevation

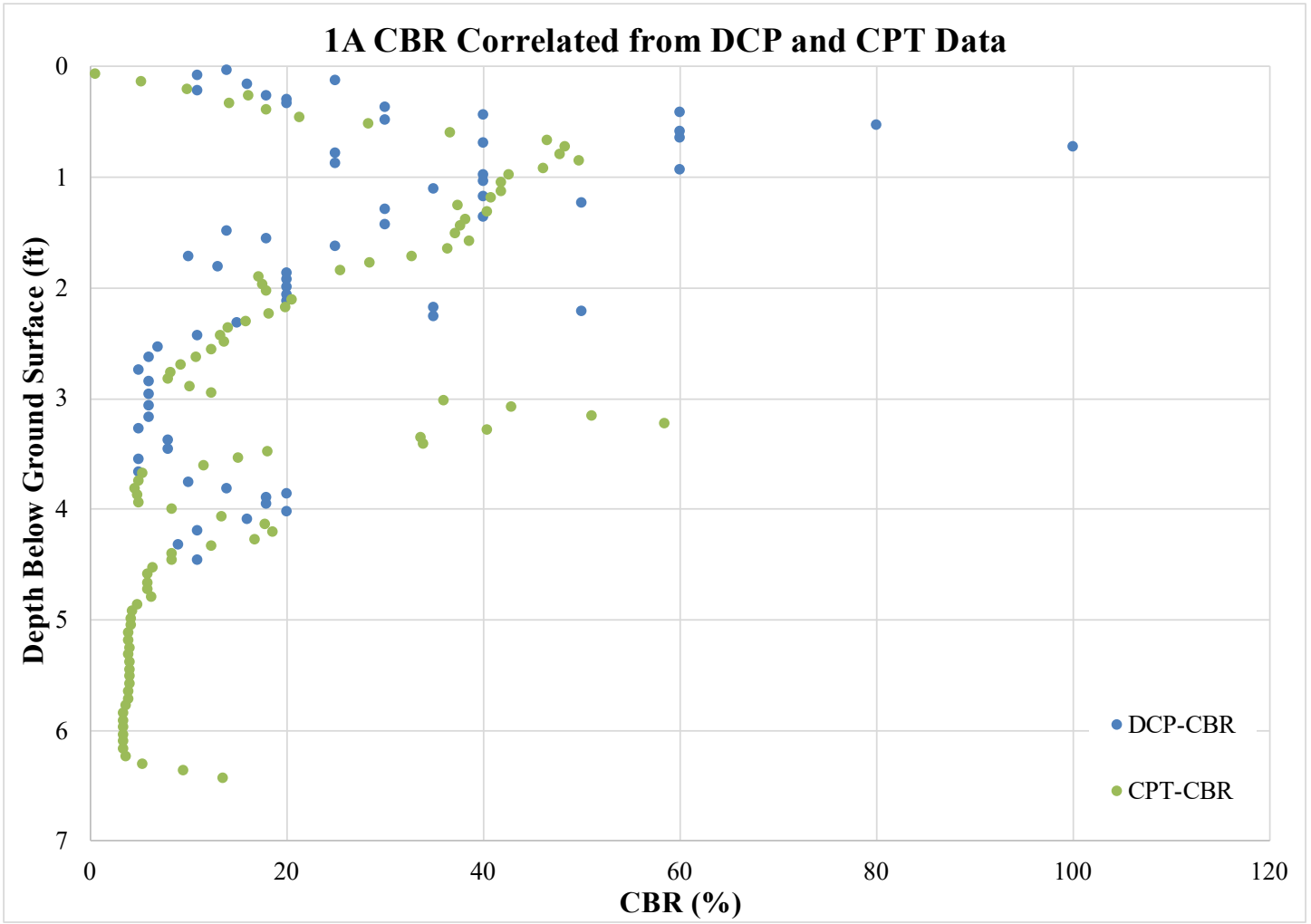

Figure 4.4 Plot showing DCP-CBR data and CPT-CBR data for location 1A

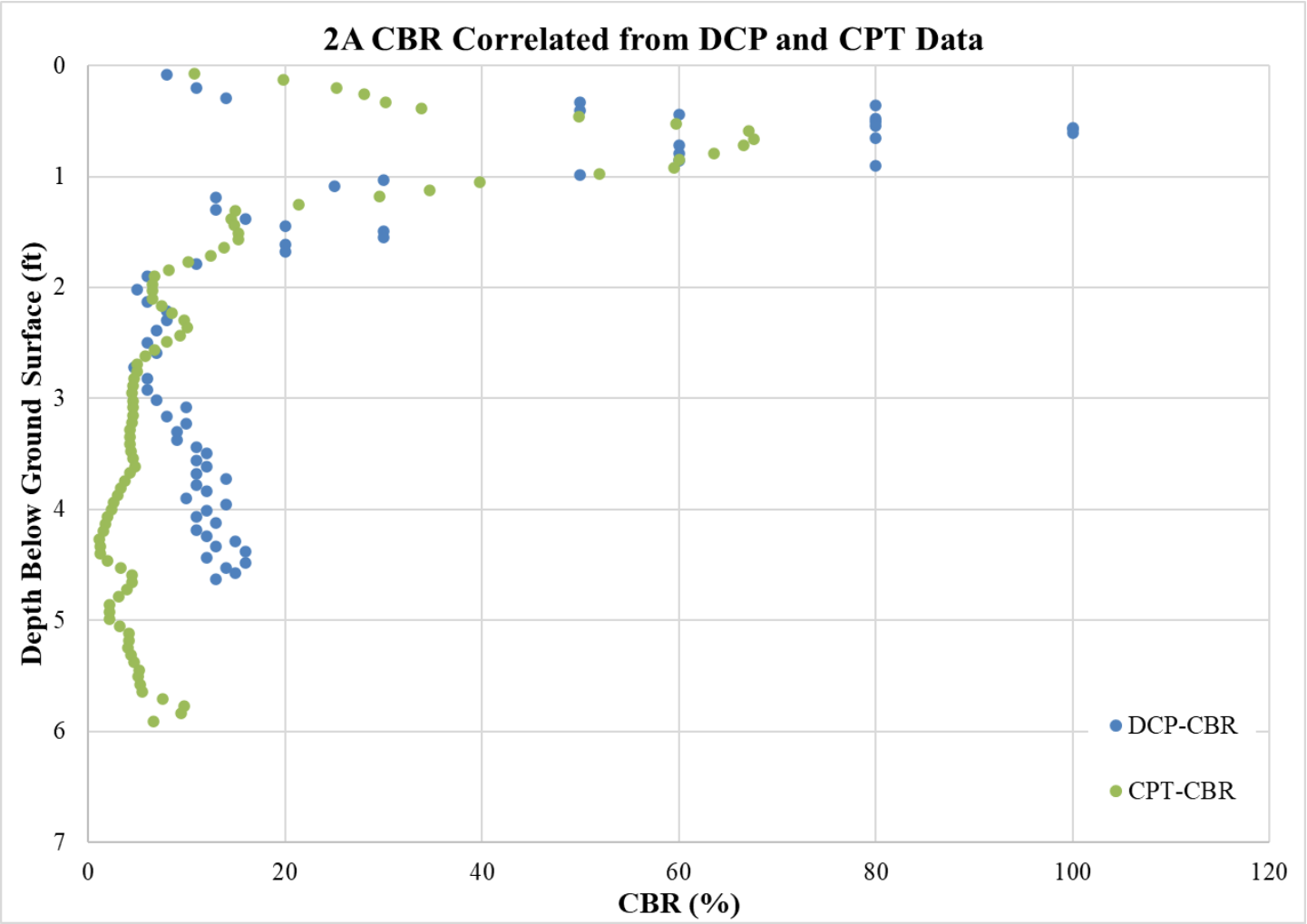

Figure 4.5 Plot showing DCP-CBR and CPT-CBR for location 2

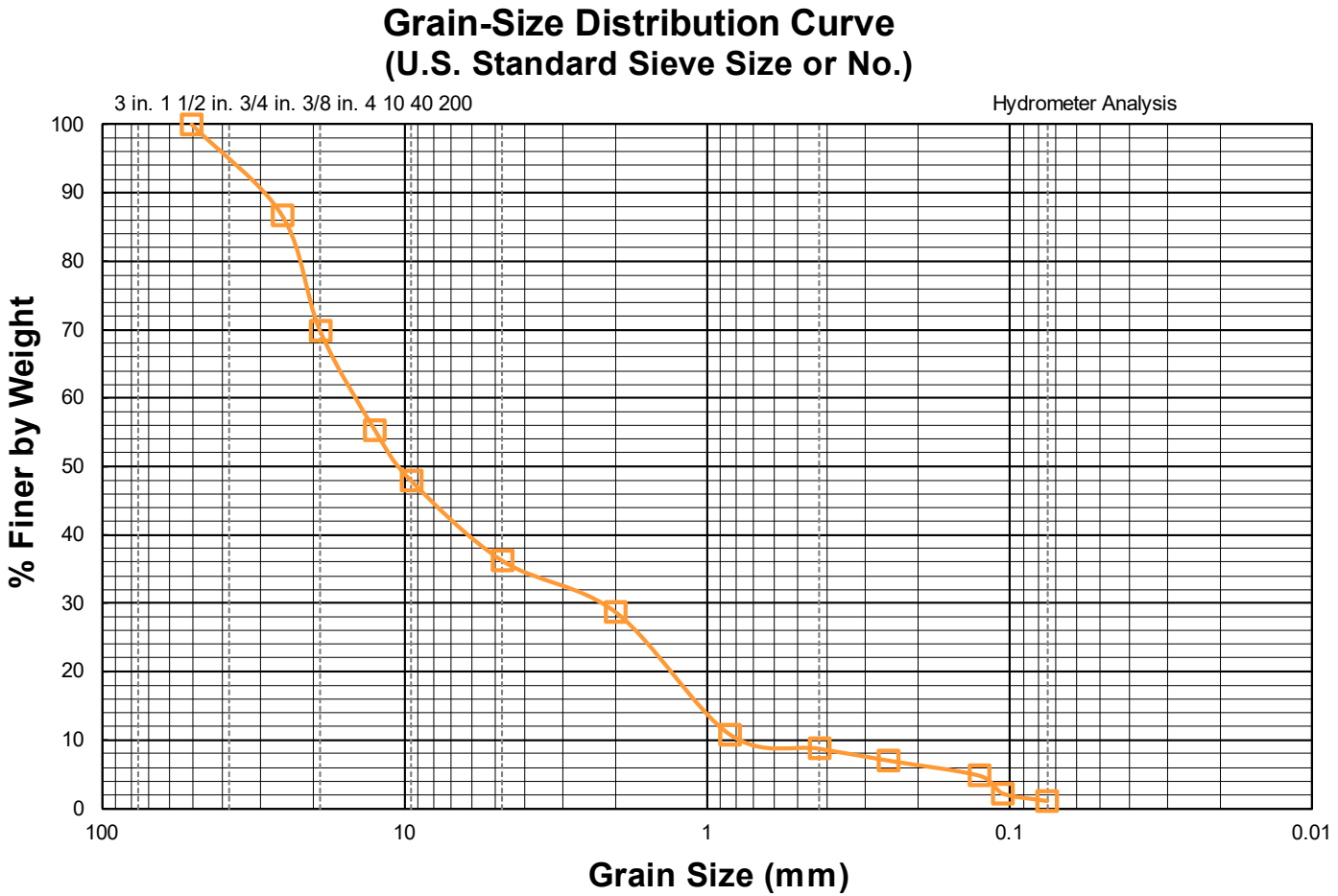

Figure 4.6 Grain-size distribution curve for GB

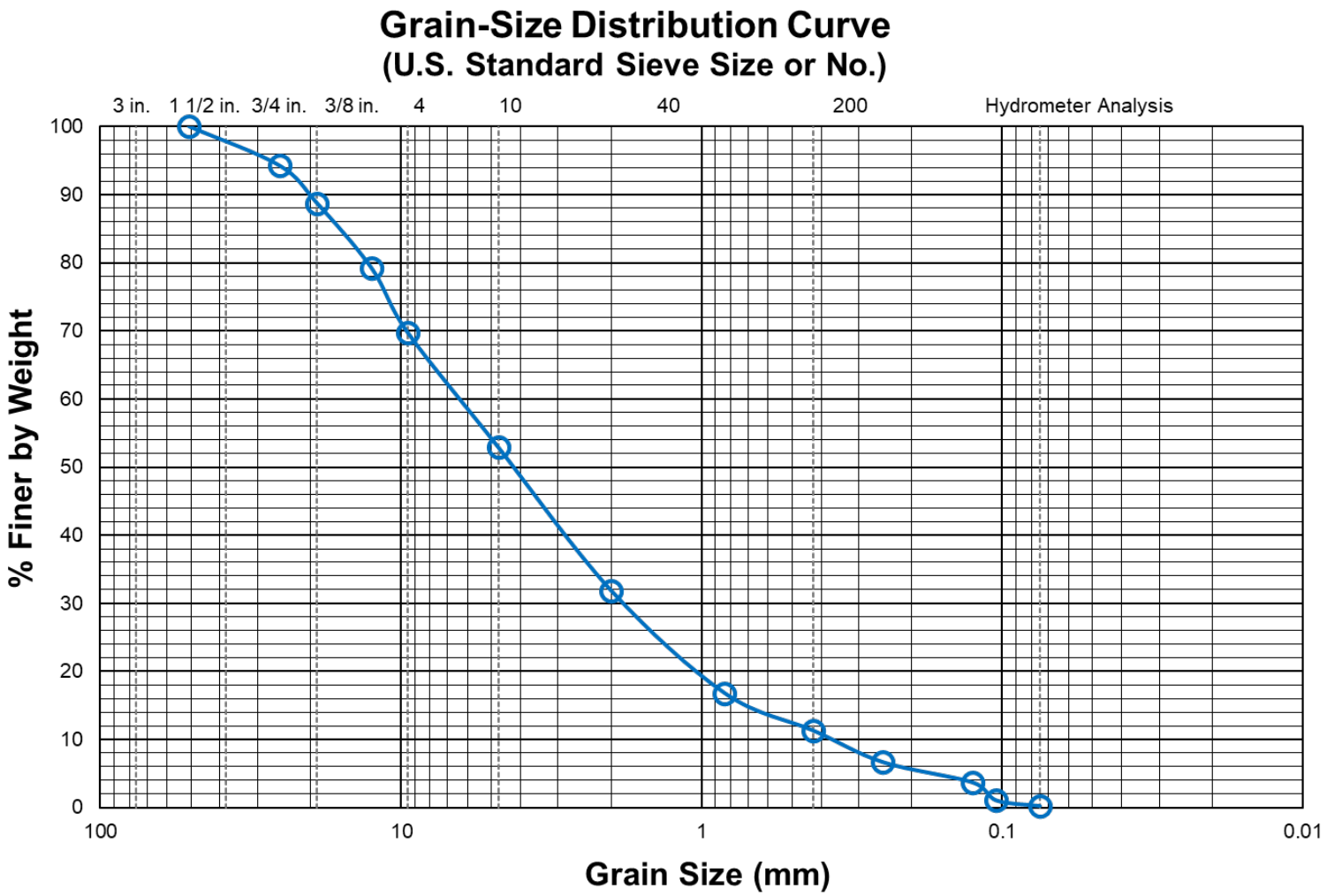

Figure 4.7 Grain-size distribution curve for UTBC material

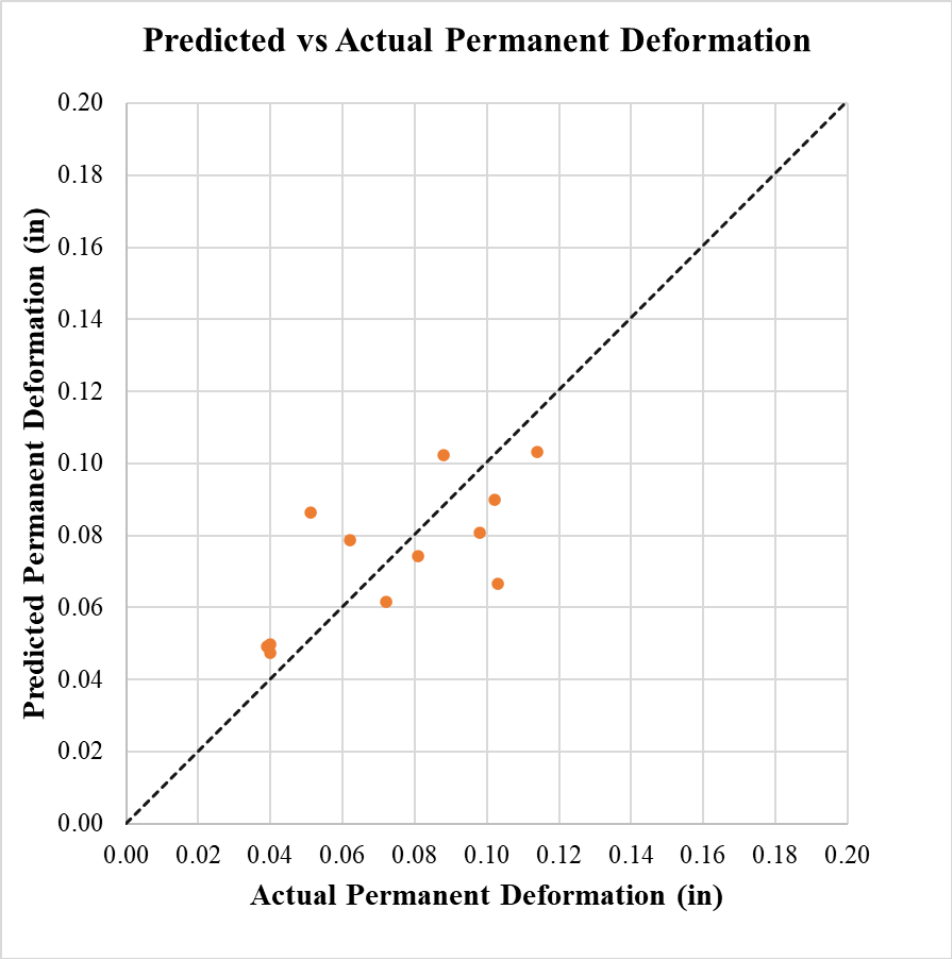

Figure 4.8 Graph showing predicted versus actual values of permanent deformation using the linear regression shown in Table 4.7

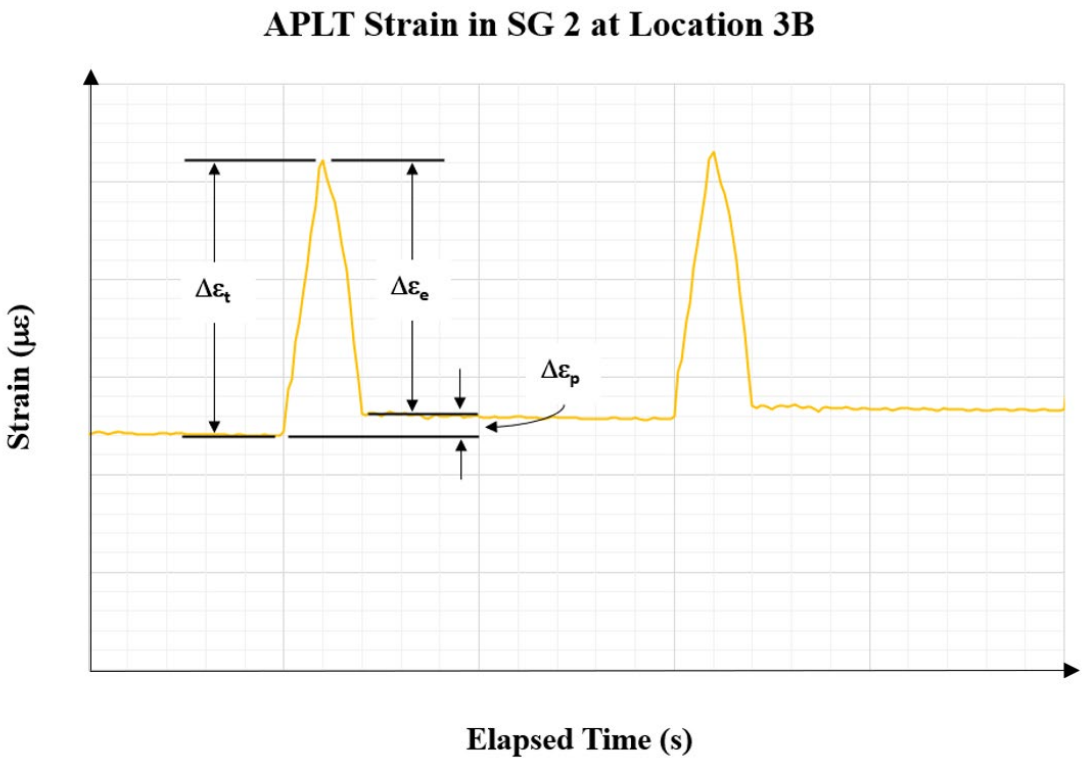

Figure 4.9 Graph showing terms for describing the change in strain experienced in the geosynthetics during APLTs

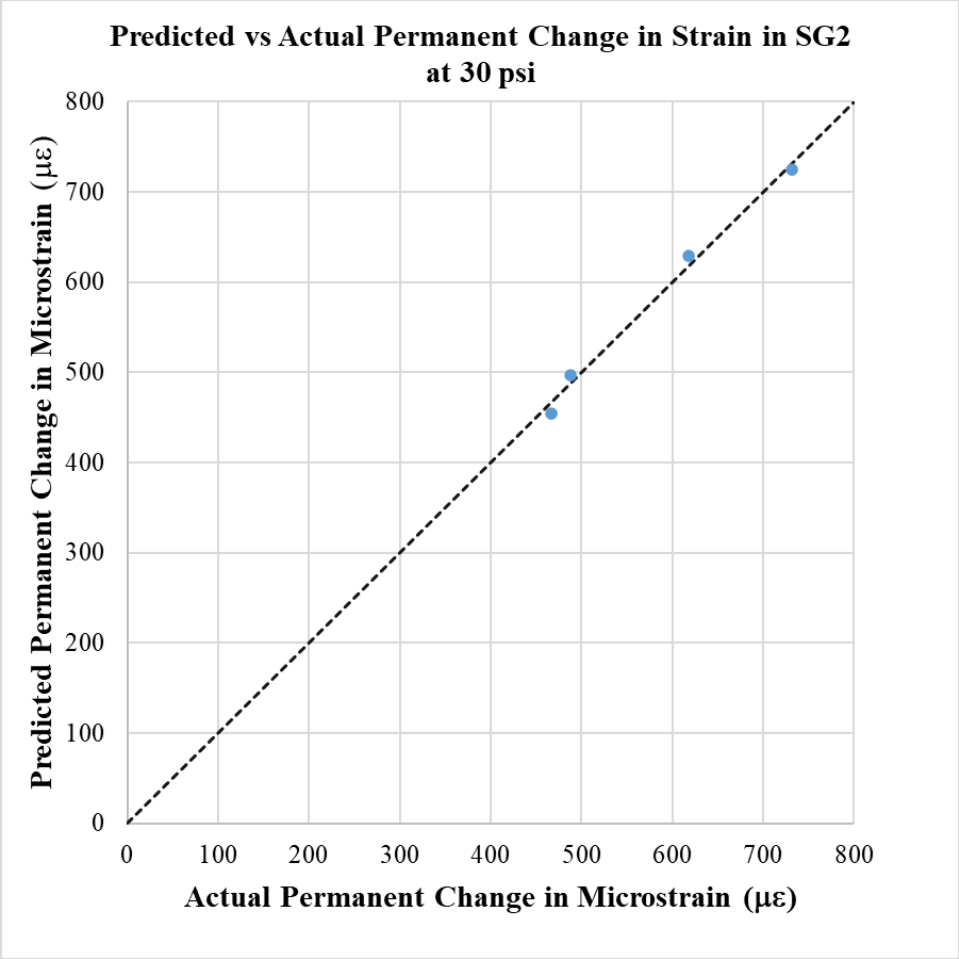

Figure 4.10 Graph of the linear regression results shown in Table 4.11 between Ingios DCP-CBR for the UTBC and the permanent change in strain in SG2 (locations 1B-3B) at the end of the 30 psi load cycles

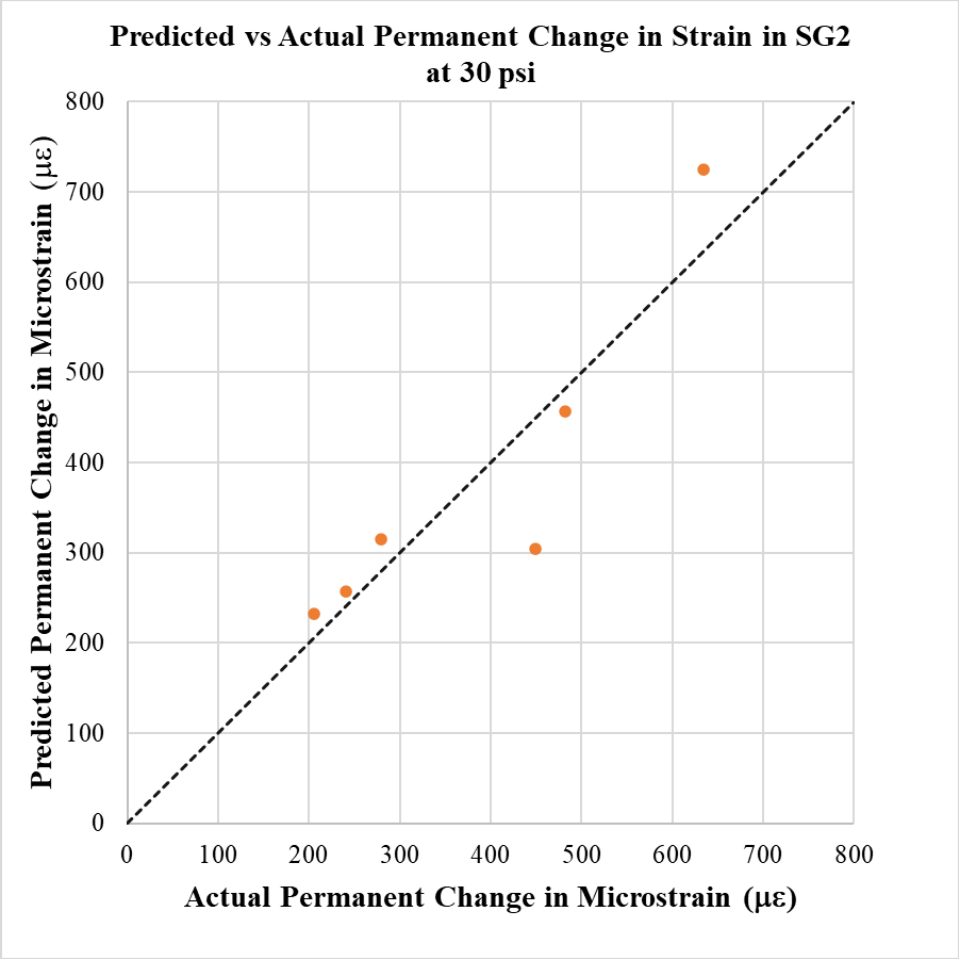

Figure 4.11 Graph of the actual permanent change in microstrain and the predicted permanent change in microstrain based on the linear regression results between Ingios DCP-CBR for the UTBC and the average absolute value of permanent change in strain in the outside strain gages at the UTBC-GB interface as seen in Table 4.12

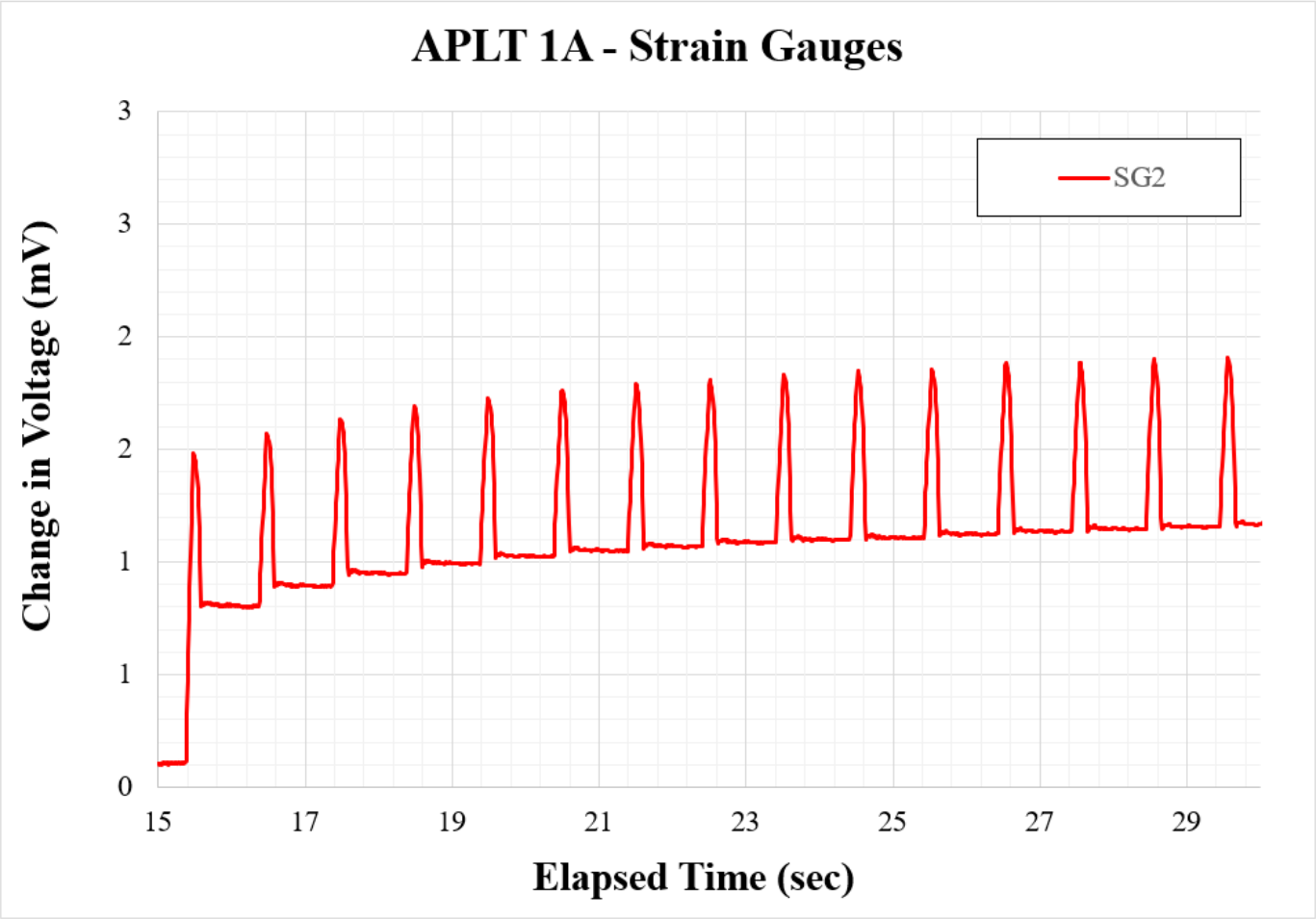

Figure 4.12 Plot of raw data from APLT

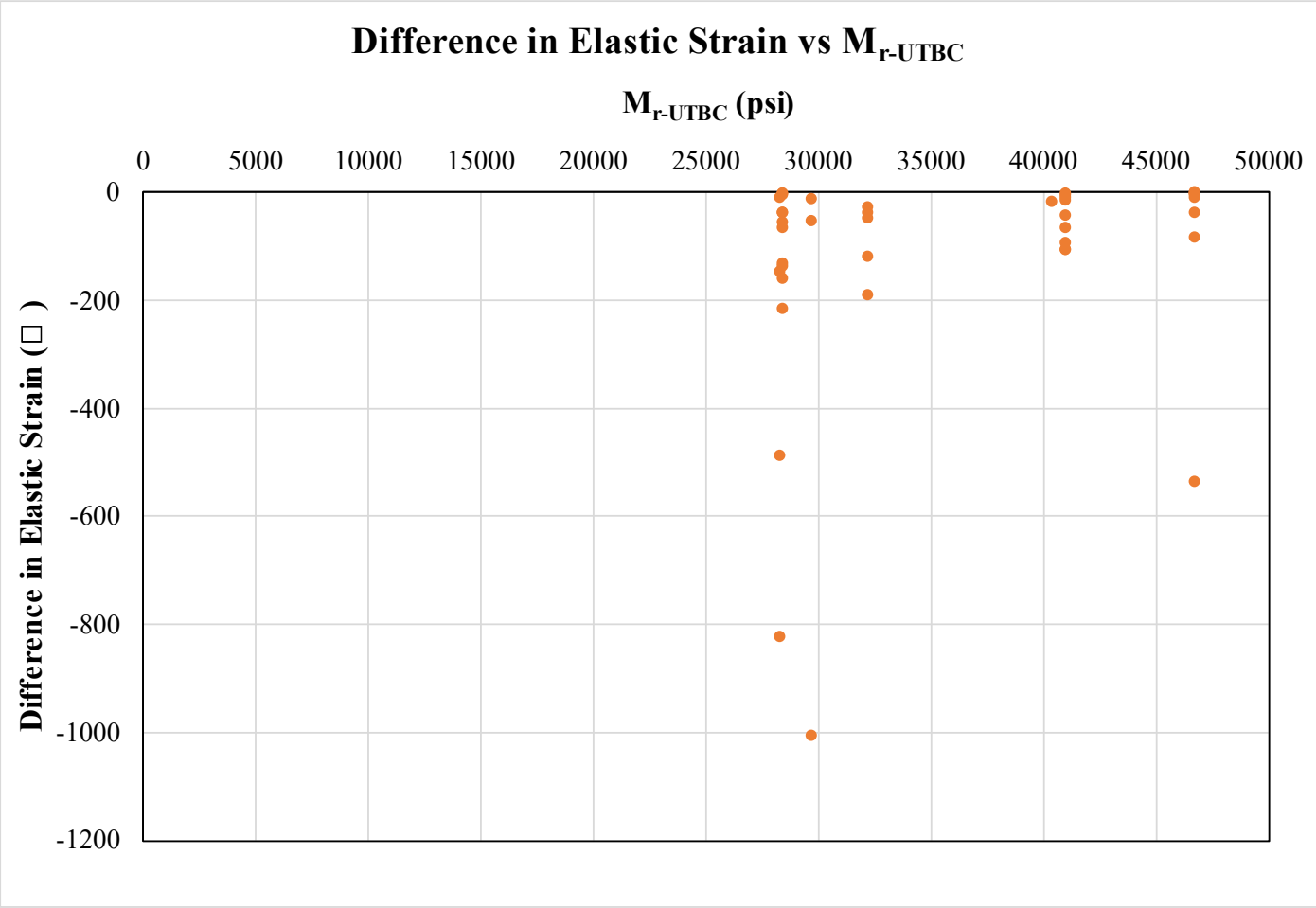

Figure 4.13 Difference in total strain from the beginning to the end of the 30-psi load cycle versus $M_{r\text{-}UTBC}$

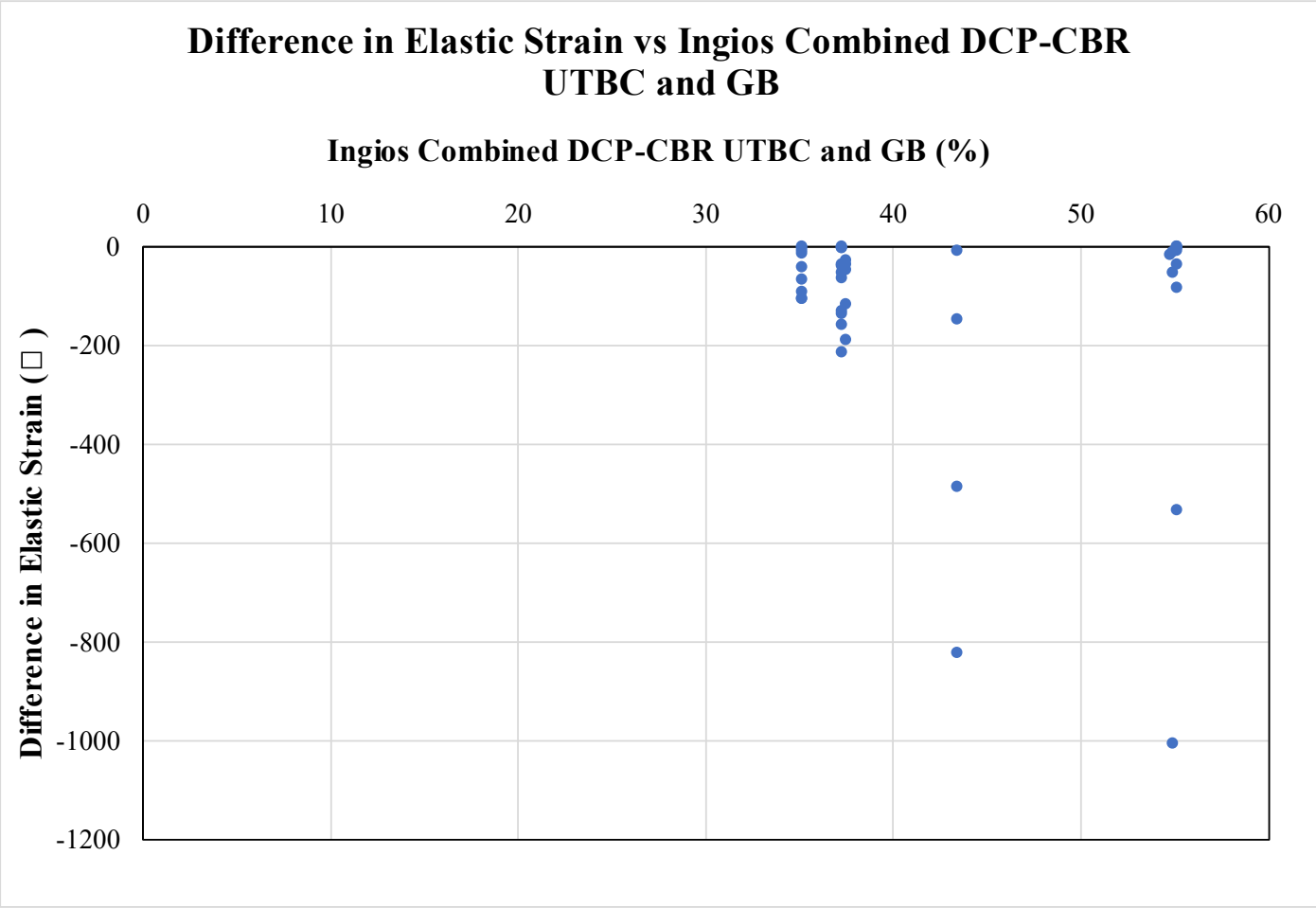

Figure 4.14 Difference in total strain from the beginning to the end of the 30-psi load cycle versus Ingios combined DCP-CBR for UTBC and GB

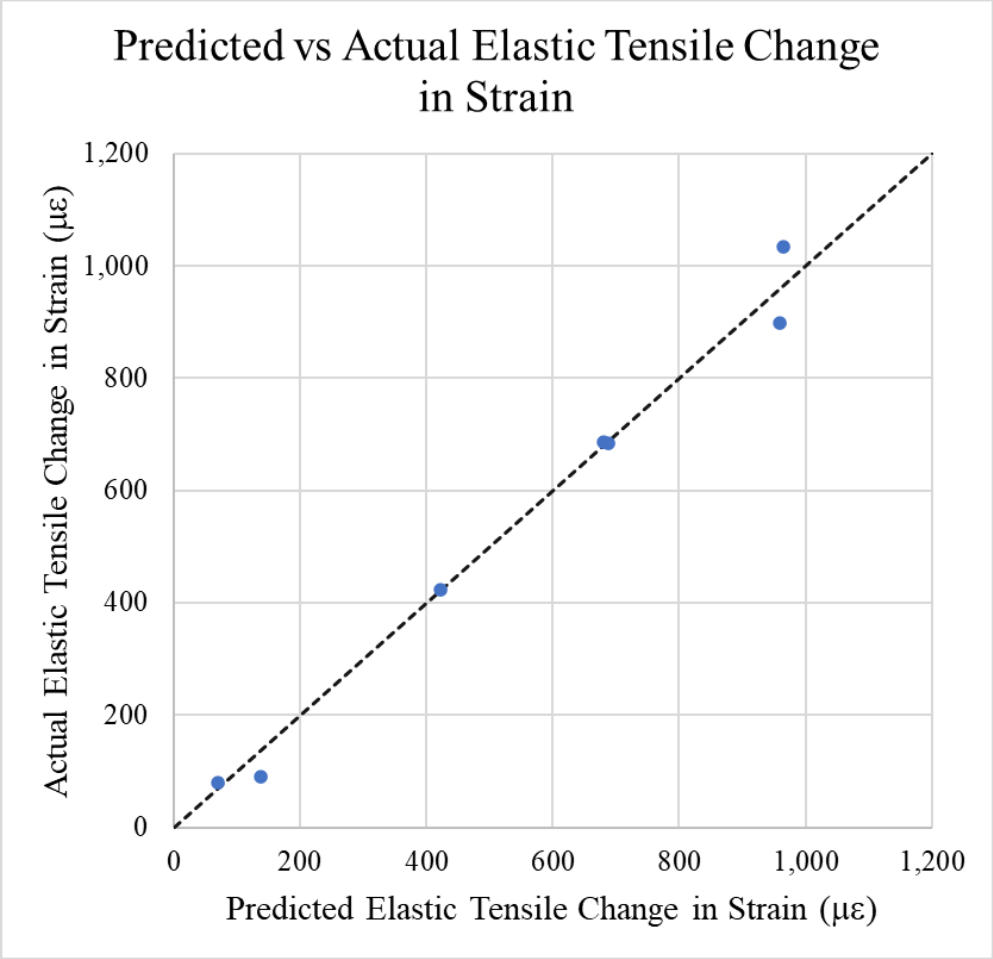

Figure 4.15 Graph showing predicted versus actual tensile change in strain in center strain gages, excluding location 1A

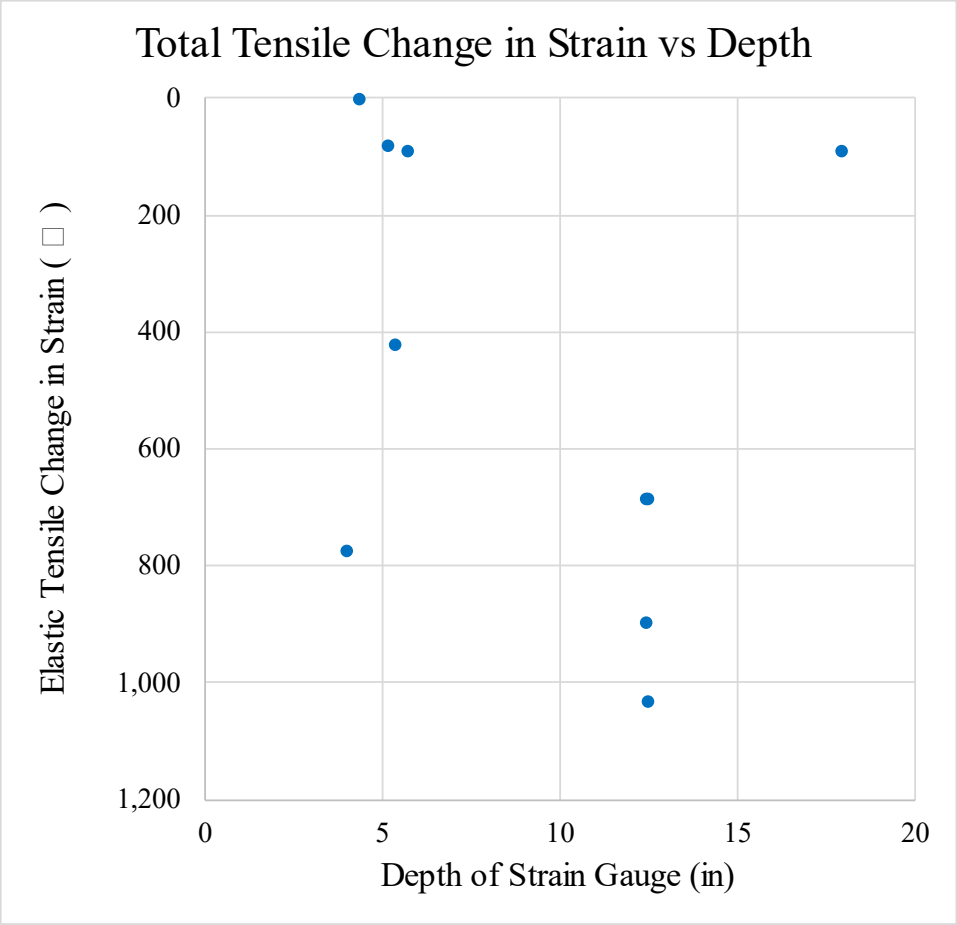

Figure 4.16 Graph showing depth of strain gage versus total tensile change in strain in inside strain gages, excluding location 1A

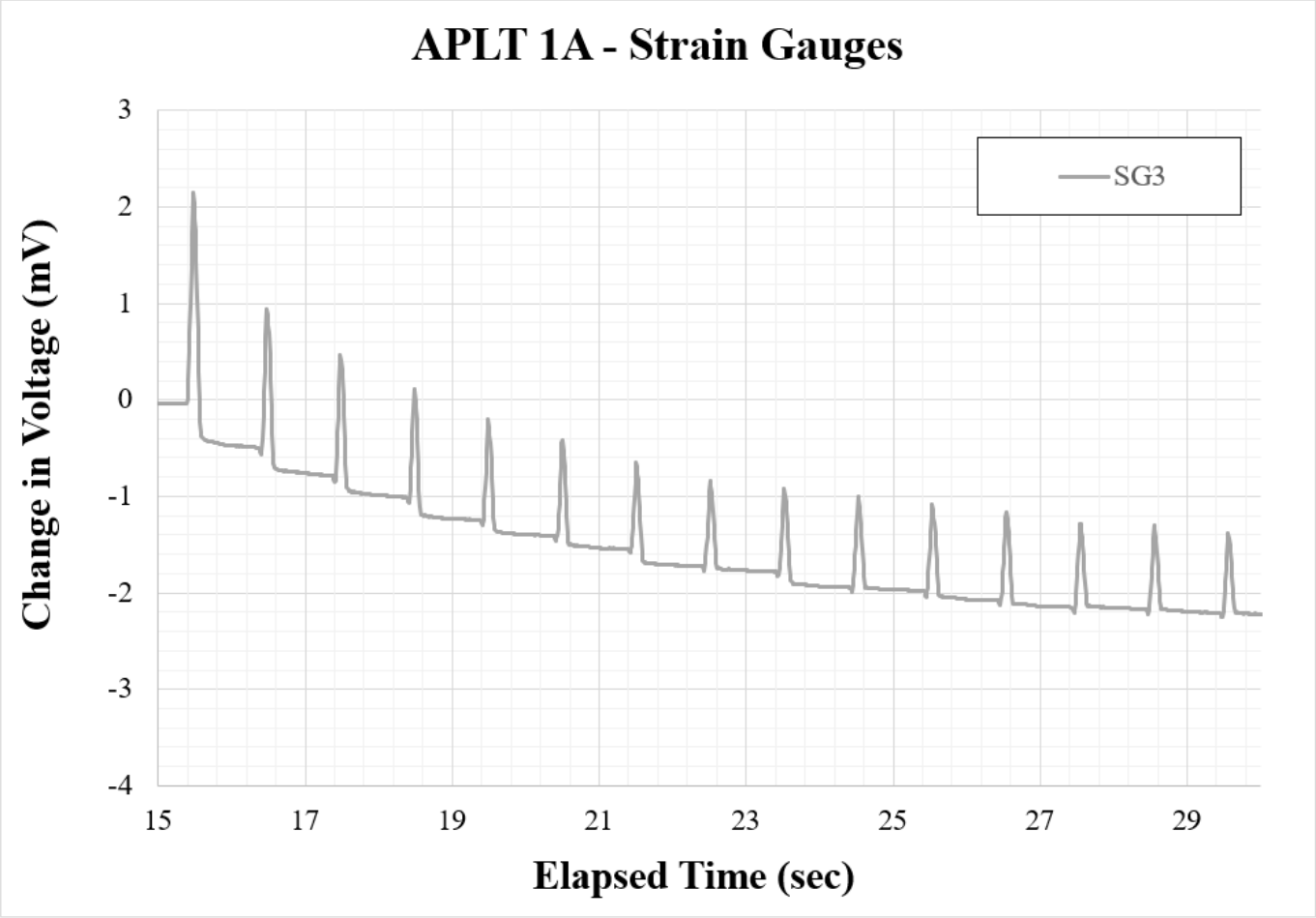

Figure 4.17 Graph of raw data from APLT showing tensile change in strain under load pulses while permanent change in strain becomes more compressive

Figure 4.18 Steel loading plate used in TLT #1

Figure 4.19 Loaded triple-axle dump truck used in TLT #1

Figure 4.20 Photo of truck set of middle dual-passenger wheels centered over loading plate during TLT #1

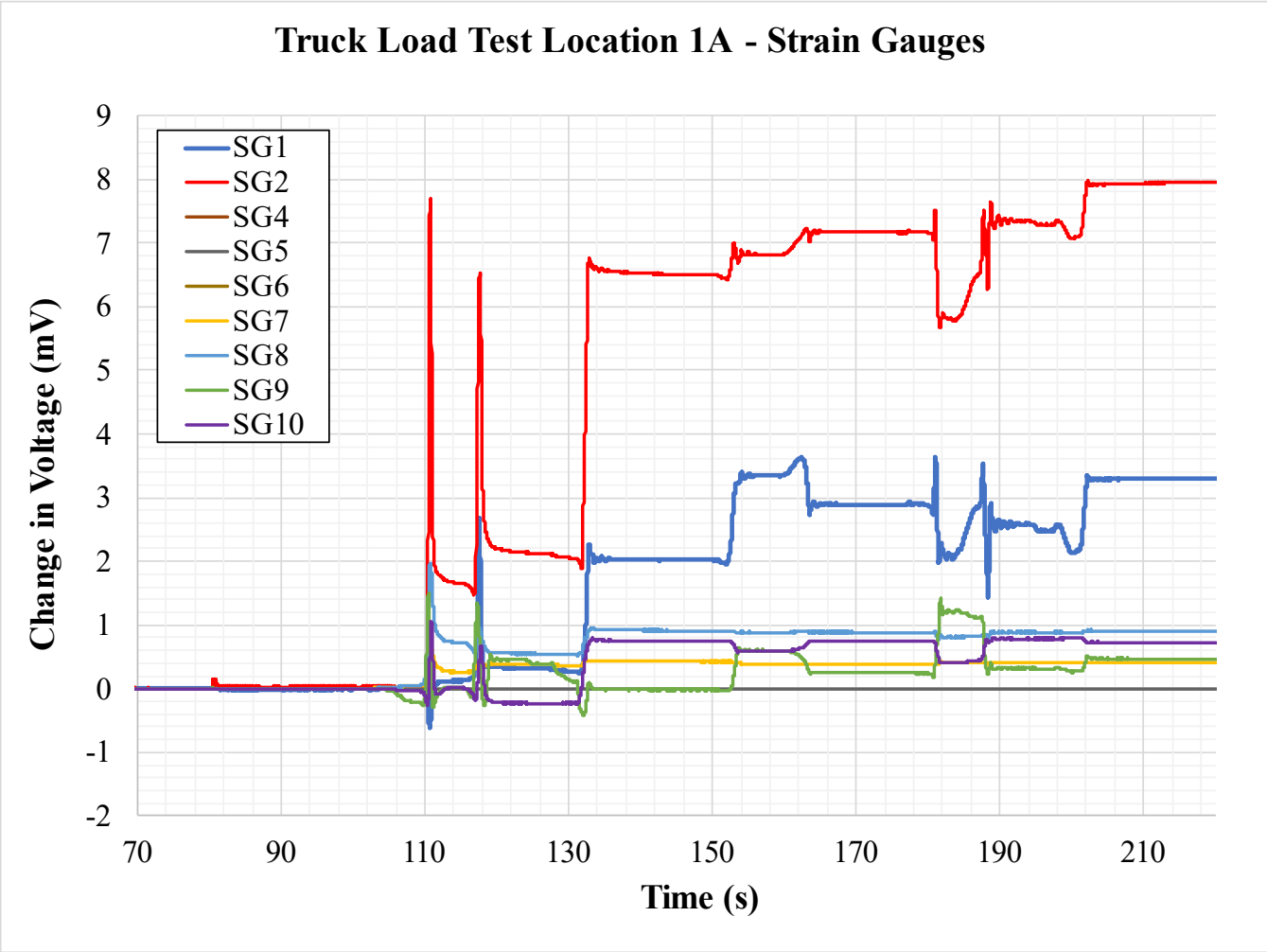

Figure 4.21 Plot showing the raw data readout from the beginning of TLT #1 at 1A

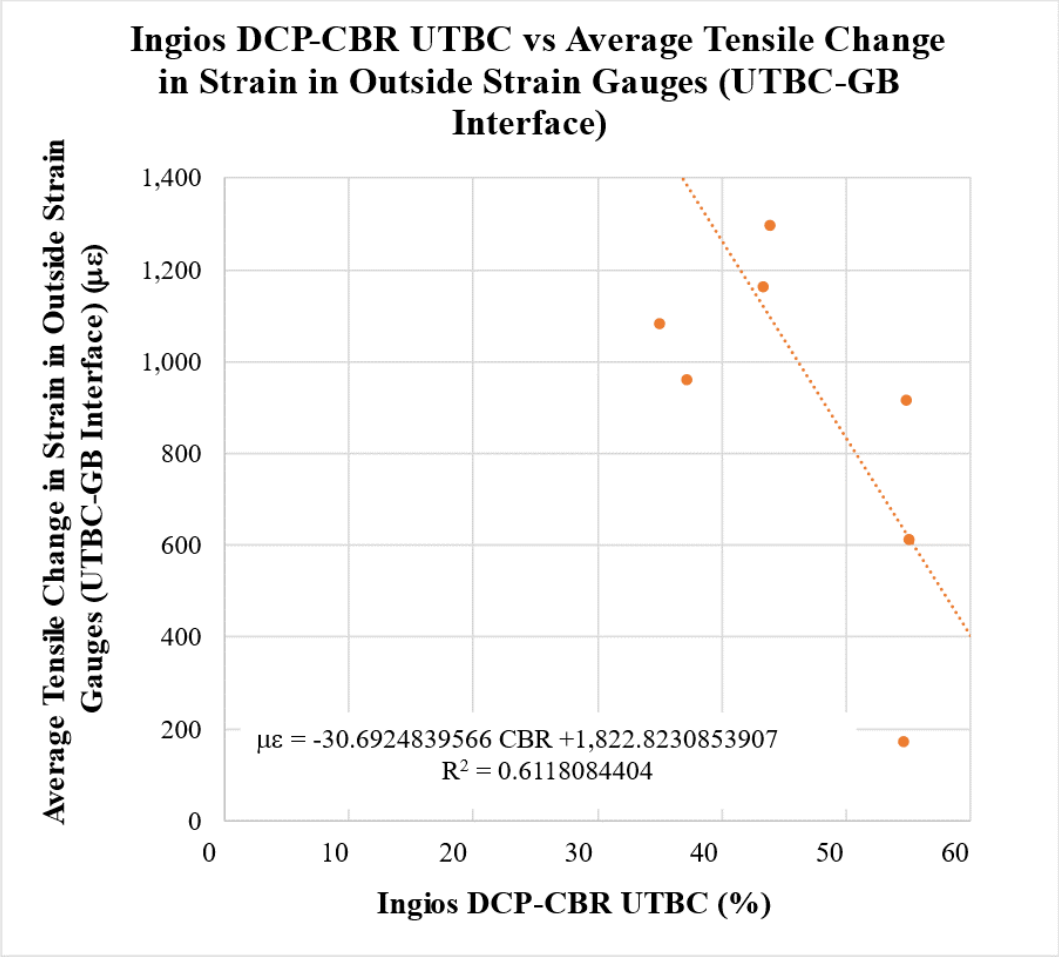

Figure 4.22 Graph of the linear regression results between Ingios DCP-CBR for the UTBC and the average tensile change in strain in the outside strain gages at the UTBC-GB interface

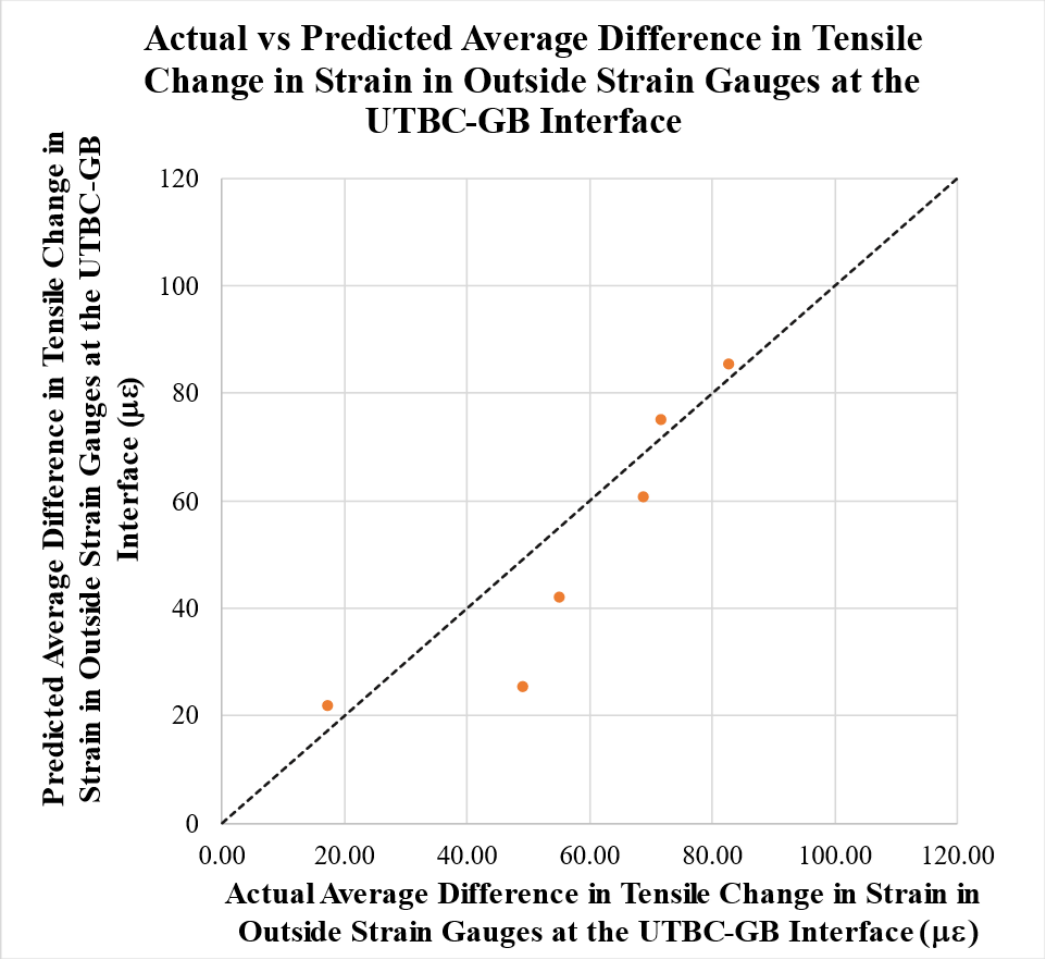

Figure 4.23 Graph of the actual versus predicted average difference in tensile change in strain in outside strain gages at the UTBC-GB interface using the results of the linear regression shown in Table 4.24

Figure 4.24 Water truck used in TLT #2

Figure 4.25 Water truck with driver-side set of dual wheels on the middle axle centered on the 34-inch diameter steel loading plate during TLT #2 at 4B

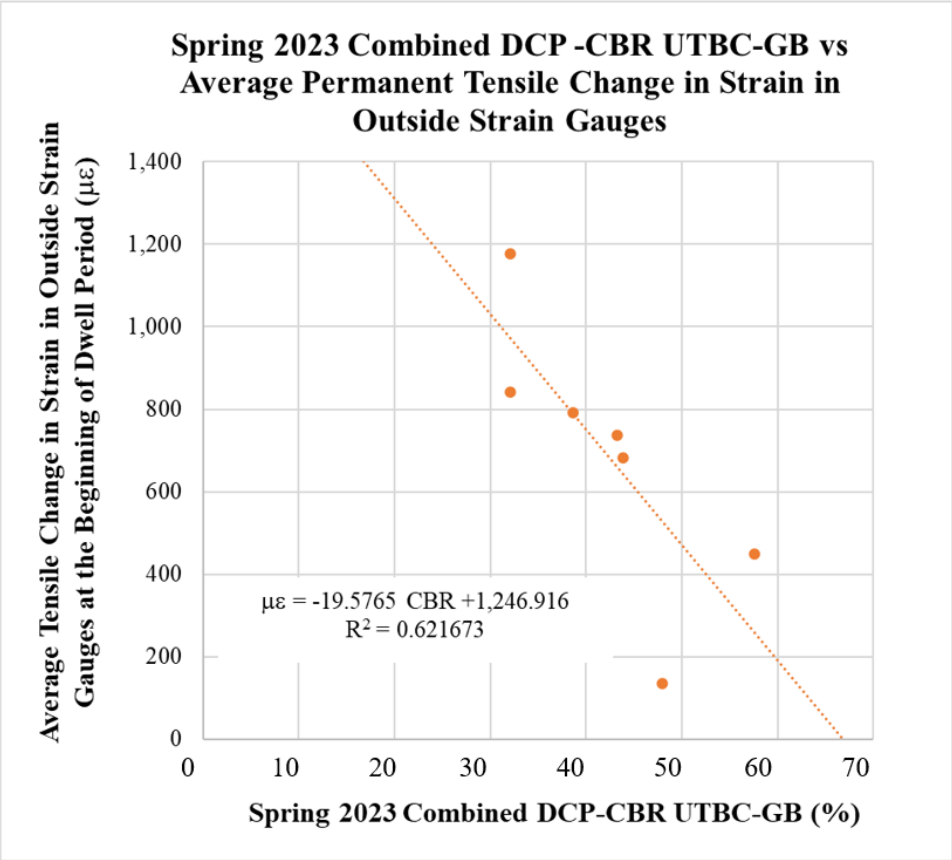

Figure 4.26 Graph of the linear regression results between Spring 2023 combined DCP-CBR UTBC-GB and the average tensile change in strain in the outside strain gages at the beginning of the truck load dwell period

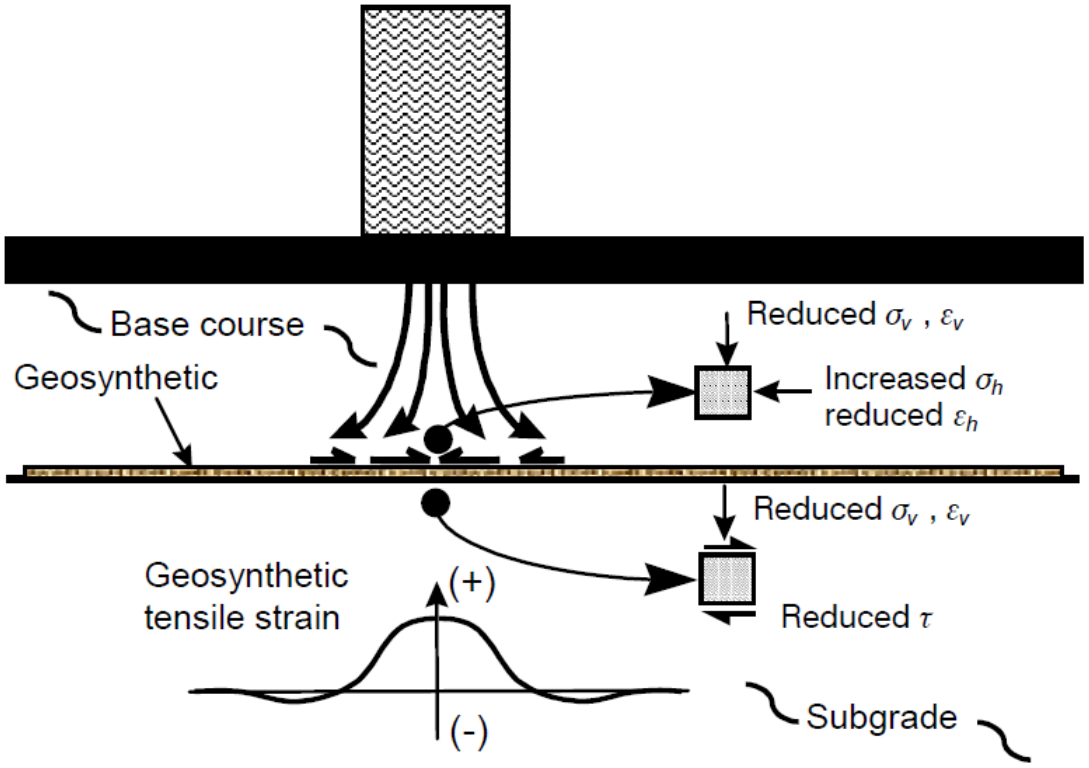

Figure 4.27 Diagram of mechanism of lateral spread, or shear-resistance interface by geosynthetic reinforcement which shows compression in the geosynthetic (Perkins, 1999), courtesy of Emerald Publishing

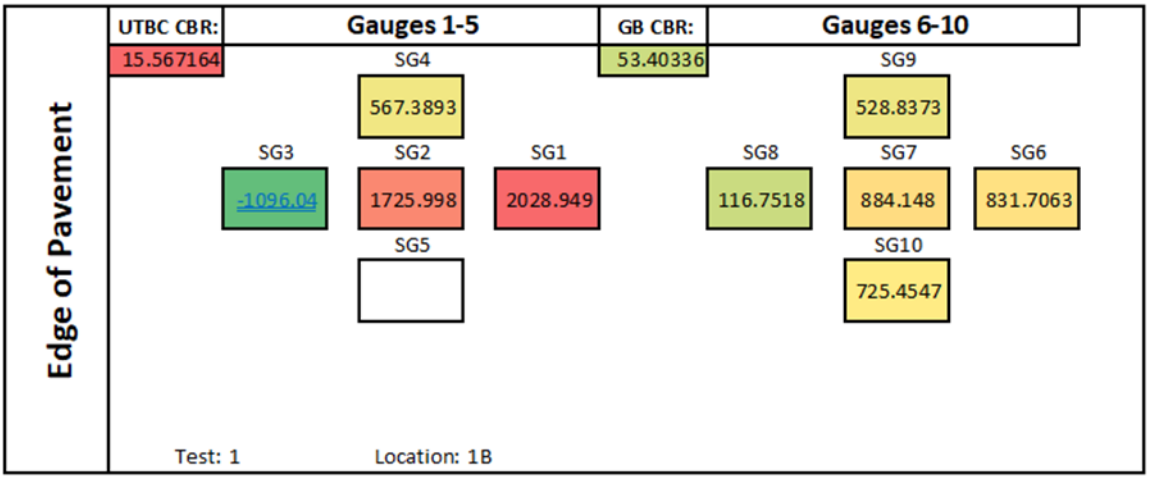

Figure 4.28 Diagram showing the response of the strain gages in an array with a compressive value in the UTBC opposite the maximum tensile change in strain during a TLT

Table 4.1 Table showing CBR values correlated from different sources for the UTBC, GB, and subgrade at A and B test locations

Test Location	UTBC Thickness (in)	GB Thickness (in)	Ingios DCP-CBR of UTBC Layer (%)	DCP-CBR of UTBC Layer (%)	CPT-CBR of UTBC Layer (%)	DCP-CBR of GB Layer Before UTBC (%)	Ingios DCP-CBR of GB Layer After UTBC (%)	CPT-CBR of GB Layer (%)	DCP-CBR of Final Subgrade Layer Before GB (%)	Ingios DCP-CBR of Final Subgrade Layer (%)	DCP-CBR of Final Subgrade Layer Spring 2023 (%)	CPT-CBR of Final Subgrade Layer (%)
1A	4.0	13.9	21.7	16.7	16.7	32.1	42.0	27.1	17.5	24.2	11.9	9.3
1B	5.4	14.0	14.1	21.7	21.7	20.3	55.4	42.8	18.8	15.3	15.3	10.1
2A	5.7	8.1	24.5	28.3	28.3	21.5	76.3	33.5	5.8	11.7	11.0	5.2
2B	4.3	8.5	36.6	15.6	15.6	24.8	64.0	52.2	33.4	16.6	16.7	12.3
3A	6.7	8.2	31.8	32.3	32.3	17.1	53.0	56.5	22.2	23.5	9.6	8.8
3B	5.1	7.6	47.9	21.9	21.9	26.4	60.0	53.6	9.9	19.2	13.6	7.1
4A	3.4	9.0	16.1	14.8	14.8	26.0	42.2	40.6	10.3	12.9	19.7	5.7
4B	4.9	7.6	24.8			16.6	45.2	-	7.1	9.8	11.9	-
Design Thickness	6.0	6.0*										
Average	4.9	8.2*	27.2	21.6	21.6	23.1	54.8	43.7	15.6	16.7	13.7	8.4
Standard Deviation	1.04	0.5*	11.2	6.6	6.6	5.2	11.9	11.0	9.3	5.3	3.4	2.5

*Average and Standard Deviation in GB Thickness for S2-S4 only.

Table 4.2 Table showing the results of the APLT and CPT tests for A and B locations

This table shows the average tensile change in strain in the outside strain gages at the end of the 30 psi loading cycles in the APLTs. It also lists the M_r values and the Ingios DCP-CBR values for the layers in the pavement system and the subgrade.

Test Location	Average Tensile Change in Strain at End of 30 psi Loading Cycles in Outside Strain Gauges, APLT (με)	$\Delta\delta_p$ (in)	$M_{r\text{-comp}}$ (psi)	$M_{r\text{-UTBC}}$ (psi)	$M_{r\ \text{top GB}}$ (psi)	Ingios UTBC Average CBR (%)	Ingios GB Average CBR (%)	Ingios Subgrade Average CBR (%)	Ingios Combined UTBC-GB Avg. CBR (%)
1A	79.6	0.072	16957.0	32184.0	13938.0	26.4	40.0	24.2	37.5
1B	-	0.088	17483.0	37221.0	12716.0	15.6	53.4	100.0	44.0
2A	21.0	0.098	10793.0	29692.0	6214.0	24.0	53.5	11.7	54.9
2B	458.5	0.039	17664.0	40386.0	12539.0	33.5	46.5	39.9	54.7
3A	314.8	0.040	16568.0	28298.0	11691.0	31.7	39.7	23.5	43.4
3B	192.5	0.040	18042.0	46748.0	12341.0	35.1	51.3	19.2	55.1
4A	245.0	0.051	15631.0	40970.0	11061.0	16.4	38.8	12.9	35.1
4B	483.2	0.103	11470.0	28447.0	6650.0	22.5	35.0	9.8	37.2

Table 4.3 Comparison of M_r values at selected stress levels from Test A

Test Location	1,550 cycle test; Step 6 (cyclic stress at surface = 40 psi) Results			$\Delta\delta_p$ at end of test (in.)
	$M_{r\text{-comp}}$ (psi)	$M_{r\text{-UTBC}}$ (psi)	$M_{r\text{-Top of GB}}$ (psi)	
1A	16,957	32,184	13,938	0.072
1B	17,483	37,221	12,716	0.088
2A	10,973	29,692	6,214	0.098
2B	17,664	40,386	12,539	0.039
3A	16,568	28,298	11,691	0.040
3B	18,042	46,748	12,341	0.040
4A	15,631	40,970	11,061	0.051
4B	11,470	28,447	6,650	0.103
Average	15,599	35,493	10,894	0.066
Standard Deviation	2,803	6,862	2,878	0.027

Table 4.4 Table of predicted $M_{r\text{-}comp}$ values and permanent deformation for test locations 1C-4C

Test Location	Predicted $M_{r\text{-}comp}$ at cyclic stress = 40 psi and N = 5,000 cycles	$\Delta\delta_p$ at end of test (in.)
1C	26,598	0.102
2C	19,346	0.051
3C	17,743	0.062
4C	15,395	0.114
Average	19,771	0.082
Standard Deviation	4,832	0.030

Table 4.5 Table showing results of a multi-variable linear regression using $M_{r\text{-}comp}$ values to predict permanent deformation

Regression Statistics	
Multiple R	0.78385379
R Square	0.61442676
Adjusted R Square	0.32524683
Standard Error	0.02242695
Observations	8

ANOVA					
	df	*SS*	*MS*	*F*	*Significance F*
Regression	3	0.003206002	0.001069	2.1247213	0.239829149
Residual	4	0.002011873	0.000503		
Total	7	0.005217875			

	Coefficients	*Standard Error*	*t Stat*	*P-value*	*Lower 95%*	*Upper 95%*	*Lower 95.0%*	*Upper 95.0%*
Intercept	0.21722247	0.06749154	3.218514	0.0323261	0.02983591	0.40460902	0.02983591	0.40460902
Mr-comp (psi)	-1.6388E-05	1.47204E-05	-1.113258	0.3279839	-5.72581E-05	2.4483E-05	-5.726E-05	2.4483E-05
Mr-UTBC (psi)	2.6189E-08	1.86898E-06	0.014013	0.989491	-5.16292E-06	5.2153E-06	-5.163E-06	5.2153E-06
Mr-Top GB (psi)	9.4987E-06	1.30498E-05	0.727884	0.507005	-2.67332E-05	4.5731E-05	-2.673E-05	4.5731E-05

Table 4.6 Table showing multi-variable regression analysis results correlating soil layer properties to permanent deformation

Regression Statistics	
Multiple R	0.78794033
R Square	0.62084997
Adjusted R Square	0.3048916
Standard Error	0.02284605
Observations	12
ANOVA	

	df	*SS*	*MS*	*F*	*Significance F*
Regression	5	0.005128014	0.001026	1.964974	0.217385805
Residual	6	0.003131653	0.000522		
Total	11	0.008259667			

	Coefficients	*Standard Error*	*t Stat*	*P-value*	*Lower 95%*	*Upper 95%*	*Lower 95.0%*	*Upper 95.0%*
Intercept	0.04425584	0.069653879	0.635368	0.5486382	-0.126181058	0.21469275	-0.1261811	0.21469275
UTBC Avg. CBR (Ingios Data)	-0.00326733	0.001158073	-2.821351	0.0303003	-0.006101036	-0.0004336	-0.006101	-0.00043363
UTBC Thickness (in)	0.00945172	0.00821415	1.150664	0.2936551	-0.010647577	0.02955102	-0.0106476	0.02955102
GB Avg. CBR (Ingios Data)	0.00119034	0.000534572	2.226725	0.0675697	-0.000117706	0.00249839	-0.0001177	0.00249839
GB Thickness (in)	0.00226261	0.004579151	0.494112	0.6387932	-0.008942164	0.01346739	-0.0089422	0.01346739
Subgrade Avg. CBR (Ingios Data)	-0.00047065	0.000451955	-1.041359	0.3378399	-0.001576543	0.00063525	-0.0015765	0.00063525

Table 4.7 Table showing results of a multi-variable linear regression using UTBC Avg. CBR (Ingios data) and GB Avg. CBR (Ingios data) to predict permanent deformation

Regression Statistics	
Multiple R	0.71626716
R Square	0.51303864
Adjusted R Square	0.40482501
Standard Error	0.02114011
Observations	12

ANOVA					
	df	*SS*	*MS*	*F*	*Significance F*
Regression	2	0.004237528	0.002119	4.7409797	0.03923966
Residual	9	0.004022138	0.000447		
Total	11	0.008259667			

	Coefficients	*Standard Error*	*t Stat*	*P-value*	*Lower 95%*	*Upper 95%*	*Lower 95.0%*	*Upper 95.0%*
Intercept	0.09154361	0.02944318	3.109162	0.0125358	0.024938509	0.15814871	0.02493851	0.15814871
UTBC Avg. CBR (Ingios Data)	-0.00258983	0.00092887	-2.788156	0.0211174	-0.004691083	-0.0004886	-0.0046911	-0.00048858
GB Avg. CBR (Ingios Data)	0.000958	0.000457169	2.095513	0.0655941	-7.61844E-05	0.00199219	-7.618E-05	0.00199219

Table 4.8 Table showing results of a multi-variable linear regression using UTBC, GB, and subgrade avg. CBR (Ingios data) to predict $M_{r\text{-}comp}$

Regression Statistics	
Multiple R	0.77782965
R Square	0.60501897
Adjusted R Square	0.45690108
Standard Error	2928.28051
Observations	12

ANOVA					
	df	*SS*	*MS*	*F*	*Significance F*
Regression	3	105077103.9	35025701	4.0847124	0.049485165
Residual	8	68598613.74	8574827		
Total	11	173675717.7			

	Coefficients	*Standard Error*	*t Stat*	*P-value*	*Lower 95%*	*Upper 95%*	*Lower 95.0%*	*Upper 95.0%*
Intercept	2855.82539	4352.997135	0.65606	0.5301985	-7182.204	12893.8548	-7182.204	12893.8548
UTBC Avg. CBR (Ingios Data)	206.735912	138.4052507	1.4937	0.1736073	-112.4271683	525.898993	-112.42717	525.898993
GB Avg. CBR (Ingios Data)	126.727838	65.6643928	1.929932	0.08973	-24.6945237	278.150199	-24.694524	278.150199
Subgrade Avg. CBR (Spring 2023)	66.3866251	38.17594508	1.738965	0.1202334	-21.64726207	154.420512	-21.647262	154.420512

Table 4.9 Table showing results of a multi-variable linear regression using UTBC and GB avg. CBR (Ingios data) to predict $M_{r\text{-}comp}$

Regression Statistics	
Multiple R	0.67506756
R Square	0.45571621
Adjusted R Square	0.33476426
Standard Error	3240.86542
Observations	12

ANOVA

	df	*SS*	*MS*	*F*	*Significance F*
Regression	2	79146839.8	39573420	3.7677458	0.064746203
Residual	9	94528877.87	10503209		
Total	11	173675717.7			

	Coefficients	*Standard Error*	*t Stat*	*P-value*	*Lower 95%*	*Upper 95%*	*Lower 95.0%*	*Upper 95.0%*
Intercept	5501.80388	4513.75989	1.218896	0.2538667	-4709.03039	15712.6381	-4709.0304	15712.6381
UTBC Avg. CBR (Ingios Data)	118.042803	142.3995268	0.828955	0.4285663	-204.087307	440.172912	-204.08731	440.172912
GB Avg. CBR (Ingios Data)	156.929277	70.08586201	2.2391	0.0519195	-1.615957407	315.474512	-1.6159574	315.474512

Table 4.10 Table showing results of a linear regression using UTBC avg. CBR (Ingios data) to predict the frequency of outside strain gages in an instrumented location recording compression

Regression Statistics	
Multiple R	0.62703299
R Square	0.39317037
Adjusted R Square	0.2920321
Standard Error	0.05890335
Observations	8

ANOVA					
	df	*SS*	*MS*	*F*	*Significance F*
Regression	1	0.013487928	0.013488	3.8874539	0.096128408
Residual	6	0.020817628	0.00347		
Total	7	0.034305556			

	Coefficients	*Standard Error*	*t Stat*	*P-value*	*Lower 95%*	*Upper 95%*	*Lower 95.0%*	*Upper 95.0%*
Intercept	0.42213363	0.07951309	5.308983	0.0018142	0.227572113	0.61669516	0.22757211	0.61669516
UTBC CBR	-0.00589843	0.002991601	-1.971663	0.0961284	-0.013218613	0.00142176	-0.0132186	0.00142176

Table 4.11 Table showing results of a linear regression using UTBC avg. CBR (Ingios data) and tensile strain in SG2

Regression Statistics	
Multiple R	0.9954001
R Square	0.99082136
Adjusted R Square	0.98623204
Standard Error	14.5285572
Observations	4

ANOVA					
	df	*SS*	*MS*	*F*	*Significance F*
Regression	1	45571.35852	45571.36	215.89719	0.0045999
Residual	2	422.1579503	211.079		
Total	3	45993.51647			

	Coefficients	*Standard Error*	*t Stat*	*P-value*	*Lower 95%*	*Upper 95%*	*Lower 95.0%*	*Upper 95.0%*
Intercept	943.285329	26.01248468	36.26279	0.0007596	831.3626412	1055.20802	831.362641	1055.20802
UTBC CBR Ingios	-13.5713216	0.923631305	-14.69344	0.0045999	-17.54538641	-9.5972569	-17.545386	-9.59725689

Table 4.12 Table showing results of a linear regression using UTBC avg. CBR (Ingios data) and the absolute value of the average strain recorded at the UTBC-GB interface

Regression Statistics	
Multiple R	0.9024089
R Square	0.81434183
Adjusted R Square	0.76792729
Standard Error	89.1927901
Observations	6

ANOVA					
	df	*SS*	*MS*	*F*	*Significance F*
Regression	1	139576.4583	139576.5	17.544972	0.013821303
Residual	4	31821.41523	7955.354		
Total	5	171397.8735			

	Coefficients	*Standard Error*	*t Stat*	*P-value*	*Lower 95%*	*Upper 95%*	*Lower 95.0%*	*Upper 95.0%*
Intercept	975.917849	146.4146309	6.665439	0.0026322	569.4056634	1382.43003	569.405663	1382.43003
UTBC Avg. CBR (Ingios Data)	-21.9464461	5.239476132	-4.188672	0.0138213	-36.49356401	-7.3993283	-36.493564	-7.39932829

Table 4.13 Table showing results of a linear regression using Ingios DCP-CBR for the UTBC layer and the difference in average total tensile change in strain in the outside strain gages from the beginning to the end of the 30 psi load cycle at locations 1B, 2A, 2B, and 3B

Regression Statistics	
Multiple R	0.7574447
R Square	0.5737225
Adjusted R Square	0.3605838
Standard Error	149.46407
Observations	4
ANOVA	

	df	*SS*	*MS*	*F*	*Significance F*
Regression	1	60133.02957	60133.03	2.69178	0.242555275
Residual	2	44679.01511	22339.51		
Total	3	104812.0447			

	Coefficients	*Standard Error*	*t Stat*	*P-value*	*Lower 95%*	*Upper 95%*	*Lower 95.0%*	*Upper 95.0%*
Intercept	445.72319	195.9759249	2.274377	0.150784	-397.4931634	1288.9395	-397.493163	1288.93953
Ingios DCP-CBR UTBC (%)	-9.658332	5.886842049	-1.64066	0.242555	-34.98736897	15.670705	-34.987369	15.6707051

Table 4.14 Table showing results of a linear regression using depth of gage in pavement system, geogrid ultimate tensile strength, and geotextile grab tensile strength and the total tensile change in strain in the center strain gages

Regression Statistics	
Multiple R	0.3573136
R Square	0.127673
Adjusted R Square	-0.30849
Standard Error	442.53001
Observations	10

ANOVA					
	df	*SS*	*MS*	*F*	*Significance F*
Regression	3	171971.5581	57323.85	0.292718	0.829599076
Residual	6	1174996.884	195832.8		
Total	9	1346968.442			

	Coefficients	*Standard Error*	*t Stat*	*P-value*	*Lower 95%*	*Upper 95%*	*Lower 95.0%*	*Upper 95.0%*
Intercept	261.67187	391.0550471	0.669143	0.528297	-695.2053556	1218.5491	-695.205356	1218.5491
Depth of Gauge (in)	18.414594	32.53789089	0.565943	0.591953	-61.20275651	98.031945	-61.2027565	98.0319452
Geogrid Ult. Tensile Strength 1 (lb/in)	0.0004796	0.013752877	0.034874	0.973311	-0.033172455	0.0341317	-0.03317245	0.0341317
Geotextile Grab Tensile Strength (lbs/in)	3.7846427	8.16451644	0.463548	0.659311	-16.19320937	23.762495	-16.1932094	23.7624947

Table 4.15 Table showing results of a linear regression using depth of gage in pavement system, geogrid ultimate tensile strength, and geotextile grab tensile strength to predict the total tensile change in strain in the center strain gages, excluding location 1A

Regression Statistics	
Multiple R	0.9947925
R Square	0.989612
Adjusted R Square	0.9818211
Standard Error	53.652357
Observations	8

ANOVA

	df	*SS*	*MS*	*F*	*Significance F*
Regression	3	1096914.11	365638	127.0204813	0.000201628
Residual	4	11514.30172	2878.575		
Total	7	1108428.412			

	Coefficients	*Standard Error*	*t Stat*	*P-value*	*Lower 95%*	*Upper 95%*	*Lower 95.0%*	*Upper 95.0%*
Intercept	-230.4981	64.14663349	-3.5933	0.022894367	-408.5977054	-52.398492	-408.597705	-52.3984923
Depth of Gauge (in)	121.97193	6.569478979	18.56645	4.95316E-05	103.7321366	140.21173	103.7321366	140.211732
Geogrid Ult. Tensile Strength (lb/in)	-0.013784	0.002593489	-5.31498	0.006025925	-0.020985019	-0.0065837	-0.02098502	-0.00658366
Geotextile Grab Tensile Strength (lbs/in)	-11.7689	1.57218356	-7.4857	0.001703105	-16.13397841	-7.4038157	-16.1339784	-7.40381571

Table 4.16 Table showing results of a linear regression using depth of gage in pavement system and geogrid ultimate tensile strength to predict the total tensile change in strain in the center strain gages, excluding location 1A

Regression Statistics	
Multiple R	0.9187426
R Square	0.8440879
Adjusted R Square	0.7817231
Standard Error	185.91255
Observations	8

ANOVA

	df	*SS*	*MS*	*F*	*Significance F*
Regression	2	935611.0368	467805.5	13.53467841	0.009598412
Residual	5	172817.3748	34563.47		
Total	7	1108428.412			

	Coefficients	*Standard Error*	*t Stat*	*P-value*	*Lower 95%*	*Upper 95%*	*Lower 95.0%*	*Upper 95.0%*
Intercept	-345.6125	215.7949025	-1.60158	0.170148821	-900.3309905	209.10592	-900.33099	209.105923
Depth of Gauge (in)	93.512043	18.56470858	5.037086	0.003976745	45.78994002	141.23415	45.78994002	141.234145
Geogrid Ult. Tensile Strength (lb/in)	0.0007268	0.005970024	0.121746	0.907841574	-0.014619608	0.0160733	-0.01461961	0.01607327

Table 4.17 Table showing results of a linear regression using depth of gage in pavement system to predict the total tensile change in strain in the center strain gages, excluding location 1A

Regression Statistics								
Multiple R	0.918491							
R Square	0.8436257							
Adjusted R Square	0.8175634							
Standard Error	169.96553							
Observations	8							
ANOVA								
	df	*SS*	*MS*	*F*	*Significance F*			
Regression	1	935098.7309	935098.7	32.36948434	0.001272395			
Residual	6	173329.6807	28888.28					
Total	7	1108428.412						
	Coefficients	*Standard Error*	*t Stat*	*P-value*	*Lower 95%*	*Upper 95%*	*Lower 95.0%*	*Upper 95.0%*
Intercept	-329.4523	155.5476847	-2.11801	0.078498497	-710.0637403	51.159206	-710.06374	51.1592057
Depth of Gauge (in)	92.895066	16.32769044	5.689419	0.001272395	52.94264694	132.84749	52.94264694	132.847485

Table 4.18 Table showing results of a linear regression using geogrid ultimate tensile strength to predict the total tensile change in strain in the center strain gages, excluding location 1A

Regression Statistics								
Multiple R	0.2300439							
R Square	0.0529202							
Adjusted R Square	-0.104926							
Standard Error	418.28423							
Observations	8							
ANOVA								
	df	*SS*	*MS*	*F*	*Significance F*			
Regression	1	58658.24573	58658.25	0.335263361	0.583643564			
Residual	6	1049770.166	174961.7					
Total	7	1108428.412						
	Coefficients	*Standard Error*	*t Stat*	*P-value*	*Lower 95%*	*Upper 95%*	*Lower 95.0%*	*Upper 95.0%*
Intercept	597.3629	241.4965109	2.473588	0.048222559	6.44222982	1188.2836	6.44222982	1188.28358
Geogrid Ultimate Tensile Strength	-0.007482	0.012921811	-0.57902	0.583643564	-0.03910051	0.0241366	-0.03910051	0.02413655

Table 4.19 Table showing the total tensile change in strain and the predicted tensile change in strain for the inside gages, using the linear regression shown in Table 4.15

Location	Strain Gauge	Elastic Tensile Change in Strain Inside Gauges (με)	Predicted Elastic Tensile Change in Strain Inside Gauges (με)
1B	2	422.3	422.3
2A	2	90.5	137.4
2B	2	0.6	-29.4
3B	2	80.6	70.1
4A	7	897.5	958.5
4A	12	685.3	681.2
4B	7	1033.2	965.8
4B	12	684.5	688.6

Table 4.20 Table showing the average change in tensile strain in the outside strain gages at the beginning of the truck load dwell time

Test Location	Average Change in Tensile Strain at Start of Truck Load Dwell Time in Outside Strain Gauges (με)
1A	916.6
1B	799.8
2A	854.6
2B	172.8
3A	1163.8
3B	611.7
4A	1313.0
4B	1211.0

Table 4.21 Table showing results of a linear regression using UTBC avg. CBR (Ingios data) and the absolute value of the average strain recorded at the UTBC-GB interface from TLT #1

Regression Statistics	
Multiple R	0.78218185
R Square	0.61180844
Adjusted R Square	0.54710985
Standard Error	248.971313
Observations	8

ANOVA

	df	*SS*	*MS*	*F*	*Significance F*
Regression	1	586164.1416	586164.1	9.4562866	0.021799052
Residual	6	371920.2896	61986.71		
Total	7	958084.4312			

	Coefficients	*Standard Error*	*t Stat*	*P-value*	*Lower 95%*	*Upper 95%*	*Lower 95.0%*	*Upper 95.0%*
Intercept	2409.2095	504.8868363	4.771781	0.0030888	1173.795913	3644.62308	1173.79591	3644.62308
Combined Ingiost DCP-CBR for UTBC and GB	-33.7789548	10.98464166	-3.075108	0.0217991	-60.65740462	-6.9005049	-60.657405	-6.90050492

Table 4.22 Table showing results of a linear regression using the combined Ingios DCP-CBR average for the UTBC and GB and the average change in strain in the outside strain gages at the UTBC-GB interface from TLT #1

Regression Statistics	
Multiple R	0.74164486
R Square	0.5500371
Adjusted R Square	0.47504328
Standard Error	312.478276
Observations	8

ANOVA					
	df	*SS*	*MS*	*F*	*Significance F*
Regression	1	716153.6091	716153.6	7.3344326	0.035189432
Residual	6	585856.0385	97642.67		
Total	7	1302009.648			

	Coefficients	*Standard Error*	*t Stat*	*P-value*	*Lower 95%*	*Upper 95%*	*Lower 95.0%*	*Upper 95.0%*
Intercept	2682.52995	633.6720728	4.233309	0.0054801	1131.990248	4233.06966	1131.99025	4233.06966
UTBC Avg. CBR (Ingios Data)	-37.337022	13.78657582	-2.708216	0.0351894	-71.07155777	-3.6024863	-71.071558	-3.60248626

Table 4.23 The percentage of strain gages that recorded a greater change in strain at the end of the dwell period in TLT #1

Test Section	Strain Gauges Reporting Greater Change in Strain at End of Dwell Period, TLT #1 (%)
1A	0.0
1B	56.0
2A	33.3
2B	0.0
3A	60.0
3B	14.0
4A	75.0
4B	0.0

Table 4.24 Table showing results of a linear regression using the average Ingios DCP-CBR value for the UTBC and the weighted composite DCP-CBR by thickness to predict the difference in the change in strain from the beginning to the end of the dwell period in TLT #1

Only data from the strain gages that recorded a tensile change in strain during TLT #1 were considered in this correlation. Of these gages, only the ones that recorded a decrease in change in strain from the beginning to the end of the dwell period were used in the correlation.

Regression Statistics	
Multiple R	0.9023005
R Square	0.8141463
Adjusted R Square	0.6902438
Standard Error	12.802306
Observations	6

ANOVA	*df*	*SS*	*MS*	*F*	*Significance F*
Regression	2	2153.916464	1076.958	6.570863	0.080122945
Residual	3	491.6971427	163.899		
Total	5	2645.613606			

	Coefficients	*Standard Error*	*t Stat*	*P-value*	*Lower 95%*	*Upper 95%*	*Lower 95.0%*	*Upper 95.0%*
Intercept	63.9036	29.1038831	2.195707	0.115635	-28.71794562	156.52514	-28.71794562	156.525145
UTBC Avg. CBR (Ingios Data)	-4.021079	1.109531838	-3.62412	0.036142	-7.55210484	-0.4900538	-7.55210484	-0.4900538
Weighted Composite DCP-CBR by Thickness (%)	2.2025168	0.87266814	2.523888	0.085883	-0.574702672	4.9797363	-0.574702672	4.97973633

Table 4.25 Table showing results of a linear regression using the average Ingios DCP-CBR value for the UTBC to predict the difference in the change in strain from the beginning to the end of the dwell period in TLT #1

Regression Statistics	
Multiple R	0.64770066
R Square	0.41951614
Adjusted R Square	0.27439518
Standard Error	19.5942338
Observations	6

ANOVA

	df	*SS*	*MS*	*F*	*Significance F*
Regression	1	1109.877617	1109.878	2.8908032	0.164309453
Residual	4	1535.735989	383.934		
Total	5	2645.613606			

	Coefficients	*Standard Error*	*t Stat*	*P-value*	*Lower 95%*	*Upper 95%*	*Lower 95.0%*	*Upper 95.0%*
Intercept	112.572994	33.36340603	3.374146	0.0279363	19.94132846	205.204659	19.9413285	205.204659
UTBC Avg. CBR (Ingios Data)	-2.02409479	1.190478578	-1.700236	0.1643095	-5.329393206	1.28120363	-5.3293932	1.28120363

Table 4.26 Table showing results of a linear regression using the average Ingios DCP-CBR value for the UTBC to predict the difference in the change in strain from the beginning to the end of the dwell period in TLT #1

The same specifications used in the regression shown in Table 4.13 were used here.

Regression Statistics	
Multiple R	0.27126185
R Square	0.07358299
Adjusted R Square	-0.15802126
Standard Error	24.7534919
Observations	6

ANOVA					
	df	*SS*	*MS*	*F*	*Significance F*
Regression	1	194.6721621	194.6722	0.31771	0.603087355
Residual	4	2450.941444	612.7354		
Total	5	2645.613606			

	Coefficients	*Standard Error*	*t Stat*	*P-value*	*Lower 95%*	*Upper 95%*	*Lower 95.0%*	*Upper 95.0%*
Intercept	20.4733092	66.46617186	0.308026	0.7734361	-164.0663683	205.012987	-164.06637	205.012987
GB Avg. CBR (Ingios Data)	0.83895966	1.488420431	0.563658	0.6030874	-3.293557965	4.97147728	-3.293558	4.97147728

Table 4.27 Table showing results of a linear regression using the average Ingios DCP-CBR value for the UTBC to predict the difference in the change in strain from the beginning to the end of the dwell period in TLT #1

The same specifications used in the regression shown in Table 4.13 were used here.

Regression Statistics	
Multiple R	0.02150123
R Square	0.0004623
Adjusted R Square	-0.24942212
Standard Error	25.7118189
Observations	6

ANOVA

	df	*SS*	*MS*	*F*	*Significance F*
Regression	1	1.223074865	1.223075	0.0018501	0.967753124
Residual	4	2644.390532	661.0976		
Total	5	2645.613606			

	Coefficients	*Standard Error*	*t Stat*	*P-value*	*Lower 95%*	*Upper 95%*	*Lower 95.0%*	*Upper 95.0%*
Intercept	59.9734211	58.4108902	1.026751	0.3625693	-102.2012091	222.148051	-102.20121	222.148051
Combined Ingios DCP-CBR for UTBC and GB	-0.05284807	1.228670561	-0.043012	0.9677531	-3.46418444	3.35848829	-3.4641844	3.35848829

Table 4.28 Table showing the average tensile change in strain in the outside strain gages at the start of the truck load dwell time in TLT #1 and TLT #2

Test Section	Average Tensile Strain at End of 30 psi Loading Cycles in Outside Strain Gauges, APLT (με)	Average Tensile Strain at Start of 85 psi Truck Load Dwell Time in Outside Strain Gauges, TLT #1 (με)	Average Tensile Strain at Start of 9 psi Truck Load Dwell Time in Outside Strain Gauges, TLT #2 (με)
1	79.6	858.2	2317.3
2	218.8	513.7	718.2
3	253.7	887.7	883.4
4	364.1	1262.0	1651.8

Table 4.29 Table showing several comparisons between average changes in strain from TLT #1 and TLT #2

Truck Load Test	Average Change in Compressive Strain in All Strain Gauges (με)	Average Change in Tensile Strain in All Strain Gauges (με)	Average Change in Tensile Strain in Outside Strain Gauges (με)
#1	-337.4	1049.8	982.9
#2	-419.7	1434.6	1594.5

Table 4.30 Table showing regression statistics for the correlation between Spring 2023 CBR UTBC and GB composite and the average tensile change in strain at the start of the dwell time in the outside strain gages

Regression Statistics								
Multiple R	0.7884624							
R Square	0.621673							
Adjusted R Square	0.5460076							
Standard Error	151.15442							
Observations	7							
ANOVA								
	df	*SS*	*MS*	*F*	*Significance F*			
Regression	1	187718.1699	187718.2	8.21608	0.03514349			
Residual	5	114238.2945	22847.66					
Total	6	301956.4644						
	Coefficients	*Standard Error*	*t Stat*	*P-value*	*Lower 95%*	*Upper 95%*	*Lower 95.0%*	*Upper 95.0%*
Intercept	1246.916	293.4151819	4.249664	0.00809	492.6682509	2001.1637	492.668251	2001.1637
CBR UTBC and GB Composite	-19.57655	6.829733988	-2.86637	0.03514	-37.1329371	-2.020157	-37.1329371	-2.0201569

Table 4.31 Table showing regression statistics for the correlation between $M_{r\ top\ of\ GB}$ and the difference in tensile change in strain from the start to the end of the dwell time in the outside strain gages

Regression Statistics	
Multiple R	0.78258198
R Square	0.61243455
Adjusted R Square	0.53492146
Standard Error	27.667115
Observations	7

ANOVA

	df	*SS*	*MS*	*F*	*Significance F*
Regression	1	6048.008366	6048.008	7.9010468	0.037509313
Residual	5	3827.346262	765.4693		
Total	6	9875.354628			

	Coefficients	*Standard Error*	*t Stat*	*P-value*	*Lower 95%*	*Upper 95%*	*Lower 95.0%*	*Upper 95.0%*
Intercept	148.669862	40.78566395	3.64515	0.0148233	43.82697465	253.512748	43.8269746	253.512748
Mr top GB (psi)	-0.01027948	0.003657033	-2.81088	0.0375093	-0.019680186	-0.0008788	-0.0196802	-0.00087878

Table 4.32 The percentage of operational strain gages in each A and B test location that reported an increase in tensile change in strain at the end of the truck load dwell time in TLT #1 and TLT #2

Test Section	Strain Gauges Reporting Increase in Change in Tensile Strain at End of Dwell Period, TLT #1 (%)	Strain Gauges Reporting Increase in Change in Tensile Strain at End of Dwell Period, TLT #2 (%)
1A	0.0	0.0
1B	56.0	14.3
2A	33.3	0.0
2B	0.0	0.0
3A	60.0	75.0
3B	14.0	75.0
4A	75.0	11.1
4B	0.0	8.3

Table 4.33 Table showing the average change in tensile strain at the end of the truck load dwell time for TLT #1 and TLT #2 and the difference in change in tensile strain from the start to end of the dwell time for each of the two tests

Test Location	Average Change in Tensile Strain at End of Truck Load Dwell Time, TLT #1 (με)	Difference in Change in Strain from Start and End of Truck Load Dwell Time, TLT #1 (με)	Average Change Tensile Strain at End of Truck Load Dwell Time, TLT #2 (με)	Difference in Change in Strain from Start and End of Truck Load Dwell Time, TLT #2 (με)
1A	296.6	-620.1	689.1	-13.9
1B	400.1	-399.8	3870.0	-61.6
2A	273.2	-581.3	1250.7	-49.2
2B	29.4	-143.4	122.0	-14.6
3A	124.8	-1038.9	797.8	5.1
3B	188.4	-423.3	939.6	-34.5
4A	986.6	-326.4	2150.8	-28.7
4B	948.0	-263.0	1007.2	-116.9

5. SUMMARY, CONCLUSION, AND RECOMMENDATIONS

5.1 Summary

In fall 2022, four test locations were instrumented on a 970-foot stretch of the West Davis Corridor UDOT project. One control section and three geosynthetic-reinforced test sections were included in the study. The control section was constructed with a design thickness of 12 inches of GB and six inches of UTBC (S1). S2-S4 had six inches of GB and six inches of UTBC. S2 had one layer of BX1200 geogrid installed at the interface between the UTBC and the GB layers. S3 was the same as S2, with the addition of a layer of GT-180 nonwoven geosynthetic at the GB-subgrade interface. S4 added a layer of BX1200 geogrid on top of the GT-180 geotextile at the GB-subgrade interface to form a geocomposite.

Each test section was instrumented with two instrument arrays, one at its east end and one at its west end. These two locations were designated “location A” and “location B.” The instrument arrays included temperature and moisture sensors at the tops of the UTBC layer, the GB layer, and the subgrade. An array of five strain gages was also installed at the UTBC-GB interface and the GB-subgrade interface. Three of the strain gages in each array were oriented transversely across the road and two were oriented longitudinally down the road.

The strain gages were bonded to the geosynthetics in locations reinforced with geosynthetics, and they were attached to small coupons of geotextile at the interfaces that were not reinforced. Each location had at least 10 strain gages, except for S4, which had 15 strain gages — five on the geogrid at the UTBC-GB interface, five on the geogrid at the GB-subgrade interface, and five on the geotextile at the GB-subgrade interface (Figure 3.8 through Figure 3.12).

As much data as possible was collected to characterize the test locations. DCP testing was used extensively to characterize the subgrade strength through a CBR correlation. DCP testing was also performed on the GB and UTBC layers. DCP testing was performed after the GB was placed and compacted, the UTBC was placed and compacted, after the APLTs, and in spring 2023 before TLT #2 was performed. Each layer of the pavement system was surveyed, so exact thicknesses of the layers could be ascertained. NDT was performed at the test locations after the APLTs and TLT #1 were completed, as were CPT soundings.

After the GB, UTBC, and all of the geosynthetics and instruments were installed, the first tests to be performed were the APLTs. The APLTs were performed at every instrumented location with a trailer mounted APLT field system from Ingios. An Incremental Cyclic Mr Test (Test A) was performed at the A and B test locations, and a Random Loading Sequence Extended Cycle Test (Test B) was performed at the center of each of the test locations. The APLTs used a 12-inch diameter loading plate during cyclic loading. In the case of Test A, the cyclic stress went up to 40 psi and lasted for approximately 20 minutes. Test B used random cyclic loading from 5 to 50 psi. The data collected during the APLTs was the displacement of the loading plate during the cyclic loads, the displacement of the top of the UTBC surface at 2 and 3 radii from the center of the load, and strain data from the strain gage arrays in the case of Test A. The stress applied and the displacement of the plate and at 2 and 3 radii was used to determine the M_r of the pavement system at each test location. In Test A and B, an $M_{r\text{-}comp}$ value was determined for the entire pavement system, and in Test A, an Mr was determined for the UTBC layer (M_r-UTBC) and for the top of the GB layer ($M_{r\text{-}Top}$ of GB).

The strain data was recorded using a CR9000x with three CR9052DC filter modules. Data was sent to a computer, and RTDAQ software was utilized to build a program to collect the data. The strain gages were sampled every 100th of a second for the duration of the tests. Temperature and water content data was also collected.

The second set of tests performed were TLTs. The first TLT was performed the week after the APLTs. A triple-axle loaded dump truck was used to statically load each test location. The passenger set of dual tires from the center axle was centered on top of a 12-inch diameter, half-inch-thick steel plate and allowed to dwell for approximately 10 minutes. During this period, strain data was acquired using the same process as during the APLTs, as were temperature and water content data.

In spring 2023, additional DCP testing was performed at the test locations. CPT soundings were also performed in the spring to collect data about the UTBC and GB layers and to characterize the subgrade. TLTs were again performed, using a loaded triple-axle water truck. A 34-inch diameter, one-inch-thick steel plate was used as the loading plate. The driver-side set of dual wheels on the middle axle of the truck were centered on the loading plate over the strain gage arrays in each test section. The truck was left to dwell for 15 minutes while strain gage readings were collected, as were temperature measurements and water content measurements.

5.2 Conclusions

Analysis of data from the experiments was inconclusive in terms of determining benefits of the geosynthetic reinforcement in the pavement system. In several cases, the most reinforced test sections performed the worst. What was determined was that the CBR of the soil layers in the pavement system heavily impacts its performance. The CBR of the soil layers showed the greatest correlation in predicting the deflection and strain measured during the APLTs and TLTs.

What was discovered about geosynthetic reinforcement was the depth of the reinforcement and the geosynthetic properties correlated strongly with the level of total strain in the geosynthetics. In this analysis, this correlation was not able to be connected to the permanent deflection, the resilient modulus, or the CBR of the pavement system. It did, however, show that in some cases increasing the depth of the geosynthetic increased the level of total strain in the geosynthetic, and that greater tensile strength in the geosynthetics decreased the amount of strain experienced. It was also shown that the geosynthetics respond very quickly to loads applied to the pavement system. Changes in strain were registered at the very beginning of the loading cycles during the APLTs. The amount of strain in the geosynthetics increased when the CBR of the UTBC decreased, and the amount of strain decreased when the CBR increased. The geosynthetics were acting as an integrated part of the pavement system, but at the level of strain and deflection that was experienced during the tests that were performed, they were unable to provide significant reinforcement.

Greater insight into field instrumentation of geosynthetics was obtained, as was more information about how geosynthetics behave during cyclic loading in the field. It was also found that tensile properties of geosynthetics can impact their total strain response to loading in a pavement system. It was discovered that compression was experienced in-plane in geosynthetics during loading. The exact reasons for this were hypothesized but not determined. The impact of the variability in real construction was seen in the data. Its effect on the ability of a geosynthetic to perform in real construction was also seen. Results obtained from this study would not have been the same if it had been performed in the laboratory. The results were a much better representation of the reality of geosynthetics use in a pavement system. The results that were pursued were not obtained, but other insights and valuable information were discovered.

5.3 Recommendations and Further Research

Performing a large-scale research project on an actual job site proved difficult. The instrumentation was installed by the research team, but preparation of the subgrade, thicknesses of the UTBC and GB, and compaction and quality control of the compaction were all under the control and direction of the contractor. Normal construction is performed at a different level of accuracy than research. The average thickness of the GB was 2.2 inches thicker than specified in the experimental design, and the UTBC was 1.1 inches thinner than specified, with a standard deviation of 1.04 inches. An even greater factor in the success of the research was the variation in the CBR of the GB and UTBC. Standard deviation in the GB layer was 11.9, and standard deviation of the CBR for the UTBC layer was 11.2 (Table 4.1).

These variations in CBR greatly impacted results of the study and made comparisons between the test sections difficult. One recommendation for other studies similar to this one would be to make sure construction and quality control of the pavement system is under the direction of the researchers. Less variation in construction of the test sections would have made analysis and performance much more comparable, and the results would have had greater significance.

Another aspect of this type of research project that was difficult was field instrumentation of geosynthetics with strain gages. In the end, failure rate of the instruments was 33.3%. Survivability of the instrumentation in the harsh conditions of construction was a difficult factor to deal with. The arrays of five strain gages were utilized to have redundancy in the instrumentation. These redundancies were useful but making direct comparisons between the strain gages was difficult. If a better way could be implemented to build redundancy into the experiment that also made direct comparisons easy and efficient, it would be helpful for further research. One way strain gages could have been more redundant and comparable in failure would be to install strain gages on the top and bottom of the geosynthetic at the same location. This has been done in previous studies, and while it is not easy to accomplish, it would help in comparing data in the event of instrument failure.

There are several aspects of further research that would add to the body of knowledge in geosynthetics and draw further conclusions from this research project. Perhaps the most important area of further research is to more fully understand the relationship between the geosynthetic properties and the total change in strain in geosynthetics in pavement systems under loading. Greater insight could be obtained by furthering studying this relationship and how this phenomenon impacts the performance of a pavement system is vital.

Another main subject of further research would be long-term performance of geosynthetics in roadways. Initial results of the study were largely inconclusive, but with the instrumentation installed, a long-term study would be beneficial. The research section is in the West Davis Corridor, which will be a major artery for traffic onto Interstate 15. The research section will experience high volumes of traffic over the next decade.

As the pavement system undergoes the stress of traffic, it is inevitable that the system will begin to deteriorate. When the roadway settles and degrades, it is expected that the geosynthetic reinforcement will play a significant role in how well the road performs in the long term. The difference in performance between the test sections after several years of traffic would give more information into how the geosynthetic reinforcement affects longevity of the pavement system. There would be greater insights and more significant results from the research if a long-term study was conducted. Not many studies are conducted long-term with instrumentation in actual major roadways. Research in this area would be valuable to understanding the long-term performance of geosynthetic-reinforced pavement systems.

Another area of further research would be continued analysis of the data already collected. Simple linear regressions were used with the data. There are more powerful statistical tools that could be utilized to further analyze the data. More conclusions could be drawn, and there is an opportunity to better understand the impact of CBR and the geosynthetic properties on the performance of the geosynthetic reinforced test sections.

Further research is also needed to understand how the APLT can measure and predict the performance of pavement systems reinforced by geosynthetics. The use of the APLT to determine the M_r of a pavement system is a relatively new development in geotechnical engineering in the United States and will become more widespread as time goes on. There is not a large body of research using APLTs with geosynthetic-reinforced pavement systems. It is a topic of further research that would be of interest and benefit to the field.

6. REFERENCES

Al-Qadi, I. L., and Appea, A. K. 2003. “Eight-year field performance of secondary road incorporating geosynthetics at subgrade-base interface.” Transp. Res. Rec., 1849 (1), 212–220.

Al-Qadi, I. L., Brandon, T. L., Valentine, R. J., Lacina, B. A., and Smith, T. E. 1994. “Laboratory evaluation of geosynthetic-reinforced pavement sections.” Transp. Res. Rec., 5 (1439), 25–31.

Aran, S. 2006. “Base reinforcement with biaxial geogrid.” Transportation Research Record, 1975 (1), 114–123.

Arbianto, R., Yuono, T., and Gunarso, G. 2021. “Comparison of California bearing ratio (CBR) value based on cone penetration test (CPT) and dynamic cone penetrometer (DCP).” JACEE, 4 (2), 70–78.

ASTM (American Society for Testing and Materials). 2020. Standard terminology for geosynthetics. ASTM D4439-20, West Conshohocken, PA: ASTM.

ASTM (American Society for Testing and Materials). 2018. Standard test method for use of the dynamic cone penetrometer in shallow pavement applications. ASTM D6951/D6951M–18, West Conshohocken, PA: ASTM.

Bathurst, R. J., and Raymond, G. P. 1987. “Geogrid reinforcement of ballasted track.” Transp. Res. Rec., 50 (1153), 8–14.

Beckham, W. K., and Mills, W. H. 1935. “Cotton-fabric-reinforced roads.” Eng. News Rec., 115 (14), 453–455.

Chen, J.-F., Gu, Z.-A., Rajesh, S., and Yu, S.-B. 2021. “Pullout behavior of triaxial geogrid embedded in a transparent soil.” Int. J. Geomech., 21 (3), 04021003.

Cuelho, E., and Perkins, S. 2009. Field investigation of geosynthetics used for subgrade stabilization, Report No. FHWA/MT-009-003/8193. Bozeman, MT: Western Transportation Institute, Montana State University.

Cuelho, E., and Perkins, S. 2017. “Geosynthetic subgrade stabilization – Field testing and design method calibration.” Transp. Geotech., 10, 22–34.

Das, B. M., and Shin, E. C. 1994. “Strip foundation on geogrid-reinforced clay: Behavior under cyclic loading.” Geotext. Geomembr., 13 (10), 657–667.

Dash, S. K., and Majee, A. 2021. “Geogrid reinforcement for stiffness improvement of railway track formation over clay subgrade.” Int. J. Geomech., 21 (9), 04021163.

David, J. W. and Vennapusa, P. K. R., 2017. “In situ resilient modulus for geogrid-stabilized aggregate layer: A case study using automated plate load testing.” Transp. Geotech., 11, 120–132.

Feng, W.-Q., Li, C., Yin, J.-H., Chen, J., and Liu, K. 2019. “Physical model study on the clay–sand interface without and with geotextile separator.” Acta Geotech., 14 (6), 2065–2081.

Giroud, J. P., and Han, J. 2004. “Design method for geogrid-reinforced unpaved roads. I. Development of design method.” J. Geotech. Geoenviron. Eng., 130(8), 775–786.

Holtz, R. D., Christopher, B. R., and Berg, R. R. 1998. Geosynthetic design and construction guidelines, Publication No. FHWA HI-95-038. Washington, DC: Federal Highway Administration.

Holtz, R. D., Christopher, B. R., and Berg, R. R. 2008. Geosynthetic design and construction guidelines, Publication No. FHWA-NHI-07-092. Washington, DC: Federal Highway Administation.

Jensen, Martha L., and Hill, Jay C., cartographers. 2018. Geologic map of the Farmington Quadrangle, Salt Lake and Davis Counties, Utah. Utah Geologic Survey, Map 279DM. Salt Lake City, UT: UGS.

Perkins, S., and Cuelho, E. 1999. "Soil-geosynthetic interface strength and stiffness relationships from pullout tests." Geosynthetics Intl., 6 (5), 321–346.

Perkins, S. W. 1999. "Mechanical response of geosynthetic-reinforced flexible pavements." Geosynth. Int., 6 (5), 347–382.

Perkins, S. W., and Lapeyre, J. A. 1997. "Instrumentation of a geosynthetic-reinforced flexible pavement system." Transp. Res. Rec., 1596 (1), 31–38.

Qian, Y., Han, J., Pokharel, S. K., and Parsons, R. L. 2010. "Experimental study on triaxial geogrid-reinforced bases over weak subgrade under cyclic loading." In Geoflorida 2010: Adv. in Anal., Model. and Des., Reston, VA: ASCE, 1208–1216.

Webster, S. L. 1993. Geogrid reinforced base courses for flexible pavements for light aircraft: Test section construction, behavior under traffic, laboratory tests, and design criteria, Technical Report GL-93-6. Washington, DC: U.S. Department of Transportation Federal Aviation Administration.

APPENDIX: CBR CORRELATION DATA FROM CPT AND DCP

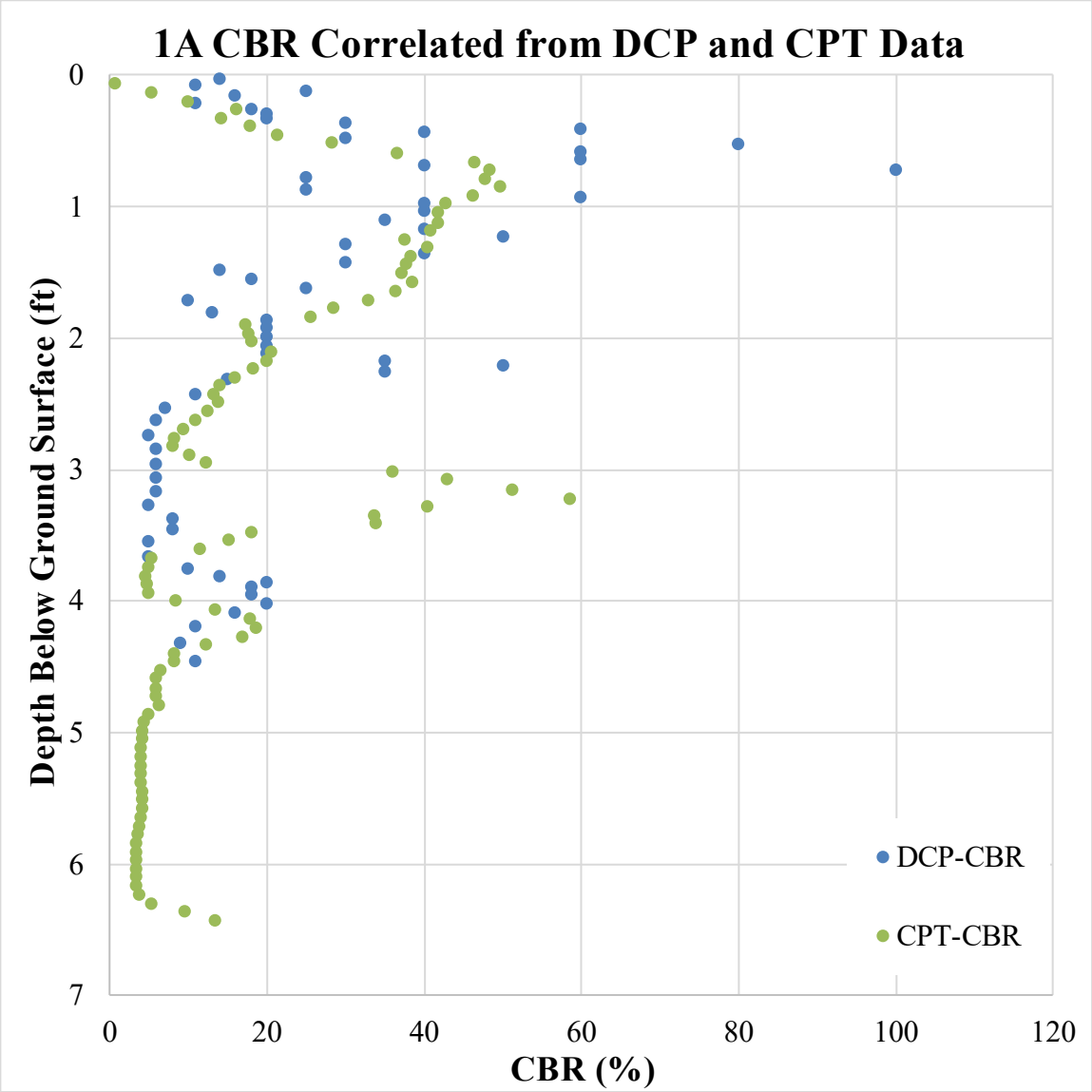

Figure A.1 Graph of correlated DCP and CPT data to CBR values for location 1A

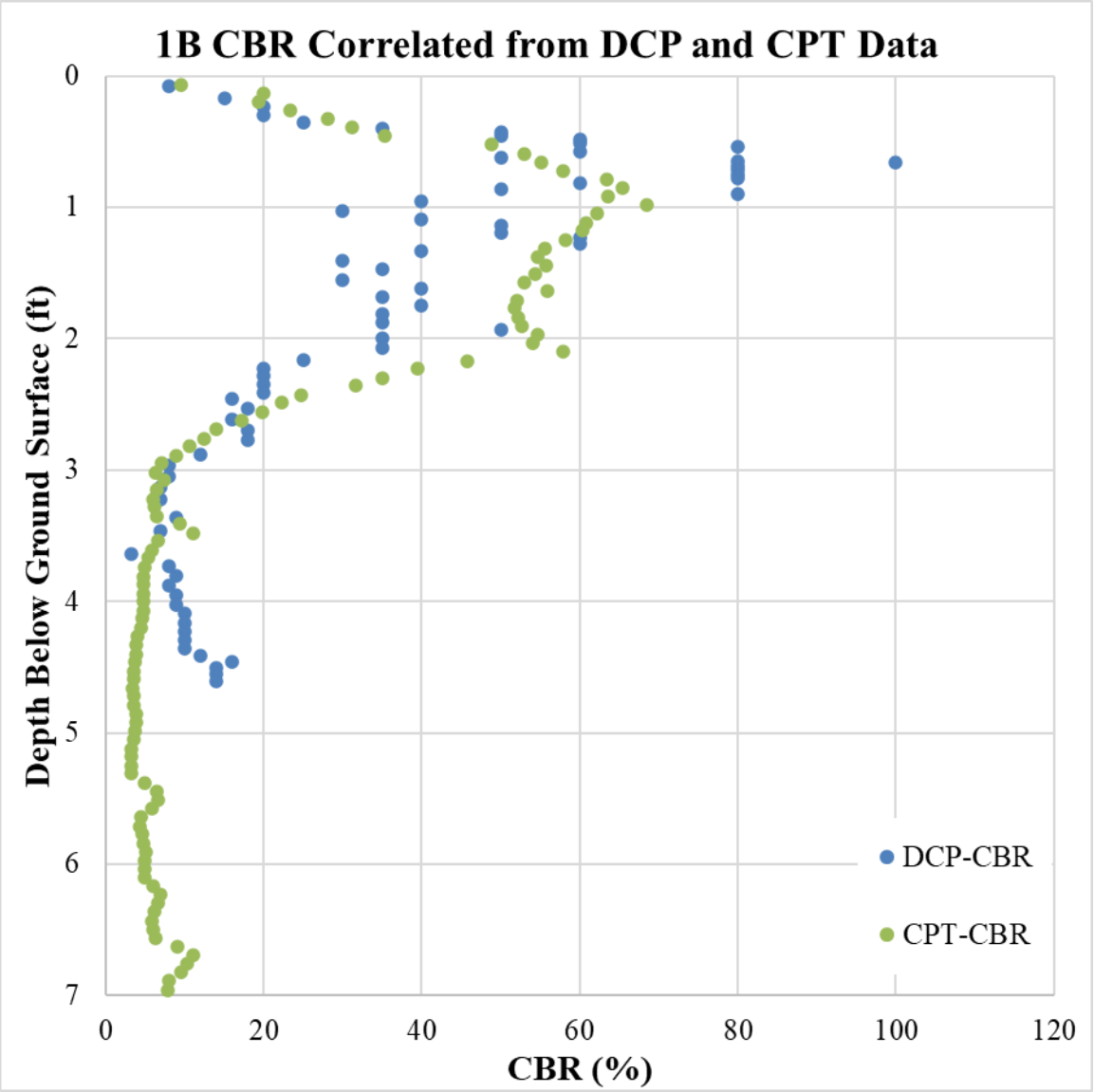

Figure A.2 Graph of correlated DCP and CPT data to CBR values for location 1B

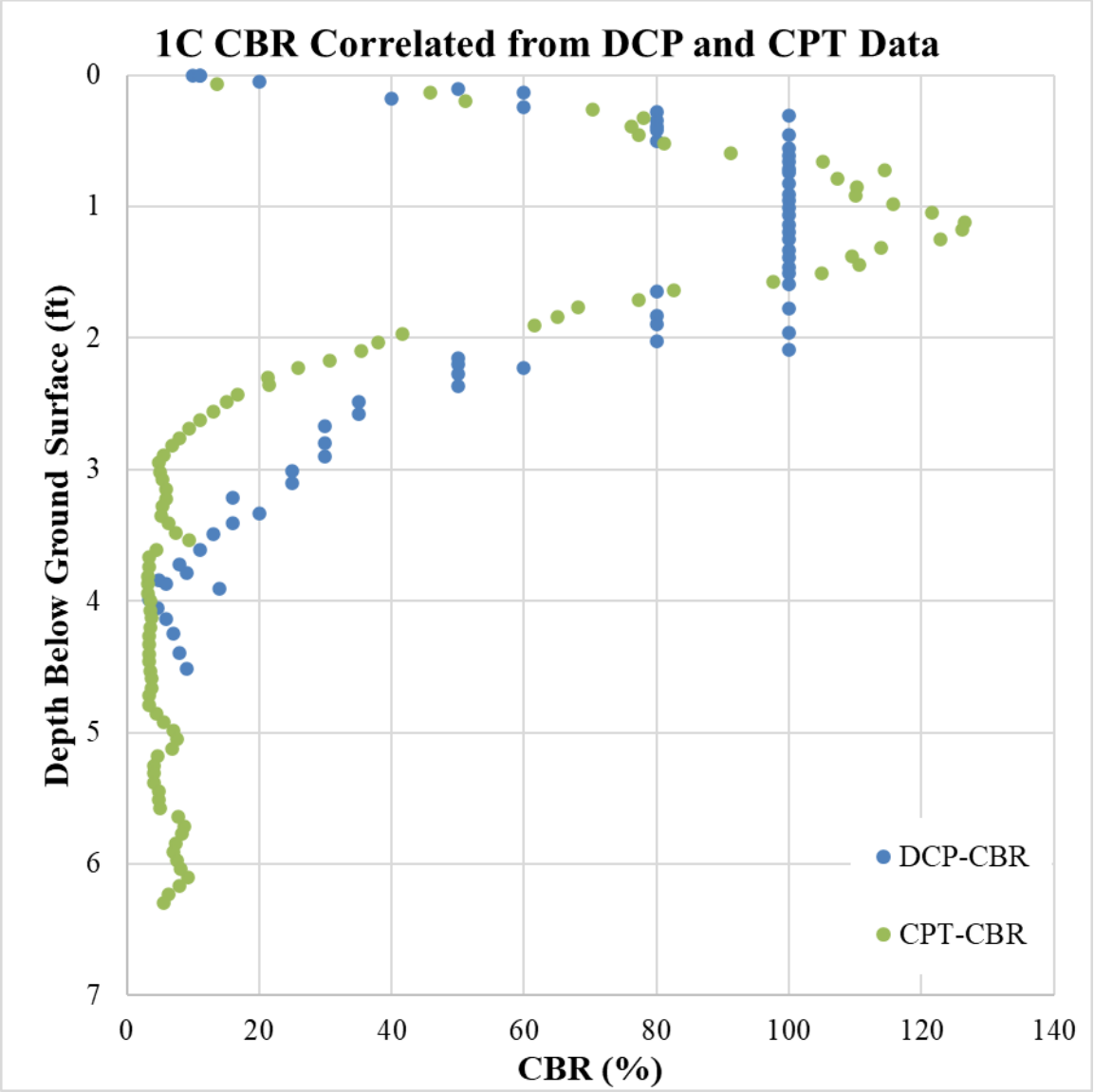

Figure A.3 Graph of correlated DCP and CPT data to CBR values for location 1C

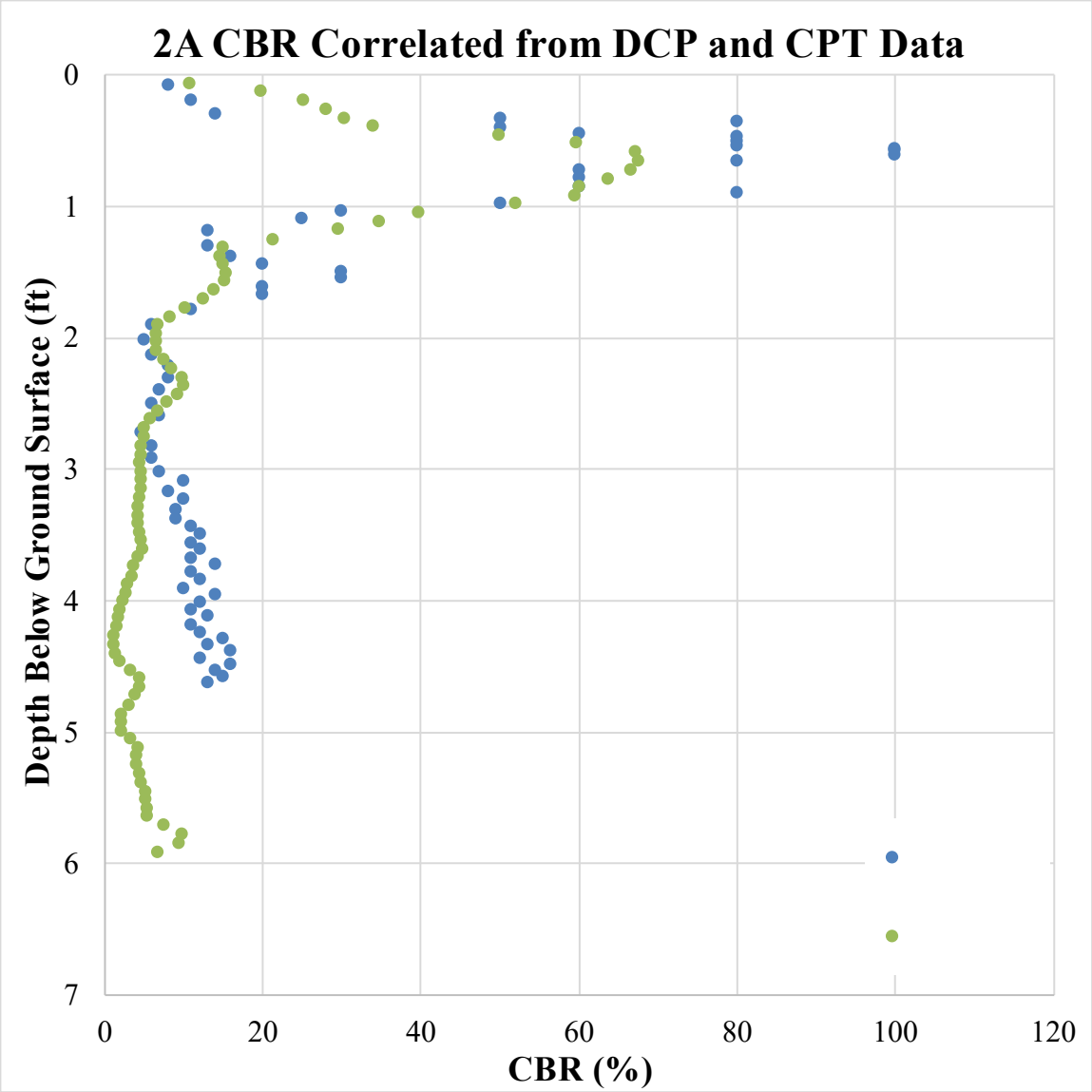

Figure A.4 Graph of correlated DCP and CPT data to CBR values for location 2A

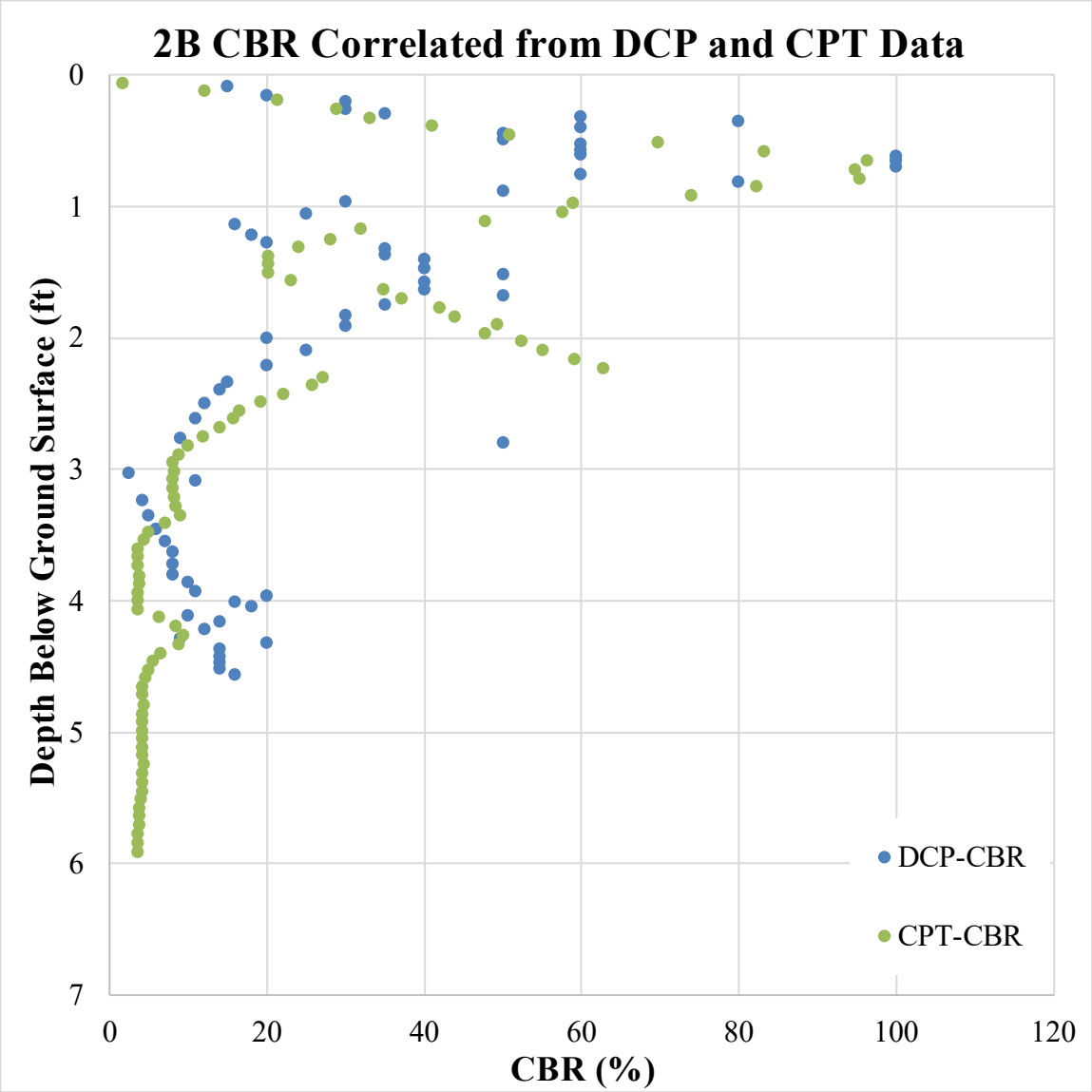

Figure A.5 Graph of correlated DCP and CPT data to CBR values for location 2B

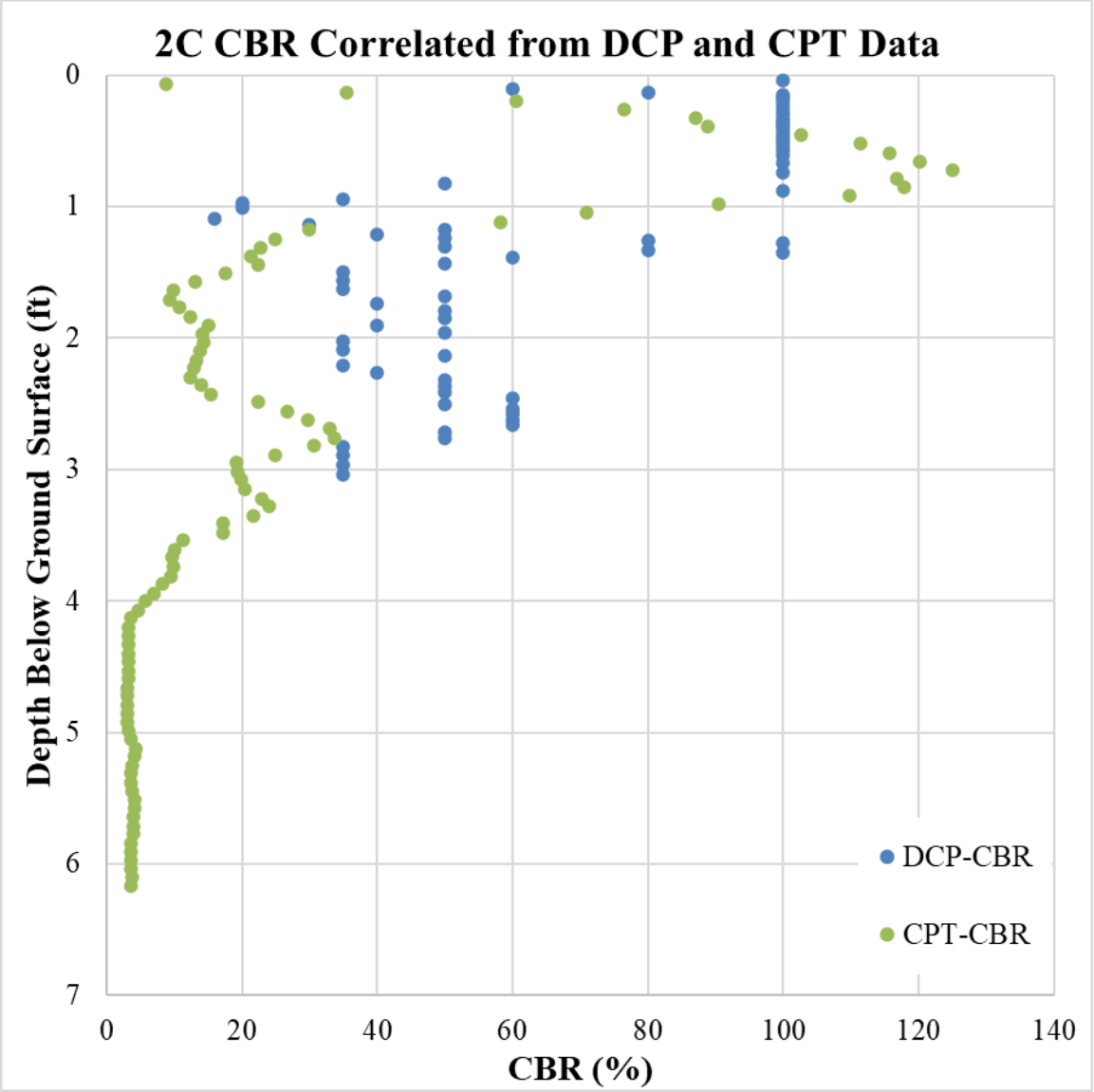

Figure A.6 Graph of correlated DCP and CPT data to CBR values for location 2C

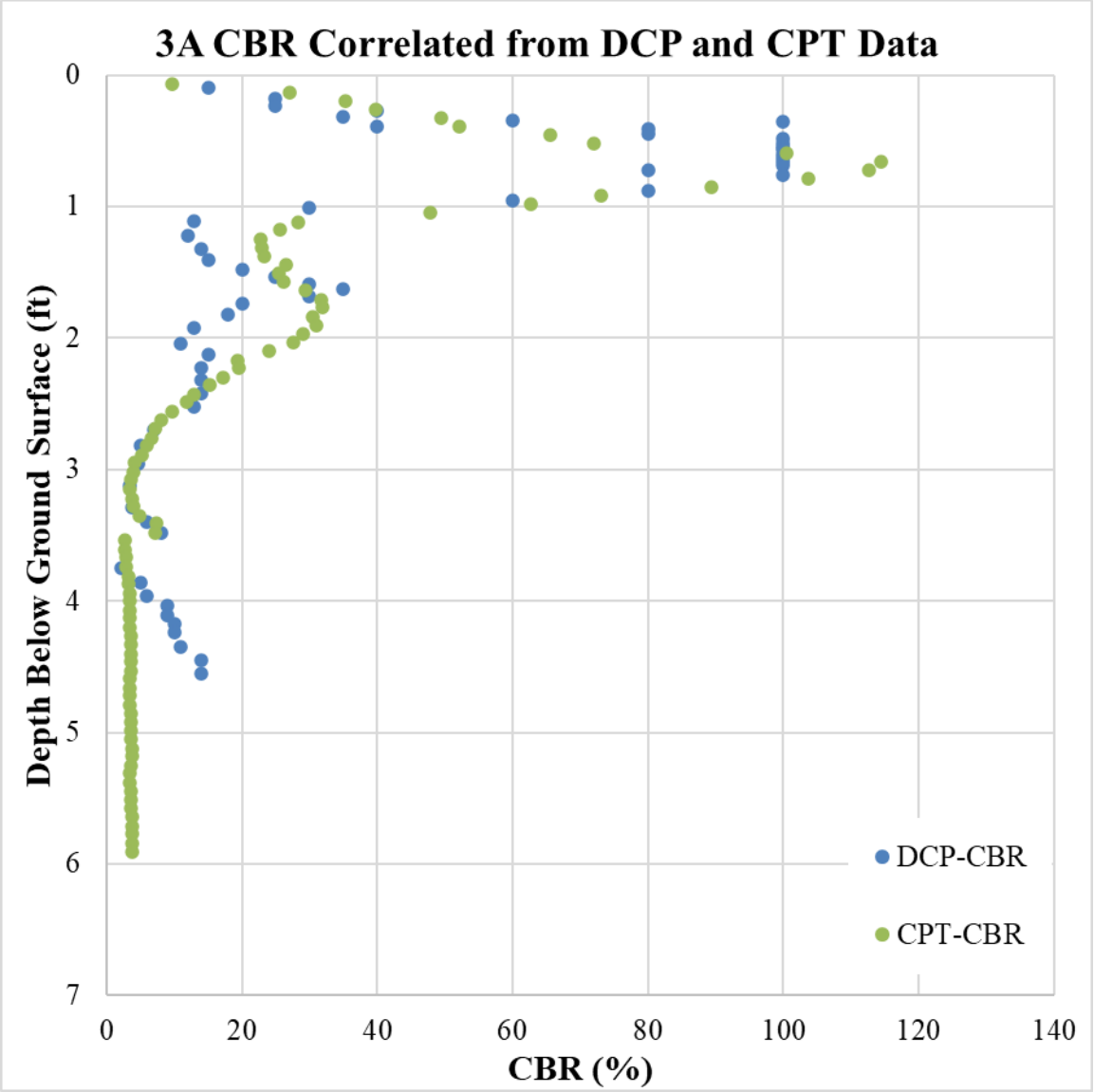

Figure A.7 Graph of correlated DCP and CPT data to CBR values for location 3A

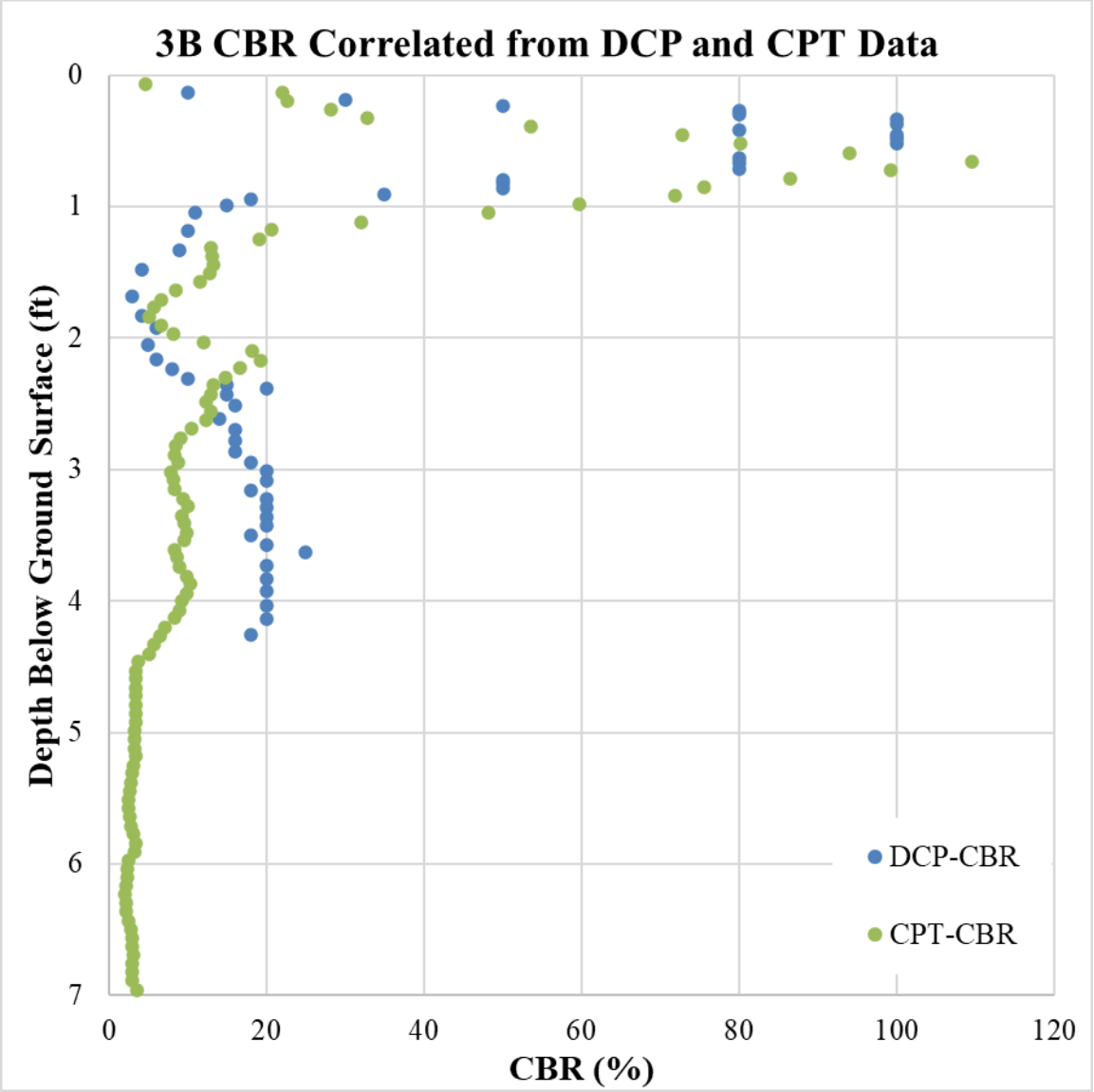

Figure A.8 Graph of correlated DCP and CPT data to CBR values for location 3B

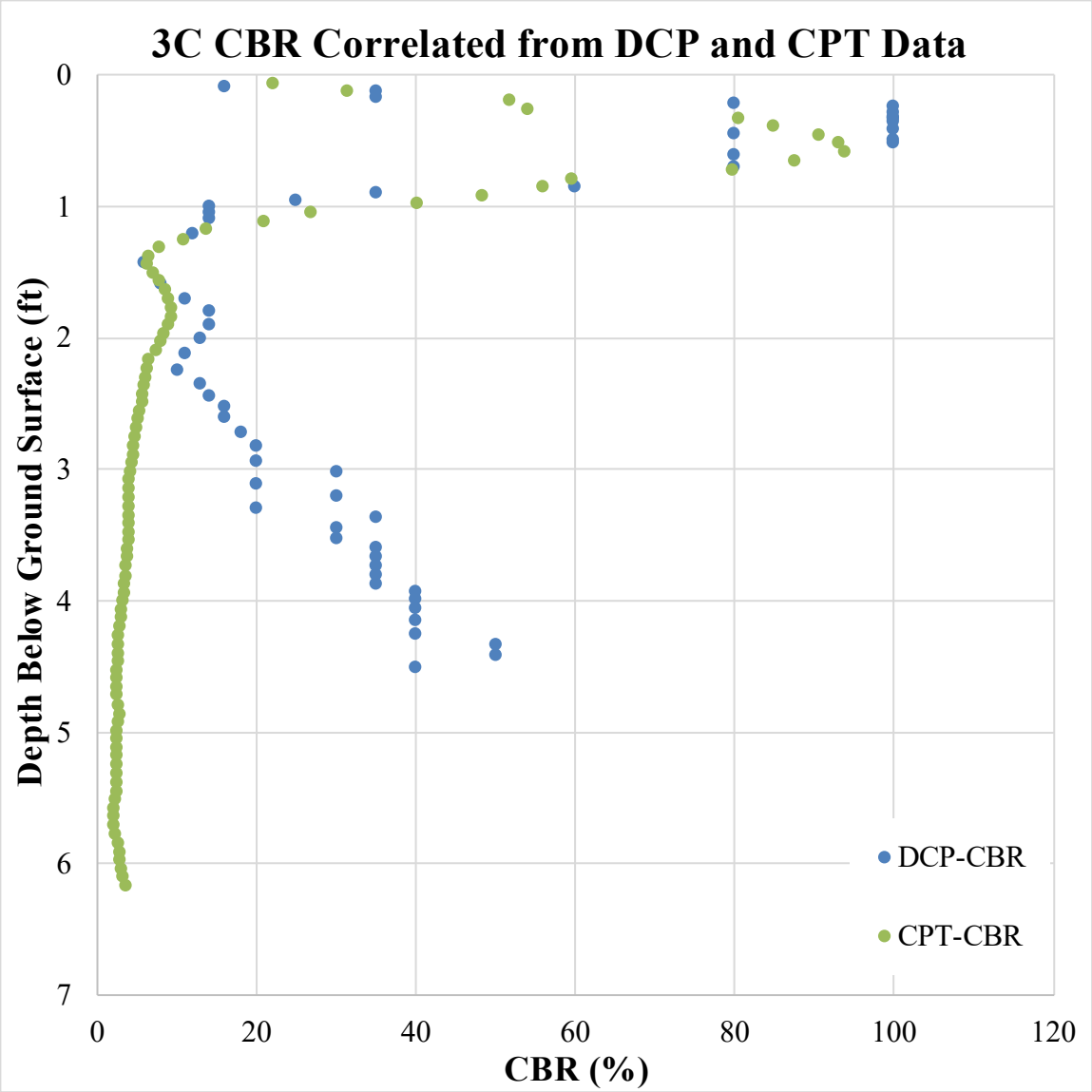

Figure A.9 Graph of correlated DCP and CPT data to CBR values for location 3C

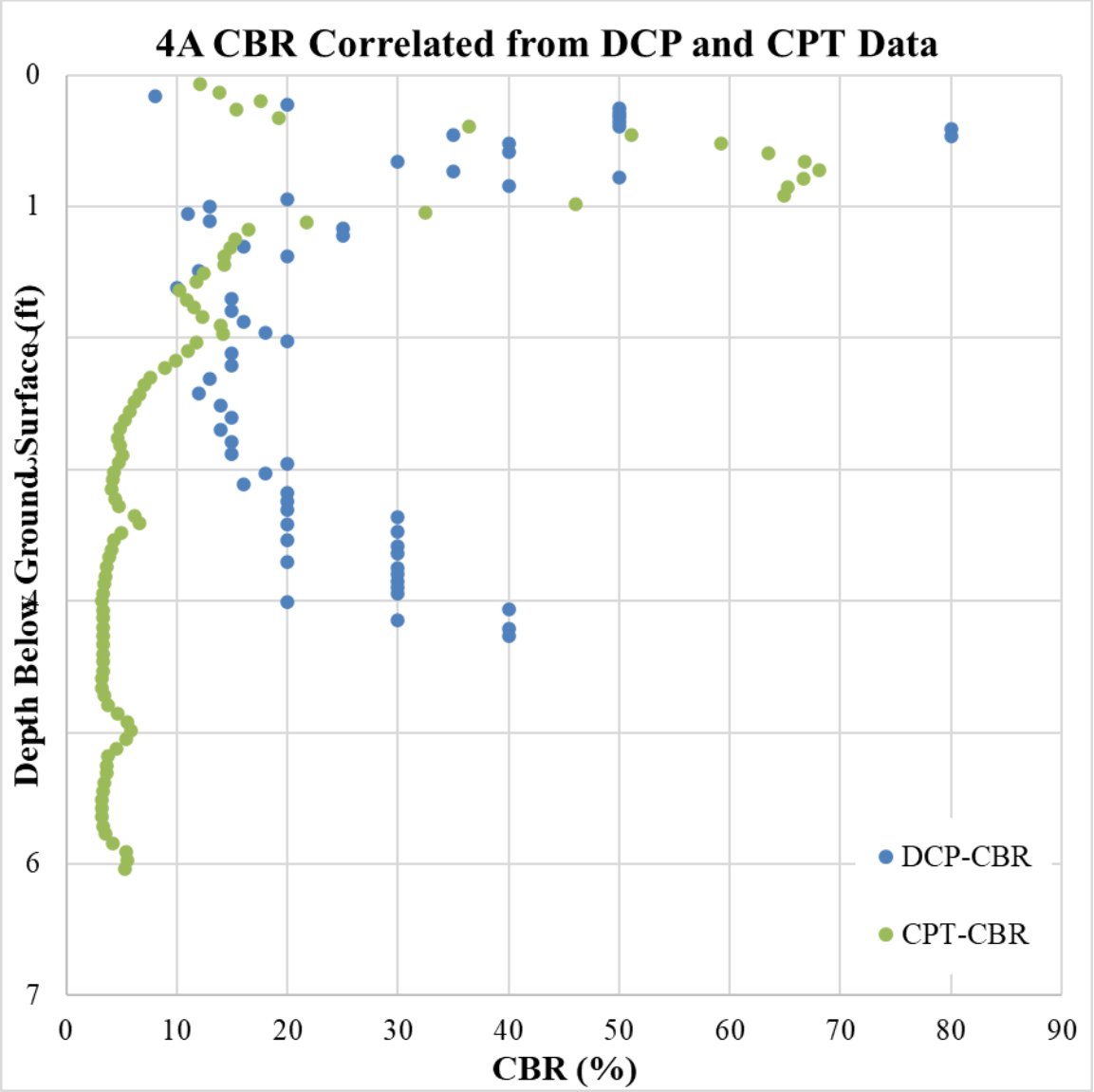

Figure A.10 Graph of correlated DCP and CPT data to CBR values for location 4A

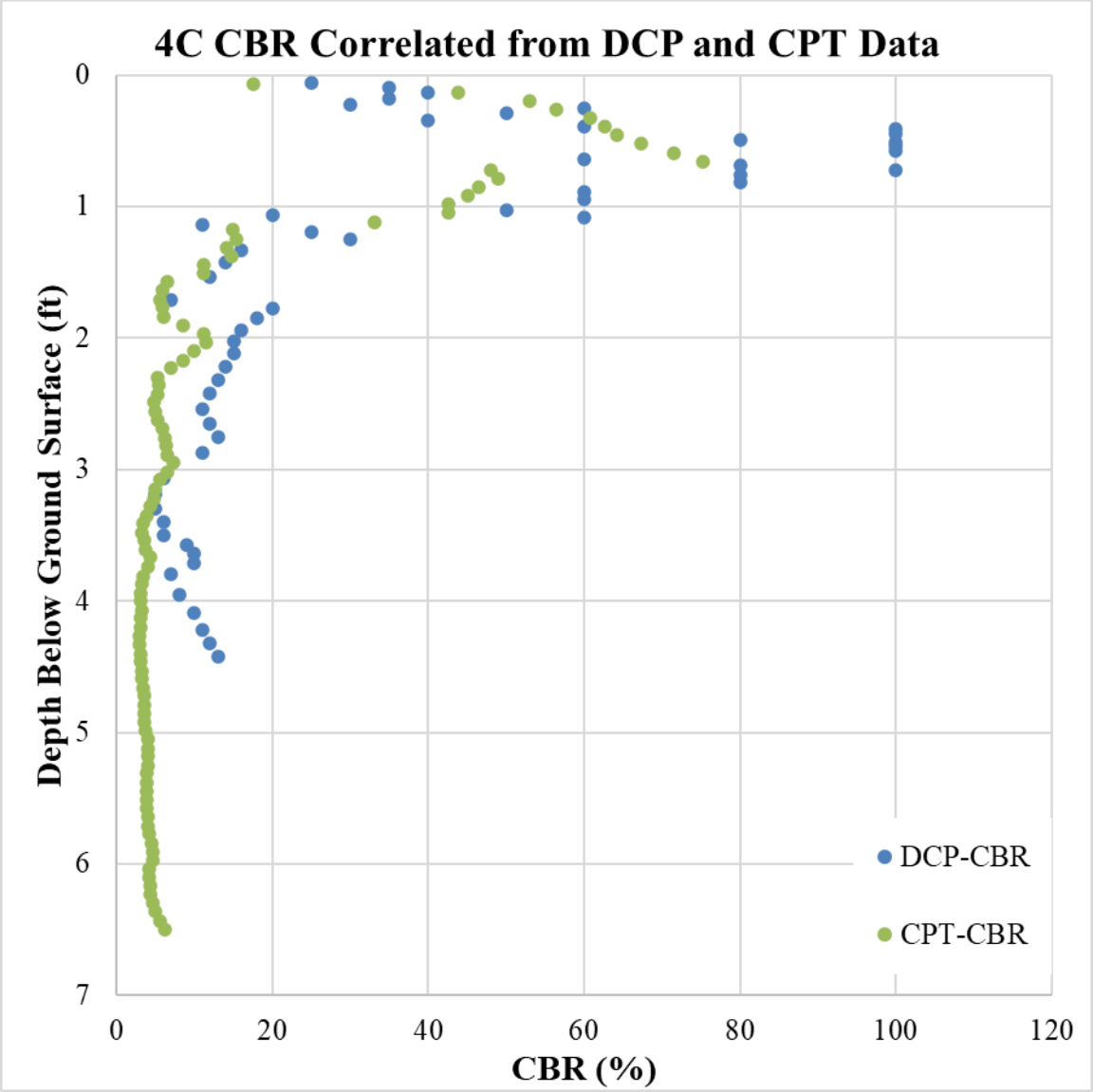

Figure A.11 Graph of correlated DCP and CPT data to CBR values for location 4C